Published in Journals: Minerals and Applied Sciences

Topic Reprint

Failure Characteristics of Deep Rocks, Volume II

Edited by
Zhenyu Han, Diyuan Li and Xin Cai

mdpi.com/topics

MDPI

Failure Characteristics of Deep Rocks, Volume II

Failure Characteristics of Deep Rocks, Volume II

Topic Editors

Zhenyu Han
Diyuan Li
Xin Cai

MDPI

Basel • Beijing • Wuhan • Barcelona • Belgrade • Novi Sad • Cluj • Manchester

Topic Editors

Zhenyu Han
School of Resources and Safety Engineering
Central South University
Changsha
China

Diyuan Li
School of Resources and Safety Engineering
Central South University
Changsha
China

Xin Cai
School of Resources and Safety Engineering
Central South University
Changsha
China

Editorial Office
MDPI AG
Grosspeteranlage 5
4052 Basel, Switzerland

This is a reprint of the Topic, published open access by the journals *Minerals* (ISSN 2075-163X) and *Applied Sciences* (ISSN 2076-3417), freely accessible at: https://www.mdpi.com/topics/F4E841319N.

For citation purposes, cite each article independently as indicated on the article page online and as indicated below:

Lastname, A.A.; Lastname, B.B. Article Title. *Journal Name* **Year**, *Volume Number*, Page Range.

ISBN 978-3-7258-6968-8 (Hbk)
ISBN 978-3-7258-6969-5 (PDF)
https://doi.org/10.3390/books978-3-7258-6969-5

Contents

minerals

MDPI

Article

Study on Stability Control Mechanism of Deep Soft Rock Roadway and Active Support Technology of Bolt-Grouting Flexible Bolt

Hao Zhang [1,2], Yingming Li [1,2,*], Xiangjun Wang [1,2], Shoudong Yu [3] and Yi Wang [1,2]

[1] State Key Laboratory of Deep Coal Mine Mining Response and Disaster Prevention and Control, Anhui University of Science and Technology, Huainan 232001, China
[2] School of Mining Engineering, Anhui University of Science and Technology, Huainan 232001, China
[3] Suzhou Qinan Industry and Trade Co., Ltd., Suzhou 234000, China
* Correspondence: yingmingli@aust.edu.cn; Tel.: +86-158-5544-9842

Abstract: In order to study the stability control mechanism of deep soft rock roadway and the active support technology of the anchor-grouting flexible bolt, this paper takes the west wing transportation roadway of Yuandian No. 2 Coal Mine of Huaibei Mining Co., Ltd., Huaibei, China as the research background. By analyzing the occurrence conditions and failure characteristics of the surrounding rock of the west wing transportation roadway and the structural characteristics and mechanical properties of the anchor-grouting flexible bolt, combined with the elastic–plastic and superimposed arch theory analysis, the superposition community theoretical model and the superposition joint support scheme of "bolt (cable) + anchor net + anchor-grouting flexible bolt + shotcrete support" are proposed. The reliability of the combined support scheme is analyzed by FLAC 3D numerical simulation software and field experiment. The results show that the maximum roof-to-floor convergence and two-side convergence of the west wing transportation roadway are only 30.7 mm and 27.1 mm after adopting the combined support scheme, and the deep displacement variation is within 7 mm, which can effectively maintain the stability of the roadway. The combined support scheme has a certain reference value for other similar roadways.

Keywords: anchor-grouting flexible bolt; deep soft rock roadway; superimposed community; FLAC 3D numerical simulation; combined support

1. Introduction

With the progress of our society and the development of the economy, the demand for coal is also increasing every day [1,2]. In order to improve coal production better and faster, the mining depth of China's mines has continued to extend downward since the 1980s. The average depth of vertical shafts has reached 600 m. At present, it is developing to the deep at an average speed of 10–20 m/year. The mining depth is getting deeper and deeper, and the difficulty of mining is also increasing [3,4]. At present, there is little coal left in the shallow part of the Huaibei mining area, and the buried depth of the new roadway is increasing [5,6]. With the increase in the buried depth of the new roadway, the geological conditions become complicated and diverse, especially the soft rock roadway. The traditional bolt support has been unable to effectively control the deformation of the roadway, and the safety is poor, which can not meet the design requirements and bring great safety hazards to coal mine production [7,8].

In order to solve the support problem of deep soft rock roadway, domestic and foreign scholars have performed a lot of research on its support theory and method [9,10]. Additionally, the combined support system is proposed to reinforce the surrounding rock of the roadway [11,12]. Guo et al. [13] studied the coupling support technology of soft rock roadway in Hecaogou No. 2 Mine, Yan'an, China. Wang et al. [14] studied the high-strength

prestressed coupling support technology in deep, extremely soft areas. Zhang et al. [15] used the orthogonal numerical experiment of FLAC 3D to study the influence of the change in bolt parameters and plastic yield zone on the deformation of the roadway's surrounding rock, which provided a basis for optimizing the support design of coal mine roadways. Wu et al. [16] proposed the support concept of "high pre-stress asymmetry" and the combined support method of the bolt, wire mesh and anchor cable, and verified the rationality of the support scheme through numerical simulation. Wang et al. [17] studied the failure mechanism of soft rock and roadways in deep coal mines. Feng et al. [18] analyzed the factors affecting the deformation and failure mechanism of deep roadways based on the space–time deformation distribution of 2233 working faces in the Fuxin Hengda Coal Mine, Fuxin, China. Zhang et al. [19] analyzed the energy evolution law of the surrounding rock of roadways under different roof strengths. Qin et al. [20] proposed a reinforcement scheme for deep dynamic soft rock roadway and applied it. Skrzypkowski et al. [21] used RS3 numerical software based on finite element method to establish a rock mass model with faults. Zhu et al. [22] used the numerical simulation method to study the influence of original geological conditions, strengthening the elastic modulus of the floor, strengthening the strength of side wall rock, and increasing the thickness of floor rock on the displacement of the roadway floor.

This paper takes the west wing transportation roadway of Yuandian No. 2 Coal Mine of Huaibei Mining Co., Ltd. as the research background. Based on the analysis of the occurrence conditions and deformation characteristics of the surrounding rock of the west wing transportation roadway, the structure and mechanical properties of the anchor-grouting flexible bolt and the difficulty of the original support scheme to maintain the stability of the current excavation roadway [23,24], put forward the superposition combined support scheme of "bolt (cable) + anchor net + anchor-grouting flexible bolt + shotcrete support". Additionally, the reliability of the combined support scheme is analyzed by FLAC 3D numerical simulation software and a field experiment. The combined support scheme has a certain reference value for other similar roadways.

2. Deformation Mechanism of Surrounding Rock in Deep Soft Rock Roadway

2.1. Background

The west wing transportation roadway of Yuandian No.2 Coal Mine belongs to Yuandian No.2 Coal Mine of Bozhou Coal Industry Co., Ltd. in the Huaibei Mining Area of Anhui Province. The geographical location of Yuandian No.2 Mine is shown in Figure 1. The location of the west wing transport lane is shown in Figure 2.

Figure 1. Location of Yuandian No.2 Mine.

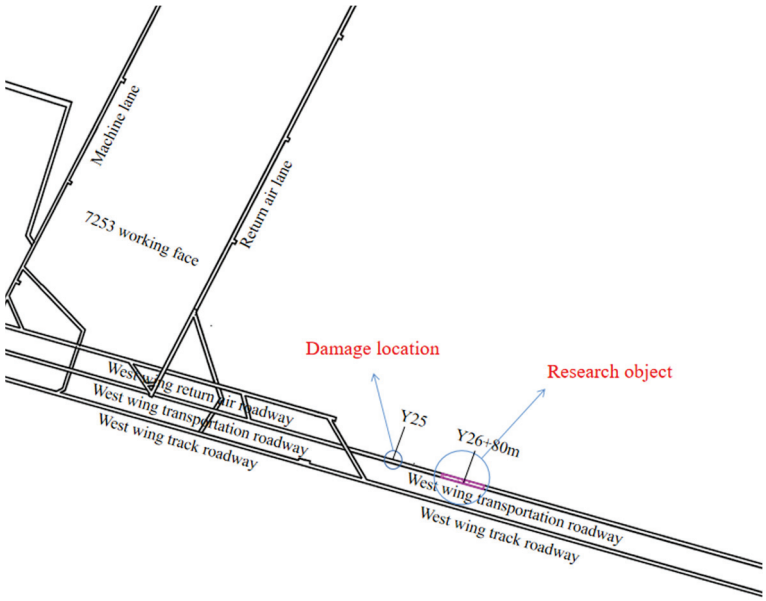

Figure 2. Location of west wing transportation roadway.

The elevation of the west wing transport roadway is −745~−740.7 m, the south is adjacent to the west wing return air roadway, the north is close to the west wing track roadway, and the west is to the JF245 fault, with an average dip angle of 20°. The construction horizon of the west wing transportation roadway is located in the roof of the No.6 coal seam. The lithology is mainly mudstone, siltstone and sandstone. The comprehensive state diagram of the surrounding rock column of the roadway is shown in Figure 3.

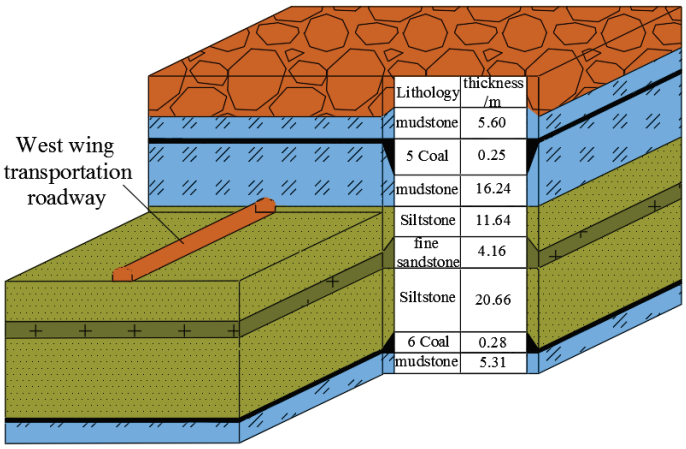

Figure 3. Comprehensive histogram of surrounding rock in Yuandian No.2 Mine.

2.2. Deformation Monitoring and Analysis of West Wing Transport Roadway

The roadway section of the west wing transportation roadway is a three-center arch, and the section size is 5.0 m × 3.6 m. The original support scheme is the ordinary anchor net spray support combined with an anchor bolt, anchor cable, anchor net and shotcrete. The support is supported by a Φ22 mm × 2800 mm rebar bolt. The row spacing is 500 mm × 800 mm. The two sides and the roof are driven into the Φ22 mm × 6200 mm anchor cable, and the row spacing is 1600 mm × 1600 mm. The 100 mm × 100 mm steel bar is used to weld the warp and weft net, and the concrete with the strength grade of C20 is used to seal the surrounding rock of the roadway. Under the original support condition, the roof and side of the roadway are seriously broken, the convergence of the two sides is large and the roof subsidence is serious, which seriously affects the stability of the roadway; the failure characteristics of the roadway are shown in Figure 4. Six surface

displacement observation stations were selected in the original support scheme of the west wing transport roadway. Each observation station was 20 m apart. The observation station was located at Y25 and 305 m away from the return airway of 7253 working face. The observation results are shown in Figure 5: the maximum roof and floor convergence of the west wing transport roadway is 496.5 mm, and the maximum two sides convergence is 416.5 mm. The displacement of the roof, floor and two sides is very large, and has exceeded the current maximum displacement deformation of the west wing transportation roadway. Reasonable support measures need to be taken to maintain the stability of the roadway.

(**a**) (**b**)

Figure 4. Damage characteristics of west wing transportation roadway. (**a**) Roof fracture. (**b**) Cracking on side of roadway.

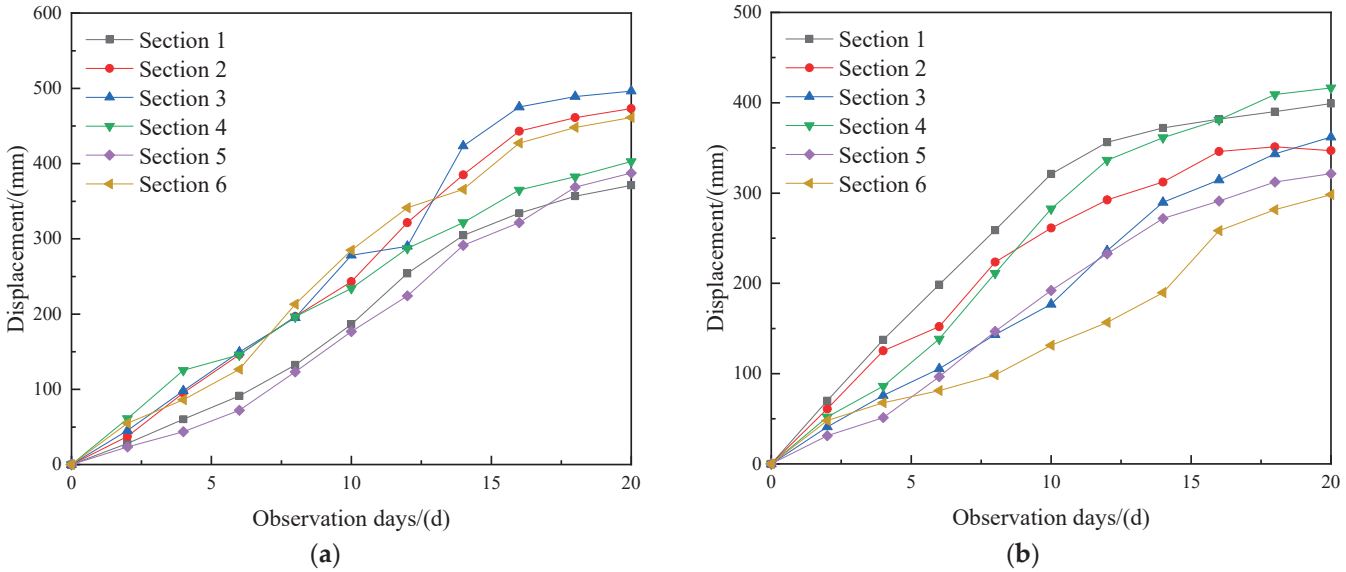

(**a**) (**b**)

Figure 5. Displacement of transportation roadway in the west wing under the original support scheme. (**a**) Top and bottom. (**b**) Two sides.

2.3. Analysis of Roadway Failure Mechanism

According to the field monitoring and research of the west wing transportation roadway and the analysis of similar roadways at home and abroad, the specific factors affecting the deformation and instability of the west wing transportation roadway are as follows: (1) The burial depth is large. The elevation of the transportation roadway in the west wing is about 740 m, and the surrounding rock pressure of the roadway is large, which makes the surrounding rock loose and difficult to control [25,26]. (2) The strength of the

surrounding rock is low. The surrounding rock of the transportation roadway in the west wing is mainly composed of mudstone, sandstone and siltstone, with low strength and poor stability [27,28]. (3) Unreasonable roadway support mode. The original support scheme of the west wing transportation roadway adopts the support method of a bolt, anchor mesh and shotcrete to reinforce the surrounding rock of the roadway, which is mainly passive support and cannot fully mobilize the self-supporting capacity of the surrounding rock.

3. Roadway Stability Control

3.1. Roadway Stability Control Technology

The section of the west wing transport roadway is a three-center arch. According to the elastoplastic theory [29], the displacement of the roadway surface and the radius of the plastic zone can be expressed as follows:

$$R = a\left[\frac{(p_0 + c \cdot \cot\varphi)(1 - \sin\varphi)}{p_i + c \cdot \cot\varphi}\right]^{\frac{1-\sin\varphi}{2\sin\varphi}} \tag{1}$$

$$u = B_0 R\left(\frac{R}{a}\right)^{(1+\eta)} \tag{2}$$

$$K = \frac{1 + \sin\varphi}{1 - \sin\varphi} \tag{3}$$

$$B_0 = \frac{(1+\mu)[(K-1)P_0 + \sigma_C]}{(\mathrm{K}+1)E} \tag{4}$$

Combined with Formulas (1)–(4), we can obtain the following:

$$u = \frac{(1+\mu)\left[\left(\frac{1+\sin\varphi}{1-\sin\varphi} - 1\right)p_0 + \sigma_c\right]R^{(2+\eta)}}{E\left(\frac{1+\sin\varphi}{1-\sin\varphi} + 1\right)a^{(1+\eta)}} \tag{5}$$

In the formula, a—equivalent radius, m; p_0—original rock stress, MPa; c—cohesion, MPa; φ—internal friction angle, °; p_i—support resistance, MPa; η—shearing gradient; μ—Poisson's ratio; R—radius of the plastic zone, m; E—modulus of elasticity, GPa; u—roadway surface displacement, m; K—side pressure coefficient; and σ_c—compressive strength, MPa.

From Formulas (1) and (5), it can be seen that the support resistance p_i, cohesion c and internal friction angle φ will affect the size of the plastic zone radius R and surface displacement u of the roadway. Therefore, the change law of the plastic zone radius R and surface displacement u of the roadway can be studied by changing the support resistance p_i, cohesion c and internal friction angle φ. The relationship curves of support resistance p_i, cohesion c and internal friction angle φ with plastic zone radius R and roadway surface displacement u are shown in Figure 6.

It can be seen from Figure 6 that when the cohesion c and the friction angle φ are constant, as the support resistance p_i increases from 0 MPa to 2 MPa, the radius R of the plastic zone decreases from 4.15 m to 3.58 m, and the surface displacement u decreases from 337.72 mm to 188.06 mm. When the support resistance p_i and friction angle φ are constant, as the cohesion c increases from 3.1 MPa to 5.1 MPa, the plastic zone radius R decreases from 3.94 m to 3.45 m, and the surface displacement u decreases from 275.3 mm to 161.62 mm. When the support resistance p_i and cohesion c are constant, with the increase in friction angle φ from 34° to 54°, the radius of plastic zone R decreases from 3.98 m to 3.14 m, and the surface displacement u decreases from 285.5 mm to 115.02 mm.

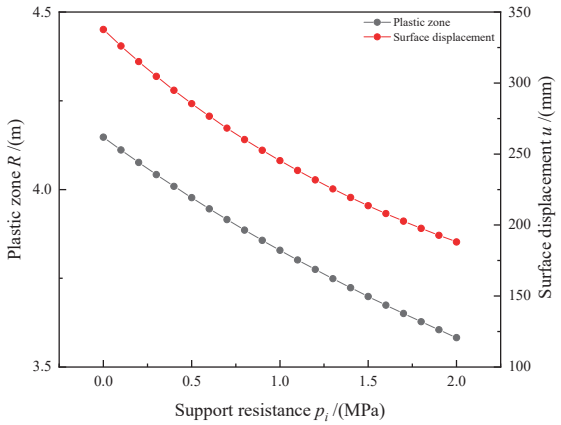

H = 740 m, η = 2, μ = 0.24, E = 0.7 GPa, σ_c = 32 GPa, a = 3 m, p_0 = 18.5 MPa, p_i = 0–2 MPa

(**a**)

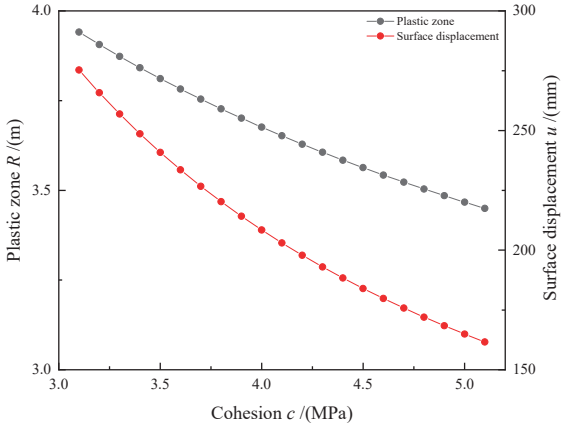

H = 740 m, η = 2, μ = 0.24, E = 0.7 GPa, σ_c = 32 GPa, a = 3 m, p_0 = 18.5 MPa, c = 3.1–5.1 MPa

(**b**)

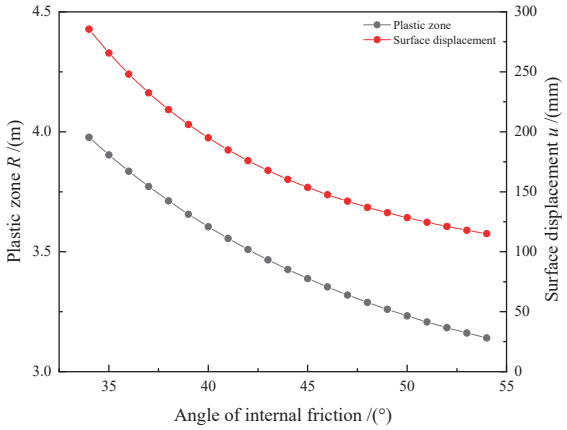

H = 740 m, η = 2, μ = 0.24, E = 0.7 GPa, σ_c = 32 GPa, a = 3 m, p_0 = 18.5 MPa, φ = 34°–54°

(**c**)

Figure 6. Curve of plastic zone radius R and roadway surface displacement u. (**a**) The relationship curve of support resistance p_i with plastic zone radius R and roadway surface displacement u; (**b**) The curve diagram of the relationship between cohesion c and plastic zone radius R, roadway surface displacement u; (**c**) The relationship curve of internal friction angle φ with plastic zone radius R and roadway surface displacement u.

3.2. Superposition Community Stability Principle

Through the above analysis, it can be seen that although the radius R of the plastic zone and the surface displacement u of the roadway decrease with the increase in the support resistance p_i, cohesion c and friction angle φ, the variation is also decreasing, indicating that only increasing the support resistance p_i, cohesion c and friction angle φ can not maintain the long-term stability of the roadway. Therefore, while improving the support resistance p_i, cohesion c and friction angle φ, increasing the bearing capacity of the superimposed arch, fully mobilizing the self-bearing capacity of the surrounding rock of the roadway, and maintaining the stability of the roadway should also be considered together. According to the theory of the superimposed arch [30], the bearing capacity of a superimposed arch can be expressed as follows:

$$q' = \frac{2Q_s(1+\sin\varphi_b)(l_s\tan a - D_a)}{D_a D_l \tan a(1-\sin\varphi_b)(2R_0 + l_s - D_a)} + \frac{2Q_c(1+\sin\varphi_b)\left(l_c\tan a' - D_a{}'\right)}{D_a{}'D_l{}'\tan a'(1-\sin\varphi_b)\left(2R_0 + l_c - D_a{}'\right)} \quad (6)$$

In the formula: q'—bearing capacity of the superimposed arch, kN; l_s—effective length of anchor bolt, m; l_c—effective length of anchor cable, m; Q_s—pullout force of anchor bolt,

kN; Q_c—pulling force of anchor cable, kN; D_a—anchor spacing, m; D_l—bolt row spacing, m; D_a'—anchor cable spacing, m; D_l'—anchor cable spacing, m; a—anchor bolt control angle, 45°; a'—anchor cable control angle, 45°; φ_b—internal friction angle of rock in the loose zone, taken as 34°; and R_0—roadway radius, m. (The effective length of the bolt and anchor cable refers to the effective length of the part of the bolt and anchor cable in the surrounding rock playing the role of anchoring).

In order to study the influence of the effective length l_s (l_c) of the anchor bolt (cable) and the row spacing D_a (D_a') of the anchor (cable) on the bearing capacity q' of the superimposed arch, the relationship curves between the effective length l_s (l_c) of the anchor bolt (cable), the spacing D_a (D_a') of the anchor (cable), the row spacing D_l (D_l') and the bearing capacity q' of the superimposed arch are drawn, as shown in Figure 7.

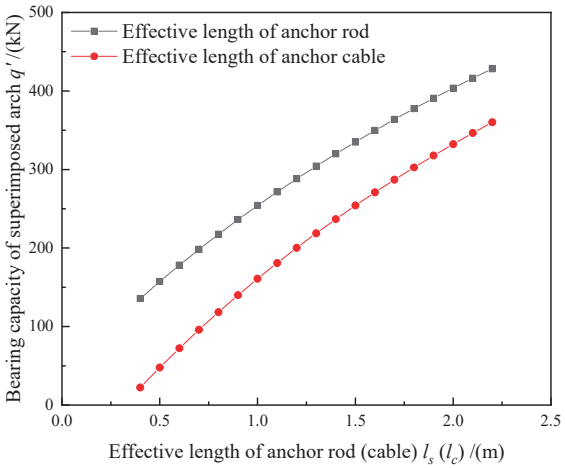

Q_s=100 kN, Q_c=200 kN, φ_b=34°, a = 45°, a' = 45°, R_0=2.5 m, l_s (l_c) = 0.4–2.2 m

(**a**)

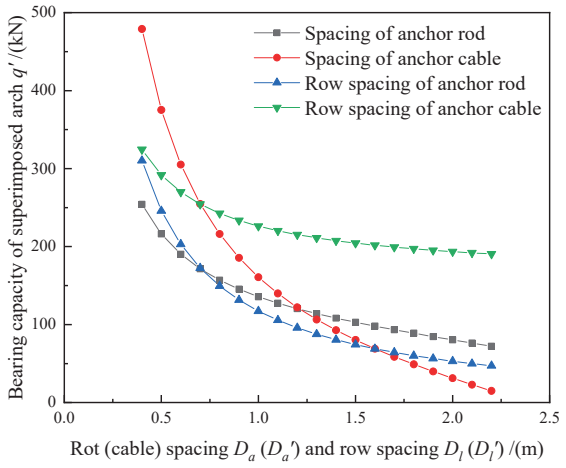

Q_s=100 kN, Q_c=200 kN, φ_b=34°, a = 45°, a' = 45°, R_0=2.5 m, D_a (D_a') = 0.4–2.2 m, D_l (D_l') = 0.4–2.2 m

(**b**)

Figure 7. Relation curve between effective length of anchor bolt (cable) l_s (l_c), spacing D_a (D_a'), row spacing D_l (D_l') and bearing capacity q' of superimposed arch. (**a**) The relationship curve between the effective length l_s (l_c) of bolt (cable) and the bearing capacity q' of superimposed arch; (**b**) The relationship curve between the spacing D_a (D_a'), the row spacing D_l (D_l') and the bearing capacity q' of the superimposed arch.

When the spacing D_a (D_a') and the row spacing D_l (D_l') are fixed, the bearing capacity q' of the superimposed arch increases with the increase in the effective length l_s (l_c) of the bolt (cable). When the effective length l_s (l_c) and the row spacing D_l (D_l') of the anchor bolt (cable) are constant, with the increase in the spacing D_a (D_a') of the anchor bolt (cable), the bearing capacity q' of the superimposed arch decreases from 254.18 kN (479.04 kN) to 72.27 kN (14.96 kN), which decreases by 181.9 kN (464.09 kN). When the effective length l_s (l_c) and spacing D_a (D_a') of the anchor bolt (cable) is constant, with the increase in the row spacing D_l (D_l') of the anchor bolt (cable), the bearing capacity q' of the superimposed arch decreases from 310.29 kN (324.53 kN) to 47.19 kN (190.55 kN), which decreases by 263.09 kN (133.98 kN). From Figure 6b, it can be seen that although the bearing capacity q' of the superimposed arch decreases with the increase in the spacing D_a (D_a') and the row spacing D_l (D_l') of the anchor bolt (cable), and although the bearing capacity q' of the superimposed arch decreases with the increase in the spacing D_a (D_a') and the row spacing D_l (D_l') of the anchor bolt (cable), the variation also decreases, so selecting the appropriate row spacing can not only improve the bearing capacity q' of the superimposed arch, but also reduce the use of anchor bolts (cable) and save construction costs.

$$q' = \ln_s Q_s + \ln_c Q_c \tag{7}$$

In the formula:

$$\ln_s = \frac{2(1+\sin\varphi_b)(l_s\tan a - D_a)}{D_a D_l \tan a(1-\sin\varphi_b)(2R_0 + l_s - D_a)} \tag{8}$$

$$\ln_c = \frac{2(1+\sin\varphi_b)\left(l_c\tan a' - D_a'\right)}{D_a' D_l' \tan a'(1-\sin\varphi_b)\left(2R_0 + l_c - D_a'\right)} \tag{9}$$

where $\ln_s$ is the degree of tension concentration coefficient of the anchor bolt, and $\ln_c$ is the degree of tension concentration coefficient of the anchor cable.

In order to study the influence of Q_s (Q_c) on q', the relationship curve between the pullout force Q_s (Q_c) of the bolt (cable) and the bearing capacity q' of the superimposed arch is drawn, as shown in Figure 8.

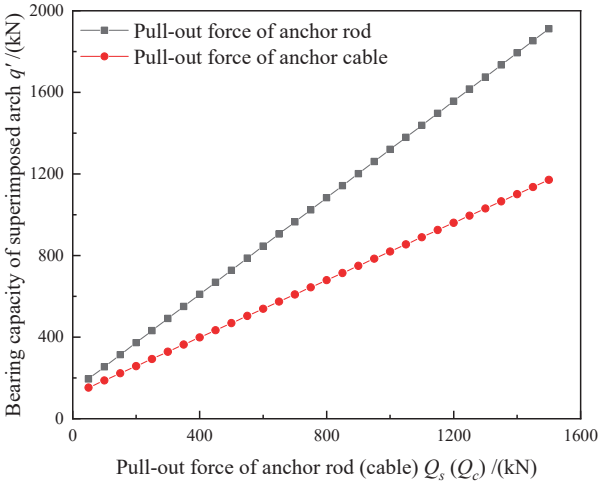

φ_b=34°, a = 45°, a' = 45°, l_s=1 m, $l_s l_c$=1.5 m, D_a=0.4 m, D_a' = 1.6 m, D_l=0.8 m, D_l' = 1.6 m, Q_s (Q_c) = 50–1500 kN

Figure 8. The relationship curve between the bearing capacity of bolt superimposed arch q' and the drawing force l of bolt (cable) Q_s (Q_c).

From Figure 8, it can be seen that the bearing capacity q' of the superimposed arch increases with the increase in the pullout force Q_s (Q_c) of the bolt (cable). The greater the pullout force Q_s (Q_c) of the bolt (cable), the greater the bearing capacity q' of the superimposed arch. In the process of roadway surrounding rock support, the bolt or anchor cable with greater strength of the bolt body is selected.

According to the above analysis, in order to maintain the long-term stability of the west wing transportation roadway in Yuandian No. 2 Coal Mine, a new support scheme that can not only improve the support resistance p_i, but also increase the cohesion c, internal friction angle φ and self-bearing capacity of the surrounding rock of the roadway is needed; that is, a "bolt (cable) + anchor net + anchor flexible bolt + shotcrete support" combined support. In the combined support scheme, the small pressure arch is formed by the mutual extrusion between the anchor bolt and the anchor bolt, the anchor bolt and the broken surrounding rock, and the large pressure arch is formed by the mutual compression combination between the anchor-grouting flexible anchor bolt and the anchor cable. Through high-pressure grouting, the slurry penetrates into the broken surrounding rock and even passes through the cracks with poor connectivity to form splitting grouting and broken surrounding rock. The small pressure arch formed between the anchor bolt and the anchor bolt, the small pressure arch formed between the anchor bolt and the broken surrounding rock, the large pressure arch formed between the anchor bolt and the anchor cable and the broken surrounding rock bonded by the grouting slurry are superimposed together to form a superposition community, which jointly maintains the stability of the

roadway. The schematic diagram of the superposition community structure is shown in Figure 9.

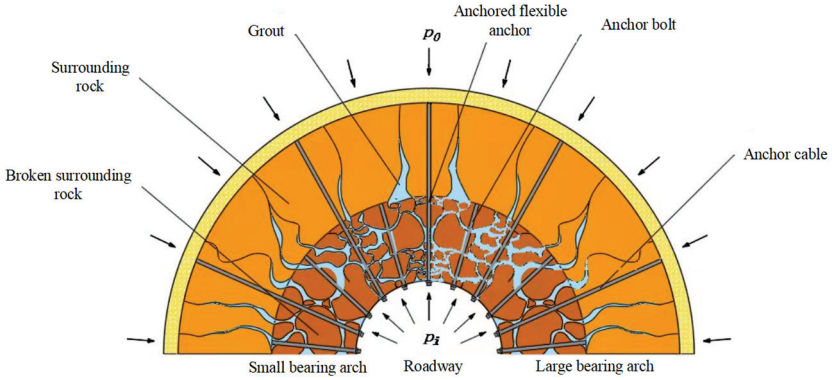

Figure 9. Schematic diagram of superimposed community structure.

3.3. Support Technical Scheme

3.3.1. Support Scheme

Based on the research background of the west wing transportation roadway of Yuandian No.2 Coal Mine of Huaibei Mining Co., Ltd., this paper puts forward the superposition combined support scheme of "bolt (cable) + anchor net + anchor flexible bolt + shotcrete support". This scheme innovatively puts forward the new combination mode of "bolt (cable) + anchor flexible bolt" to maintain the stability of the surrounding rock of the roadway.

3.3.2. Anchoring Flexible Bolt Technology

As shown in Figure 10, the bolt-grouting flexible bolt is composed of a steel strand bolt, fastening sleeve, nut, pressure ring, tray, self-locking plate and grouting device. With a high-strength steel strand as the bolt body, it is a kind of high-prestress anchoring bolt. Through the combination of nut, tray, self-locking plate and baffle on the joint of the grouting device, the steel strand bolt body does not rotate when tightening the nut, which can meet the design torque force requirements. The grouting device can facilitate grouting and realize the organic combination of full-length anchoring of bolt and grouting reinforcement of surrounding rock. In addition, the anchor-grouting flexible bolt adopts high-pressure grouting, and the grouting pressure is more than 3 MPa. Under the condition of high-pressure grouting, the slurry can not only flow through the gap between the broken surrounding rock but also pass through the cracks with poor connectivity to form splitting grouting and combine them to form a whole.

The installation comparison diagram of the anchored flexible bolt and ordinary bolt is shown in Figure 11. Compared with ordinary bolts, the structure of the anchored flexible bolt is simple, the construction is convenient and efficient, and the cost of the anchored flexible bolt is much lower than that of a traditional bolt and grouting support. In the early stage, it is used as an ordinary support bolt, and in the later stage, it is used as a grouting anchor cable. It only needs to be drilled and installed once, and it is not necessary to install the grouting bolt again, which greatly simplifies the construction steps. After installation, it can bear the load immediately, and the support strength is far more than that of the same specification ordinary grouting anchor bolt (cable). After grouting, the support is formed as a whole, which is very beneficial to ensure the support effect, which is far greater than the support effect of an ordinary anchor bolt (cable). The new bolt structure is adopted to minimize the diameter of the bolt body under the premise of ensuring smooth grouting, and the required installation aperture is small. The bolt structure itself meets the requirements of high-pressure grouting, and truly realizes the integration of anchor and grouting. Grouting is convenient and timely, and grouting can be arranged at a certain distance behind the head, so that the roadway can be reinforced in advance when it is

only deformed but not destroyed, reducing the amount of roadway maintenance. The mechanical properties parameters of the anchor-grouting flexible bolt are shown in Table 1.

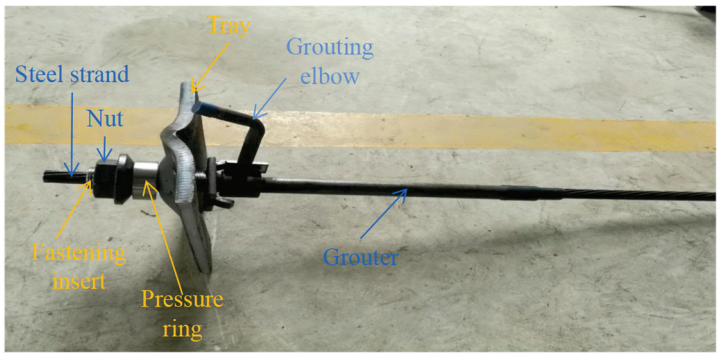

Figure 10. Anchor-grouting flexible bolt physical drawing.

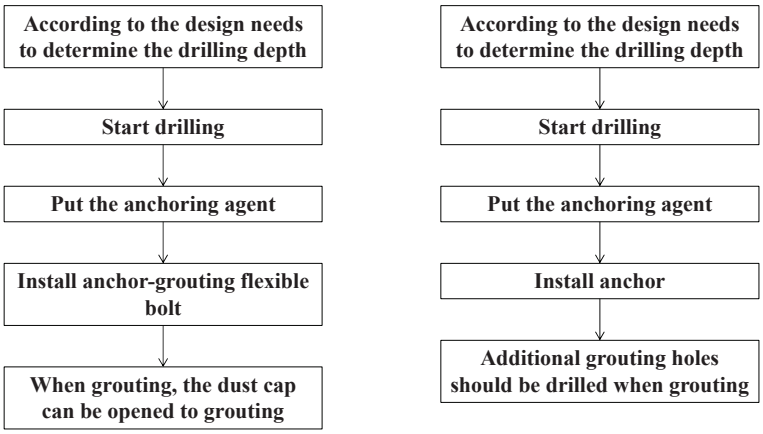

Figure 11. Installation comparison diagram of anchor-grouting flexible bolt and ordinary bolt.

Table 1. Mechanical performance parameter table of anchor-grouting flexible bolt.

Component Name	Mechanical Property	Technical Specifications	Test Result			Average Value
Bolt body	Maximum force of bolt body (kN)	≥583	601	602	600	601
	Bolt elongation (%)	≥3.5	5.2	5.4	5.7	5.4
Tail thread	Bearing capacity (kN)	≥524	532	532	537	534
Tray	Bearing capacity (kN)	≥524	541	541	541	541
Anchor bolt	Anchoring force (kN)	≥367	397	401	403	400

3.3.3. Combined Support Technology Design

After the above analysis, it is finally determined that the whole section of the west wing transport roadway is supported by a Φ22 mm × 2800 mm high-strength screw steel bolt, the row spacing is 500 mm × 800 mm, and each bolt is anchored by two K2950 resin anchoring agent. Two Φ22 mm × 6200 mm anchor cables are driven into the two sides, and the spacing between rows is 1600 mm × 1600 mm. Each anchor cable is anchored by one K2950 type and two Z2950 type anchoring agents; the length of all anchoring agents is 30 mm. At the top of the roadway, Φ22 mm × 6300 mm anchored flexible bolts were driven, with an interval of 1600 mm × 1600 mm and three bolts in a row. Welded warp and weft mesh with 100 mm × 100 mm steel bar is used. The surrounding rock of the concrete closed roadway with a strength grade of C20 is used. The thickness of the initial spray layer is 30–50 mm, and the secondary spray is 100 mm. Youante is used as grouting material. Youante is divided into A material and B material. Before grouting, A and B materials are, respectively, placed in different mixing barrels for mixing. After mixing,

they are mixed together for grouting. The grouting time depends on the depth of the borehole and the site conditions. It is characterized by high stability, strong permeability, quick effect, fast solidification speed, high solidification strength and green environmental protection. The grouting schematic diagram is shown in Figure 12. The specific process is as follows: grouting preparation → knocking → installing grouting pipe → connecting injection gun and grouting pump with high-pressure hose → inserting two pipettes into the barrel containing Youante A material and B material, respectively → opening pump grouting → washing machine after grouting → stopping pump → dismantling injection gun. According to the deformation characteristics of the surrounding rock of the west wing transportation roadway, the grouting time should be 15 to 20 days after the excavation of the roadway section, and the final support section is shown in Figure 13.

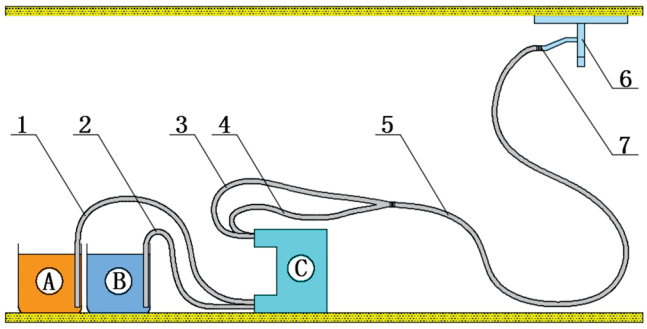

Figure 12. Anchor-grouting flexible bolt grouting diagram. A—A material mixing barrel; B—B material mixing barrel; C—grouting pump; 1—feed pipe A; 2—feed pipe B; 3—discharge pipe A; 4—discharge pipe B; 5—discharge pipe; 6—anchor flexible bolt; 7—grouting hole.

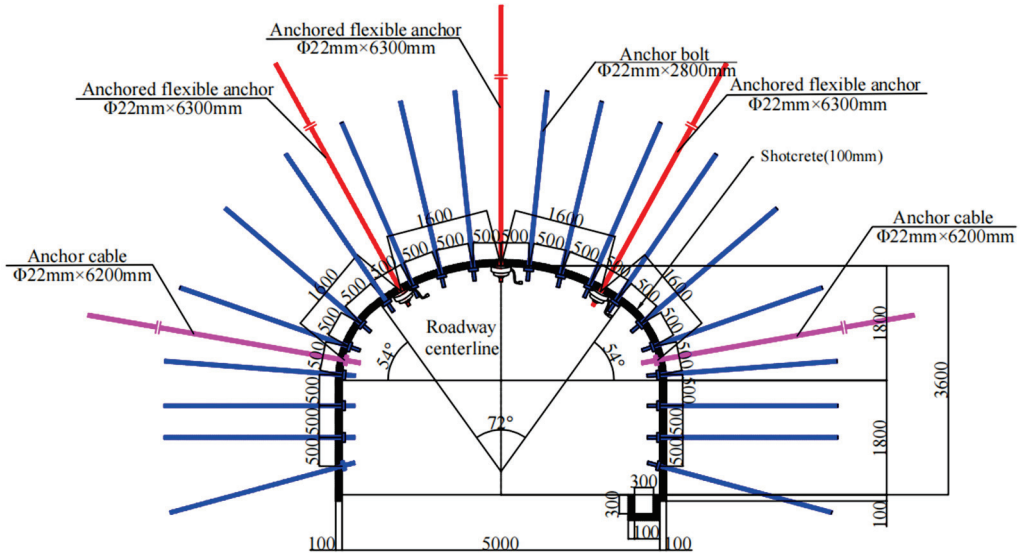

Figure 13. Bolting-grouting flexible bolt roadway support section diagram.

4. FLAC 3D Numerical Simulation

According to the geological conditions of the west wing transportation roadway, the numerical simulation model shown in Figure 14 is established by using FLAC 3D numerical simulation software. The section of the west wing transportation roadway adopts a three-center arch, the roadway width is 5 m, the wall height is 1.8 m, and the model size is 60 m × 20 m × 65.6 m. The roadway section adopts a 2800 mm bolt to simulate support, the spacing between rows is 500 mm × 800 mm, the two sides are driven into a 6200 mm anchor cable, the spacing between those rows is 1600 mm × 1600 mm, and the top of the roadway is driven into a 6300 mm anchor-grouting flexible bolt, the spacing those between

those rows is 1600 mm × 1600 mm, three in a row, and the simulated support structure is shown in Figure 15. According to the surrounding rock condition of the west wing transportation roadway, the model can be divided into eight layers, which are mudstone, 5 coal, mudstone, siltstone, fine sandstone, siltstone, 6 coal and mudstone, from top to bottom. The model adopts the Mohr–Coulomb criterion. The displacement constraints in the Y direction and X direction are applied to the front and back, left and right of the model, respectively. The displacement constraints in the Z direction are applied to the bottom, and the stress constraints are applied to the top. The buried depth of the simulated roadway is 740 m, and the load applied to the top of the model is 18.5 MPa. The model has 503,810 cells and 534,693 nodes. In order to improve the efficiency of model calculation and better reflect the changes in stress and displacement of surrounding rock around the roadway, the surrounding rock of the roadway is set to a smaller grid size, the minimum size of which is 0.2 m × 0.2 m, and the remaining grid size is increased exponentially with the distance from the roadway, up to a maximum size of 1 m × 1 m. The corresponding physical parameters of each rock layer are given to the numerical simulation model. The physical and mechanical parameters of the required rock mass mainly include the following: density ρ, bulk modulus K, shear modulus G, cohesion c, internal friction angle φ and tensile strength t. The mechanical parameters of rock strata are determined according to the laboratory results, and the rock strength is transformed into rock mass strength through certain weakening. Finally, the effective physical and mechanical parameters of rock mass are determined, as shown in Table 2.

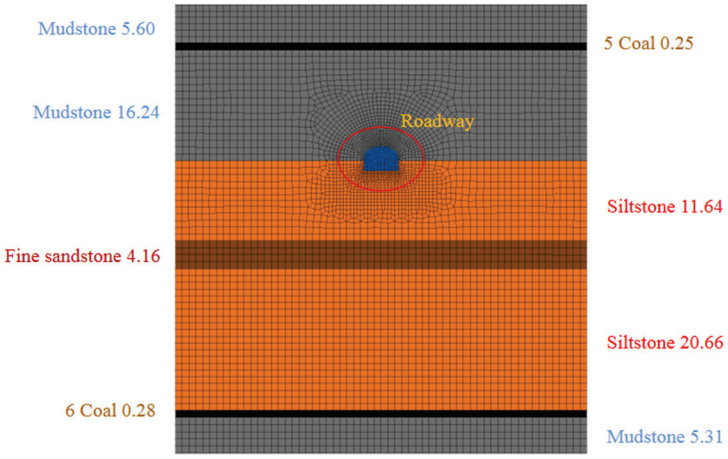

Figure 14. FLAC 3D numerical simulation model of west wing transport roadway (m).

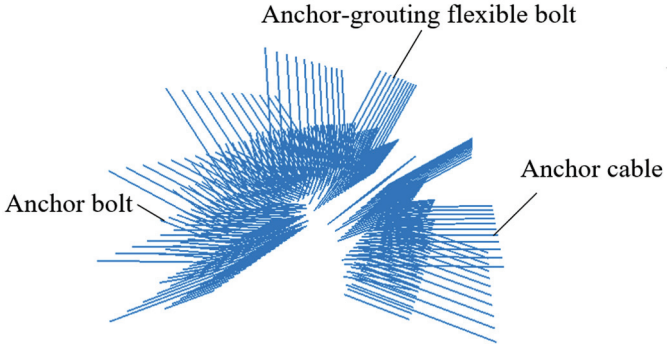

Figure 15. Numerical simulation model of supporting structure.

Table 2. Mechanical parameters of surrounding rock of west wing transport roadway.

Rock Stratum	*K*/ GPa	*G*/ GPa	*Q*/ (Kg/m^3)	σ_c/ MPa	*t*/ MPa	*c*/ MPa	φ/ (°)
Coal	1.2	0.6	1380	0.9	0.5	0.8	32
Mudstone	1.6	1.0	2890	18.5	0.9	1.6	39
Fine sandstone	3.4	1.5	2690	52.3	2.0	2.8	36
Siltstone	2.8	1.2	2800	39.8	1.2	1.8	35

The vertical and horizontal displacement nephogram of numerical simulation before and after the support of the west wing transport roadway is shown in Figure 16. According to the analysis of the numerical simulation displacement cloud diagram of the roadway before support, the maximum roof subsidence of the west wing transportation roadway is 213.33 mm, the maximum floor heave is 174.93 mm, and the maximum two-side displacement is 410.71 mm. After the support, the maximum subsidence of the roadway roof is 33.894 mm, the maximum floor heave is 50.907 mm, and the maximum displacement of the two sides is 66.129 mm. Compared to before the roadway support, the maximum subsidence of the roof is reduced by 179.436 mm, and the maximum floor heave is reduced by 124.023 mm. At the same time, the maximum displacement of the two sides is reduced by 344.581 mm.

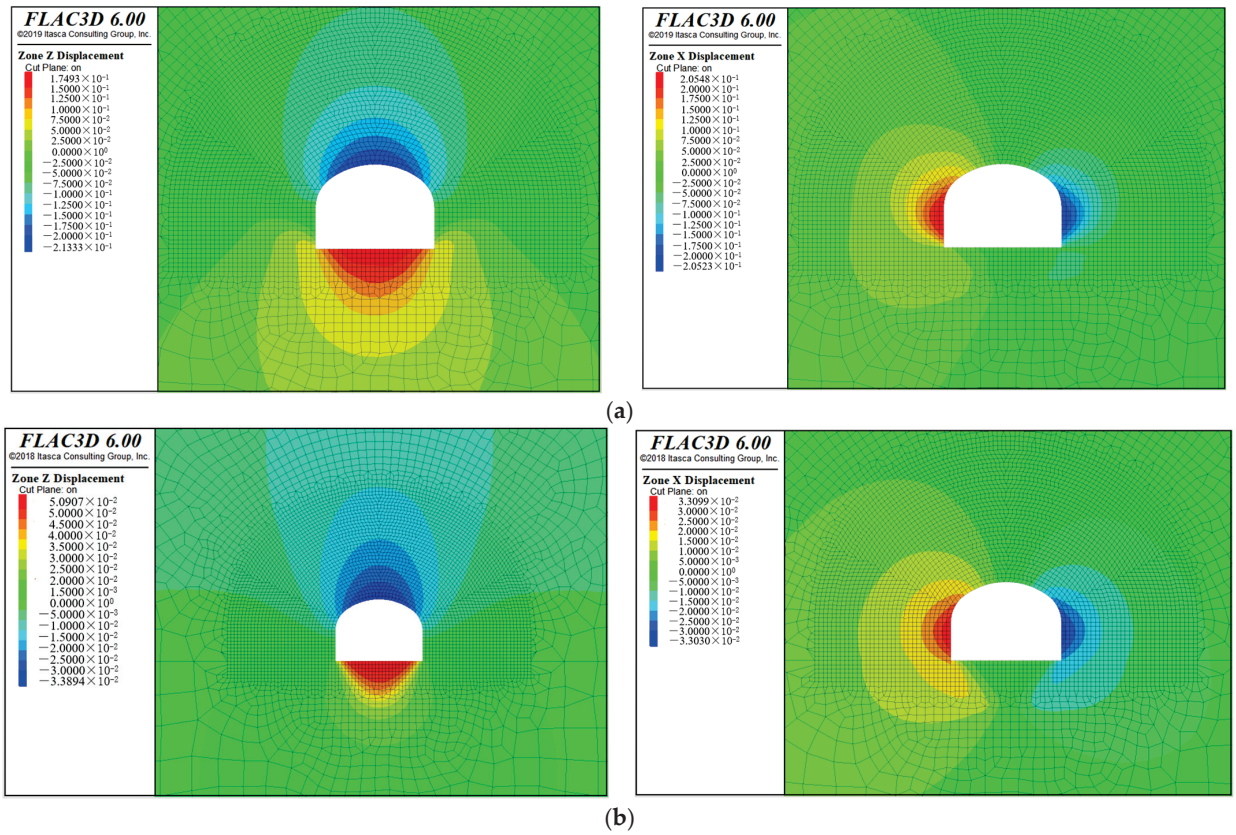

Figure 16. Numerical simulation of vertical and horizontal displacement cloud before and after support of west wing transportation roadway. (**a**) Numerical simulation of displacement cloud before support (m). (**b**) Numerical simulation of displacement cloud after support (m).

Figure 17 shows the distribution of plastic zone in numerical simulation before and after the support of the west wing transportation roadway. It can be seen from the figure that the plastic zone range is obviously reduced after the combined support scheme is adopted, and the overall strength of the surrounding rock of the roadway is improved

after the support. Through numerical simulation, it can be seen that the combined support scheme of "bolt (cable) + anchor net + anchor flexible bolt + shotcrete" can effectively reduce the distribution range of the plastic zone of the roadway's surrounding rock and effectively control the deformation of roadway's surrounding rock.

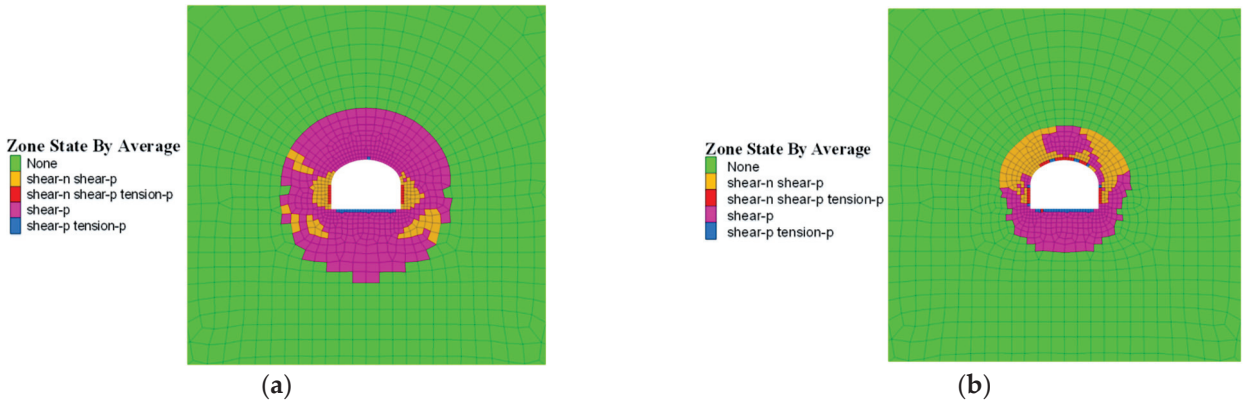

Figure 17. Numerical simulation of plastic zone distribution before and after support of west wing transportation roadway. (**a**) Before support. (**b**) After support.

5. Industrial Experiment

In order to verify the on-site support effect of the combined support scheme of "bolt (cable) + anchor net + anchor-grouting flexible bolt + shotcrete", Y26 + 80 m–Y26 + 200 m of the west wing transportation roadway was selected as the experimental section. The surface and deep displacement changes after roadway support were observed, and six surface displacement monitoring stations and one deep displacement monitoring station were set up. The layout of the observation station of the west wing transportation roadway is shown in Figure 18. The displacement observation method is as follows: the distance between the roof and floor of the roadway is measured by steel tape, and the distance between the ends of the two sides of the roadway is measured by leather tape. Through the observation of 60 days, the surface displacement monitoring results are shown in Figure 19. The maximum displacement of the top and bottom is 30.7 mm, and it tends to be stable after 24 days. The maximum displacement of the two sides is 27.1 mm. The deformation is large in the first 7 days, and tends to be stable after 26 days.

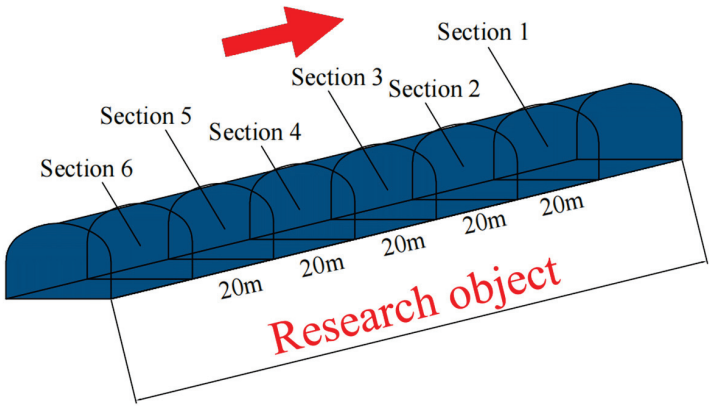

Figure 18. Layout of observation station in west wing transportation roadway.

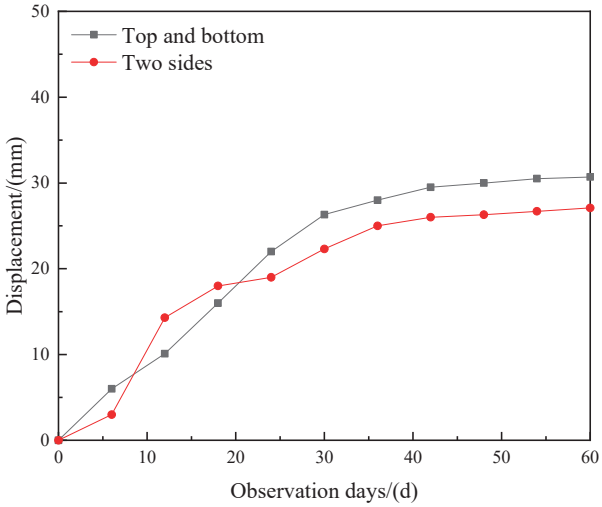

Figure 19. Monitoring results of roadway surface displacement.

The monitoring results of deep displacement are shown in Figure 20. According to the monitoring data, the maximum displacement at 1 m in the shallow part is 11.8 mm, and the maximum displacement at 7 m in the deep part is 18.5 mm. In the early stage, due to the influence of excavation disturbance, the deep displacement increment is large. When the measuring point is about 80 m away from the excavation surface, the displacement gradually tends to be gentle. The displacement change trend of the surrounding rock of the roadway within 1~7 m is basically consistent, the change is within 7 mm, and there is no separation between the rock layers.

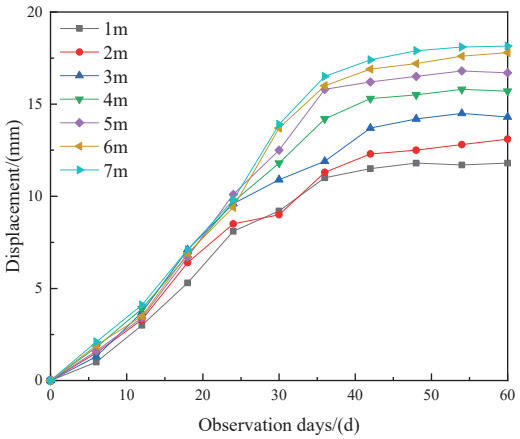

Figure 20. Monitoring results of roadway deep displacement.

From the observation results of surface and deep displacement during the excavation of the experimental section of the west wing transportation roadway, it can be seen that during the observation period, the deformation of the roadway in the experimental section was small, and no cracking of the side and roof rupture occurred. The field observation data show that the maximum displacement of the two sides and the roof and floor of the roadway in the experimental section is within 31 mm, and the roadway is stable. The deep displacement observation shows that the integrity of the surrounding rock of the roadway after support is better, and the support scheme has an obvious inhibitory effect on the fracture expansion of the rock mass, which plays a role in strengthening the surrounding rock. The support effect of the experimental section is shown in Figure 21.

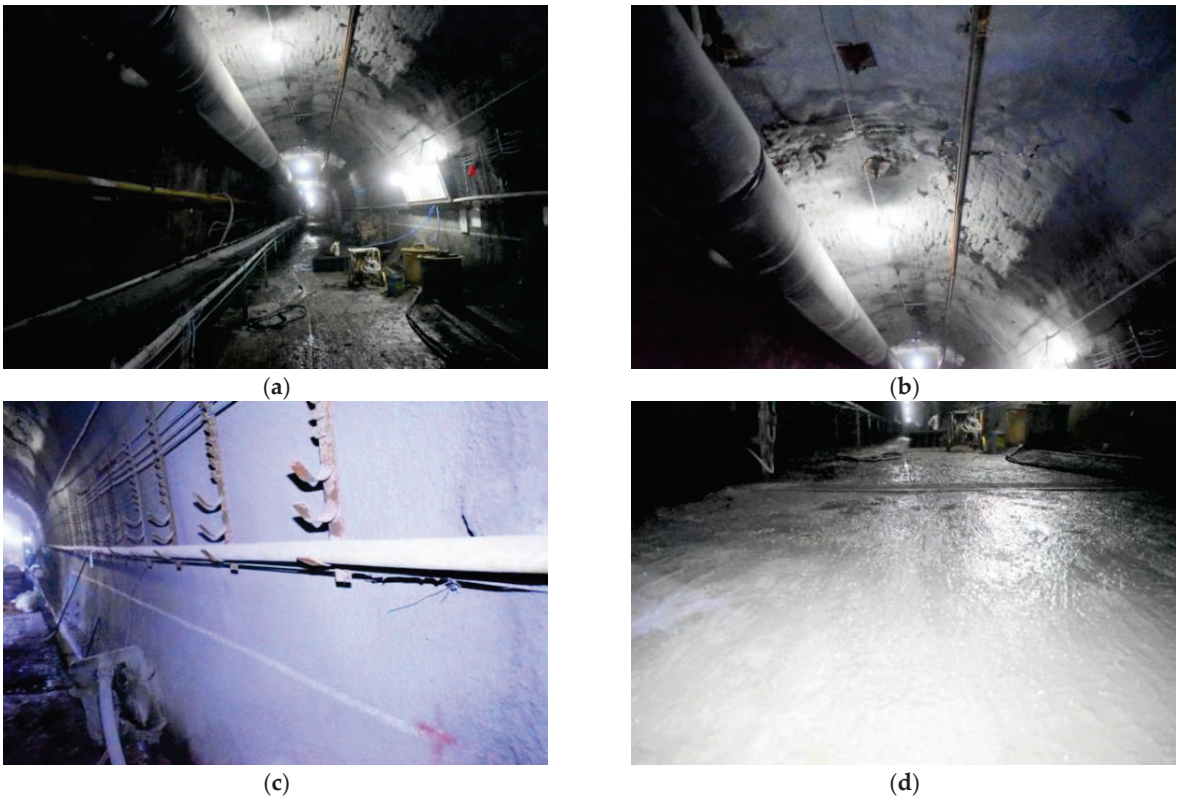

Figure 21. Field support effect diagram of west wing transportation roadway. (**a**) Section of roadway. (**b**) Roof of roadway. (**c**) Side of roadway. (**d**) Floor of roadway.

6. Conclusions

(1) Aiming at the characteristics of large buried depth and low strength of the surrounding rock in the west wing transportation roadway of Yuandian No.2 well coal mine, the anchor-grouting flexible bolt is proposed to solve the stability control problem of surrounding rock in this kind of roadway. Compared with ordinary anchor bolts, the structure of anchor-grouting flexible bolts is a simple and convenient construction. It is a kind of high pre-tightening anchoring bolt with a high-strength steel strand as the bolt body. It only needs to be installed once, and it is convenient to install a grouting bolt without re-drilling. At the same time, a new bolt structure is adopted to minimize the diameter of the bolt body under the premise of ensuring smooth grouting, so as to realize the integration of bolting and grouting.

(2) In order to maintain the stability of the roadway in the west wing transportation roadway, a combined support scheme of "bolt (cable) + anchor net + bolt-grouting flexible bolt + shotcrete support" was proposed, and its support mechanism was analyzed. The results show that the small pressure arch formed between the bolt and the bolt, the bolt and the broken surrounding rock, the large pressure arch formed between the bolt-grouting flexible bolt and the anchor cable, and the broken surrounding rock bonded by the grouting slurry are superimposed together to form a superimposed community, so as to realize the combined support to jointly control the deformation of the roadway's surrounding rock.

(3) FLAC 3D numerical simulation and field monitoring show that the surface displacement monitoring of the roadway after adopting the combined support scheme of "bolt (cable) + anchor net + anchor injection flexible bolt + shotcrete support" shows that the maximum roof-to-floor convergence is only 30.7 mm, and the maximum two-side convergence is 27.1 mm. The deep displacement monitoring of the roadway shows that the trend change in deep displacement within 1–7 m is basically the same, and the change amount is within 7 mm, which can effectively control the stability of the roadway, improve the self-bearing capacity of surrounding rock and maintain the long-term stability of the

roadway. The combined support scheme has a certain reference value for other similar roadways.

Author Contributions: Conceptualization, H.Z. and Y.L.; methodology, H.Z. and X.W.; software, H.Z. and Y.W.; first draft preparation, H.Z.; writing—original draft preparation, H.Z.; visualization, H.Z. and S.Y.; supervision, Y.L. All authors have read and agreed to the published version of the manuscript.

Funding: This research has been supported by the National Natural Science Foundation of China (Grant No. 52174102, 51874002), the Anhui Provincial Key Research and Development Plan (Grant No. 2022m07020007) and the Graduate Innovation Fund (Grant No. 2021CX2014).

Institutional Review Board Statement: Not applicable.

Informed Consent Statement: Not applicable.

Data Availability Statement: Not applicable.

Acknowledgments: We thank Huaibei Mining Co., Ltd. Yuandian Well 2 Coal Mine for providing the test platform, and thank Zhao Nannan for his help and data support in the fieldwork. The authors of this article are also so grateful to the anonymous reviewers for their valuable comments and modification suggestions on the improvement of this paper.

Conflicts of Interest: The authors declare no conflict of interest.

References

1. Sun, Y.; Li, G.; Zhang, J.; Xu, J. Failure Mechanisms of Rheological Coal Roadway. *Sustainability* **2020**, *12*, 2885. [CrossRef]
2. Shreedharan, S.; Kulatilake, P.H.S.W. Discontinuum—Equivalent Continuum Analysis of the Stability of Tunnels in a Deep Coal Mine Using the Distinct Element Method. *Rock Mech. Rock Eng.* **2016**, *49*, 1903–1922. [CrossRef]
3. Yu, K.; Ren, F.; Puscasu, R.; Lin, P.; Meng, Q. Optimization of combined support in soft-rock roadway. *Tunn. Undergr. Space Technol.* **2020**, *103*, 103502. [CrossRef]
4. Wu, G.; Chen, W.; Jia, S.; Tan, X.; Zheng, P.; Tian, H.; Rong, C. Deformation characteristics of a roadway in steeply inclined formations and its improved support. *Int. J. Rock Mech. Min. Sci.* **2020**, *130*, 104324. [CrossRef]
5. Kang, H.; Wu, Y.; Gao, F.; Jiang, P.; Cheng, P.; Meng, X.; Li, Z. Mechanical performances and stress states of rock bolts under varying loading conditions. *Tunn. Undergr. Space Technol.* **2016**, *52*, 138–146. [CrossRef]
6. Wang, P.; Zhang, N.; Kan, J.; Wang, B.; Xu, X. Stabilization of Rock Roadway under Obliquely Straddle Working Face. *Energies* **2021**, *14*, 5759. [CrossRef]
7. Yang, X.; Pang, J.; Liu, D.; Liu, Y.; Tian, Y.; Ma, J.; Li, S. Deformation mechanism of roadways in deep soft rock at Hegang Xing'an Coal Mine. *Int. J. Min. Sci. Technol.* **2013**, *23*, 307–312. [CrossRef]
8. Shen, B. Coal mine roadway stability in soft rock: A case study. *Rock Mech. Rock Eng.* **2014**, *47*, 2225–2238. [CrossRef]
9. Chen, Y.; Meng, Q.; Xu, G.; Wu, H.; Zhang, G. Bolt-grouting combined support technology in deep soft rock roadway. *Int. J. Min. Sci. Technol.* **2016**, *26*, 777–785. [CrossRef]
10. He, M.C.; Xie, H.P.; Peng, S.P.; Jiang, Y.D. Study on rock mechanics of deep mining. *Chin. J. Rock Mech. Eng.* **2005**, *16*, 2803–2813.
11. Wang, Q.; Jiang, B.; Pan, R.; Li, S.C.; He, M.C.; Sun, H.M.; Qin, Q.; Yu, H.C.; Luan, Y.C. Failure mechanism of surrounding rock with high stress and confined concrete support system. *Int. J. Rock Mech. Min. Sci.* **2018**, *102*, 89–100. [CrossRef]
12. Sun, X.M.; Liu, X.; Liang, G.F.; Wang, D.; Jiang, Y.L. Study on key parameters of thin coal seam roof cutting and pressure relief gob side entry retaining. *J. Rock Mech. Eng.* **2014**, *33*, 1449–1456.
13. Guo, P.; He, M.; Wang, J. Study on Coupling Support Technique in the Roadway of Hecaogou No. 2 Coal Mine with Soft Roadway of Large Deformation. *Geotech. Geol. Eng.* **2018**, *36*, 1161–1173. [CrossRef]
14. Wang, Z.; Wang, C.; Wang, X. Research on High Strength and Pre-stressed Coupling Support Technology in Deep Extremely Soft Rock Roadway. *Geotech. Geol. Eng.* **2018**, *36*, 3173–3182. [CrossRef]
15. Zhang, S.; Yin, S. Analytical Approach Based on Full-Space Synergy Technology to Optimization Support Design of Deep Mining Roadway. *Minerals* **2022**, *12*, 746. [CrossRef]
16. Wu, P.; Chen, L.; Li, M.; Wang, L.; Wang, X.; Zhang, W. Surrounding Rock Stability Control Technology of Roadway in Large Inclination Seam with Weak Structural Plane in Roof. *Minerals* **2021**, *11*, 881. [CrossRef]
17. Wang, Q.; Pan, R.; Jiang, B.; Li, S.; He, M.; Sun, H.; Wang, L.; Qin, Q.; Yu, H.; Luan, Y. Study on failure mechanism of roadway with soft rock in deep coal mine and confined concrete support system. *Eng. Fail. Anal.* **2017**, *81*, 155–177. [CrossRef]
18. Feng, X.; Ding, Z.; Hu, Q.; Zhao, X.; Ali, M.; Banquando, J.T. Orthogonal Numerical Analysis of Deformation and Failure Characteristics of Deep Roadway in Coal Mines: A Case Study. *Minerals* **2022**, *12*, 185. [CrossRef]
19. Zhang, D.; Guo, W.; Zhao, T.; Zhao, Y.; Chen, Y.; Zhang, X. Energy Evolution Law during Failure Process of Coal–Rock Combination and Roadway Surrounding Rock. *Minerals* **2022**, *12*, 1535. [CrossRef]

20. Qin, D.D.; Wang, X.F.; Zhang, D.S.; Chen, X.Y. Study on surrounding rock-bearing structure and associated control mechanism of deep soft rock roadway under dynamic pressure. *Sustainability* **2019**, *11*, 1892. [CrossRef]
21. Skrzypkowski, K.; Zagórski, K.; Zagórska, A.; Apel, D.B.; Wang, J.; Xu, H.; Guo, L. Choice of the Arch Yielding Support for the Preparatory Roadway Located near the Fault. *Energies* **2022**, *15*, 3774. [CrossRef]
22. Zhu, L.; Liu, C.; Gu, W.; Yuan, C.; Wu, Y.; Liu, Z.; Song, T.; Sheng, F. Research on Floor Heave Mechanisms and Control Technology for Deep Dynamic Pressure Roadways. *Processes* **2023**, *11*, 467. [CrossRef]
23. Li, Y.; Zhang, D.; Fang, Q.; Yu, Q.; Xia, L. A physical and numerical investigation of the failure mechanism of weak rocks surrounding tunnels. *Comput. Geotech.* **2014**, *61*, 292–307. [CrossRef]
24. Yang, S.Q.; Chen, M.; Jing, H.W.; Chen, K.F.; Meng, B. A case study on large deformation failure mechanism of deep soft rock roadway in Xi'an coal mine, China. *Eng. Geol.* **2017**, *217*, 89–101. [CrossRef]
25. Zhao, C.; Liu, J.; Lyu, C.; Chen, W.; Li, X.; Li, Z. Experimental study on mechanical properties, permeability and energy characteristics of limestone from through-coal seam (TCS) tunnel. *Eng. Geol.* **2022**, *303*, 106673. [CrossRef]
26. Zhao, C.; Liu, J.; Xu, D.; Zhang, L.; Lyu, C.; Ren, Y. Investigation on Mechanical Properties, AE Characteristics, and Failure Modes of Longmaxi Formation Shale in Changning, Sichuan Basin, China. *Rock Mech. Rock Eng.* **2022**, *56*, 1239–1272. [CrossRef]
27. Lyu, C.; Liu, J.; Ren, Y.; Liang, C.; Liao, Y. Study on very long-term creep tests and nonlinear creep-damage constitutive model of salt Rock. *Int. J. Rock Mech. Min. Sci.* **2021**, *146*, 104873. [CrossRef]
28. Lyu, C.; Liu, J.; Ren, Y.; Liang, C.; Zeng, Y. Mechanical characteristics and permeability evolution of salt rock under thermal-hydro-mechanical (THM) coupling condition. *Eng. Geol.* **2022**, *302*, 106633. [CrossRef]
29. Zhao, C.X.; Li, Y.M.; Liu, G.; Meng, X.R. Mechanism analysis and control technology of surrounding rock failure in deep soft rock roadway. *Eng. Fail. Anal.* **2020**, *115*, 104611. [CrossRef]
30. Xu, M.T.; Li, K.; Xu, Y.L. Partitioning Control Mechanism and Engineering Practice of Rebuilding Bearing Arch in Surrounding Rock under High Ground Stress. *Adv. Civ. Eng.* **2021**, *9*, 6667182. [CrossRef]

minerals

MDPI

Article

A Quantitative Method to Predict the Shear Yield Stress of Rock Joints

Zhenyu Han [1,2], Shijie Xie [1,*], Hang Lin [3], Hongyu Duan [4] and Diyuan Li [3,*]

[1] School of Civil Engineering, Southeast University, Nanjing 210096, China; zhenyu_han@seu.edu.cn
[2] Department of Civil Engineering, Monash University, Melbourne, VIC 3800, Australia
[3] School of Resources and Safety Engineering, Central South University, Changsha 410083, China; linhangabc@126.com
[4] Discipline of Civil, Surveying and Environmental Engineering, School of Engineering, University of Newcastle, Callaghan, NSW 2308, Australia; hongyuduan@foxmail.com
* Correspondence: xieshijieabc@126.com (S.X.); diyuan.li@csu.edu.cn (D.L.)

Abstract: The shear mechanical properties of rock joints are crucial in assessing the stability and safety of rock structures, including slopes, rock dams, and tunnels. The yield stress serves as a pivotal point that distinguishes the linear and non-linear mechanical characteristics of rock joints. Due to its significance in risk monitoring and safety evaluation, this paper first provides an overview of the commonly employed methods for identifying the yield stress. Then, a novel displacement reduction method based on the displacement reduction coefficient is proposed and systemically examined. The comparison between the proposed method and existing methods based on shear experimental data suggests that the former is more adept at accurately determining the yield stress without subjective interference. Finally, this innovative method is employed to estimate the effects of external environmental factors on the yield stress of rock joints.

Keywords: rock mechanics; shear tests; yield strength; peak stress; rock joints

1. Introduction

Fractured rock masses are often characterized by extensive and intricate rock joints, which exert a significant influence on their mechanical behavior [1–6]. Multitudinous geotechnical engineering applications, including, but not limited to, rock foundations, mining operations, bridge piers, and tunnelling projects, have demonstrated that the shear slip along these joints will lead to serious structural instability [7–11]. Numerous extensively- recorded geological calamities, such as landslides, fault-slip rock bursts, and tunnel collapses, are induced by the shear failure of rock joints [12–14]. Therefore, extensive and intensive studies on the shear strength characteristics of rock joints perform crucial theoretical and practical significance for ensuring the engineering safety and preventing geological disasters [15–20].

Numerous scholars have studied the shear deformation process of rock joints through various approaches and obtained abundant results [21–31]. Currently, there are three main categories of research methods for analyzing the shear mechanical properties of rock joints: physical model experiments (laboratory and field tests), numerical simulations, and theoretical analyses [32–42]. The non-uniform fluctuation of joint surface, uneven contact between two walls, elastic deformation of rough bodies, and progressive deterioration frequently result in the shear mechanical behavior of rock joints exhibiting alternatingly linear and nonlinear characteristics [43,44]. Yield stress, peak strength, and residual strength are the key stress thresholds to classify these characteristics. In terms of peak strength, dozens of models have been introduced successively since Patton incorporated the shear dilatancy effect into the Mohr–Coulomb criterion to establish the bilinear strength model [45–47]. The joint roughness coefficient—joint compressive strength (JRC—JCS) model, proposed

by Barton and Choubey [48], has gained widespread acceptance among researchers and engineers in the field of rock engineering. Furthermore, it has been explicitly adopted by the International Society for Rock Mechanics (ISRM) Commission [49]. The residual strength, also referred to as the ultimate strength, is an ideal concept that defines the shear stress at an adequate shear displacement. However, shear displacement is finite in laboratory tests, making it difficult to obtain the true residual strength as defined. Therefore, the ISRM commission suggests that once the shear displacement reaches 10% of the joint length, the corresponding shear stress can be regarded as the residual strength. Nevertheless, concerning the yield stress, despite its widely accepted definition, its estimation method is still in its infancy stage since existing prediction methods cannot precisely identify the yield stress. In fact, the safe and optimal design of rock structures (such as slopes and drifts) relies not only on peak strength but also on yield stress [50]. As stress reaches the yield level, interior damage gradually accumulates and considerable plastic deformation occurs along rock joints, resulting in notable non-linear mechanical characteristics, such as the nonlinear shear constitutive curve and smaller-asperity breaking on joint surfaces [51]. A comprehensive examination of the shear stress-shear displacement behavior of rock joints in the past half-century has revealed that relying solely on peak strength is inadequate for assessing the strength properties of such joints [52–57]. Instead, greater emphasis should be placed on determining the yield stress, as this can serve as an effective early warning indicator for potential engineering hazards. Therefore, it is imperative to develop a reliable prediction method for estimating yield stress [58].

Notwithstanding the extant research endeavors, the yield stress has not been comprehensively studied. If a correlation between stress levels and yield stress can be identified in either laboratory or field settings, it would enable precise assessment and evaluation of joint stability and damage degree of rock masses. This study aims to propose a novel method to accurately identify the shear yield stress. The paper is structured as follows: Section 2 provides an overview of existing methods for determining yield stress, and critically evaluates their strengths and limitations. In Section 3, a novel method is proposed in a simple and objective manner by introducing a displacement reduction coefficient to process shear stress-shear displacement data, eliminating the dependence on elastic parameters. To validate the efficacy of the proposed method, the results of the new method are compared with those of existing methods. Section 4 investigates the effect of external environmental factors on the determined yield stress. Finally, Section 5 summarizes the findings and outlines future research directions.

2. Literature Review

In direct shear tests, a certain normal stress is applied to the specimen prior to the application of shear stress parallel to the joint plane. Figure 1 illustrates a typical shear stress-shear displacement curve, which comprises two distinct stages: pre-peak and post-peak (stage III). The pre-peak stage can be further divided into two sub-stages: sub-stage I, characterized by linear elasticity, and sub-stage II, marked by yield, with the demarcation point at the yield point [59]. During the stage of linear elasticity, the shear stress exhibits a linear increase in proportion to the shear displacement, and the shear stiffness can be determined by calculating the slope of this line. The asperities between the joint surface perform prominent elasticity during this stage. Subsequently, the shear constitutive curve enters the yield stage, wherein the plastic shear displacement starts to occur, the asperities gradually wear and break, the shear stiffness is noticeably reduced, and the hanging side and heading side slip along the joint. Upon reaching the maximum peak shear stress, the contact plane experiences significant collapse, which in turn results in greater slipping along the joint. The roughness and undulation of the rock joints give rise to normal displacement, ultimately leading to the occurrence of dilation. Once the shear stress surpasses the bearing capacity of the asperities, the cumulative damage will cause a marked drop in shear stress, as displayed in Figure 1. Herein, the present study is centered on the identification of the yield point, which performs a crucial role in determining the shear mechanical

behavior variation of rock joints. Over the past few decades, numerous investigations have been conducted to ascertain the yield point of the shear constitutive curve, which can be categorized as follows:

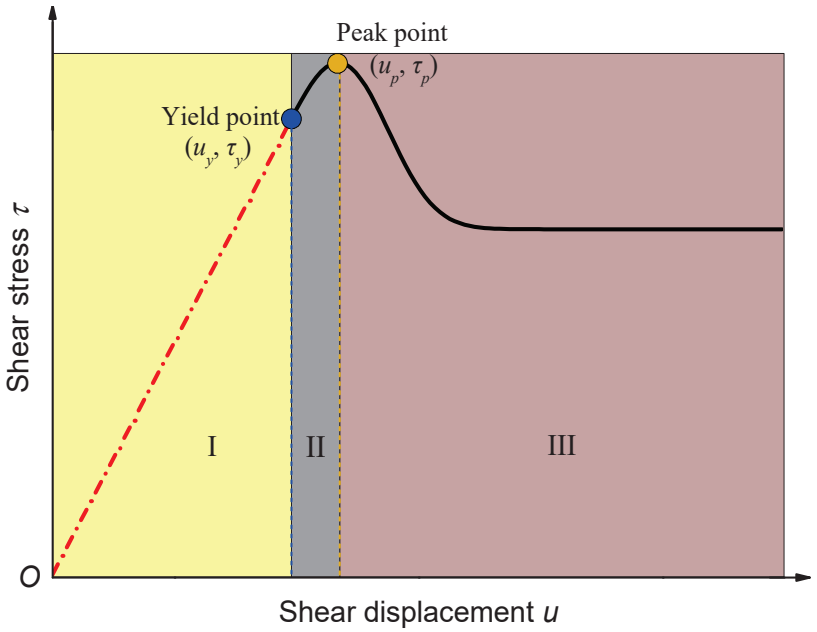

Figure 1. Schematic diagram of the shear stress–shear displacement curve (u_y and u_p are yield displacement and peak shear displacement, respectively; τ_y and τ_p are yield stress and peak shear stress, respectively).

(1) Empirical methods

According to extensive direct shear experimental results conducted on rock joints by Goodman [60], it is typically observed that the yield point occurs within the range of 70% to 90% of the peak shear stress. Using this method, Xiao et al. [61] took a yield point equivalent to 70% of the peak shear stress to analytically derive a shear constitutive model. Similarly, Sun et al. [62] reported that the ratio between yield shear stress and peak shear stress is approximately 0.85. From the perspective of shear displacement, one-third of the peak shear displacement is regarded as the yield displacement by many researchers [52,53,63,64]. Although empirical methods may be convenient for engineering projects, they are highly subjective and do not account for important factors, such as lithology and pre-existing defects.

(2) Shear stiffness method

The pre-peak stage of shear stress–shear displacement curves of rock joints are usually fitted using a hyperbolic function [65]. The following equation was adopted by Kulhawy [66] to replicate the pre-peak curve:

$$\tau = \frac{u_i}{m + nu_i} \tag{1}$$

where u_i is the shear displacement at a certain shear stress, m represents the reciprocal of the initial shear stiffness (K_{st}), and n is the reciprocal of the horizontal asymptote to the hyperbolic curve. By using Equation (1) to fit the experimental data, it is possible to readily derive the initial shear stiffness. Subsequently, a line originating from the origin O, with a slope of K_{st}, intersects with the shear stress-shear displacement curve at point F, which represents the yield point [67], as shown in Figure 2. This method is on the basis of shear test results. However, it is worth noting that determining the initial shear stiffness may be

imprecise in situations where the shear stress–shear displacement curve does not exhibit a hyperbolic shape.

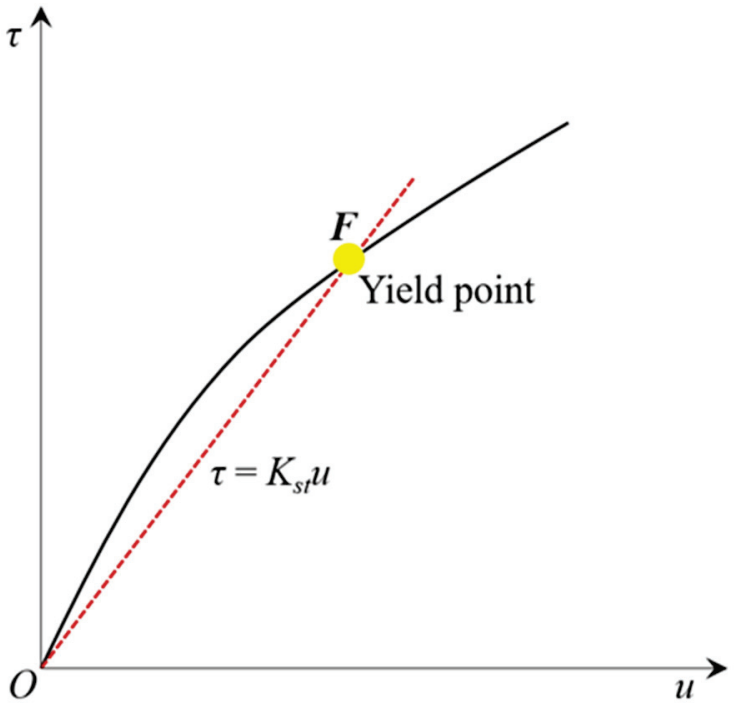

Figure 2. Schematic diagram of the shear stiffness method.

(3) Inflection point method

The linear fitting method was used by Xie et al. [68] to fit the experimental data in the pre-peak stage, and the resultant slope is the initial shear stiffness (K_{st}), as shown in Figure 3a. The shear stress difference ($\triangle\tau$) can then be obtained, and its relation versus shear displacement is illustrated in Figure 3b. The inflection point clearly corresponds to the yield point. Nonetheless, accurately pinpointing the inflection point remains a challenging task, as it is susceptible to subjective errors.

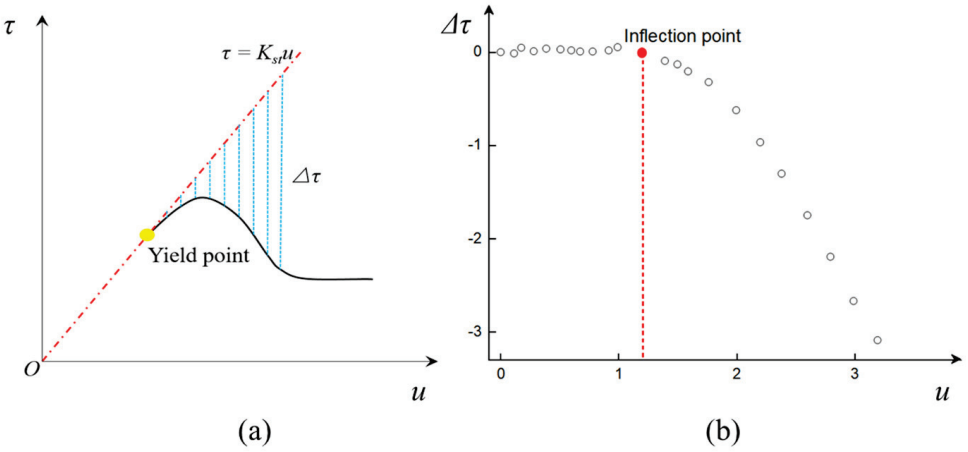

Figure 3. Schematic diagram of the inflection point method, (**a**) τ-u curve (**b**) $\Delta\tau$-u curve.

3. A New Displacement Reduction Method

Up to now, neither the ISRM nor the American Society for Testing and Materials have put forth any prescribed methods for accurately discerning the yield point [69]. Given the limitations of experience and subjective judgment, more academic approaches that enable

a rapid and precise identification of the shear yield point are imperative to be established. To enhance the precision of determination and streamline the mathematical representation, a new method (i.e., displacement reduction method) is proposed herein to identify the yield stress of the shear constitutive curve. Additionally, the superiority of this method is validated by comparing it with existing methods.

3.1. Modeling Process

The displacement reduction method is used to determine the yield point by comparing the normalized shear displacement response (u_i/u_p). The specific steps are as follows:

(1) A direct shear test is first carried out on rock joints to obtain the shear stress−shear displacement curve. Then, a new variable w is defined, which represents the displacement reduction coefficient:

$$w_i = 1 - u_i/u_p \tag{2}$$

where u_i is the displacement data in the pre-peak stage of the shear stress–shear displacement curve, and u_p is the peak shear displacement. It is evident that w is a scalar quantity.

(2) The relationship between shear stress τ and displacement reduction coefficient w can be acquired, as shown in Figure 4. By applying Equation (2), points A (0, τ_p) and B (1, 0) can be identified, which correspond to the origin (0,0) and the peak point (u_p, τ_p) on the shear–stress displacement curve, respectively. It is obvious that points A (0, τ_p) and B (1, 0) always lie on the shear stress-w curve. Connecting these two points results in a reference line denoted as AB in Figure 4.

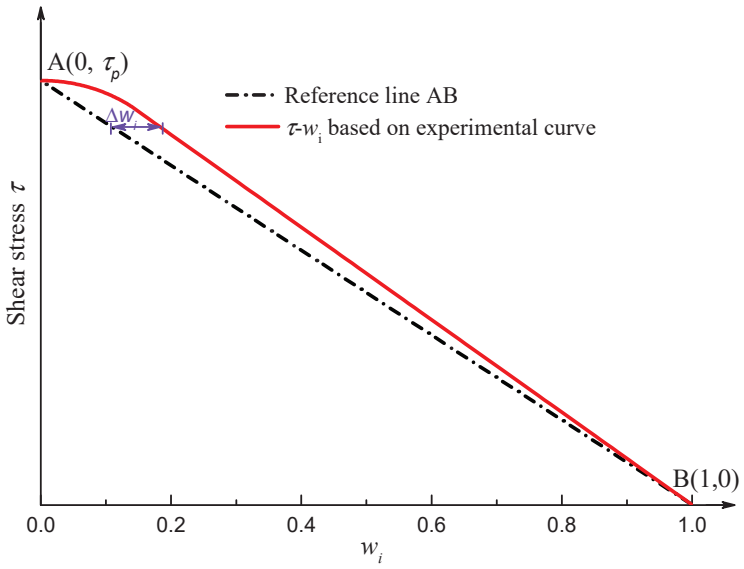

Figure 4. Schematic diagrams of theoretical and experimental shear stress-w curves.

(3) Consequently, the difference Δw between the experimental shear–stress displacement curve and the reference line AB can be calculated, as plotted in Figure 5. During the linearly elastic stage (stage I), Δw increases proportionally with the increase in shear stress τ. In contrast, during the yield stage (stage II), the shear displacement exhibits non-linear characteristics. Hence, the yield point is the cut-off point between the linearly elastic stage (stage I) and the yield stage (stage II), where Δw reaches the maximum value. Consequently, this method enables easy identification of the yield point while ensuring accuracy and objectivity and eliminating human interference. This method provides a scientific and efficient means of determining the shear yield stress of rock joints.

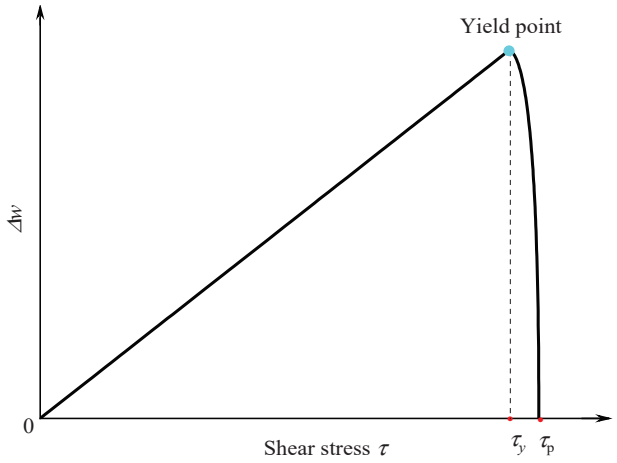

Figure 5. Δw-τ curve under direct shear tests.

3.2. Verification and Applications

The experimental data were collected through direct shear tests conducted on cement mortar specimens containing a saw-tooth triangular joint, as displayed in Figure 6. The specimens were composed of a mixture of water, high-strength cement, and fine quartz sand with a mass ratio of 1:2:4 [70]. The dimensional size and the undulating angle of the specimen were 100 × 100 × 100 mm^3 and 45°, respectively. The uniaxial compressive strength, indirect tensile strength, Young's modulus, Poisson's ratio, cohesion, and internal friction angle of the cement mortar material are 18.97 MPa, 1.637 MPa, 2.202 GPa, 0.2, 1.84 MPa, and 58.47°, respectively. During the test, prior to the application of shear stress, the specimen was subjected to a normal stress of 0.4 MPa. The test was completed once the shear displacement reached or exceeded 10 mm.

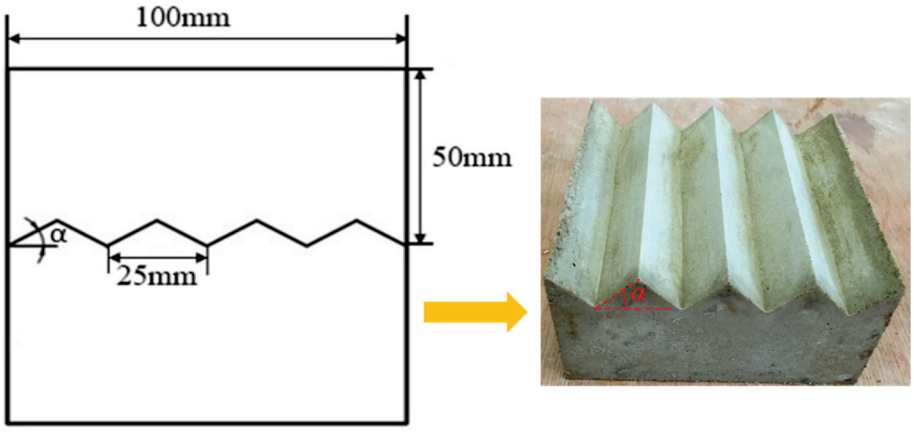

Figure 6. Schematic diagrams of saw-tooth triangular joint cement mortar specimens (Modified after Xie et al. [70]).

A typical shear stress–shear displacement curve is plotted in Figure 7. It can be observed that the shear stress first rose in a linear way with the increase in shear displacement, and a minor yield stage was present before reaching the peak stress. Subsequently, the shear stress dropped rapidly after its apex and generally leveled off. According to the definitions in Section 2, the peak shear stress τ_p and the peak shear displacement u_p were 2.93 MPa and 1.39 mm, respectively. Then, w_i can be obtained based on Equation (2), and its relation versus shear stress τ, and the reference line are shown in Figure 8. The w variation between the experimental curve and the reference line exhibited a significant alteration with the increase in w, which is further illustrated in Figure 9. The yield shear stress corresponds

to the maximum value of Δw, as shown in Figure 9, where it is determined as 2.42 MPa, accounting for 82.6% of the maximum shear stress.

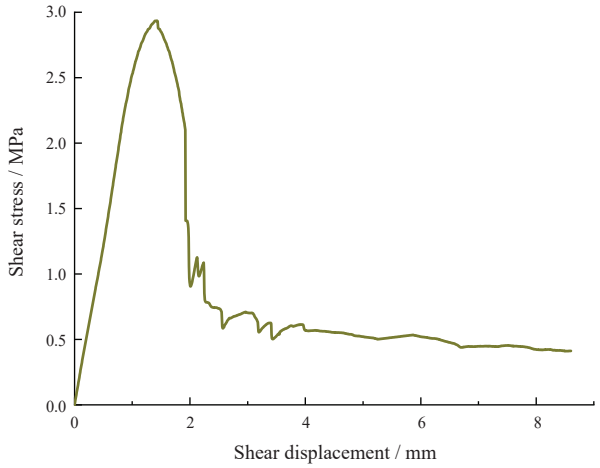

Figure 7. Shear stress–shear displacement curve from the direct shear test [70].

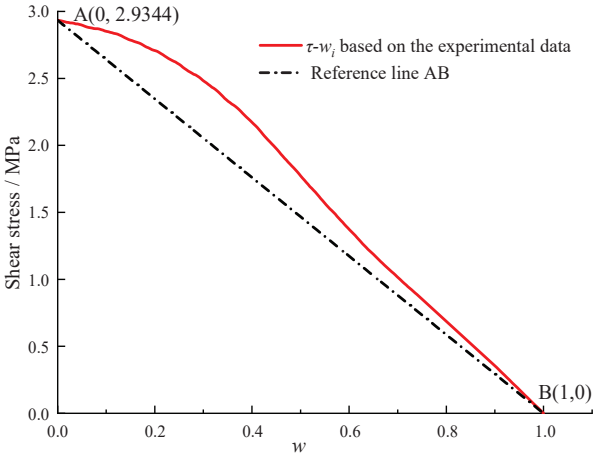

Figure 8. τ-w_i based on the experimental data and the reference line.

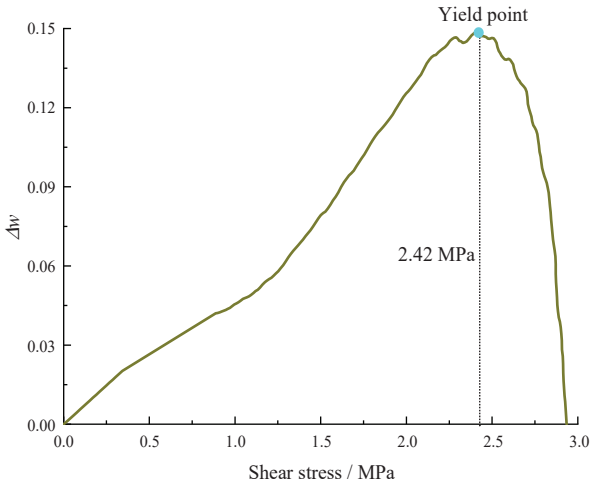

Figure 9. Determination of the yield point.

Based on the above analysis, the proposed method can better identify the yield shear stress and thus provides a viable approach to characterize the demarcation point between linear elasticity and pre-peak nonelasticity.

3.3. Comparative Analysis

(1) Empirical methods

From the description in Section 2, the ratio of yield stress to peak stress is regarded as 70%–90% [60], 70% [61], and 85% [62], respectively. As the shear displacement occupies one-third of the peak shear displacement, the corresponding stress only accounts for 38.2% of the peak stress. Obviously, the result of the empirical displacement method is far from the true yield point, indicating that this method could produce fairly large errors. The result obtained using our method is close to the approximation ratio (85%) [62].

(2) Shear stiffness method

Figure 10 illustrates the pre-peak stage of the shear stress–shear displacement curve fitted using Equation (1). As described in Section 2, the yield stress can be acquired by the intersection point in Figure 11. However, it can be seen that the two curves only intersect at the original point, indicating that this method cannot identify the yield point of the shear stress–shear displacement curve.

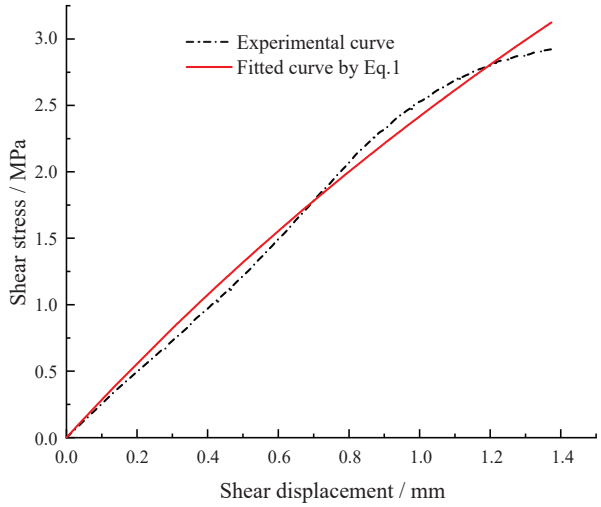

Figure 10. Pre-peak τ-u curve.

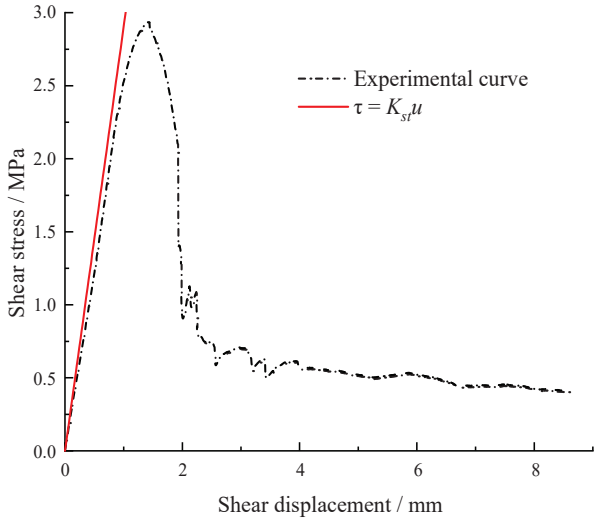

Figure 11. Determination by the shear stiffness method.

(3) Inflection point method

Figure 12 displays the linear fitting curve of the partial pre-peak stage of the shear–stress displacement curve. As described in Section 2, the yield stress can be determined

by the inflection point of the $\Delta\tau - u$ curve in Figure 12b. The yield stress is identified as 2.29 MPa, 78.16% of the peak stress.

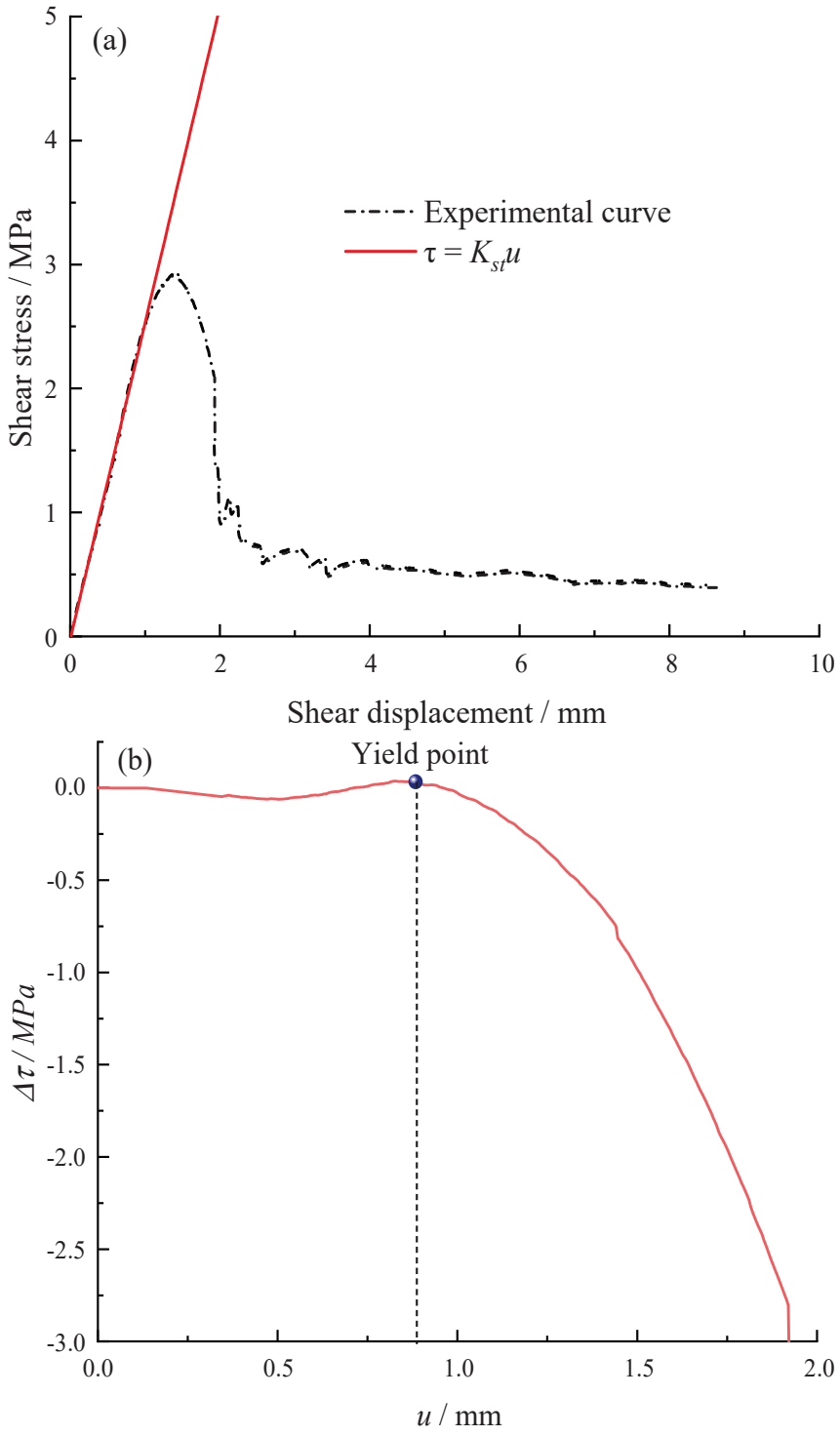

Figure 12. Determination by the inflection point method, (**a**) τ-u curve (**b**) $\Delta\tau$-u curve.

Based on experimental data from previous publications, Table 1 lists the ratio between the yield stress identified by various methods and the peak stress. It can be noticed that with the implementation of the new method, several ratios of yield stress to peak stress are less than 70%, implying that the empirical stress method may occasionally overestimate the yield stress. With regard to the empirical displacement method, in most cases, the

result contradicts the in situ condition. For the shear stiffness method, it is inadequate for predicting the yield stress because the majority of pre-peak stages of experimental shear stress–shear displacement curves do not comply with the hyperbolic distribution. The results determined by the inflection point method exhibit the smallest error (~10%) in comparison to those by the newly proposed method, but it poses a challenge to ascertain the inflection point in an objective manner devoid of any human subjectivity.

Table 1. Yield point identified by various methods.

References	τ_y/τ_p/%						
	New Proposed Method	Empirical Methods				Shear Stiffness Method [65]	Inflection Point Method [68]
		Goodman [60]	Xiao et al. [61]	Sun et al. [62]	Oh, Cording and Moon [53]		
Bandis et al. [67]	83.70	70–90	70	85	76.83	2.48	90.96
Papaliangas et al. [71]	77.98	70–90	70	85	58.72	6.80	70.12
Grasselli [72]	92.80	70–90	70	85	39.11	9.88	97.20
Nasir and Fall [73]	62.69	70–90	70	85	17.27	–	57.57
	68.42	70–90	70	85	72.93	–	61.50
Bahaaddini [74]	90.67	70–90	70	85	68.00	–	82.67
	80.00	70–90	70	85	63.43	–	69.14
Ge et al. [75]	82.23	70–90	70	85	49.31	–	68.21
	77.11	70–90	70	85	49.37	–	82.10
	53.84	70–90	70	85	40.82	–	45.19
	71.95	70–90	70	85	43.88	–	54.82
Ong and Choo [76]	78.77	70–90	70	85	74.82	–	65.63
	74.71	70–90	70	85	71.73	–	66.73
Xie et al. [70]	82.6	70–90	70	85	38.2	–	78.16

4. Discussion

The shear characteristics of rock joints are highly susceptible to external environmental factors, such as the temperature, normal stress, shear velocity, joint roughness coefficient (JRC), etc., which could significantly amplify the non-linear mechanical properties of rocks and thereby lead to the change of the shear yield point. Hence, this section aims to examine the effects of various external environmental factors.

4.1. Effect of the Temperature

The cubic Beishan granite specimens, collected from Gansu Province, China, were axially split to generate an artificial discontinuity. Then, they underwent thermally treatment at temperatures of 100 °C, 200 °C, 300 °C, and 400 °C, respectively [77]. Table 2 and Figure 13 show the detailed stress values and their variation tendency with temperatures, respectively. The yield stress and peak stress overall decrease as the temperature increases from room temperature to 400 °C, but the proportion of yield stress in peak stress approximately remains relatively constant, as displayed in Figure 13. This manifests that the effect of high temperature ($\leq$400 °C) on the ratio of yield stress to peak stress of Beishan granite is insignificant. It can also be inferred that very limited micro defects exist in the Beishan granite, thus, this type of rock materials is dense. When subjected to external loads, it is more likely to exhibit elastic−brittle characteristics, which is the reason why τ_y/τ_p is larger than 90%.

Table 2. Yield stress under various temperatures.

Temperature/°C	τ_y/MPa	τ_p/MPa	τ_y/τ_p/%
20	10.49	10.69	98.13
100	9.00	9.50	94.74
200	9.00	9.61	93.65
300	8.94	9.03	99.00
400	7.78	8.36	93.06

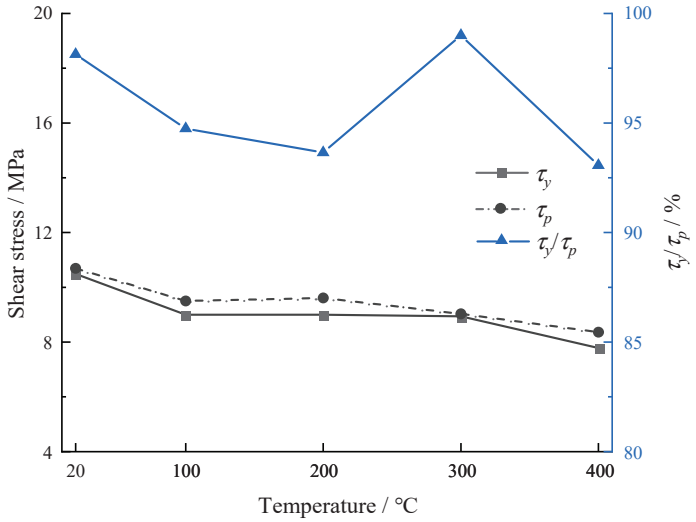

Figure 13. Yield stresses after thermal treatment (Note: τ_p data are from Zhao et al. [77]).

4.2. Effect of the Normal Stress

Zhou et al. [78] adopted marble to investigate the effects of undulation and normal stress on shear characteristics. Here, we selected the experimental data at a given dentate height of 3 mm to examine the effect of normal stress on shear mechanical properties, as shown in Table 3 and Figure 14. Both the yield stress and peak stress exhibit an overall increasing variation tendency as the normal stress increases from 10 MPa to 60 MPa, but the proportion of yield stress in peak stress remains relatively constant, with the exception of the condition under a normal stress of 50 MPa, as illustrated in Figure 14. Similarly, the effect of normal stress on the yield point is limited.

Table 3. Yield stress under various normal stresses.

Normal Stress/MPa	τ_y/MPa	τ_p/MPa	τ_y/τ_p/%
10	14.96	15.40	97.20
20	24.90	25.19	98.86
30	35.02	35.89	97.60
40	40.64	42.37	95.92
50	34.69	48.34	71.76
60	51.43	55.14	93.26

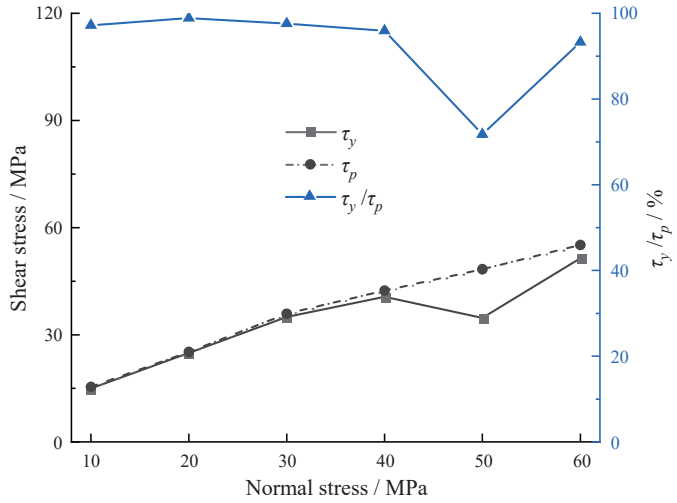

Figure 14. Yield stresses under different normal stresses (Note: τ_p data are from Zhou et al. [78]).

4.3. Effect of the Shear Velocity

Marble was chosen by Wang et al. [79] to study the shear behavior subjected to high-velocity impacts. Table 4 and Figure 15 show that both the yield stress and peak stress exhibit an increasing trend with the increasing shear velocity, but the yield point first increases, then decreases within the same shear velocity range. More laboratory tests under high-velocity impacts need to be carried out to systemically examine the relationship between yield stress and shear velocity.

Table 4. Yield stress under high velocity impact.

Shear Velocity/m/s	τ_y/MPa	τ_p/MPa	τ_y/τ_p/%
4.15	5.80	7.50	77.40
5.29	6.39	9.34	68.34
7.07	10.79	13.30	81.13

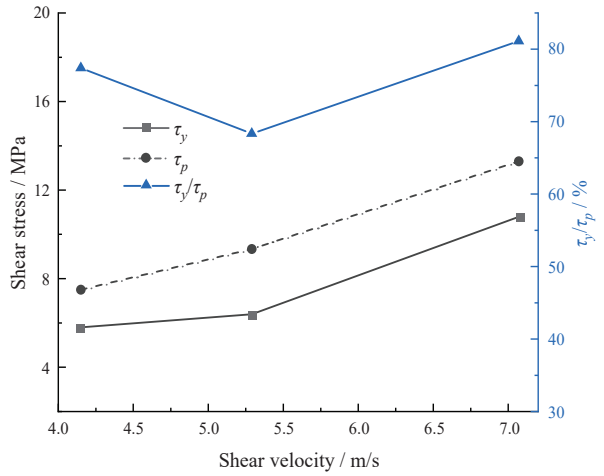

Figure 15. Yield stresses under high velocity impact (Note: τ_p data are from Wang et al. [79]).

4.4. Effect of the JRC

Cement mortar was adopted to study the effect of JRC on the shear characteristics of hard−soft interfacial discontinuities [80]. Figure 16 indicates that the yield stress, peak stress, and the ratio of yield stress to peak stress all increase with the increasing JRC, and the corresponding values are listed in Table 5. As the joint surface becomes rougher, the upper and lower parts are more likely to be incorporated together, leading to the enhancement of shear mechanical properties. Hence, the yield point is also increased to resist the external shear stress as the JRC increases.

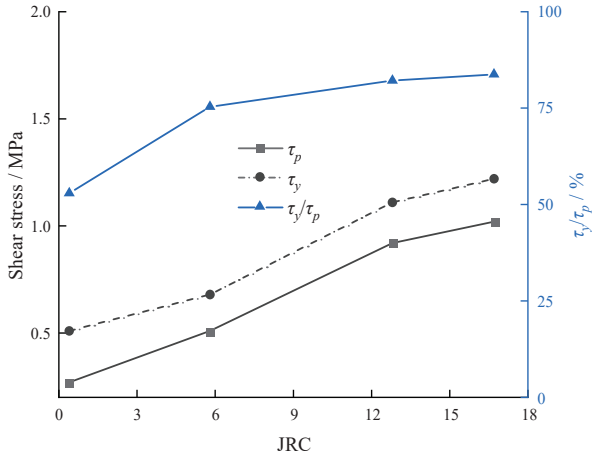

Figure 16. Yield stresses under the high velocity impact (Note: τ_p data are from Fan et al. [80]).

Table 5. Yield stress under various JRC.

JRC	τ_y/MPa	τ_p/MPa	τ_y/τ_p/%
0.4	0.27	0.51	52.93
5.8	0.51	0.68	75.36
12.8	0.92	1.11	82.15
16.7	1.02	1.22	83.77

4.5. Effect of the Shear Direction

In rock engineering, rock joints are subjected to shear stress along different directions, which can eventually give rise to the anisotropic instability of rock masses. Bao et al. [81] used 3D laser scanning technology to obtain digital information of joint morphology of a tunnel engineering (Figure 17), and a number of rock joints were made by 3D printing. On this basis, the anisotropic shear behavior of rock joints is studied by direct shear tests under a constant normal load. Hence, the resultant data were selected herein to analyze the shear stress variation, as listed in Table 6. The relation between the feature points of shear stress and the shear direction is displayed in Figure 18. It can be observed that both the yield stress and peak stress maximize at the shear direction of 90°, while the percentage of yield stress in peak stress reaches the minimum value at the same direction, indicating that the increasing rate of the yield stress is lower than that of peak stress. When the shear direction exceeds the critical value (90°), the yield stress and peak stress increase first, then decrease, but the percentage of yield stress in peak stress performs an inverse tendency.

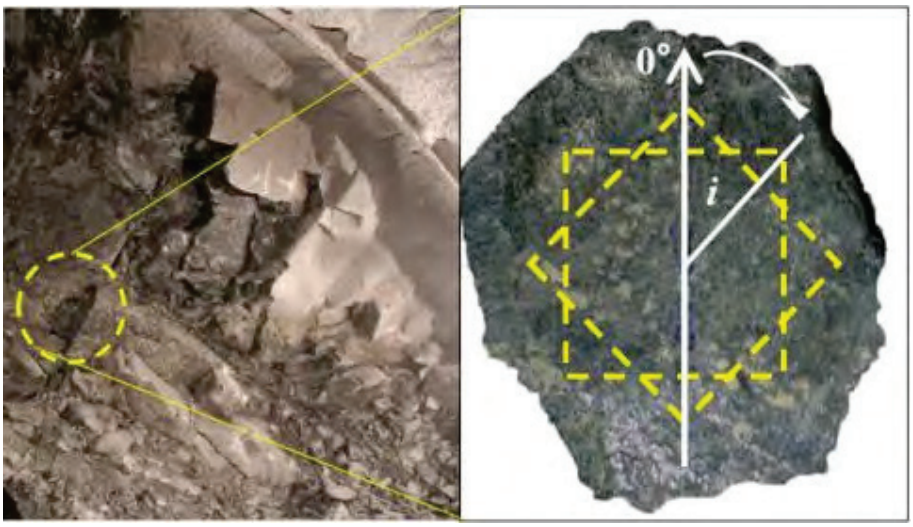

Figure 17. Schematic diagram of the selected rock joints [81].

Table 6. Yield stress under different shear directions.

Shear Direction/°	τ_y/MPa	τ_p/MPa	τ_y/τ_p/%
0	0.36	0.45	81.81
45	0.39	0.49	80.39
90	0.40	0.61	65.50
135	0.36	0.47	76.14
180	0.42	0.56	74.78

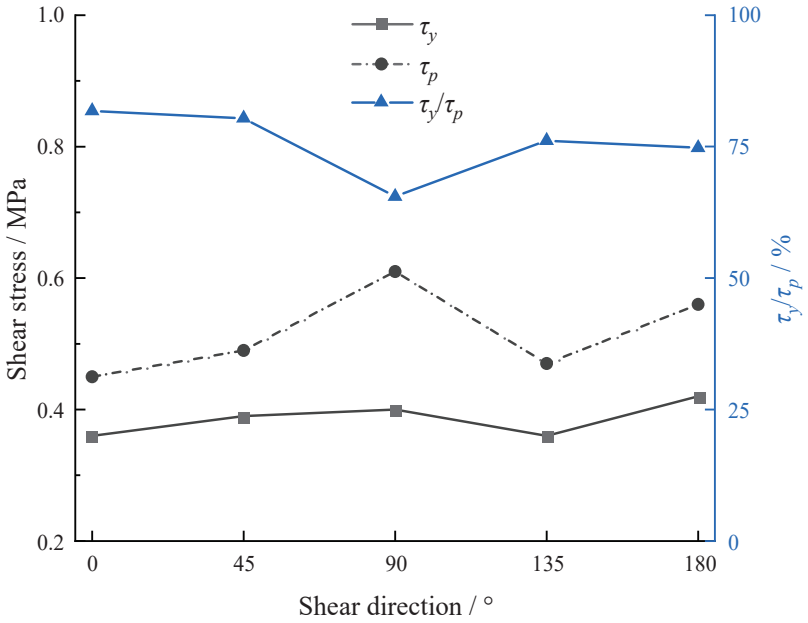

Figure 18. Yield stresses under different shear directions (Note: τ_p data are from Bao et al. [81]).

5. Conclusions

Based on the displacement reduction coefficient, a new method is proposed in this paper to accurately identify the yield point of stress–shear displacement curves. In this method, a reference line connected by points A (0, τ_p) and B (1, 0) is introduced. The yield stress can then be determined as the displacement reduction coefficient difference between the experimental shear–stress displacement curve and the reference line maximizes. The effectiveness and precision are validated by many experimental data from published papers. Compared with previous methods, this method can enhance objectivity and effectively reduce human interference. Furthermore, the effects of external environmental factors except JRC on the yield stress are limited, which demonstrates that the yield stress of rock materials is dependent on in situ lithology to a large extent, and can be significantly affected by the joint surface roughness.

Author Contributions: Z.H.: methodology, data curation, writing and editing, funding acquisition. S.X.: conceptualization, review and editing. H.L.: investigation, funding acquisition. H.D.: investigation. D.L.: supervision. All authors have read and agreed to the published version of the manuscript.

Funding: The authors would like to acknowledge the financial support from the Postgraduate Research and Practice Innovation Program of Jiangsu Province (No. KYCX21_0119), and Project (42277175) supported by National Natural Science Foundation of China.

Data Availability Statement: Not applicable.

Conflicts of Interest: The authors declare no conflict of interest.

References

1. Develi, K. Computation of direction dependent joint surface parameters through the algorithm of triangular prism surface area method: A theoretical and experimental study. *Int. J. Solids Struct.* **2020**, *202*, 895–911. [CrossRef]
2. Xie, H.; Zhu, J.; Zhou, T.; Zhang, K.; Zhou, C. Conceptualization and preliminary study of engineering disturbed rock dynamics. *Geomech. Geophys. Geo-Energy Geo-Resour.* **2020**, *6*, 34. [CrossRef]
3. Han, Z.; Li, D.; Li, X. Dynamic mechanical properties and wave propagation of composite rock-mortar specimens based on SHPB tests. *Int. J. Min. Sci. Technol.* **2022**, *32*, 793–806. [CrossRef]
4. Han, Z.; Li, D.; Li, X. Effects of axial pre-force and loading rate on Mode I fracture behavior of granite. *Int. J. Rock Mech. Min. Sci.* **2022**, *157*, 105172. [CrossRef]

5. Xie, S.J.; Han, Z.Y.; Chen, Y.F.; Wang, Y.X.; Zhao, Y.L.; Lin, H. Constitutive modeling of rock materials considering the void compaction characteristics. *Arch. Civ. Mech. Eng.* **2022**, *22*, 60. [CrossRef]
6. Wen, G.P.; Hu, J.H.; Jie, W.; Yang, D.J.; Rui, X. Characteristics of stress, crack evolution, and energy conversion of anchored granite containing two preexisting fissures under uniaxial compression. *Bull. Eng. Geol. Environ.* **2023**, *82*, 1–14. [CrossRef]
7. Xie, H.P.; Sun, H.Q.; Ju, Y.; Feng, Z.G. Study on generation of rock fracture surfaces by using fractal interpolation. *Int. J. Solids Struct.* **2001**, *38*, 5765–5787. [CrossRef]
8. Singh, H.K.; Basu, A. Evaluation of existing criteria in estimating shear strength of natural rock discontinuities. *Eng. Geol.* **2018**, *232*, 171–181. [CrossRef]
9. Elmo, D.; Donati, D.; Stead, D. Challenges in the characterisation of intact rock bridges in rock slopes. *Eng. Geol.* **2018**, *245*, 81–96. [CrossRef]
10. Yu, W.J.; Li, K.; Liu, Z.; An, B.F.; Wang, P.; Wu, H. Mechanical characteristics and deformation control of surrounding rock in weakly cemented siltstone. *Environ. Earth Sci.* **2021**, *80*, 1–5. [CrossRef]
11. Asadizadeh, M.; Hossaini, M.F.; Moosavi, M.; Masoumi, H.; Ranjith, P.G. Mechanical characterisation of jointed rock-like material with non-persistent rough joints subjected to uniaxial compression. *Eng. Geol.* **2019**, *260*, 105224. [CrossRef]
12. Salmi, E.F.; Nazem, M.; Karakus, M. Numerical analysis of a large landslide induced by coal mining subsidence. *Eng. Geol.* **2017**, *217*, 141–152. [CrossRef]
13. Lin, Q.B.; Cao, P.; Wen, G.P.; Meng, J.J.; Cao, R.H.; Zhao, Z.Y. Crack coalescence in rock-like specimens with two dissimilar layers and pre-existing double parallel joints under uniaxial compression. *Int. J. Rock Mech. Min. Sci.* **2021**, *139*, 104621. [CrossRef]
14. Cai, W.Q.; Zhu, H.H.; Liang, W.H. Three-dimensional tunnel face extrusion and reinforcement effects of underground excavations in deep rock masses. *Int. J. Rock Mech. Min. Sci.* **2022**, *150*, 104999. [CrossRef]
15. Liu, J.; Wang, J. Numerical study of crack propagation in an indented rock specimen. *Comput. Geotech.* **2018**, *96*, 1–11. [CrossRef]
16. Han, Z.; Li, D.; Zhou, T.; Zhu, Q.; Ranjith, P.G. Experimental study of stress wave propagation and energy characteristics across rock specimens containing cemented mortar joint with various thicknesses. *Int. J. Rock Mech. Min. Sci.* **2020**, *131*, 104352. [CrossRef]
17. Chen, W.; Wan, W.; Zhao, Y.L.; Peng, W.Q. Experimental study of the crack predominance of rock-like material containing parallel double fissures under uniaxial compression. *Sustainability* **2020**, *12*, 5188. [CrossRef]
18. Zheng, C.S.; Jiang, B.Y.; Xue, S.; Chen, Z.W.; Li, H. Coalbed methane emissions and drainage methods in underground mining for mining safety and environmental benefits: A review. *Process. Saf. Environ.* **2019**, *127*, 103–124. [CrossRef]
19. Sow, D.; Carvajal, C.; Breul, P.; Peyras, L.; Rivard, P.; Bacconnet, C.; Ballivy, G. Modeling the spatial variability of the shear strength of discontinuities of rock masses: Application to a dam rock mass. *Eng. Geol.* **2017**, *220*, 133–143. [CrossRef]
20. Zhou, X.; Xie, Y.J.; Long, G.C.; Li, J.T. Effect of surface characteristics of aggregates on the compressive damage of high-strength concrete based on 3D discrete element method. *Constr. Build. Mater.* **2021**, *301*, 124101. [CrossRef]
21. Xie, S.; Lin, H.; Wang, Y.; Chen, Y.; Xiong, W.; Zhao, Y.; Du, S. A statistical damage constitutive model considering whole joint shear deformation. *Int. J. Damage Mech.* **2020**, *29*, 988–1008. [CrossRef]
22. Babanouri, N.; Asadizadeh, M.; Hasan-Alizade, Z. Modeling shear behavior of rock joints: A focus on interaction of influencing parameters. *Int. J. Rock Mech. Min. Sci.* **2020**, *134*, 104449. [CrossRef]
23. Xie, S.; Lin, H.; Cheng, C.; Chen, Y.; Wang, Y.; Zhao, Y.; Yong, W. Shear strength model of joints based on Gaussian smoothing method and macro-micro roughness. *Comput. Geotech.* **2022**, *143*, 104605. [CrossRef]
24. Xie, S.; Han, Z.; Zhou, T. A semiempirical constitutive relationship for rocks under uniaxial compression considering the initial damage recovery. *Fatigue Fract. Eng. Mater. Struct.* **2023**, *46*, 1300–1313. [CrossRef]
25. Zhu, C.G.; Long, S.C.; Zhang, J.X.; Wu, W.H.; Zhang, L.Y. Time series multi-sensors of interferometry synthetic aperture radar for monitoring ground deformation. *Front. Environ. Sci.* **2022**, *10*, 952. [CrossRef]
26. Pirzada, M.A.; Bahaaddini, M.; Moradian, O.; Roshan, H. Evolution of contact area and aperture during the shearing process of natural rock fractures. *Eng. Geol.* **2021**, *291*, 106236. [CrossRef]
27. Renaud, S.; Bouaanani, N.; Miquel, B. Numerical simulation of experimentally shear-tested contact specimens from existing dam joints. *Comput. Geotech.* **2020**, *125*, 103630. [CrossRef]
28. Singh, H.K.; Basu, A. Shear behaviors of 'real' natural un-matching joints of granite with equivalent joint roughness coefficients. *Eng. Geol.* **2016**, *211*, 120–134. [CrossRef]
29. Saadat, M.; Taheri, A. A cohesive discrete element based approach to characterizing the shear behavior of cohesive soil and clay-infilled rock joints. *Comput. Geotech.* **2019**, *114*, 103109. [CrossRef]
30. Xin, J.; Jiang, Q.; Liu, Q.; Zheng, H.; Li, S.J. A shear constitutive model and experimental demonstration considering dual void portion and solid skeleton portion of rock. *Eng. Fract. Mech.* **2023**, *281*, 109066. [CrossRef]
31. Zhou, X.; Xie, Y.J.; Long, G.C.; Zeng, X.H.; Li, J.T.; Yao, L.; Jiang, W.H.; Pan, Z.L. DEM analysis of the effect of interface transition zone on dynamic splitting tensile behavior of high-strength concrete based on multi-phase model. *Cem. Concr. Res.* **2021**, *149*, 106577. [CrossRef]
32. Zhao, Y.L.; Luo, S.L.; Wang, Y.X.; Wang, W.J.; Zhang, L.Y.; Wan, W. Numerical analysis of karst water inrush and a criterion for establishing the width of water-resistant rock pillars. *Mine Water Environ.* **2017**, *36*, 508–519. [CrossRef]
33. Yuan, Z.G.; Zhao, J.T.; Li, S.Q.; Jiang, Z.H.; Huang, F. A unified solution for surrounding rock of roadway considering seepage, dilatancy, strain-softening and intermediate principal stress. *Sustainability* **2022**, *14*, 8099. [CrossRef]

34. Wu, H.; Jia, Q.; Wang, W.J.; Zhang, N.; Zhao, Y.M. Experimental test on nonuniform deformation in the tilted strata of a deep coal mine. *Sustainability* **2021**, *13*, 13280. [CrossRef]
35. Xie, S.; Han, Z.; Hu, H.; Lin, H. Application of a novel constitutive model to evaluate the shear deformation of discontinuity. *Eng. Geol.* **2022**, *304*, 106693. [CrossRef]
36. Zou, S.H.; Li, K.Q.; Han, Q.Y.; Yu, C.W. Numerical simulation of the dynamic formation process of fog-haze and smog in transport tunnels of a hot mine. *Indoor Built Environ.* **2017**, *26*, 1062–1069. [CrossRef]
37. Sun, Z.; Niu, D.T.; Wang, X.Q.; Zhang, L.; Luo, D.M. Bond behavior of coral aggregate concrete and corroded Cr alloy steel bar. *J. Build Eng.* **2022**, *61*, 105294. [CrossRef]
38. Sun, Z.; He, W.D.; Niu, D.T.; Zhang, L.; Su, L.; Wang, X.Q. Resistivity prediction model for basalt-polypropylene fiber-reinforced concrete. *Buildings* **2023**, *13*, 84. [CrossRef]
39. Haghgouei, H.; Kargar, A.R.; Amini, M.; Esmaeili, K. An analytical solution for analysis of toppling-slumping failure in rock slopes. *Eng. Geol.* **2020**, *265*, 105396. [CrossRef]
40. Wu, Y.Q.; Zhou, Y.S. Hybrid machine learning model and Shapley additive explanations for compressive strength of sustainable concrete. *Constr. Build. Mater.* **2022**, *330*, 127298. [CrossRef]
41. Wu, Y.Q.; Zhou, Y.S. Prediction and feature analysis of punching shear strength of two-way reinforced concrete slabs using optimized machine learning algorithm and Shapley additive explanations. *Mech. Adv. Mater. Struc.* **2022**. [CrossRef]
42. Lin, Q.B.; Cao, P.; Meng, J.J.; Cao, R.H.; Zhao, Z.Y. Strength and failure characteristics of jointed rock mass with double circular holes under uniaxial compression: Insights from discrete element method modelling. *Theor. Appl. Fract. Mec.* **2020**, *109*, 102692. [CrossRef]
43. Thirukumaran, S.; Indraratna, B. A review of shear strength models for rock joints subjected to constant normal stiffness. *J. Rock Mech. Geotech. Eng.* **2016**, *8*, 405–414. [CrossRef]
44. Zhao, Y.L.; Tang, J.Z.; Chen, Y.; Zhang, L.Y.; Wang, W.J.; Wan, W.; Liao, J.P. Hydromechanical coupling tests for mechanical and permeability characteristics of fractured limestone in complete stress-strain process. *Environ. Earth Sci.* **2017**, *76*, 1–18. [CrossRef]
45. Patton, F.D. Multiple modes of shear failure in rock. In Proceedings of the 1st Congress of International Society of Rock Mechanics, Lisbon, Portugal, 25 September–1 October 1966.
46. Cai, W.; Zhu, H.; Liang, W. Three-dimensional stress rotation and control mechanism of deep tunneling incorporating generalized Zhang–Zhu strength-based forward analysis. *Eng. Geol.* **2022**, *308*, 106806. [CrossRef]
47. Zhao, Y.L.; Zhang, C.S.; Wang, Y.X.; Lin, H. Shear-related roughness classification and strength model of natural rock joint based on fuzzy comprehensive evaluation. *Int. J. Rock Mech. Min. Sci.* **2021**, *137*, 104550. [CrossRef]
48. Barton, N.; Choubey, V. The shear strength of rock joints in theory and practice. *Rock Mech.* **1977**, *10*, 1–54. [CrossRef]
49. Ulusay, R. *The ISRM Suggested Methods for Rock Characterization, Testing and Monitoring: 2007–2014*; Springer: Berlin/Heidelberg, Germany, 2014.
50. Xie, S.; Lin, H.; Duan, H. A novel criterion for yield shear displacement of rock discontinuities based on renormalization group theory. *Eng. Geol.* **2023**, *314*, 107008. [CrossRef]
51. Xie, S.; Lin, H.; Chen, Y. New constitutive model based on disturbed state concept for shear deformation of rock joints. *Arch. Civ. Mech. Eng.* **2022**, *23*, 26. [CrossRef]
52. Li, Y.; Oh, J.; Mitra, R.; Hebblewhite, B. A constitutive model for a laboratory rock joint with multi-scale asperity degradation. *Comput. Geotech.* **2016**, *72*, 143–151. [CrossRef]
53. Oh, J.; Cording, E.J.; Moon, T. A joint shear model incorporating small-scale and large-scale irregularities. *Int. J. Rock Mech. Min. Sci.* **2015**, *76*, 78–87. [CrossRef]
54. Zhao, Y.L.; Liu, Q.; Zhang, C.S.; Liao, J.; Lin, H.; Wang, Y.X. Coupled seepage-damage effect in fractured rock masses: Model development and a case study. *Int. J. Rock Mech. Min. Sci.* **2021**, *144*, 104822. [CrossRef]
55. Feng, W.L.; Zou, D.J.; Wang, T.; Qiao, C.S.; Xu, S.F. Study on a nonlinear shear damage constitutive of structural plane and application of discrete element. *Comput. Geotech.* **2023**, *155*, 105190. [CrossRef]
56. Parrinello, F.; Failla, B.; Borino, G. Cohesive–frictional interface constitutive model. *Int. J. Solids Struct.* **2009**, *46*, 2680–2692. [CrossRef]
57. Cai, W.; Zhu, H.; Liang, W.; Wang, X.; Su, C.; Wei, X. A post-peak dilatancy model for soft rock and its application in deep tunnel excavation. *J. Rock Mech. Geotech. Eng.* **2023**, *15*, 683–701. [CrossRef]
58. Tong, D.; Yi, X.-W.; Tan, F.; Jiao, Y.Y.; Liang, J. Three-dimensional numerical manifold method for heat conduction problems with a simplex integral on the boundary. *Sci. China Technol. Sci.* **2023**.
59. Leong, E.C.; Randolph, M.F. A model for rock interfacial behavior. *Rock Mech. Rock Eng.* **1992**, *25*, 187–206. [CrossRef]
60. Goodman, R. The mechanical properties of joints. In Proceedings of the 3rd Int Congr International Society of Rock Mechanics, Denver, CO, USA, 1–7 September 1974; pp. 1–7.
61. Xiao, W.; Dui, G.; Chen, T.; Ren, Q. A study of constitutive model coupling dilatancy and degradation for jointed rock. *Chin. J. Rock Mech. Eng.* **2009**, *28*, 2535–2543.
62. Sun, W.; Gao, J.; Zhang, W.; Yang, K. Experimental study on the shear mechanical properties of discontinuities in rock masses. *China Water Transp.* **2008**, *8*, 159–160.
63. Lee, S. *Stability around underground Openings in Rock with Dilative, Non-Persistent and Multi-Scale Wavy Joints Using a Discrete Element Method*; University of Illinois at Urbana-Champaign: Chicago, IL, USA, 2003.

64. Xu, L.; Ren, Q. A new constitutive model for rock discontinuities. *Rock Soil Mech.* **2011**, *32*, 217–224. [CrossRef]
65. Gens, A.; Carol, I.; Alonso, E.E. A constitutive model for rock joints formulation and numerical implementation. *Comput. Geotech.* **1990**, *9*, 3–20. [CrossRef]
66. Kulhawy, F.H. Stress deformation properties of rock and rock discontinuities. *Eng. Geol.* **1975**, *9*, 327–350. [CrossRef]
67. Bandis, S.C.; Lumsden, A.C.; Barton, N.R. Fundamentals of rock joint deformation. *Int. J. Rock Mech. Min. Sci.* **1983**, *20*, 249–268. [CrossRef]
68. Xie, S.; Lin, H.; Chen, Y.; Yong, R.; Xiong, W.; Du, S. A damage constitutive model for shear behavior of joints based on determination of the yield point. *Int. J. Rock Mech. Min. Sci.* **2020**, *128*, 104269. [CrossRef]
69. Xie, S.; Han, Z.; Shu, R.; Chen, Y.; Feng, F. A new method to determine the crack closure stress based on stress difference. *Theor. Appl. Fract. Mec.* **2022**, *119*, 103337. [CrossRef]
70. Xie, S.J.; Lin, H.; Wang, Y.X.; Cao, R.H.; Yong, R.; Du, S.G.; Li, J.T. Nonlinear shear constitutive model for peak shear-type joints based on improved Harris damage function. *Arch. Civ. Mech. Eng.* **2020**, *20*, 1–14. [CrossRef]
71. Papaliangas, T.; Hencher, S.R.; Lumsden, A.C.; Manolopoulou, S. The effect of frictional fill thickness on the shear strength of rock discontinuities. *Int. J. Rock Mech. Min. Sci.* **1993**, *30*, 81–91. [CrossRef]
72. Grasselli, G. Manuel Rocha Medal recipient-Shear strength of rock joints based on quantified surface description. *Rock Mech. Rock Eng.* **2006**, *39*, 295–314. [CrossRef]
73. Nasir, O.; Fall, M. Shear behaviour of cemented pastefill-rock interfaces. *Eng. Geol.* **2008**, *101*, 146–153. [CrossRef]
74. Bahaaddini, M. Effect of boundary condition on the shear behaviour of rock joints in the direct shear test. *Rock Mech. Rock Eng.* **2017**, *50*, 1141–1155. [CrossRef]
75. Ge, Y.F.; Tang, H.M.; Eldin, M.; Wang, L.Q.; Wu, Q.; Xiong, C.R. Evolution process of natural rock joint roughness during direct shear tests. *Int. J. Geomech.* **2017**, *17*, E4016013. [CrossRef]
76. Ong, D.E.L.; Choo, C.S. Assessment of non-linear rock strength parameters for the estimation of pipe jacking forces. Part 1. Direct shear testing and backanalysis. *Eng. Geol.* **2018**, *244*, 159–172. [CrossRef]
77. Zhao, Z.H.; Dou, Z.H.; Xu, H.R.; Liu, Z.N. Shear behavior of Beishan granite fractures after thermal treatment. *Eng. Fract. Mech.* **2019**, *213*, 223–240. [CrossRef]
78. Zhou, H.; Cheng, G.T.; Zhu, Y.; Chen, J.; Lu, J.J.; Cui, G.J.; Yang, P.Q. Experimental study of shear deformation characteristics of marble dentate joints. *Rock Soil Mech.* **2019**, *40*, 852–860. [CrossRef]
79. Wang, F.; Xia, K.; Yao, W.; Wang, S.; Wang, C.; Xiu, Z. Slip behavior of rough rock discontinuity under high velocity impact: Experiments and models. *Int. J. Rock Mech. Min. Sci.* **2021**, *144*, 104831. [CrossRef]
80. Fan, X.; Deng, Z.Y.; Cui, Z.M.; He, Z.M.; Lin, H. A new peak shear strength model for soft-hard joint. *Rock Soil Mech.* **2021**, *42*, 1861–1870. [CrossRef]
81. Bao, H.; Xu, X.; Lan, H.; Yan, C.; Xu, J. Stiffness model of rock joint by considering anisotropic morphology. *J. Traffic Transp. Eng.* **2021**, *11*, 1–18. (In Chinese)

minerals

MDPI

Article

Evaluation Model of Hard Limestone Reformation and Strength Weakening Based on Acidic Effect

Mingxiao Hou, Bingxiang Huang *, Xinglong Zhao, Xuejie Jiao, Xufei Jiang and Zheng Sun

State Key Laboratory of Coal Resources and Safe Mining, China University of Mining and Technology, Xuzhou 221116, China; hou036@cumt.edu.cn (M.H.)
* Correspondence: huangbingxiang@cumt.edu.cn

Abstract: The typical thick-hard limestone roof with high failure pressure and easy fracture closure under in situ stress is extremely prone to induce disasters, which seriously threatens the safe production of coal mines. The modification of carbonate minerals by acidic effects can effectively realize the weakening control of hard limestone strata. In this study, a multi-factor orthogonal experiment was designed for limestone acidification reactions, and the evaluation model for the reformation and strength weakening of hard limestone based on the acidic effect was established accordingly. The results showed that there is an order in the influence of various factors on the reaction parameters and strength indices of acidified limestone, and the improvement of rock properties by the level difference of acid concentration is significantly better than that of acid type and acidification time. Through numerical analysis, the evaluation model of limestone reformation and strength weakening considering the acid reaction parameters is given. The reliability of the model passed the credibility test and experimental verification, which can effectively reflect the strength response characteristics of acidified limestone. The simulated annealing (SA) algorithm is introduced to derive the optimal acidification system suitable for limestone weakening. Combined with the model, the control mechanism of the acidic effect on hard limestone strata was analyzed. The acidic effect can not only induce the rapid generation and expansion of micro-cracks at mineral-containing crystal defects, but also make the cracks remain relatively open under in situ stress due to the differential interaction on mineral components, which is conducive to the bearing capacity reduction and structural damage of limestone rock mass. The research results provide theoretical guidance for the acidification control of hard limestone strata in underground mines.

Keywords: acidic effect; hard stratum; evaluation model; crystal defect; strength weakening

1. Introduction

In China, more than one third of the coal seam roofs are thick-hard roofs with high rock strength, undeveloped joint fissures, and strong bearing capacity, which can easily induce roof accidents and derived mine pressure disasters [1–3]. For the thick-hard rock strata (especially limestone strata) overlying the working face of longwall mining, such as Jincheng mining area [4], Datong mining area [5], and Shendong mining area [6], due to the extreme fracture pressure and the secondary closure of cracks under in situ stress, the effect of conventional strata control methods such as hydraulic fracturing [7,8] and blasting [9] is limited, which seriously threatens the safety production of coal mines. Therefore, it is urgent to find a more suitable treatment method for hard limestone. The strong reaction of acid to limestone can improve the rock structure and reduce the strength properties, which is a novel and effective way to control the hard limestone strata in coal mines [10]. The acidification method of strata is derived from the stimulation of low permeability carbonate reservoirs. Specifically, it changes the rock structure through acid–rock chemical reactions, and has the ability to etch cracks, dissolve cementation, and etch diversion [11].

The existing rock acidification theories and evaluation models focus on the structural reformation of reservoir-bearing strata and construct a highly conductive wormhole

network in the strata through the acidic effect to promote the efficient output of oil, gas, or geothermal resources [12,13]. Since the establishment of the classical N-K empirical formula considering the equivalent relationship between rock dissolution and fracture conductivity in 1973 [14], the acidification model based on this has been continuously refined and optimized for the evaluation of acid etching fracture morphology, acid penetration distance, and acid etching fracture conductivity [15,16]. The corresponding relationship between the conductivity of acid etching fractures has also evolved from the single factor models (Gangi model [17], Walsh model [18], T-W model [19], etc.) that only consider closure stress, lithology, and surface roughness, and then gradually developed into the models under different factors (Gong model [20], Mou model [21], etc.). In recent years, the refined models of rock characteristics under various acidic effects are mostly applied to the analysis of acid fluid filtration, the identification of multiphase flow and the description of fracture behavior. The existing acidification theory system and related evaluation are mainly limited to the improvement of permeability and conductivity of reservoir-bearing strata under different occurrence conditions and reservoir spaces.

However, there are obvious differences in the acidification environment between the reservoir and the rock strata in the underground mine [22–24], and the rock strata control area of the longwall mining surface of the coal mine is relatively concentrated and basically homogeneous [25–27]. The acidification of hard rock strata should ensure that the acid pressure fluid is injected into the surrounding rock through drilling methods, so as to achieve the purpose of weakening the strength of rock mass and rapidly destroy the structural integrity. Therefore, the response law of reformation characteristics and mechanical properties of hard rock strata under the acidic effect is the primary purpose of this research. The existing acidic effect evaluation model is not suitable for the reformation and strength influence of limestone strata in coal mines, so it cannot be further systematically and accurately applied to field projects.

Therefore, in this study, the reformation test of hard limestone under the acidic effect was carried out. Based on the sensitivity and significance analysis of reaction results and mechanical indices under different acidification factors, the reformation and strength evaluation model of limestone considering acid reaction parameters was established. The optimized acid reaction system suitable for the weakening of hard limestone was given, and the damage mechanism of the acidic effect on the mineral crystals contained in hard limestone was discussed in order to provide guidance for the weakening control of hard limestone strata in underground mines by the acidic effect.

2. Orthogonal Simulation Experiment

2.1. Chemical Reaction Principle

Limestone is a carbonate rock with calcite group minerals ($CaCO_3$) and dolomite group minerals ($CaMg(CO_3)_2$) as the main components [28]. It can undergo metathesis reactions with acidic media, and the reaction products are neutral compounds containing calcium and magnesium ions. Most of them can be dissolved in water, which has little effect on the geological environment of the stope. The premise of acid–rock reactions is the dissolution and ionization of carbonate mineral components in limestone under liquid phase. Taking the calcite group as an example, Equation (1) is the dissolution and ionization equilibrium equation of calcium carbonate, the main composition of the calcite group, which is a strong electrolyte and can undergo complete ionization when dissolved in water.

$$CaCO_3(s) \rightleftharpoons CaCO_3(aq) = Ca^{2+}(aq) + {CO_3}^{2-}(aq) \quad (1)$$

For the overlying limestone strata of the stope in underground mining operations, the acid solution is pumped into the control area through the dense drilling of the roof, and the acid ions penetrate deep into the surrounding rock. The carbonate minerals in the area are completely ionized under acidic conditions to produce carbonate ions, and salt compounds, carbon dioxide gas, and water are generated according to the acid reaction of different

media (Equation (2)), which will promote the dissolution reaction of mineral components to be positive, resulting in the acid etching behavior of the macroscopic limestone matrix.

$$\begin{cases} CaCO_3 + 2HCOOH \rightarrow Ca(HCOO)_2 + CO_2 \uparrow + H_2O \\ CaCO_3 + 2HCl \rightarrow CaCl_2 + CO_2 \uparrow + H_2O \\ CaCO_3 + 2HF \rightarrow CaF_2 + CO_2 \uparrow + H_2O \end{cases} \quad (2)$$

The acid–rock chemical reaction behavior is mainly reflected in the initial stage containing a high concentration of hydrogen ions, and the reactants are sufficient to make the ion replacement capacity within the system stronger. At the same time, it is known from Van's law [29] that the activated particles involved in the replacement will collide more frequently and effectively along with the exothermic reaction, so the initial stage has the most significant acidic effect on limestone. In the later stages of the reaction, the hydrogen ions in the solution system are consumed. In addition, some of the generated carbon dioxide gas will dissolve in water to form carbonic acid, which can cause certain dissolution of carbonate minerals in limestone, but the effect is limited.

2.2. Specimen Preparation and Experimental Device

The specimens were taken from the hard limestone roof strata on the longwall working face of a coal mine in Gaoping City, Shanxi Province, China (rock density was 2.72 g/cm^3, water content was 0.49%). In order to reduce the influence of specimen dispersion on the experimental results, the standard rock specimens with a diameter of 50 mm and a height of 100 mm were prepared by dense drilling in the same rock block (Figure 1).

Figure 1. Limestone specimens.

Figure 2a is the reaction device of the acidizing modification test. The surface and lining materials of the device were an ANSI stainless steel with high pressure resistance and polytetrafluoroethylene (PTFE) with strong acid corrosion resistance, which can be used for long-term simulated experiments of limestone acidification reformation under confined and high temperature environment.

The rock strength characteristic test system included MTS C64.106 electro-hydraulic servo universal testing machine and YBY-2001 static resistance strain gauge (Figure 2b), which is used to test the strength index of acidified specimens. The MTS testing machine has a high strength six-column load frame configuration, with beam displacement limit protection, force overload protection, overheating protection, voltage overload protection, and other functions. The matching TestWork software can realize the monitoring of parameters such as R_{eH} (upper yield strength), R_{eL} (lower yield strength), $R_{p0.2}$ (specified non-proportional extension strength), and $R_{t0.5}$ (specified total extension strength). The maximum loading pressure of the test machine was 1000 kN, the load accuracy was 0.5%, and the sampling frequency was 1000 Hz. The YBY-2001 resistance strain gauge was used to record the strain values during the strength test. The strain gauge adopts a 24-bit

A/D resolution, the maximum sampling frequency of 10 Hz, and the maximum range of measured strain of ±19,999 με. The strain gauge met the test environment of −20 °C to 50 °C, and collected all the data of up to 20 channels at the same time.

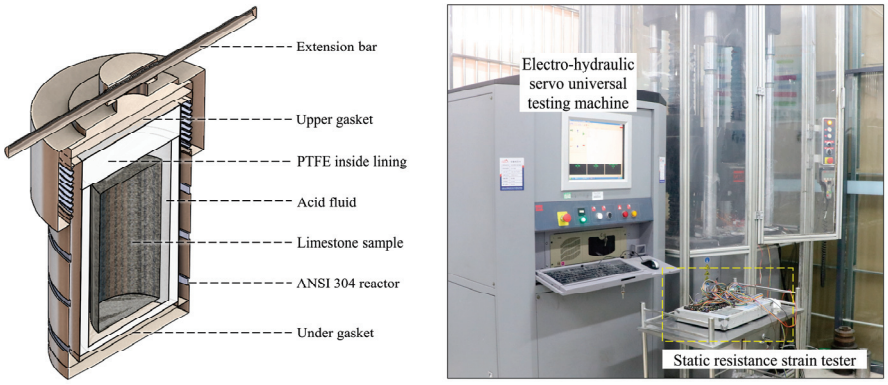

(**a**) (**b**)

Figure 2. Experimental devices, (**a**) acidification reaction device and (**b**) rock strength characteristic test system.

2.3. Orthogonal Experimental Design

This experiment was a three-factor three-level parameter test (Table 1), and the empty column was set as a random error column for subsequent significance analysis. Based on the Taguchi orthogonal method, the $L_9(3^4)$ orthogonal design was established. The three acid types were selected as hydrochloric acid, formic acid, and mud acid (4%–12% HCl + 1%–3% HF), respectively.

Table 1. Factors and levels of the orthogonal experimental design.

Factor \ Level	A: Acid Type	B: Acid Concentration (%)	C: Acidification Time (min)
1	Hydrochloric acid (HCl)	5	60
2	Formic acid (HCOOH)	10	120
3	Mud acid (4%–12%HCl + 1%–3%HF)	15	180

2.4. Experimental Process

To carry out the limestone acidizing reformation experiment, the limestone standard sample was dried and weighed in advance. After photographing and recording the morphological characteristics of the rock sample, the specimen was placed in the PTFE lining of the acidizing reformation experimental device. According to the scheme, the acid reaction liquid was prepared in the lining to ensure that the specimen could be completely immersed, and then the reactor cover was closed to seal the device well. The mass of the specimen and the concentration of acid solution were measured at intervals. The mass of the specimen at each time i was recorded as M_i, and the acid dissolution rate of limestone at time i was calculated according to Equation (3). According to Equation (4), the acid–rock reaction rate constant K (used to reflect the speed of the acid–rock reaction rate) was calculated. After acidification, the specimen was taken out from the device, the residual acid and residue on the surface were carefully cleaned, and then placed in a drying oven at 105 °C for 24 h. Finally, the specimen was naturally cooled to room temperature for later use.

$$\omega_i = \left(\frac{M_0}{M_i} - 1\right) \times 100\% \quad (3)$$

where M_0 represents the initial mass of the specimen.

$$K = \frac{J}{C^n} \tag{4}$$

where K represents the reaction rate constant, J is the reaction rate at time t, C is the corresponding acid solution concentration at time t, and n is the reaction order.

Due to the influence of acid etching behavior of limestone, the surface of the specimen was polished and corrected in advance before the strength test, so as to ensure that the flatness and parallelism of the specimen met the standard. Two sets of strain gauges were symmetrically arranged on the central surface of the specimen at 1/2 height. Each group was composed of two foil strain gauges that were vertically distributed along the lateral and axial directions of the specimen. The substrate size of the strain gauge was 9.5 × 4.0 mm, the resistance value was 120 Ω, and the sensitivity was 2.0 mV/V. The strain gauge was connected to the static resistance strain gauge channel to monitor the axial and lateral strain values of the specimen under load. In order to reduce the influence of the end effect, grease was evenly applied to the upper and lower surfaces of the specimen. Then, the specimen was placed in the center of the test bench, and the spherical bearing plate was covered to make the specimen uniformly stressed during compression. The testing machine adopted displacement loading mode, and the loading rate was set to 0.5 mm/min. The loading system and strain gauge were started synchronously, after that, the loading was stopped until the specimen was completely destroyed. Finally, the experimental data were saved, the maximum failure load was recorded, and the mechanical parameters such as uniaxial compressive strength, strain value, and elastic modulus were calculated.

3. Orthogonal Experiment Results and Analysis

Through the acidizing reformation and strength test of hard limestone, the acid reaction data and macroscopic mechanical parameters of limestone were obtained, including the acidification indexes of the limestone acid dissolution rate ω and acid–rock reaction rate constant K, as well as the strength indexes of uniaxial compressive strength σ_c, elastic modulus E, peak strength corresponding to the axial strain ε_{ca}, and lateral strain $\varepsilon_c l$, as detailed in Table 2. Furthermore, the influencing factors were analyzed based on the test results of the parameters.

Table 2. Results of the orthogonal experiment.

No.	Factors				ω/%	K/mol$^{(1-n)}$·L$^{(n-1)}$·s^{-1}·10^{-4}	σ_c/MPa	ε_{ca}/10^{-2}	ε_{cl}/10^{-2}	E/GPa
	A	B/%	C/min	Null						
1	1	1	1	1	3.69	8.51	63.01	1.46	−0.83	7.97
2	1	2	2	2	6.65	34.04	41.94	1.17	−0.56	5.94
3	1	3	3	3	9.07	36.22	32.19	1.01	−0.48	5.2
4	2	1	2	3	2.92	3.63	71.50	1.59	−0.89	8.81
5	2	2	3	1	5.29	20.80	47.86	1.25	−0.63	6.23
6	2	3	1	2	4.81	9.86	49.59	1.20	−0.61	6.74
7	3	1	3	2	4.16	8.24	63.38	1.41	−0.81	7.91
8	3	2	1	3	4.86	13.77	51.76	1.25	−0.65	6.47
9	3	3	2	1	7.65	32.27	39.09	1.07	−0.51	5.84

3.1. Sensitivity Analysis

The range analysis method is widely used in the sensitivity analysis of influencing factors. The arithmetic mean values of the observed variables (limestone acidizing parameters and strength indexes) of the influencing factors (A, B, C) at different levels were obtained, respectively, and the range was calculated by the maximum and minimum mean values. The larger the range value, the greater the influence degree of the factor under the same conditions. Therefore, the influence order of factors can be determined according to the

range analysis, and the optimal level of each factor can be selected. According to the mean value and range at each level, Figure 3 shows the influence of A, B, and C on the acidizing reformation and strength characteristics of limestone.

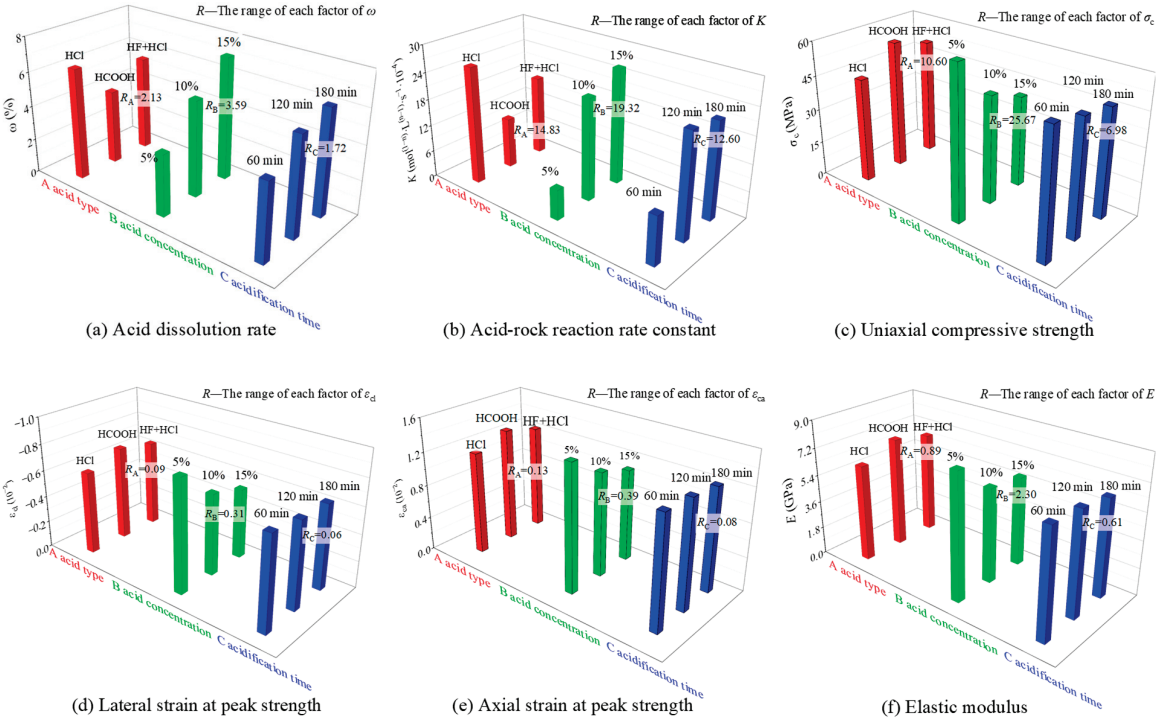

Figure 3. Influence of various factors on limestone acidification and strength characteristics.

For the factor sensitivity analysis of the limestone acidizing reformation effect, it can be seen that the influence order of the factors on the acid dissolution rate ω and the acid–rock reaction rate constant K are: B (acid concentration) > A (acid type) > C (acidification time). Among them, hydrochloric acid as an acid reaction solution is more effective than other acids for limestone acidizing reformation, specifically, ω increased by 49.07% and 16.38% compared to formic acid and mud acid, and K was 129.74% and 45.14% higher than formic acid and mud acid. The limestone acidizing parameters tend to increase uniformly with increasing mass concentration, specifically, ω from 3.59% (5% concentration) to 7.18% (15% concentration) and K from 6.80 × 10^{-4} $mol^{(1-n)}{\cdot}L^{(n-1)}{\cdot}s^{-1}$ (5% concentration) to 26.12 × 10^{-4} $mol^{(1-n)}{\cdot}L^{(n-1)}{\cdot}s^{-1}$ (15% concentration), indicating that high concentration acid reactants have a better ability to reform limestone. When the acidification time was 120 min, the acidification effect of limestone is significantly improved compared with that of 60 min. However, when the acidification time is increased to 180 min, the degree of limestone acid etching only slightly increases, and the acid–rock reaction rate decreases. This is because the hydrogen ions ionized in the acid–rock reaction system have been consumed in large quantities after 120 min, and the concentration of reactants have significantly reduced, resulting in a decrease in the reaction rate with carbonate minerals. Correspondingly, the acid dissolution efficiency of limestone also slowed down.

For the factor sensitivity analysis of the strength characteristics of the limestone after acidification, it can be seen that the influence order of the factors on uniaxial compressive strength σ_c, peak axial/lateral strain $\varepsilon_{ca}/\varepsilon_{cl}$, and elastic modulus E are also: B (acid concentration) > A (acid type) > C (acidification time). Among them, the strength parameters of limestone after formic acid reaction were the highest, followed by mud acid, and hydrochloric acid being the lowest, indicating that the strength weakening effect of hydrochloric acid on limestone after acidification was better than that of formic acid and mud acid. Specifically, σ_c decreased by 18.83% and 11.08%, respectively, ε_{ca} decreased

by 9.90% and 2.41%, respectively, ε_{cl} decreased by 12.21% and 5.08%, respectively, and E decreased by 12.26% and 5.49%, respectively. The acid concentration was positively correlated with the weakening degree of acidified limestone strength. Specifically, σ_c decreased from 65.96 MPa (5% concentration) to 40.29 MPa (15% concentration), ε_{ca} decreased from 1.49×10^{-2} (5% concentration) to 1.09×10^{-2} (15% concentration), ε_{cl} decreased from 0.84×10^{-2} (5% concentration) to 0.53×10^{-2} (15% concentration), and E decreased from 8.23 GPa (5% concentration) to 5.93 GPa (15% concentration), indicating that the strength of limestone was more weakened after the action of high concentration acidic reactants. With the increase of acid reaction time, the strength weakening degree of limestone increased slightly. The uniaxial compressive strength, peak strain, and elastic modulus of limestone with acid reaction for 180 min were the lowest (σ_c was 47.81 MPa, ε_{ca} was 1.22×10^{-2}, ε_{cl} was -0.64×10^{-2}, E was 6.45 GPa).

3.2. Significance Analysis

The range analysis method is widely used in the sensitivity analysis of influencing factors.

Variance analysis can be used to study whether the control variables can have a significant impact on the observed variables (dependent variables). Specifically, by analyzing the contribution of different sources of variation in the observed variables to the total variation, the significance of the influence of controllable factors on the research results is determined. Multivariate analysis of variance first identifies the observed variables and several control variables, and on this basis, gives the original hypothesis that the control variables do not have a significant impact on the observed variables. In this experiment, the total variation of each observed variable value (limestone acidizing parameters and strength index) was composed of four parts: factor A (acid type), factor B (acid mass concentration), factor C (acidification time), and the variation caused by random factor error. Therefore, the decomposition of sum of squared deviations and degree of freedom in variance analysis is:

$$SS_T = SS_A + SS_B + SS_C + SS_e \tag{5}$$

where SS_T represents the sum of the total squared deviations of the observed variables; SS_A, SS_B, and SS_C are the sum of squared deviations of factors A, B, and C, respectively; and SS_e is the sum of squared deviations of the error (sum of squared deviations within the group).

$$df_T = df_A + df_B + df_C + df_e \tag{6}$$

where df_T represents the total degree of freedom of the observed variable; df_A, df_B, and df_C are the degrees of freedom of factors A, B, and C, respectively; and df_e is the freedom of error.

$$\begin{cases} SS_T = \frac{1}{rst} \sum_{i=1}^{r} \sum_{j=1}^{s} \sum_{k=1}^{t} \left(X_{ijk} - \overline{X}\right)^2 \\ \overline{X} = \frac{1}{rst} \sum_{i=1}^{r} \sum_{j=1}^{s} \sum_{k=1}^{t} X_{ijk} \end{cases} \tag{7}$$

$$\begin{cases} SS_A = st \sum_{i=1}^{r} \left(\overline{X}_{i\cdot\cdot} - \overline{X}\right)^2 = \sum_{i=1}^{r} \frac{1}{st} X_{i\cdot\cdot}^2 - n\overline{X}^2 \\ \overline{X}_{i\cdot\cdot} = \frac{1}{st} \sum_{j=1}^{s} \sum_{k=1}^{t} X_{ijk} \end{cases} \tag{8}$$

$$\begin{cases} SS_B = rt \sum_{j=1}^{s} \left(\overline{X}_{\cdot j\cdot} - \overline{X}\right)^2 = \sum_{j=1}^{s} \frac{1}{rt} X_{\cdot j\cdot}^2 - n\overline{X}^2 \\ \overline{X}_{\cdot j\cdot} = \frac{1}{rt} \sum_{i=1}^{r} \sum_{k=1}^{t} X_{ijk} \end{cases} \tag{9}$$

$$\begin{cases} SS_{\mathrm{C}} = rs\sum\limits_{k=1}^{t}\left(\overline{X}_{\cdot\cdot k} - \overline{X}\right)^2 = \sum\limits_{k=1}^{t}\frac{1}{rs}X_{\cdot\cdot k}^2 - n\overline{X}^2 \\ \overline{X}_{\cdot\cdot k} = \frac{1}{rs}\sum\limits_{i=1}^{r}\sum\limits_{j=1}^{s}X_{ijk} \end{cases} \tag{10}$$

$$SS_{\mathrm{e}} = \sum_{i=1}^{r}\sum_{j=1}^{s}\sum_{k=1}^{t}\left(X_{ijk} - \overline{X}_{i\cdot\cdot} - \overline{X}_{\cdot j\cdot} - \overline{X}_{\cdot\cdot k} + 2\overline{X}\right)^2 = SS_{\mathrm{T}} - SS_{\mathrm{A}} - SS_{\mathrm{B}} - SS_{\mathrm{C}} \tag{11}$$

where r, s, and t represent the level numbers of factor A, B and C respectively (in this experiment, r, s, and t are all 3); X_{ijk} is the sample value corresponding to the i level of factor A, the j level of factor B, and the k level of factor C; $\overline{X}$ is the mean value of the overall observed variables; $\overline{X}_{i\cdot\cdot}$ is the mean value of the observed variables at the ith level of factor A; $\overline{X}_{\cdot j\cdot}$ is the mean of the observed variables at the jth level of factor B; and $\overline{X}_{\cdot\cdot k}$ is the mean of the observed variables at the kth level of the C factor.

After calculation, the analysis of variance table (Table 3) was listed, and the homogeneity of variance test (F test) was performed on the statistics. According to the comparison between the F value of each factor and the quantile $F_{1-\alpha}$ at different significance levels α, if the factor F value is greater than $F_{1-\alpha}$, the null hypothesis should be rejected. It is considered that there are significant differences in the mean values of the observed variables at different levels of the factor; that is, the different levels of the factor have a significant impact on the observed variables. On the contrary, it is considered that different levels of the factor have no significant effect on the results.

Table 3. Analysis of variance table.

Source	Sum of Squared Deviations *SS*	Degree of Freedom *df*	Mean Square *MS*	*F*-Value
A	SS_{A}	$df_{\mathrm{A}} = r - 1$	$MS_{\mathrm{A}} = SS_{\mathrm{A}}/df_{\mathrm{A}}$	$F_{\mathrm{A}} = MS_{\mathrm{A}}/MS_{\mathrm{e}}$
B	SS_{B}	$df_{\mathrm{B}} = s - 1$	$MS_{\mathrm{B}} = SS_{\mathrm{B}}/df_{\mathrm{B}}$	$F_{\mathrm{B}} = MS_{\mathrm{B}}/MS_{\mathrm{e}}$
C	SS_{C}	$df_{\mathrm{C}} = t - 1$	$MS_{\mathrm{C}} = SS_{\mathrm{C}}/df_{\mathrm{C}}$	$F_{\mathrm{C}} = MS_{\mathrm{C}}/MS_{\mathrm{e}}$
Error	SS_{e}	$df_{\mathrm{e}} = df_{\mathrm{T}} - df_{\mathrm{A}} - df_{\mathrm{B}} - df_{\mathrm{C}}$	$MS_{\mathrm{e}} = SS_{\mathrm{e}}/df_{\mathrm{e}}$	
Total T	SS_{T}	$df_{\mathrm{T}} = n - 1$		

Table 4 shows the significance characteristics of three influencing factors A, B, and C of limestone acidification and strength characteristics based on variance analysis. According to the significant analysis of the effect of limestone acidizing reformation, the confidence of the three influencing factors in the F test of limestone acidizing parameters (ω, K) was above 90%, indicating that the different influencing factors set up in this experiment have an impact on the characteristics of limestone acidification. Among them, the confidence of factor A and factor B was between 95% and 99%, showing that the difference of acid type and acid mass concentration had a significant impact on limestone acidizing parameters. The confidence of factor C was between 90% and 95%, showing that the acidification time had a certain influence on the limestone acidizing parameters. The significance analysis of the influencing factors of the strength characteristics of limestone after acidification showed that, consistent with the statistical results of the acidizing reformation F test, the confidence levels of the three types of influencing factors A, B, and C of the strength indices of acidified limestone were also above 90%. Among them, the level difference of acid mass concentration had a very significant effect on the strength indices of acidified limestone. The level difference of acid type and acidification time had a significant effect and a certain effect on the strength indices, respectively. The acidification time also had a certain effect. In general, the effect of acid mass concentration on the acidification and strength weakening of limestone was particularly significant.

Table 4. Significance analysis of influencing factors of limestone acidification and strength characteristics.

Observation Variable	Source of Variance	Sum of Squared Deviations *SS*	Degree of Freedom *df*	Mean Square *MS*	*F*-Value
Acid dissolution rate ω	A	6.847	2	3.423	24.084 *
	B	19.399	2	9.699	68.240 *
	C	4.793	2	2.396	16.861 °
	Error	0.284	2	0.142	
	Total	2.460	8		
Acid–rock reaction rate constant K	A	331.012	2	165.506	19.297 *
	B	642.276	2	321.138	37.444 *
	C	282.919	2	141.460	16.494 °
	Error	17.153	2	8.577	
	Total	1273.360	8		
Uniaxial compressive strength σ_c	A	168.958	2	84.479	27.681 *
	B	1059.247	2	529.624	173.539 **
	C	73.425	2	36.712	12.029 °
	Error	6.104	2	3.052	
	Total	1307.734	8		
Peak axial strain ε_{ca}	A	0.029	2	0.015	26.959 *
	B	0.241	2	0.120	221.286 **
	C	0.010	2	0.005	9.143 °
	Error	0.001	2	0.001	
	Total	0.281	8		
Peak lateral strain ε_{cl}	A	0.011	2	0.006	24.571 *
	B	0.155	2	0.078	333.000 **
	C	0.005	2	0.003	11.286 °
	Error	0.000	2	0.000	
	Total	0.173	8		
Elastic modulus E	A	1.199	2	0.600	21.241 *
	B	9.454	2	4.727	167.434 **
	C	0.588	2	0.294	10.421 °
	Error	0.056	2	0.028	
	Total	11.299	8		

** indicates extremely significant effect ($F > F_{0.01}(2,2)$), * indicates significant effect ($F_{0.05}(2,2) < F < F_{0.01}(2,2)$), ° indicates certain effect ($F_{0.1}(2,2) < F < F_{0.05}(2,2)$). F-test threshold: $F_{0.01}(2,2) = 99$, $F_{0.05}(2,2) = 19$, $F_{0.1}(2,2) = 9$.

4. Evaluation Analysis of Limestone Acidizing Reformation and Strength Characteristics

4.1. Model Establishment

Based on the results of factor sensitivity and significance analysis, it was confirmed that factors A, B, and C as parameter variables had a significant impact on the evaluation index of limestone acidification and strength characteristics, and the relationship between each factor and different response values did not satisfy the general linear law. Therefore, the nonlinear multivariate polynomial solution was used to determine the relationship between the response parameters and the level values of each factor, and then the multiple regression model of limestone acidification and strength characteristics considering the influencing factors of the acid reaction system was established. The model can evaluate and predict the strength of acidified limestone, determine the optimal level of factors through model optimization, and analyze the acidification and strength response under different parameter combinations.

As the establishment of the regression model needs to quantify the acid type of the influencing factors, the definition of the acidity coefficient pK_a in the acid–base proton theory was introduced to characterize the degree of difficulty in converting acid into hydrated hydrogen ion H_3O^+ and conjugated base by proton transfer, which can be used to reflect the strength of acid solution. The smaller the pK_a value is, the stronger the acidity is. The pK_a values of hydrochloric acid, formic acid, and mud acid selected in this experiment

were –8.00, 3.75, and 0.346, respectively. Combined with the relationship between the response value of limestone acidification and strength characteristics with the change of each factor level in the sensitivity analysis, there was a nonlinear relationship between factors A, B, and C on different response values, and, in addition, there was an interaction effect between factors B and C (acid mass concentration decreases with acidification time). In summary, the multiple nonlinear regression model based on the least squares method was established:

$$y = \beta_0 + \beta_1 x_1 + \beta_2 x_2 + \beta_3 x_3 + \beta_4 x_1^2 + \beta_5 x_2^2 + \beta_6 x_3^2 + \beta_7 x_2 x_3 \quad (12)$$

where y represents the response value of the regression equation, β_i is the regression coefficient of least squares estimation (i = 0, 1, 2, 3, 4), and x_1, x_2, and x_3 are the assignment of factors A, B, and C, respectively.

The regression analysis was carried out based on the results in Table 2, and according to the principle of the least square method, the parameter value that minimizes the sum of squared deviations of the function was selected as the estimation of the regression coefficient. The results of the obtained regression model parameters are shown in Table 5. The regression model analysis showed that the effect of limestone acidizing was negatively correlated with factor A; that is, the greater the acidity coefficient, the weaker the acidity, resulting in a decrease in the degree of acid dissolution and acid–rock reaction rate. It was positively correlated with factors B, C, and their interaction, showing that the greater the acid mass concentration or the longer the acid–rock reaction time, the more favorable the full interaction between more acid ions and limestone minerals in the reaction system, which strengthens the acid etching ability and efficiency. The correlation between the coefficient of the strength characteristic model of limestone after acidification was opposite to the result of acidification; that is, it was positively correlated with factor A, and negatively correlated with factor B, C, and the interaction, showing that the acid with a smaller acidity coefficient had a greater degree of weakening of the mechanical properties of limestone. At the same time, the content and time of reaction acid were beneficial to rock damage, which weakened the ability of limestone to resist deformation, and also confirmed that acidification will promote the deterioration of limestone strength.

Table 5. Regression model coefficient and reliability test.

Evaluating Indicator		β_0	β_1	β_2	β_3	β_4	β_5	β_6	β_7
Acidizing reformation	ω	0.010	−0.256	0.384	1.569	−0.025	−0.009	−0.360	0.074
	K (10^{-4})	−36.082	−1.556	6.570	12.970	−0.098	−0.264	−2.577	0.325
Strength characteristics	σ_c	104.381	1.143	−6.977	−7.350	0.073	0.236	1.373	−0.155
	ε_{ca} (10^{-2})	2.014	0.021	−0.096	−0.114	0.002	0.003	0.014	0.002
	ε_{cl} (10^{-2})	−1.292	−0.012	0.094	0.032	−0.001	−0.003	0.002	−0.001
	E	12.454	0.109	−0.864	−0.725	0.011	0.034	0.172	−0.024

4.2. Model Validation

The credibility of the model was tested, and the goodness of fit of the regression model with different evaluation indexes for the observed values was obtained. The statistical measure of goodness of fit is called the coefficient of determination R^2, which is the overall relationship between the dependent variable and all the independent variables. R^2 is equal to the ratio of the regression sum of squares in the total sum of squares; that is, the percentage of the variability of the dependent variable that the regression model can explain. Table 6 is the credibility test of each index, and it can be seen that the calculated value R^2 of the goodness of fit of each evaluation index model is close to 1, indicating that the credibility of the regression model was high, and the regression model fitted the observed value better.

Table 6. Credibility test of the model.

Regression Model		Regression Sum of Squares	Residual Sum of Squares	R^2
Acidizing reformation	y (ω)	32.502	0.017	0.999
	y (K)	1288.449	52.577	0.959
Strength characteristics	y (σ_c)	1309.201	6.771	0.995
	y (ε_{ca})	0.283	0.002	0.992
	y (ε_{cl})	0.230	0.001	0.995
	y (E)	11.679	0.197	0.983

In addition, the model was verified by the research results of Huang et al. [10]. The test results of Huang's repetitive experimental schemes 7 to 9 on limestone acidification reformation were selected. The test reaction acid was 10% hydrochloric acid and the reaction time was 360 min. As it was a repetitive experiment, the average value of the experimental results of each measured parameter were calculated and compared with the model output, and the results are shown in Table 7. It can be seen that the relative error between the acidification experimental results and the model outputs was within 10%. The credibility test and experimental verification confirmed that the obtained limestone reformation and strength evaluation model based on acidic effect was reliable.

Table 7. Results comparison.

Measured Parameters	ω/%	K/mol$^{(1-n)}$·L$^{(n-1)}$·s^{-1}·10^{-4}	σ_c/MPa	ε_{ca}/10^{-2}	ε_{cl}/10^{-2}	E/GPa
Huang's scheme 7	4.60	19.50	41.07	1.15	−0.44	6.83
Huang's scheme 8	4.14	11.53	48.44	1.00	−0.37	8.16
Huang's scheme 9	3.99	12.13	52.22	1.41	−0.48	6.88
Average experimental results	4.24	14.39	47.24	1.19	−0.43	7.29
Model outputs	4.30	13.91	49.75	1.23	−0.41	7.40
Error/%	1.43	3.42	5.05	2.97	4.30	1.53

4.3. Optimal Analysis of the Model

In order to explore the optimal level of influencing factors of the strength weakening effect after limestone acidification, it is urgent to analyze the optimal value of the model. It can be seen from Table 5 that the acidification strength model is a quaternary high-order equation, which is not suitable for general partial derivative solution and local optimization method. A simulated annealing (SA) algorithm is an optimization algorithm based on Metropolis iterative solution strategy. The algorithm has probabilistic global optimization performance in theory. It has been widely used in control engineering, machine learning, neural network, and other engineering fields [30]. The essence of the SA algorithm is based on the physical principle of solid annealing where the internal energy of the solid in the high temperature state is large. At this time, the internal particles of the solid are in a fast disordered motion behavior. In the process of slowly decreasing the temperature, the internal energy of the solid will decay, and the internal particles will gradually become orderly, until the internal energy of the solid reaches the minimum at room temperature, and the particles are in a stable ground state.

In this study, the process of parameter optimization based on the SA algorithm was the process of finding the minimum value of the objective function in the solution space (the minimum value of the strength after acidification). The starting point of the algorithm was based on the similarity between the annealing process of the solid material in physics and the optimization of the strength weakening effect after the acidification of limestone. A higher initial value (set initial temperature) is given to the acidification strength model by the SA algorithm, with the continuous decline (cooling) of the control parameters, combined with the Metropolis criterion as the probability jump criterion to randomly find

the solution (particle state) of the objective function in the solution space (state space). That is, it can jump out of the local optimal solution interval and eventually tend to the global optimal solution (minimum energy). Equation (13) is the specific probability jump algorithm, and the optimization problem min $f_{(i)}$ is set, where S is the set of feasible solutions of the objective function $f_{(i)}$. If a new solution j is generated from the current solution I; whether i is accepted as the current solution is determined by the transition probability shown. Therefore, it can ensure a higher solution accuracy under the condition of satisfying the function constraints.

$$P_t(i \Rightarrow j) = \begin{cases} 1 & f_{(i)} < f_{(j)} \\ \exp\left(\frac{f_{(i)} - f_{(j)}}{T}\right) & f_{(i)} \geq f_{(j)} \end{cases} \quad (13)$$

where T represents the control parameter, which is used to simulate the temperature in the SA algorithm, set at an initial value T_0 of 100, then slowly decreased to T_k (k = 1, 2, ...). Each T value needs to perform the L_k times Metropolis criterion, and then transition to the next control parameter T_{k+1}. That is, to fully simulate the molecular thermal motion and detect the region with search potential, the number of iterations L_k was 1000.

The acidification strength model was introduced into the SA algorithm by MATLAB programming, and the annealing attenuation coefficient α was set to 0.95. The SA algorithm is independent of the initial value, and the solution obtained by the algorithm is independent of the initial solution state (the starting point of the algorithm iteration). Therefore, the initial value is random, and the boundary conditions need to be determined. According to the actual engineering background and acid–rock reaction characteristics, the boundary value conditions of independent variable parameters were determined, in which the value interval of acidity coefficient x_1 was −10 to 10 (between perchloric acid $HClO_4$ and silicic acid H_2SiO_3), the value interval of acid mass concentration x_2 was 0% to 20%, and the value interval of acidification time x_3 was 0 min to 300 min. The iterative calculation of the model shows that the minimum compressive strength output of limestone after acidification was 28.28 MPa, the elastic modulus was 4.27 GPa, the corresponding acidity coefficient was −6.45, the acid mass concentration was 15.06%, and the acidification time was 249.41 min.

Figure 4 shows the response surface of acidified limestone strength under different acid reaction parameter combinations based on the limestone acidification strength model. It can be found that regardless of the acidity coefficient and acid reaction time, the acidified limestone strength σ_c decreased with the increase of the acid mass concentration. Therefore, the acid mass concentration is the optimal parameter of σ_c, which is consistent with the conclusion of the above factor significance analysis. The change of σ_c with the acidity coefficient was stronger than that of acidification time, and the response trend of σ_c was more obvious when the acidity coefficient exceeded 0 (weak acid). The change level of σ_c decreased when the acidity coefficient was between −5 and −10. In addition, the decrease rate of σ_c was faster in the early stage of limestone acid reaction (acidification time from 0 min to 120 min). With the extension of the acidification reaction time, the trend of σ_c gradually tended to be stable, and basically remaind constant after 240 min.

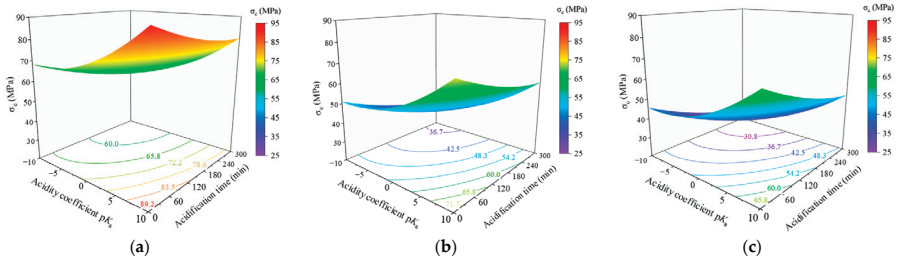

Figure 4. Strength response surface of acidified limestone under different acid reaction parameter combinations, (**a**) 5% mass concentration; (**b**) 10% mass concentration; (**c**) 15% mass concentration.

5. Analysis of Acidification Control Mechanism of Hard Limestone Strata

To discuss the influence of acidification control on limestone strata, it is necessary to first understand the essence of macroscopic fracture of limestone strata under external force. According to Griffith strength theory [31], the failure of brittle rock depends on the stress state around the microcracks in rock. Therefore, the essence of macroscopic fracture of hard limestone strata is the mechanical behavior and damage activity of mineral crystals under load, which is mainly reflected in the dislocation movement of grains in limestone polycrystals. In fact, due to the existence of the Hall–Petch relationship in microscopic crystals, the effect of external force on limestone polycrystals not only needs to overcome the hindering slip stress, but also produce dislocation pile-up in the mineral grains of polycrystals [32]. This part of the force mainly acts on dislocations, so that the grains can maintain equilibrium in the pile-up group. Specifically, under the action of applied stress, the dislocation source in the most favorable position of the mineral grain in the limestone crystal first starts. Due to the strong hindrance effect of the grain boundary on the dislocation movement, the leading dislocation emitted by the dislocation source encounters resistance after approaching the grain boundary and stops moving. Subsequently, the emitted dislocation will accumulate on the slip surface of the favorable position in turn to form the dislocation pile-up phenomenon. As shown in Figure 5, stress concentration occurs at the top of the pile-up of grain 1 and penetrates through the grain boundary. When the critical stress required for the dislocation activation of adjacent grain 2 is reached, the adjacent grain 2 activates again near the grain boundary dislocation, and the dislocation pile-up is formed in grain 2 and drives the dislocation in the next grain to activate. In this way, the limestone crystal is deformed under the cycle. The essence of crack initiation and propagation in limestone is that the stress accumulation at the dislocation pile-up in the grain boundary reaches a critical value, causing intergranular separation or cleavage development. Under the external force, the potential energy accumulated in the hard limestone rock mass gradually expands (local fracture) after exceeding the critical value. Multiple cracks collude with each other to form the macroscopic failure of rock mass. Therefore, the initiation and propagation of microcracks in hard limestone polycrystals is the key to the failure of rock strata.

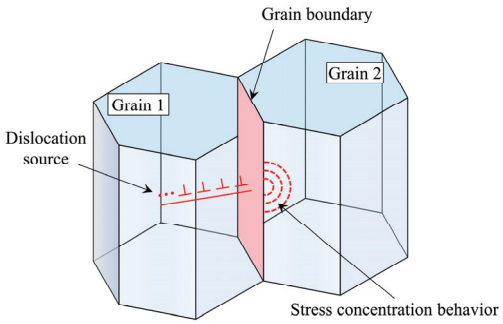

Figure 5. Diagram of dislocation pile-up.

According to the model, the acid reaction parameters involved weakened the mechanical characteristics of limestone, and the strength response law after acidification obtained by the model also confirms the effectiveness of acidification control of hard limestone strata. The essence of the strength deterioration of acidified limestone lies in the influence of the acidic effect on the crystal structure of minerals. The acidic effect causes multiple crystal defects in limestone minerals, which are more prone to induce the rapid expansion of microcracks under external force. This phenomenon can be confirmed by the acid corrosion morphology of hard limestone surface under different acid treatment conditions (Figure 6). It can be seen from the AO-5870 electron microscope of AOSVI company that under the local magnification of 50 times, the surface of limestone before acidification is smooth and has few primary fissures, and the limestone mineral composition is dominated by calcite

minerals with lighter color and doped with some darker dolomite minerals. Due to the close cementation of mineral particles on the surface of natural limestone, and the high density of mineral particles at the meso-level, the overall distribution is continuous and uniform, so the natural limestone has a fine texture and good structural integrity. After acidification, the surface morphology of limestone tends to be complex and rough, and the dissolution traces of minerals by acid reaction are obvious. There are fissures and gullies along the boundary between the minerals (circled in white), and the exposed transparent calcite crystals are clearly visible on the surface of some specimens. Therefore, under the acidic effect, many minerals in limestone are dissolved to form voids, which change the original continuous cementation structure, and some areas produce flake subsidence due to the large-scale acidic effect, so that the mineral grains show irregular distribution. In summary, the acidic effect promotes the destruction of the crystal structure of limestone minerals and forms a range of defects, which are more likely to induce the initiation and expansion of mineral crystals under load. The deformation degree required for the destruction of internally damaged limestone is reduced, and the bearing capacity of hard limestone strata is weakened.

Figure 6. Acid etching characteristics of hard limestone, (**a**) Specimen 1; (**b**) Specimen 2; (**c**) Specimen 3; (**d**) Specimen 4; (**e**) Specimen 5; (**f**) Specimen 6; (**g**) Specimen 7; (**h**) Specimen 8; (**i**) Specimen 9.

In addition, the high strength of hard limestone is the reason why the strata are difficult to control; the fracture cracks of deep rock masses are also easy to re-close under the action of strong ground stress. Due to the difference of acid reactions between various minerals contained in limestone, the cracks in limestone can maintain a certain degree of opening under acidic effects, which effectively improves this phenomenon. Carbonate minerals basically account for more than 90% of the limestone mineral components, among which are mainly calcite minerals and dolomite minerals. Limestone acidification does not produce new mineral species, but the reaction efficiency of calcite ($CaCO_3$) and dolomite ($CaMg(CO_3)_2$) is different. Figure 7 shows that the two minerals have similar lattice models (both belong to the trigonal system) and contain the same cation valence and charge number. However, according to the Born–Lander lattice energy formula, the ionic bond strength is inversely proportional to the ionic radius, so the bond energy of dolomite with larger cationic particle size is lower than that of calcite, and the corresponding lattice structure is more compact and stable. The dolomite with a chemical bond that is difficult to break has a lower reaction efficiency with acid, while the acid reaction process of calcite is more efficient. Therefore, during the process of slow acid etching of dolomite crystals in limestone, the surrounding calcite crystals have obvious defects under the influence of large-scale acidification. This phenomenon promotes the formation of an uneven corrosion surface in the limestone rock mass, and the acid corrosion cracks in the rock mass can still maintain a certain degree of opening even under the action of load, effectively preventing the occlusion of the rock blocks on both sides of the cracks, which is more conducive to the weakening and destruction of the hard limestone strata.

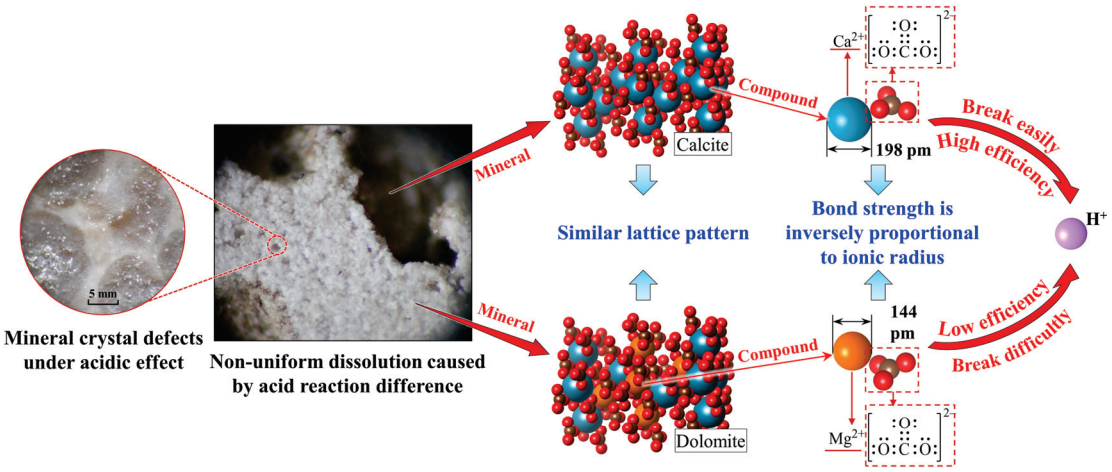

Figure 7. Non-uniform dissolution principle of limestone minerals under the acidic effect.

6. Conclusions

In this paper, through the orthogonal simulation test of hard limestone acidification, the variation of limestone reaction parameters and strength indexes under different acidification factors were analyzed. The optimized acid reaction system suitable for hard limestone weakening is given, and the damage mechanism of the acidic effect on hard limestone strata was discussed. The following conclusions are drawn.

(1) The influence order of various factors on the acid reaction results and strength indexes of limestone under acidic effect was confirmed: mass concentration > acid type > acidification time. The level difference of acid concentration had a particularly significant effect on the acidification and strength weakening of limestone. The reason is that an appropriate increase in acid concentration supplements the reaction amount of active ions in the system, and the large-scale acid action is more conducive to promoting the limestone to generate defects and weakening.

(2) The evaluation model of limestone reformation and strength weakening based on acid reaction parameters was established, and the validity was demonstrated according

to the credibility test and model verification. The SA algorithm is used to give the optimal acidification system suitable for the strength weakening of hard limestone: the acidity coefficient is −6.45, the acid mass concentration is 15.06%, and the acidification time is 249.41 min. Through the optimal analysis of the model, it was concluded that strength response trend is more obvious when the acidity coefficient exceeds 0 (weak acid), and the strength weakening behavior for limestone acidification time from 0 min to 120 min is the most prominent.

(3) The acidification control mechanism of hard limestone strata was revealed to be the change of mineral crystal characteristics. The acidic effect is beneficial to improve the shortcomings of high strength of hard limestone rock mass and easy closure of cracks in deep underground mining. On the one hand, the crystal defects caused by the acidic effect can induce the initiation and propagation of mineral microcracks under load, and the bearing capacity of the internal damaged limestone rock mass is weakened macroscopically. On the other hand, the acid reaction difference of various minerals will promote the fracture to maintain a certain degree of opening under in situ stress and reduce the occlusion of rock blocks on both sides of the fracture, which is conducive to the destruction of hard limestone strata.

Author Contributions: Conceptualization, M.H. and B.H.; methodology, X.Z.; software, M.H. and X.J. (Xuejie Jiao); validation, X.J. (Xufei Jiang), and Z.S.; formal analysis, M.H.; investigation, M.H; resources, B.H. and X.Z.; data curation, M.H.; writing—original draft preparation, M.H.; writing—review and editing, B.H. and X.Z.; visualization, X.J. (Xuejie Jiao); supervision, X.J. (Xufei Jiang), and Z.S.; project administration, B.H.; funding acquisition, B.H. and X.Z. All authors have read and agreed to the published version of the manuscript.

Funding: This research was supported by the National Key Research and Development Program of China (2021YFC2902102), and the Young Talent Support Project of Jiangsu Association for Science and Technology (JSTU-2022-066).

Data Availability Statement: Data associated with this research are available and can be obtained by contacting the first author.

Acknowledgments: The authors would like to thank the hydraulic fracturing team of the State Key Laboratory of Coal Resources and Safe Mining, China University of Mining and Technology, for their assistance.

Conflicts of Interest: The authors declare no conflict of interest.

References

1. Xie, C.; Nguyen, H.; Bui, X.N.; Nguyen, V.T.; Zhou, J. Predicting roof displacement of roadways in underground coal mines using adaptive neuro–fuzzy inference system optimized by various physics–based optimization algorithms. *J. Rock Mech. Geotech.* **2021**, *13*, 1452–1465. [CrossRef]
2. Li, J.; Liu, S.; Ren, W.; Liu, H.; Li, S.; Yan, K. Research on Engineering Practice and Effect Evaluation Method of Pressure Relief in Deep Rock Burst Danger Area of Coal Mine. *Minerals* **2023**, *13*, 570. [CrossRef]
3. Zhang, Q.; Wang, E.; Feng, X.; Wang, C.; Qiu, L.; Wang, H. Assessment of Rockburst Risk in Deep Mining: An Improved Comprehensive Index Method. *Nat. Resour. Res.* **2021**, *30*, 1817–1834. [CrossRef]
4. Xie, P.; Hower, J.C.; Nechaev, V.P.; Ju, D.; Liu, X. Lithium and redox–sensitive (Ge, U, Mo, V) element mineralization in the Pennsylvanian coals from the Huangtupo coalfield, Shanxi, northern China: With emphasis on the interaction of infiltrating seawater and exfiltrating groundwater. *Fuel* **2021**, *300*, 120948. [CrossRef]
5. Pan, C.; Xia, B.; Zuo, Y.; Yu, B.; Ou, C. Mechanism and control technology of strong ground pressure behaviour induced by high–position hard roofs in extra–thick coal seam mining. *Int. J. Min. Sci. Technol.* **2022**, *32*, 499–511. [CrossRef]
6. Wang, F.; Tu, S.; Yuan, Y.; Feng, Y.; Chen, F.; Tu, H. Deep–hole pre–split blasting mechanism and its application for controlled roof caving in shallow depth seams. *Int. J. Rock Mech. Min. Sci.* **2013**, *64*, 112–121. [CrossRef]
7. Xu, J.; Zhu, W.; Xu, J.; Wu, J.; Li, Y. High–intensity longwall mining–induced ground subsidence in Shendong coalfield, China. *Int. J. Rock Mech. Min. Sci.* **2021**, *141*, 104730. [CrossRef]
8. Chen, D.; Li, N.; Wang, E.Y. Reliability Assessment of the Hydraulic Fracturing Process in Coal Mine Based on the Analysis of Micro–Seismic Source Parameters. *Nat. Resour. Res.* **2021**, *30*, 2317–2332. [CrossRef]
9. Zhang, X.; Pak, R.Y.; Gao, Y.; Liu, C.; Zhang, C.; Yang, J.; He, M. Field experiment on directional roof presplitting for pressure relief of retained roadways. *Int. J. Rock Mech. Min. Sci.* **2020**, *134*, 104436. [CrossRef]

10. Huang, B.; Hou, M.; Zhao, X.; Xing, Y. Experimental investigation on the reformation and strength weakening of hard limestone by acidizing. *Int. J. Min. Sci. Technol.* **2022**, *32*, 965–979. [CrossRef]
11. Mustafa, A.; Aly, M.; Aljawad, M.S.; Dvorkin, J.; Solling, T.; Sultan, A. A green and efficient acid system for carbonate reservoir stimulation. *J. Petrol. Sci. Eng.* **2021**, *205*, 108974. [CrossRef]
12. Jafarpour, H.; Aghaei, H.; Litvin, V.; Ashena, R. Experimental optimization of a recently developed matrix acid stimulation technology in heterogeneous carbonate reservoirs. *J. Petrol. Sci. Eng.* **2021**, *196*, 108100. [CrossRef]
13. Ali, M.; Ziauddin, M. Carbonate acidizing: A mechanistic model for wormhole growth in linear and radial flow. *J. Petrol. Sci. Eng.* **2020**, *186*, 106776. [CrossRef]
14. Nierode, D.; Kruk, K. An evaluation of acid fluid loss additives retarded acids, and acidized fracture conductivity. In Proceedings of the Fall Meeting of the Society of Petroleum Engineers of AIME, Las Vegas, NV, USA, 30 September–3 October 1973.
15. Sarmah, A.; Ibrahim, A.F.; Nasr–El–Din, H.; Jackson, J. A new cationic polymer system that improves acid diversion in heterogeneous carbonate reservoirs. *SPE J.* **2020**, *25*, 2281–2295. [CrossRef]
16. Shi, W.; Yao, Y.; Cheng, S.; Shi, Z. Pressure transient analysis of acid fracturing stimulated well in multilayered fractured carbonate reservoirs: A field case in Western Sichuan Basin, China. *J. Petrol. Sci. Eng.* **2020**, *184*, 106462. [CrossRef]
17. Gangi, A.F. Variation of whole and fractured porous rock permeability with confining pressure. *Int. J. Rock Mech. Min. Sci. Geomech. Abstr.* **1978**, *15*, 249–257. [CrossRef]
18. Walsh, J. Effect of pore pressure and confining pressure on fracture permeability. *Int. J. Rock Mech. Min. Sci. Geomech. Abstr.* **1981**, *18*, 429–435. [CrossRef]
19. Tsang, Y.W.; Witherspoon, P. Hydromechanical behavior of a deformable rock fracture subject to normal stress. *J. Geophys. Res.-Sol. Earth* **1981**, *86*, 9287–9298. [CrossRef]
20. Gong, M.; Lacote, S.; Hill, A. New model of acid–fracture conductivity based on deformation of surface asperities. *SPE J.* **1999**, *4*, 206–214. [CrossRef]
21. Mou, J.; Zhu, D.; Hill, A.D. Acid–etched channels in heterogeneous carbonates—A newly discovered mechanism for creating acid–fracture conductivity. *SPE J.* **2010**, *15*, 404–416. [CrossRef]
22. Jirankova, E.; Konicek, P. Ground surface uplift during hardcoal longwall mining. *Int. J. Rock Mech. Min. Sci.* **2022**, *153*, 105099. [CrossRef]
23. Wang, B.; Feng, G.; Gao, Z.; Ma, J.; Zhu, S.; Bai, J.; Li, Z.; Wu, W. Study on the Mechanism and Prevention of Frequent Mine Seismic Events in Goaf Mining under a Multi-Layer Thick Hard Roof: A Case Study. *Minerals* **2023**, *13*, 852. [CrossRef]
24. Qian, D.; Jiao, H.; Deng, J.; Yang, J.; Jiao, M.; Xian, G.; Yu, C.; Zhu, Y.; Liu, J.; Huang, S.; et al. Instability Mechanism, Pressure Relief, and Long Anchorage Control Countermeasures for Surrounding Rock of Strong Mining Roadway at Large Mining Height Working Face. *Minerals* **2023**, *13*, 391. [CrossRef]
25. Liu, X.; Fan, D.; Tan, Y.; Ning, J.; Song, S.; Wang, H.; Li, X. New detecting method on the connecting fractured zone above the coal face and a case study. *Rock Mech. Rock Eng.* **2021**, *54*, 4379–4391. [CrossRef]
26. Wei, C.; Zhang, C.; Canbulat, I.; Huang, W. Numerical investigation into impacts of major fault on coal burst in longwall mining—A case study. *Int. J. Rock Mech. Min. Sci.* **2021**, *147*, 104907. [CrossRef]
27. Mi, C.; Zuo, J.; Sun, Y.; Zhao, S. Investigation on Rockburst Mechanism Due to Inclined Coal Seam Combined Mining and its Control by Reducing Stress Concentration. *Nat. Resour. Res.* **2022**, *31*, 3341–3364. [CrossRef]
28. Zhang, W.Q.; Lv, C. Effects of mineral content on limestone properties with exposure to different temperatures. *J. Petrol. Sci. Eng.* **2020**, *188*, 106941. [CrossRef]
29. Cengel, Y.A.; Boles, M.A.; Kanoğlu, M. *Thermodynamics: An Engineering Approach*; McGraw–Hill Education Press: New York, NY, USA, 2011.
30. Abdel–Basset, M.; Ding, W.P.; El–Shahat, D. A hybrid Harris Hawks optimization algorithm with simulated annealing for feature selection. *Artif. Intell. Rev.* **2021**, *54*, 593–637. [CrossRef]
31. Griffith, A.A. The phenomena of rupture and flow in solids. *Philos. Trans. R. Soc. Lond. Ser. A* **1921**, *221*, 163–198.
32. Liu, G.; Winwood, S.; Rhodes, K.; Birosca, S. The effects of grain size, dendritic structure and crystallographic orientation on fatigue crack propagation in IN713C nickel–based superalloy. *Int. J. Plast.* **2020**, *125*, 150–168. [CrossRef]

applied sciences

MDPI

Article

Experimental Investigation on Rock Failure Characteristics of Large-Span Goafs Using Digital Image Correlation Analysis and Acoustic Emission Monitoring

Chenglu Hou [1,2], Xibing Li [1], Tubing Yin [1], Longjun Dong [1] and Daoyuan Sun [1,*]

[1] School of Resources and Safety Engineering, Central South University, Changsha 410083, China; houchenglu@sd-gold.com (C.H.); xbli@csu.edu.cn (X.L.); tubing_yin@csu.edu.cn (T.Y.); lj.dong@csu.edu.cn (L.D.)
[2] Sanshandao Gold Mine, Shandong Gold Min Laizhou Co., Ltd., Laizhou 261442, China
* Correspondence: sundaoyuan@csu.edu.cn

Abstract: Rockmass in deep mining is highly susceptible to large-scale collapses under high stress and blast-induced disturbances, leading to casualties and economic losses. To investigate the evolution characteristics of goaf instability and the types of seismic sources that induce instability, an experiment on goaf instability was designed under uniaxial compression conditions based on actual mining operations. The entire experimental process was monitored using digital image correlation analysis and acoustic emission monitoring. By calculating the digital speckle field on the surface of the rock specimen during the experiment, the evolution characteristics of the deformation and strain fields from the beginning of loading to complete failure were analyzed. The study explored the dynamic behavior of cracks from initiation to propagation and eventually inducing large-scale collapse. The results show that the instability process of the goaf begins with the formation of tensile cracks. As stress increases, shear cracks occur in the specimen, leading to macroscopic failure. Furthermore, based on the differences in overall microfracture types measured by RA-AF characteristic parameters during specimen failure, large amplitude acoustic emission events corresponding to the formation of dominant macroscopic cracks were selected, and the focal mechanisms of these events were inverted. The results indicate that shear failure sources are significantly more prevalent than tensile failure sources in acoustic emission events leading to goaf instability. These findings can provide useful guidance for the support design and the prevention and control of rockmass instability disasters.

Keywords: failure characteristics; mining engineering; digital image correlation analysis; acoustic emission monitoring

1. Introduction

As the mining depth continues to increase, the impact of ground stress on the tunnels and goafs after excavation becomes more pronounced, leading to rock instability disasters [1–6], such as rockburst, roof collapse, spalling, and floor heave. It not only poses serious safety hazards for mining operations, but also increases the difficulty for vehicles and workers to pass through, significantly reducing the efficiency of mining operations [7]. Therefore, it is crucial to monitor the stress distribution around the goaf and analyze the characteristics of rockmass failure [4].

To study the deformation characteristics and failure mechanism of the surrounding rocks during the mining process, many scholars have combined field monitoring data, theoretical methods, and machine learning algorithms to establish various multi-indicator models for the evaluation of the goaf stability. Wang et al. [8] utilized physical and numerical model experiments to study the deformation and failure mechanisms of goaf-side entries driving adjacent to a longwall top coal caving panel. Hao et al. [9] proposed a calculation model to determine the appropriate treatment range for the goaf on the road.

Zhang et al. [10] established a stress model for goafs based on elastoplastic mechanics, through which the stress composition of roof, floor, and two sides of roadway under a goaf are analyzed. Trigueros et al. [11] studied the overall stability after the backfilling of a goaf using traditional techniques, numerical simulation, and remote sensing technology. Wang et al. [12] established a back-propagation model based on the dung beetle optimizer algorithm and applied it to evaluate the hazard of goafs. Yadav et al. [13] proposed a machine learning model using generated data from field-validated numerical cases to assess the stability of chain pillars under high-depth cover. Ke et al. [14] developed a goaf stability risk early warning model based on D-number theory, RES theory, and asymmetric fuzzy association cloud to prevent safety risks in the mining goaf. Gadepaka and Jaiswal [15] proposed a three-dimensional model to simulate the caving behavior during the extraction of an underground mine, by which the area of goaf exposure can be predicted. Dong et al. [16] proposed a novel reliability analysis method considering both microseismic loads and the uncertainty of rockmass parameters. Gu et al. [17] put forward the dynamic stability criterion from the perspectives of energy and stress, and further proposed some optimization approaches in practice. Chen et al. [18] established a numerical simulation of a high steep rock slope disturbed by a room and pillar mine to analyze the deformation and sliding characteristics of a high steep rock slope induced by the pillar deterioration.

On the other hand, laboratory physical and mechanical experiments are also an effective method for studying the instability characteristics of rockmasses under different stress conditions [19,20]. It has been widely applied in practice and provides valuable guidance for practical engineering projects. Wang et al. [21] conducted biaxial compression tests on marble specimens, combined with acoustic emission monitoring and moment tensor inversion, to explore the relationship between the evolution of tensile cracks and shear cracks during the loading process. By analyzing the wave velocity changes and acoustic characteristics of uniaxial and biaxial acoustic emission experiments, Dong et al. [22,23] proposed a method for identifying principal stress directions and rock failure precursors under different stress conditions. Arora et al. [24] tested the failure mode of layered shale specimens under biaxial stress conditions and found that the specimens exhibited shear failures along multiple shear planes. Wang et al. [25] carried out tests on coal samples soaked in salt solutions with different concentrations and obtained the dynamic evolution of the pore–fracture structure of coal. Kumar et al. [26] presented the assessment of the impact of a sand-stowing-based backfill on the peak strength and post-failure behavior of coal pillars. Das et al. [27] designed different underground structures and support systems under complex geological conditions and derived an energy-based safety factor using numerical simulations to determine the yield zones in the surrounding rockmass. Bednarek et al. [28] presented the results of in situ research of two roadways behind the longwall face and revealed the phenomena occurring near the advancing longwall face. Szurgacz et al. [29] discussed a method of combating the threat of endogenous fires by feeding an ash and water mixture or an ash and water mixture with carbon dioxide to goafs.

Although significant progress has been made in the simulation and evaluation of goafs stability, studies that simultaneously investigate the strain and deformation characteristics during the mining process and the types of fracture seismic sources are relatively rare. Therefore, this work uses digital image correlation (DIC) technology to analyze the strain and deformation characteristics of the surrounding rock in the stope during loading and further employs acoustic emission (AE) technology to analyze the source mechanism of fractures and seismic events generated during the loading process.

2. Materials and Methods

As is well known, due to the presence of numerous joints, faults, and other weak structural planes in practical engineering rockmass, the mechanical parameters are different from the results obtained using intact samples in laboratory tests. Therefore, the results from laboratory tests using intact rock cannot be directly applied to engineering sites. The

samples with artificially prefabricated joints also show significant differences from actual conditions because the joints are in an unbonded state. To better simulate engineering reality, the samples in this paper are all made from phyllite with distinct layered joints.

2.1. Specimen Preparation

The phyllite selected in this study has a set of nearly horizontal bedding. First, the rock materials were processed into cuboid specimens with a length of 150 mm, width of 80 mm, and height of 105 mm, and then the corresponding goafs were excavated in the middle of the cuboid specimens. The dimensions of the goafs are 70 mm in length, 80 mm in width, and 35 mm in height. Although the specimens in this study are all non-standard, their flatness and verticality were processed in accordance with the International Society for Rock Mechanics (ISRM) Suggested Methods for Rock Characterization, Testing and Monitoring: 2007–2014 [30]. The surface of the samples was polished with sandpaper to minimize end effects and the impact of rough surfaces on acoustic emission during loading.

2.2. Test System and Experimental Procedure

Before starting the experiment, a layer of white matte paint was evenly sprayed on the front of each specimen to cover the original rock particles and structural surfaces, avoiding their impact on speckle analysis. After the white paint dried, black matte paint was sprayed diagonally upward into the air to allow it to fall evenly on the white painted surface, and then let to dry naturally. The camera used in the experiments was a GS3-U3-123S6M-C monochrome industrial camera (Point Gray Research Inc., Richmond, BC, Canada), with a resolution of 2592 $\times$ 2048 px, a full frame rate of 73 fps, a pixel size of 4.8 $\times$ 4.8 μm, and a shooting frame rate of 10 frames per second.

Acoustic emission monitoring is an important analysis method in this study. In the designed experiment, to ensure that the acoustic emission sensors can envelop the specimen to the maximum extent, 30 acoustic emission sensors need to be arranged on the surface of a specimen. Considering the influence of the loading surface and the arrangement of the acoustic emission sensors, the experiment in this work arranges 30 acoustic emission sensors on the four sides of the specimen. Since the front of the specimen is sprayed with speckles and digital speckle photography will be conducted, only 4 sensors are placed at the four corners of the front of the specimen, while the back, left, and right sides of the specimen have a denser arrangements of sensors. The Vallen acoustic emission (AE) monitoring system AMSY-6 from Germany was used to monitor the rupture signal during the loading process. The sensor type is VS45-H, with a natural frequency of 280 kHz and a response frequency range of 20–450 kHz. The sampling frequency of the acoustic emission system is set to 10 MHz. Before the experiment, 30 acoustic emission sensors were arranged on the 4 sides of the specimen, and the sensor coordinates were accurately measured. The sensor coordinates were shown in Table 1.

Table 1. Coordinates of the acoustic emission sensors.

No.	X mm	Y mm	Z mm	No.	X mm	Y mm	Z mm	No.	X mm	Y mm	Z mm
S1	10	0	10	S11	150	80	10	S21	100	80	90
S2	140	0	10	S12	110	80	10	S22	140	80	90
S3	10	0	90	S13	80	80	10	S23	140	80	65
S4	140	0	90	S14	50	80	10	S24	140	80	40
S5	150	10	10	S15	10	80	10	S25	0	70	10
S6	150	70	10	S16	10	80	35	S26	0	10	10
S7	150	70	90	S17	10	80	60	S27	0	10	50
S8	150	10	90	S18	10	80	90	S28	0	10	90
S9	150	10	50	S19	40	80	90	S29	0	70	90
S10	150	50	50	S20	70	80	90	S30	0	50	50

The experiment was conducted on the INSTRON 1346 testing machine designed by INSTRON company, Norwood, MA, USA, which can perform mechanical experiments such as uniaxial compression, biaxial compression, direct shear, and variable angle shear tests. The vertical and horizontal loads can reach 2000 kN and 250 kN, respectively. The experiments adopt Z direction loading, with a constant loading rate of 500 N/s. It should be noted that although the uniaxial compression condition cannot fully meet the deep three-dimensional stress conditions, it still meets the one-dimensional stress conditions of isolated pillars and some other structures. The loading process, AE monitoring, and speckle image capture begin simultaneously. The technical roadmap of the research is shown in Figure 1.

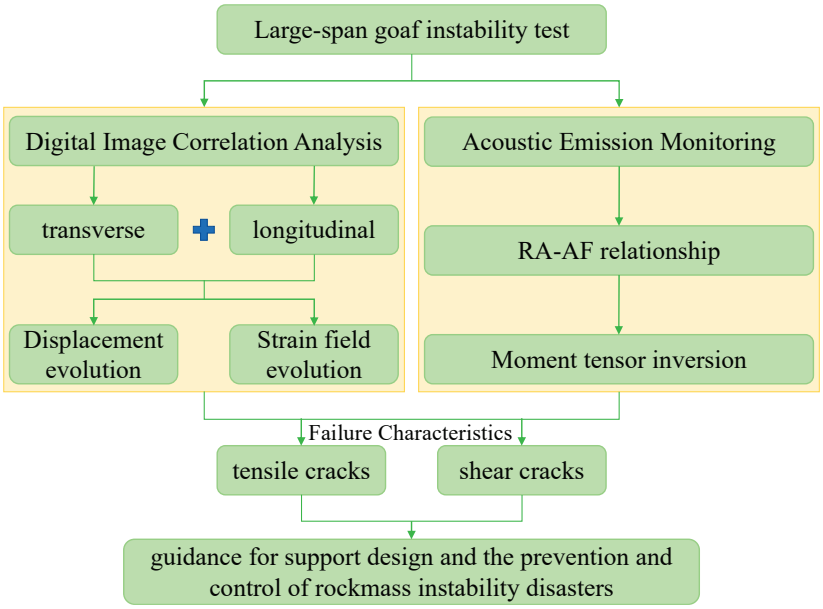

Figure 1. Technical roadmap of the research.

3. Experimental Results

3.1. Mechanical Property Curves

The changes in force and stress over time during the loading process are shown in Figure 2a. It can be seen from Figure 2a that when the loading process continues for about 1400 s, the loading curve begins to shake, indicating that the cracks inside the specimen have begun to gradually propagate. When the loading continues to 1421.7 s, the load reaches its peak value of about 724.36 kN, and the corresponding peak stress is about 60.36 MPa. Since a relatively large goaf was excavated in the middle of the specimen, the strength of the specimen was decreased. The stress–strain curve during the experimental process is shown in Figure 2b. It can be seen from the figure that when loaded to the peak stress, the corresponding peak strain is 0.00924. After loaded to the peak stress, the cracks expand rapidly and the whole specimen loses its bearing capacity.

3.2. Failure Mode

The failure characteristics of the specimen during different loading stages are shown in Figure 3. Due to the force-controlled mode of the loading system, the loading process is stable before the occurrence of macroscopic cracking. When loading for about 21 min, occasional cracking sounds were heard, but no obvious cracks were observed in the speckle imaging system. When loading for about 23 min, the speckle imaging system showed evident spalling at the left side and upper left corner of the goaf of the specimen, as shown in Figure 3b. Subsequently, cracks gradually appeared below the goaf of the specimen, as shown in Figure 3c. As the loading continued, several cracks on the left and middle sides

of the specimen bottom suddenly expanded in an instant, leading to extensive damage to the specimen, as shown in Figure 3d.

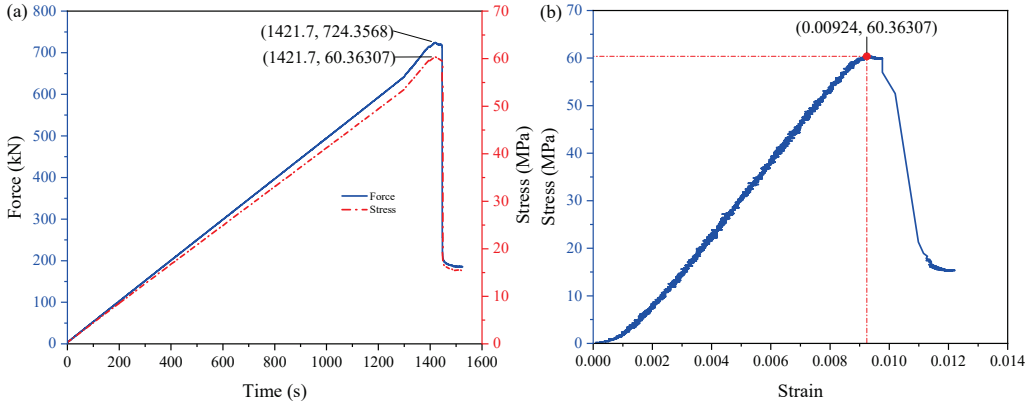

Figure 2. The curves of the loading process in the goaf failure test: (**a**) the force–time curve and the corresponding stress–time curve; (**b**) the stress–strain curve.

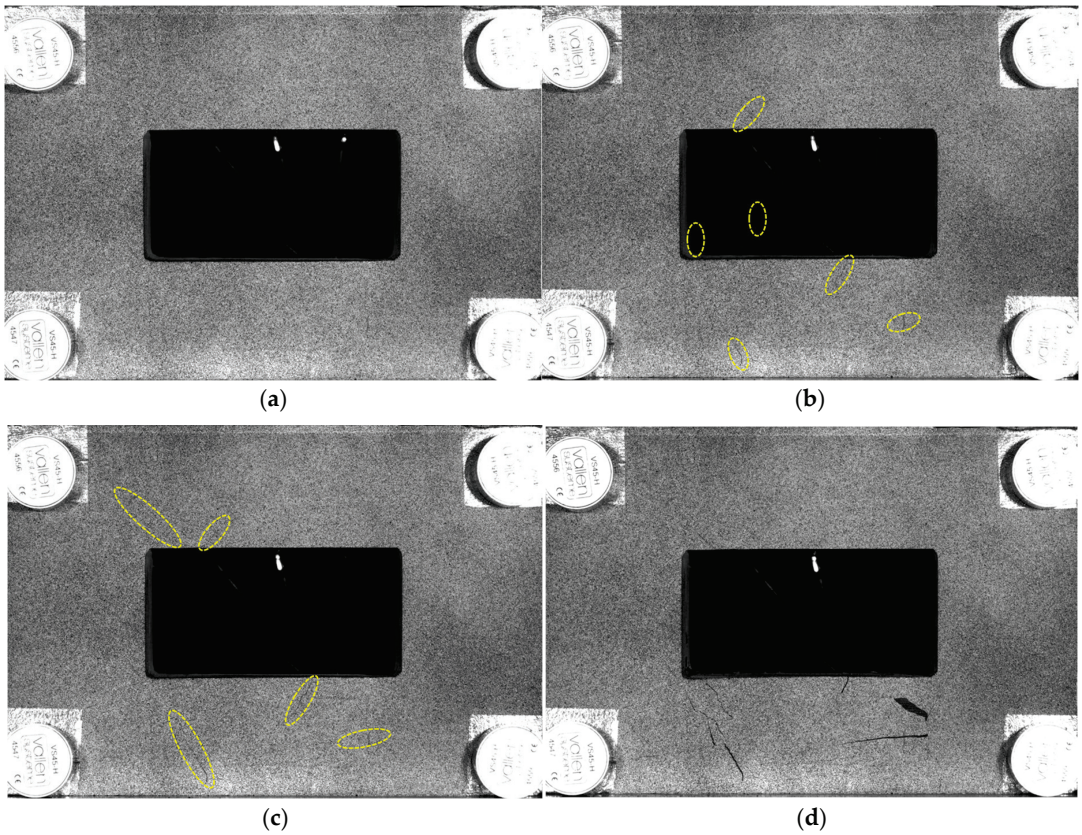

Figure 3. The failure conditions of the specimen at each stage of the loading process during the goaf failure test. (**a**) Initial state, t = 0 s; (**b**) upper left corner fracture, $t \approx 1420$ s; (**c**) bottom fracture, $t \approx 1421$ s; (**d**) overall instability, $t > 1421$ s. The yellow circles indicate the locations of the cracks during the loading process.

4. Analysis Results and Discussion

4.1. Digital Image Correlation Analysis

When conducting digital speckle analysis, it was found that the variation trend of the deformation field was more pronounced than that of the strain field at different loading stages. Additionally, the variation patterns of the strain field and deformation field differed in both the horizontal and vertical directions. For comparative analysis, the moments with

significant horizontal deformation were selected for a slicing analysis of the horizontal deformation patterns, followed by analyzing the horizontal strain changes at the same time points. Similarly, the moments with obvious vertical deformation were selected as time points to slice and analyze the vertical deformation patterns, followed by analyzing the vertical strain changes at the same time points.

The horizontal displacement evolution results of the specimen during the loading process are shown in Figure 4, corresponding to the results of the X direction in the specimen coordinate system. It can be seen from the figure that during the process from the beginning of loading to 654 s, the overall horizontal deformation of the specimen is relatively small, approximately distributed between −0.06 mm and −0.07 mm, indicating that the horizontal deformation occurs along the negative direction of the X-axis (to the left in the figure). Meanwhile, two deformation difference zones are formed on the left and right sides of the roof and floor of the goaf, respectively. The horizontal deformation of the surrounding rock on the left side of the goaf is obviously greater than that on the right side, indicating that two tensile stress regions have formed.

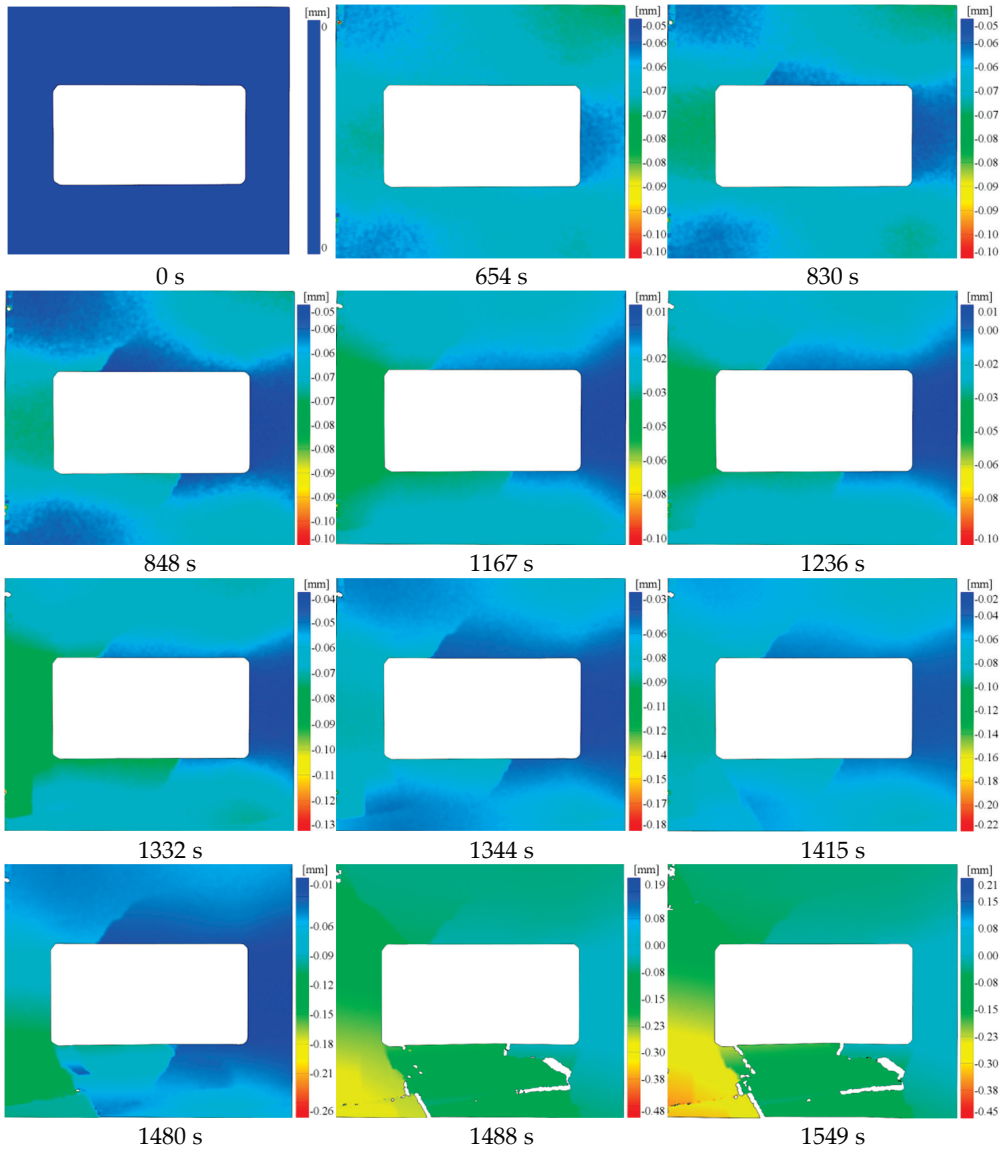

Figure 4. Displacement evolution in the X direction of the goaf instability experiment. The white square indicates the excavated goaf in the specimen.

During the continued loading process, the deformation difference between the left and right sides of the goaf becomes increasingly significant, and the tensile stress in the surrounding rocks above and below the goaf also increases. When loaded to about 830 s, a sudden change in horizontal deformation occurs above the goaf, indicating the formation of a crack. As the loading continues to around 848 s, a crack also occurs in the surrounding rock below the goaf, with another sudden mutation region appearing. During the further loading processes, the deformation difference between the left and right sides continues to increase. When loading to 1167 s, a region with a significant deformation difference appears in the inclined direction of the upper left corner of the goaf, and the surrounding rock of the floor exhibits a horizontal deformation stratification phenomenon. When the loading reaches 1236 s, the horizontal deformation difference at the upper left corner of the goaf and the horizontal deformation stratification in the floor surrounding rock become more pronounced, indicating the potential formation of a crack.

As the loading process continued to 1332 s, a horizontal deformation difference area appeared in the lower left corner of the goaf, along an inclined left direction. Additionally, an abnormal horizontal deformation area was observed at the horizontal deformation stratification position, indicating that cracks had begun to initiate and develop in the floor rocks. After 2 more seconds of loading, the difference in the lower left corner of the goaf became increasingly noticeable, clearly indicating the presence of cracks. At 1415 s, a rightward-inclined crack was clearly visible in the lower left corner of the goaf, extending through the floor rock of the specimen. Over the next minute, the horizontal deformation difference near the crack in the floor rocks increased significantly. By around 1488 s, these cracks suddenly expanded, tearing the speckles sprayed on the specimen surface, and forming a white area along the crack direction in Figure 5. Simultaneously, the horizontal deformation difference near the crack in the upper left corner of the goaf also increased. Within one more minute of continued loading, the specimen experienced macroscopic failure, with the surface horizontal displacement reaching approximately -0.38 mm. The locations and propagation directions of these cracks are clearly visible in Figure 3d.

In this test, the changes in the strain field in the X direction of the specimen during the loading process are shown in Figure 5. By comparing the horizontal deformation at the same time points in Figure 4, it was found that during the loading process up to 654 s, there were noticeable differences in horizontal displacement at different positions, but the differences in lateral strain were very small. By 830 s, a region of horizontal strain accumulation began to appear in the top plate of the goaf, indicating the start of a crack, corresponding to the results in Figure 5; there were still no significant differences in lateral strain at other locations.

As loading continued to 848 s, a crack also initiated in the middle of the surrounding rock at the bottom plate of the goaf, with lateral strain accumulating near the crack. By 1236 s, the lateral strain near the cracks in the top and bottom plates of the goaf increased, and a difference in lateral strain began to emerge in the surrounding rock at the bottom left and right corners of the specimen. In the following minute, the accumulation of lateral strain in the lower left corner of the goaf intensified rapidly, more evident than the comparison at 1332 s in Figure 5. Shortly thereafter, a linear region of lateral strain accumulation appeared near the right side of the crack in the lower left corner of the goaf, indicating another potential crack initiation.

By 1415 s, the crack in the lower left corner of the goaf gradually expanded, and the crack propagation path became more apparent. At 1480 s, the expansion of cracks on the left side and middle of the bottom plate accelerated, with lateral strain reaching 5% to 6% near the cracks. Soon, at 1488 s, sudden cracking occurred in the surrounding rock of the bottom plate of the goaf, with several cracks forming and connecting almost simultaneously, and strain accumulation rapidly increased. Additionally, a linear accumulation of lateral strain quickly appeared in the upper left corner of the goaf, with a sudden occurrence of an inclined crack. Compared to the results in Figure 5, the sensitivity of lateral strain to the formation of this crack was much lower than that of deformation, with the appearance of

the crack in the lateral strain field lagging far behind that in the lateral deformation field. As loading continued, the cracks in the specimen rapidly expanded, leading to the overall failure of the specimen within one minute.

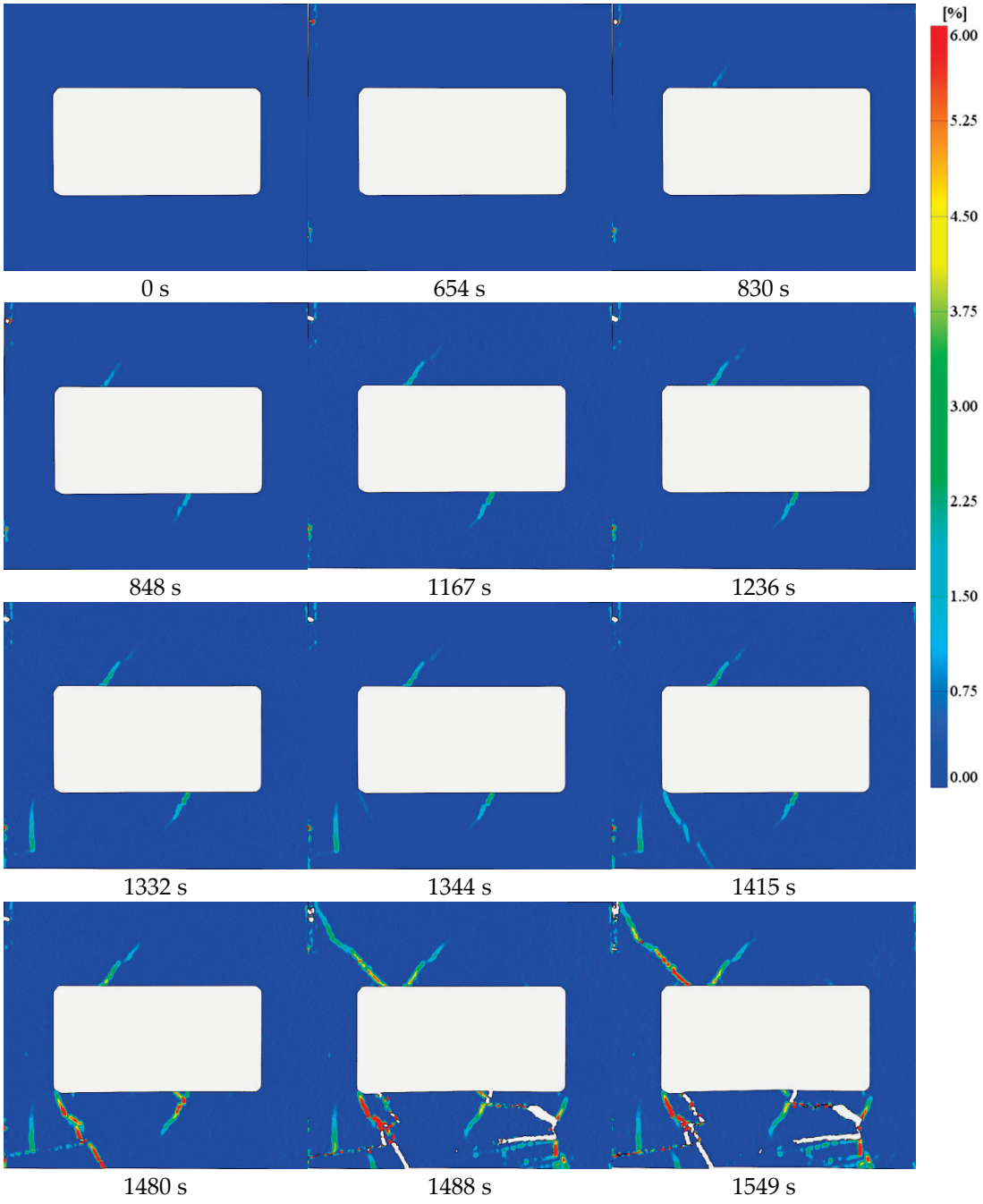

Figure 5. Strain field evolution in the X direction of the goaf instability experiment.

Similarly, the longitudinal strain and deformation analysis were performed. The calculation results of the longitudinal deformation field in this experiment are shown in Figure 6. Since the INSTRON 1346 testing machine loads upwards from the lower loading block, i.e., moving in the positive Z-axis direction, the overall deformation of the sample is positive, that is, in the positive Z-axis direction. As shown in Figure 7, at the initial stage of loading, the sample begins to undergo slow longitudinal deformation. During the loading process up to 654 s, the differences in deformation size at different positions of the sample gradually appear. The longitudinal deformation of the bottom plate of the goaf is about

0.06 mm, which is significantly greater than the longitudinal deformation of the top plate of the goaf (about −0.01 mm). When loading reaches around 830 s, a line-shaped deformation difference area gradually appears on the left side of the top plate of the goaf. Combined with the changes in the transverse deformation in Figure 5, it can be seen that a tensile failure crack is formed here due to the uncoordinated transverse deformation on both sides. The deformation difference between the top and bottom plates continues to increase during this process, reaching 0.08 mm and −0.02 mm, respectively.

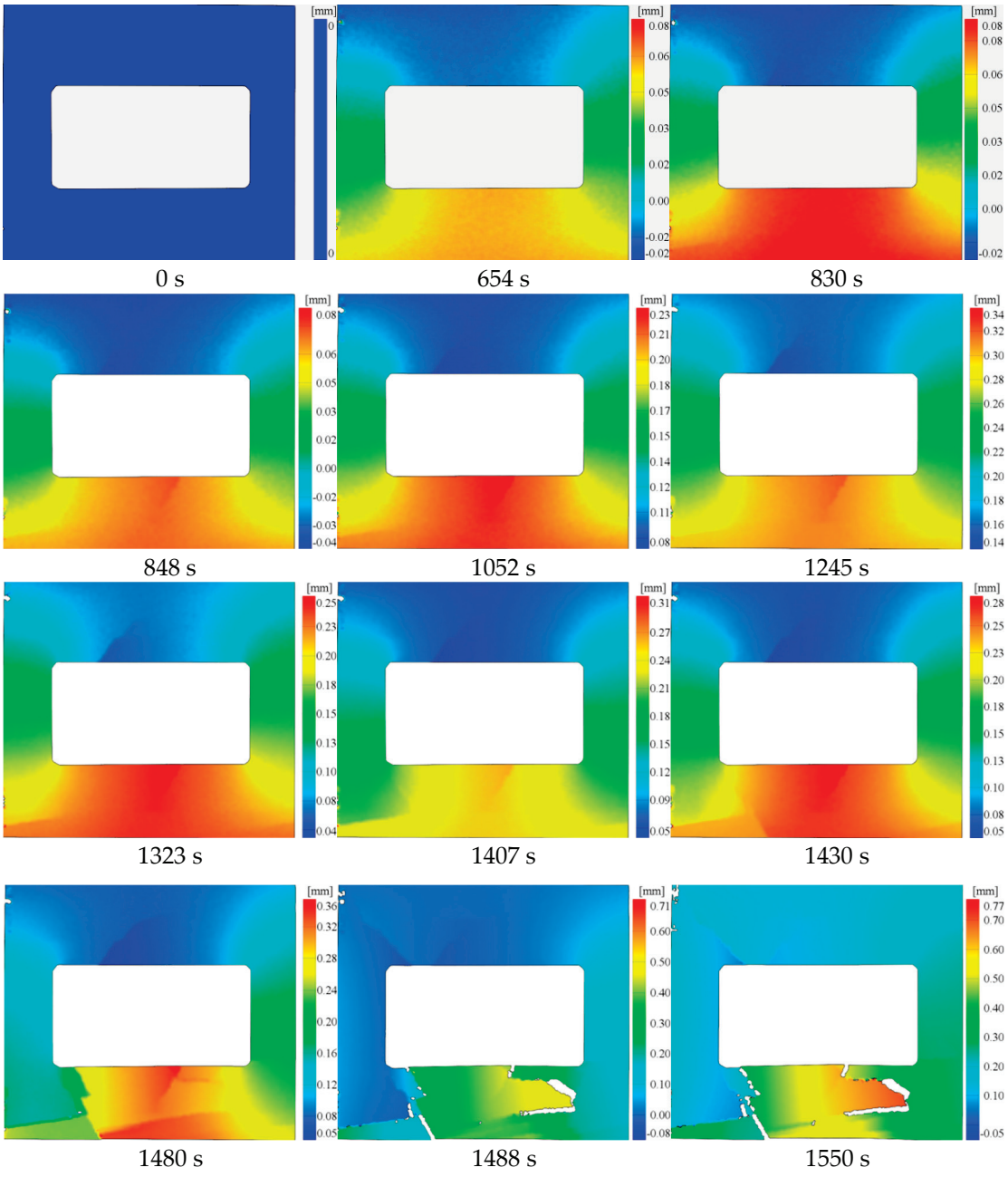

Figure 6. Displacement evolution in the Z direction of the goaf instability experiment.

When loading continues up to 848 s, the surrounding rock of the bottom plate in the goaf also produces a longitudinal deformation difference zone, indicating the formation of a crack. The longitudinal deformation difference between the upper and lower sides of the lower left corner of the goaf becomes increasingly large and shows a trend of gradually moving downward. During the continuous loading process up to 1052 s, the longitudinal

deformation of the surrounding rock near the cracks in the top and bottom plates of the goaf becomes more significant. The differences in the surrounding rock at the four corners of the goaf are also becoming more apparent. During the additional 3 min of loading, the longitudinal deformation of the surrounding rock near the cracks in the top and bottom plates of the goaf is not very noticeable, but the deformation differences in the surrounding rock on the upper and lower sides of the lower left corner of the goaf become more distinct.

Figure 7. Strain field evolution in the Z direction of the goaf instability experiment.

When loading continues up to 1323 s, Figure 6 shows that an approximately horizontal longitudinal displacement difference area appears in the lower right corner of the sample. Combined with the transverse deformation results at 1332 s in Figure 5, it can be seen that a crack is gradually forming in this area. As loading continues up to 1407 s, the longitudinal deformation difference on both sides of the crack in the lower left part of the sample

gradually increases, reaching approximately 0.24 mm and 0.20 mm, respectively. Since the sample undergoes compressive deformation, it can be inferred that the crack formed at this time is a shear crack, with dislocation occurring on both sides of the crack. When loading continues to 1430 s, a longitudinal deformation difference area forms at the right end of the transverse crack in the lower left corner of the sample and connects with the deformation difference area in the lower left corner of the goaf, indicating that a crack also forms here.

During the continuous loading process up to 1480 s, the longitudinal deformation differences on both sides of the through crack in the lower left corner of the goaf become increasingly apparent. Additionally, a large longitudinal deformation difference area forms on the bottom plate of the goaf, indicating the formation of a large shear crack. A small transverse crack also starts to form on the right side of the crack in the middle of the bottom plate of the goaf that formed at 848 s. In the following 8 s, the cracks in the surrounding rock of the bottom plate in the goaf rapidly expand and break, quickly splitting into multiple small cracks. Several areas experience excessive cracking, causing the sprayed speckles to tear, shown as white areas in the figure. An obvious upward diagonal longitudinal deformation anomaly appears in the upper left corner of the goaf, and combined with the transverse strain deformation, it can be seen that a large tensile crack forms here. By around 1550 s, the cracks in the sample continue to expand, leading to the overall failure of the sample.

The results of the strain field evolution in the Z direction at different positions of the sample during the loading process of this set of experiments are shown in Figure 7. From the figure, it can be seen that at the initial stage of loading, the strain field on the surface of the sample changes uniformly, with slight longitudinal strain accumulation occurring in the surrounding rock on the top and bottom plates of the goaf. By 830 s of loading, a faint line-shaped strain anomaly appears in the surrounding rock of the top plate, indicating the formation of a crack. When loading continues to 848 s, the longitudinal strain accumulation at the crack in the surrounding rock of the top plate in the goaf becomes more pronounced, and a line-shaped longitudinal strain accumulation gradually forms in the surrounding rock of the bottom plate, indicating the emergence of a crack there.

As loading continues to 1052 s, the longitudinal strain accumulation near the cracks in the surrounding rock of the top and bottom plates in the goaf becomes increasingly evident, with regions of longitudinal strain accumulation also appearing in the rock around the cracks. By 1245 s, the longitudinal strain near the cracks in the surrounding rock of the top and bottom plates in the goaf becomes more apparent, and a nearly horizontal longitudinal strain accumulation region appears below the crack in the surrounding rock of the bottom plate. As loading continues to 1323 s, the newly formed line-shaped longitudinal strain accumulation in the surrounding rock of the bottom plate in the goaf becomes more distinct, and areas of longitudinal strain accumulation in the surrounding rock of the top and bottom plates continue to increase. As loading continues, around 1407 s, an inclined line-shaped longitudinal strain accumulation appears in the lower left corner of the goaf, and longitudinal strain near other cracks continues to increase.

When loading continues for another 23 s, the line-shaped strain accumulation in the lower left corner of the goaf becomes more apparent, indicating the formation of an inclined shear crack. By 1480 s of continuous loading, the longitudinal strain accumulation in the surrounding rock near the inclined crack in the lower left corner of the goaf increases rapidly, and another crack forms above it. Additionally, an approximately horizontal longitudinal strain accumulation region forms near the first crack in the middle of the bottom plate of the goaf and continues to grow, while the line-shaped strain accumulation above the crack branch in the top plate of the goaf also increases rapidly. After another 8 s of continuous loading, the existing longitudinal strain accumulation regions on the top and bottom plates of the goaf expand rapidly. A large-scale inclined longitudinal strain accumulation region suddenly appears in the upper left of the goaf, with an approximately horizontal longitudinal strain accumulation region forming above the strain bifurcation area. The surrounding rock of the bottom plate in the goaf quickly develops two major

macroscopic cracks and several smaller cracks, with the longitudinal strain accumulation rapidly increasing. When loading continues to 1550 s, the surrounding rock in the top and bottom plates of the goaf rapidly expands, leading to the overall instability of the sample.

Comparing the deformation and strain variation patterns between the transverse and longitudinal directions, it can be concluded that since the experiment is loaded along the longitudinal direction, the specimen undergoes compressive deformation in the longitudinal direction and tensile deformation in the transverse direction. Meanwhile, as there is no horizontal force, its deformation is not limited. Therefore, the deformation and strain variation in the transverse direction are more pronounced than those in the longitudinal direction. Through the above analysis, it is found that in the goaf instability test, during the loading process, tensile cracks first appeared in the surrounding rock of the top and bottom plates. As the pressure continued to increase, shear cracks gradually appeared and eventually led to overall instability. The digital image correlation analysis results indicate that for tensile cracks, the deformation and strain perpendicular to the crack direction are very sensitive, while the deformation and strain parallel to the crack direction are not obvious. Conversely, for shear cracks, the deformation and strain parallel to the crack direction are very sensitive, while the deformation and strain perpendicular to the crack direction are not obvious. This phenomenon can serve as a characteristic indicator for identifying tensile and shear cracks. For inclined cracks, the crack type can be analyzed and determined based on their distribution in the coordinate system and the changes in strain and displacement in different directions.

4.2. Failure Mechanism

The ratio of risetime/amplitude (RA) and average frequency (AF) has been widely used for classifying the failure mechanism and crack mode in rock and concrete materials. Crack propagation in tensile mode corresponds to a high AF value and a low RA value. Conversely, a low AF value and a high RA value correspond to crack propagation in shear mode. When analyzing the RA-AF values of acoustic emission hits, outlier processing should be performed. The box plot outlier detection method can be considered, assuming that the raw data follow a normal distribution and filter out values that deviate more than three times from the mean. This method sequentially removes outliers in the RA and AF values. When analyzing the RA-AF values of acoustic emission events, it is necessary to consider the attenuation and dissipation effects of elastic waves during their propagation in the medium, which can affect the characteristic parameters of acoustic emission. It is recommended that the RA and AF values of acoustic emission events be determined by the RA and AF values of the initially triggered acoustic emission hits.

In this study, the data collected by the acoustic emission monitoring system were filtered based on the criterion that a single event triggered at least 10 sensors. A total of 204 acoustic emission events were obtained through filtering. In the analysis, the overall micro-fracture analysis does not quantify the specific proportion of the two micro-fracture types using a transition line. Instead, the relative proportion of micro-crack types in the same mechanical environment is compared by analyzing the numerical differences in the RA-AF distribution. The results are shown in Figure 8a. As can be seen from the figure, the distribution range and density center of the RA values for the acoustic emission events in this experiment are 0–100 ms/V and 8 ms/V, respectively, while the distribution range and density center of the AF values are 0–140 kHz and 50 kHz, respectively. This shows that the cracks in this experiment are characterized by low RA values and relatively low AF values, or even moderate AF values, indicating that the cracks are mixed-mode cracks containing both tensile and shear components.

The RA-AF relationship is more qualitative in understanding micro-fracture types through acoustic emission hits. Therefore, after using the RA-AF ratio to assess the differences in overall micro-fracture types during specimen failure, large amplitude acoustic emission events that contribute to the formation of dominant macroscopic cracks are selected. Considering the P-wave first motion polarity of each acoustic emission signal, the

moment tensor inversion method is used to invert the source mechanism. This method allows for a deeper discussion of the differences in the main fracture types across the samples. Ma et al. [31] defined Green's function library for inverting the source mechanisms of mine microseismic events. They successfully inverted the source mechanisms of microseismic events induced by mining activities and distinguished between fault slip sources, mine pillar instability sources, and roof collapse sources based on the source mechanism solutions. In this section, the same method is applied to invert the source mechanisms of the dominant sample failures in the goaf instability test using acoustic emission data. The results are then compared with DIC and RA-AF analysis results to analyze the relationship between macroscopic failure and microseismic source mechanisms.

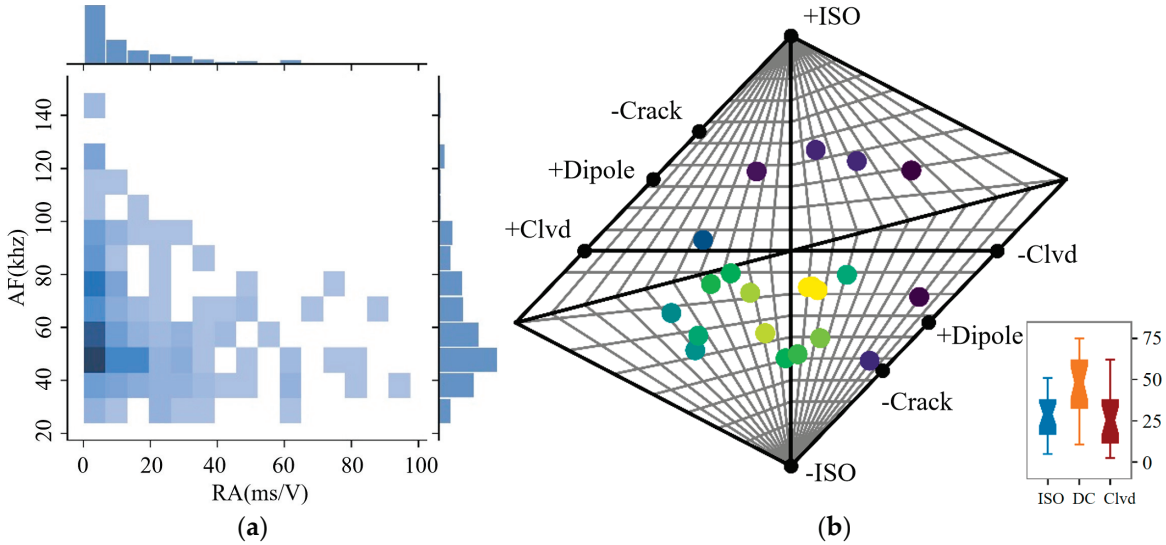

Figure 8. Results of failure source mechanism: (**a**) RA-AF relationship results; (**b**) moment tensor inversion results. The colors in the figure indicate the corresponding density of probability.

The moment tensor inversion results of the acoustic emission monitoring data are represented on a Hudson plot, as shown in Figure 8b. The source mechanism inversion results indicate that none of the 204 acoustic emission events are purely tensile or shear sources; all are mixed-type sources, which corresponds with the results from the RA-AF relationship. On the other hand, the box plot in the lower right corner of Figure 8b reveals that among the moment tensor components of the selected acoustic emission sources, the double-couple component has the highest proportion. This is because, during the final stage of loading, the rapid macroscopic failure of the specimen, due to the generation of shear cracks, resulted in a large number of acoustic emission sources dominated by shear components, thereby exhibiting a high proportion of double-couple components. This result is consistent with the findings from the digital speckle analysis and RA-AF analysis.

In further research, we will consider the different stages of sample failure, combining the time series of acoustic emission events to select appropriate parameters. By utilizing the acoustic emission events that have already occurred, we aim to predict potential future rockmass instabilities, providing guidance for monitoring mine goafs and preventing instability-related disasters.

5. Conclusions

(1) Based on the changes in strain and displacement, it can be inferred that the initial cracks are tensile cracks. When the load continues to increase, the primary cracks gradually open, rapidly expanding under the load, inducing the formation of shear cracks, which then become the main factor controlling the failure of the surrounding rock.

(2) In the goaf failure tests, tensile cracks are likely to first occur in the roof and floor. In actual engineering practice, this may manifest as roof subsidence or a collapse in the

roof, and as floor heave in the floor. After the formation of tensile cracks, as the load continues to increase, these tensile cracks gradually evolve into shear cracks, which in turn induce large-scale instability and failure.

(3) High-amplitude acoustic emission events, which dominate the formation of macroscopic cracks, were selected, and the moment tensor inversion method was used to identify the source types leading to macroscopic fractures in each test. The inversion results indicate that the shear component-dominated acoustic emission sources are significantly more prevalent in the moment tensor inversion results than those dominated by tensile failure.

Author Contributions: Conceptualization, C.H., X.L. and D.S.; Methodology, C.H. and D.S.; Software, D.S.; Validation, C.H., X.L. and D.S.; Formal analysis, T.Y.; Investigation, L.D.; Resources, L.D.; Data curation, D.S.; Writing—original draft preparation, C.H. and D.S.; Writing—review and editing, D.S.; Visualization, D.S.; Supervision, X.L.; Project administration, D.S.; Funding acquisition, D.S. All authors have read and agreed to the published version of the manuscript.

Funding: This research was funded by the National Natural Science Foundation of China, grant number 52304164, and the National Natural Science Foundation of Hunan Province, grant number 2023JJ40746.

Institutional Review Board Statement: Not applicable.

Informed Consent Statement: Not applicable.

Data Availability Statement: The original contributions presented in the study are included in the article, further inquiries can be directed to the corresponding author.

Acknowledgments: The authors would like to thank the handling editor and anonymous reviewers. All authors have consented to the acknowledgement.

Conflicts of Interest: Author Chenglu Hou was employed by the company Shandong Gold Min Laizhou Co., Ltd. The remaining authors declare that the research was conducted in the absence of any commercial or financial relationships that could be construed as a potential conflict of interest.

References

1. Yang, G.; Yang, X.; He, M.; Zhang, J.; Wang, H.; Shi, Z.; Yang, F.; Hou, S. Experimental and numerical investigations of goaf roof failure and bulking characteristics based on gob-side entry retaining by roof cutting. *Eng. Fail. Anal.* **2024**, *158*, 108000. [CrossRef]
2. Dong, L.; Sun, D.; Shu, W.; Li, X. Exploration: Safe and clean mining on Earth and asteroids. *J. Clean. Prod.* **2020**, *257*, 120899. [CrossRef]
3. Li, M.; Li, K.; Liu, Y.; Wu, S.; Qin, Q.; Yue, R. Goaf risk prediction based on IAOA–SVM and numerical simulation: A case study. *Undergr. Space* **2024**, *15*, 153–175. [CrossRef]
4. Vinay, L.S.; Bhattacharjee, R.M.; Ghosh, N.; Kumar, S. Machine learning approach for the prediction of mining-induced stress in underground mines to mitigate ground control disasters and accidents. *Geomech. Geophys. Geo-Energy Geo-Resour.* **2023**, *9*, 159. [CrossRef]
5. Dong, L.; Sun, D.; Han, G.; Li, X.; Hu, Q.; Shu, L. Velocity-Free Localization of Autonomous Driverless Vehicles in Underground Intelligent Mines. *IEEE Trans. Veh. Technol.* **2020**, *69*, 9292–9303. [CrossRef]
6. Zhang, Y.; Wen, Z.; Zhang, J.; Huang, J.; Qi, J.; Li, M. Study on stability evaluation of goaf based on AHP and EWM-taking the northern new district of Liaoyuan city as an example. *Sci. Rep.* **2024**, *14*, 17876. [CrossRef]
7. Yadav, A.R.; Islavath, S.R. Numerical Investigation for Estimation of Behaviour of Barrier Pillars, Gateroads and Face of a Deep Longwall Mine: A Case Study. *Min. Metall. Explor.* **2024**, *41*, 463–478. [CrossRef]
8. Wang, H.; He, M.; Wang, J.; Wang, R.; Ming, C.; Zhu, D.; Ma, Z. Deformations and failures of goaf-side entries driving adjacent to longwall top coal caving panel. *J. Cent. South Univ.* **2024**, *31*, 1542–1559. [CrossRef]
9. Hao, Q.; Zheng, Q.; Liu, S.; Hao, W.; Wu, X. Study on the Influence of Grouting Treatment on the Movement and Deformation of Surface in Longwall Coal Mining Goaf Areas. *Min. Metall. Explor.* **2024**, *41*, 1835–1858. [CrossRef]
10. Zhang, J.; Zhang, Y.; Han, Y.; Fan, W.; Song, Z.; Yu, H.; Zhang, J.; Zhang, H.; Liu, J. Study on stress distribution law of surrounding rock of roadway under the goaf and mechanism of pressure relief and impact reduction. *Eng. Fail. Anal.* **2024**, *160*, 108210. [CrossRef]
11. Trigueros, E.; Cánovas, M.; Arzúa, J.; Baraibar, J.M. Evaluating the influence of backfilling on the stability of an abandoned room-and-pillar mine: A case study in northern Spain. *Geomech. Geophys. Geo-Energy Geo-Resour.* **2024**, *10*, 116. [CrossRef]

12. Wang, W.; Zhang, Q.; Guo, S.; Li, Z.; Li, Z.; Liu, C. Hazard evaluation of goaf based on DBO algorithm coupled with BP neural network. *Heliyon* **2024**, *10*, e34141. [CrossRef]
13. Yadav, A.; Singh, G.S.P.; Behera, B. A Machine Learning Model for Evaluation of Chain Pillar Stability in Deep Longwall Workings in India. *Min. Metall. Explor.* **2023**, *40*, 2119–2137. [CrossRef]
14. Ke, L.; Wu, M.; Ye, Y.; Hu, N.; Meng, Y. Stability risk early warning for mine goaf: Based on D-RES and asymmetric fuzzy connection cloud model. *J. Comput. Sci.* **2024**, *78*, 102279. [CrossRef]
15. Gadepaka, P.R.; Jaiswal, A. A novel approach for the assessment of caving behaviour in a bord and pillar depillaring panel by using continuum modelling. *Int. J. Rock Mech. Min. Sci.* **2023**, *170*, 105476. [CrossRef]
16. Dong, L.; Sun, D.; Li, X.; Ma, J.; Zhang, L.; Tong, X. Interval non-probabilistic reliability of surrounding jointed rockmass considering microseismic loads in mining tunnels. *Tunn. Undergr. Space Technol.* **2018**, *81*, 326–335. [CrossRef]
17. Gu, H.; Lai, X.; Tao, M.; Momeni, A.; Zhang, Q. Dynamic mechanical mechanism and optimization approach of roadway surrounding coal water infusion for dynamic disaster prevention. *Measurement* **2023**, *223*, 113639. [CrossRef]
18. Chen, L.; Yu, X.; Luo, R.; Zeng, L.; Cao, H. High Steep Rock Slope Instability Mechanism Induced by the Pillar Deterioration in the Mountain Mining Area. *Mathematics* **2023**, *11*, 1889. [CrossRef]
19. Han, Z.; Li, J.; Wang, H.; Zhao, J. Initiation and propagation of a single internal 3D crack in brittle material under dynamic loads. *Eng. Fract. Mech.* **2023**, *285*, 109299. [CrossRef]
20. Han, Z.; Li, J.; Li, D.; Zhao, J. 3D spatial fracture behavior of sandstone containing a surface flaw under uniaxial compression. *Int. J. Rock Mech. Min. Sci.* **2023**, *171*, 105583. [CrossRef]
21. Wang, Z.; Feng, X.; Yang, C.; Zhou, Y.; Xu, H.; Han, Q.; Gao, Y. Experimental investigation on fracturing process of marble under biaxial compression. *J. Rock Mech. Geotech. Eng.* **2020**, *12*, 943–959. [CrossRef]
22. Dong, L.; Chen, Y.; Sun, D.; Zhang, Y. Implications for rock instability precursors and principal stress direction from rock acoustic experiments. *Int. J. Min. Sci. Technol.* **2021**, *31*, 789–798. [CrossRef]
23. Dong, L.; Chen, Y.; Sun, D.; Zhang, Y.; Deng, S. Implications for identification of principal stress directions from acoustic emission characteristics of granite under biaxial compression experiments. *J. Rock Mech. Geotech. Eng.* **2023**, *15*, 852–863. [CrossRef]
24. Arora, S.; Mishra, B. Investigation of the failure mode of shale rocks in biaxial and triaxial compression tests. *Int. J. Rock Mech. Min. Sci.* **2015**, *79*, 109–123. [CrossRef]
25. Wang, M.; Tian, Y.; Zhang, Z.; Guo, Q.; Wu, L. Dynamic Evolution of Coal Pore-Fracture Structure and Its Fractal Characteristics under the Action of Salty Solution. *Mathematics* **2024**, *12*, 72. [CrossRef]
26. Kumar, S.; Sinha, R.K.; Jawed, M.; Murmu, S. Assessment of coal pillar strength under the influence of sand stowing in deep coal mines. *Geotech. Geol. Eng.* **2024**, *42*, 2815–2831. [CrossRef]
27. Das, A.J.; Mandal, P.K.; Ghosh, N.; Singh, A.P.; Kumar, R.; Tewari, S.; Bhattacharjee, R. Evaluation of energy accumulation, strain burst potential and stability of rock mass during underground extraction of a highly stressed coal seam under massive strata-a field study. *Eng. Geol.* **2023**, *322*, 107178. [CrossRef]
28. Bednarek, Ł.; Małkowski, P.; Niedbalski, Z.; Mucha, K. Steel Arch and Rock Bolt Support in Terms of the Gateroad Stability Maintaining behind the Longwall Face. *Appl. Sci.* **2024**, *14*, 3594. [CrossRef]
29. Szurgacz, D.; Tutak, M.; Brodny, J.; Sobik, L.; Zhironkina, O. The Method of Combating Coal Spontaneous Combustion Hazard in Goafs—A Case Study. *Energies* **2020**, *13*, 4538. [CrossRef]
30. Ulusay, R. *The ISRM Suggested Methods for Rock Characterization, Testing and Monitoring: 2007–2014*; Springer International Publishing: Cham, Switzerland, 2015.
31. Ma, J.; Dong, L.; Zhao, G.; Li, X. Discrimination of seismic sources in an underground mine using full waveform inversion. *Int. J. Rock Mech. Min. Sci.* **2018**, *106*, 213–222. [CrossRef]

applied sciences

MDPI

Article

Long-Distance Shield Tunnelling Performance Prediction Based on Informer

Min Hu [1,2] and Peng Cheng [1,3,*]

[1] SHU-SUCG Research Centre for Building Industrialization, Shanghai University, Shanghai 200072, China; minahu@shu.edu.cn
[2] SHU-UTS SILC Business School, Shanghai University, Shanghai 201800, China
[3] School of Mechanical and Electrical Engineering and Automation, Shanghai University, Shanghai 200072, China
* Correspondence: chengpeng@shu.edu.cn

Abstract: Shield performance prediction plays a critical role in construction decision-making. However, current models suffer from significant performance degradation in long-distance prediction. To address this gap, we propose a novel Long-Distance Shield Performance Prediction model (LSPP), which leverages the long-term prediction capabilities of Informer. The LSPP model incorporates conventional monitoring data, tunnelling parameters, and stratigraphic spatial information and is optimized using a ProbSparse self-attention mechanism and dynamic decoding techniques. A series of experiments demonstrate that LSPP significantly outperforms traditional models, such as LSTM and GRUs, particularly in long-distance predictions and under conditions of stratigraphic changes. Notably, the model achieves an R^2 of 0.82 when predicting penetration after six rings, making it highly accurate and stable for engineering decision-making.

Keywords: shield; long-distance prediction; tunnelling performance; Informer

1. Introduction

Shields are widely used in tunnel construction because of their safety, high efficiency, and environmental protection. The tunnelling performance of the shield is a key concern in project management, which not only reflects the progress of the project but also reflects whether the control of the shield is reasonable and whether the efficiency of the equipment is fully utilized. Therefore, it is important to accurately predict the changes in the tunnelling performance of the shield and analyze the factors affecting the tunnelling performance to guide engineers and technicians in adjusting the tunnelling parameters and improving the efficiency and safety of the project.

At present, the perspectives for evaluating the performance of shield tunnelling can be divided into two categories. One is to focus on the shield tunnelling efficiency, using micro indicators such as thrust, penetration, propulsion speed, and other measures [1]; the second is to judge from the perspective of shield construction energy consumption and progress, construction power consumption, average daily propulsion, and other macro indicators [2]. Since the macro indicators have too many influencing factors, the general evaluation of tunnelling performance is based on micro indicators, of which penetration is the most commonly used shield tunnelling performance evaluation index [3]. The penetration comprehensively reflects the state of propulsion and cutting during the advancement of the

shield, which embodies the ability of the cutter plate of the shield to penetrate the ground in the process of boring.

In order to predict the performance of shield tunnelling, scholars have carried out a great deal of research, of which 'penetration' is the most commonly used evaluation index. Early studies mainly include experimental methods based on experience [4,5], theoretical techniques rooted in soil mechanics [6,7], and experimental techniques utilizing tools such as finite element analysis [8,9]. However, these methods still have some limitations. Firstly, empirical methods rely on regression analysis to establish the relationship between soil or rock parameters and shield tunnelling parameters. Still, this method is highly dependent on physical assumptions under specific geological conditions and lacks universality. Secondly, in traditional theoretical approaches (e.g., Colorado School of Mines' prediction model, CSM) [6], the prediction results often have a large deviation due to the lack of simulation ability regarding the interaction between shields and soils. Finally, although the experimental method based on finite element analysis can simulate the shield tunnelling process more accurately, a large amount of computation and the fact that the results are only applicable to a specific stratum, which requires the establishment of multiple models according to different geological conditions, lead to poor model generality and robustness.

The models used by researchers in the initial studies are mostly non-time series regression models, such as support vector regression (SVR) [10], back-propagation neural networks (BPNNs) [11,12], and Extreme Gradient Boosting (XGBoost) [13,14]. These studies verified the adaptability of data-driven methods in shield performance prediction, but it is difficult for the above models to capture the information contained in the feature changes over time. Also, because shield construction data are time-dependent, ignoring the temporal relationship between the data will affect the reasonableness and accuracy of TBM performance prediction [15]. Recurrent neural network (RNN)-based long short-term memory neural networks (LSTMs) and gated recurrent unit networks (GRUs), which are deep learning algorithms that have a significant advantage in processing time series data and can effectively record the long-term and short-term dependencies of the data, capture patterns in the sequences, and handle long series data well [16], have become the focus of some researchers. Xu et al. [17] and Wang et al. [18] compared different models predicting the shield performance one second in the future and found that LSTM had the best prediction. Jin et al. [19] achieved a better prediction of the average speed in the next 1 min through a hybrid model based on GRUs. However, most of these studies focus on short-term prediction, which has difficulty reflecting the long-term trend of tunnel construction and cannot improve the strong theoretical support for construction decision-making.

Several scientists have recently begun looking at predictions over extended periods and distances. Flor et al. [20] used LSTM to predict the penetration of the next ring and the next fifth ring, but the prediction effect was not good, with a coefficient of determination (R^2) of 0.65, which is much lower than the prediction of the next ring in a short period of time, with a value of R^2 of 0.97. Gao et al. introduced the attention mechanism to build an Attention–ResNet–LSTM hybrid model to predict performance after 20 min and 60 min, but the root mean square errors (RMSEs) were 0.523 and 1.948, meaning the prediction accuracy decreases dramatically with increasing time [21]. It can be seen that there is still a challenge in predicting the performance of tunnelling over long distances or long periods of time [22]. Both LSTM and GRUs are based on RNNs, whose structure restricts them from performing long-distance prediction, which needs to be realized by multi-step recursion. This inevitably produces error accumulation, leading to a significant degradation of the

prediction ability, and, therefore, new network architectures need to be sought to solve this problem.

The Informer algorithm is a deep learning model designed for long time series prediction. It was presented at the AAAI conference in 2021, where it was recognized as the best paper of the year, primarily for addressing the problem of accuracy degradation in time series prediction [23]. Based on the actual construction decision-making needs [24], this paper defines the research objective as predicting future performance beyond the fifth ring and refers to it as the long-distance prediction. This paper utilizes the advantages of the Informer algorithm to design a shield long-distance tunnelling performance prediction model (LSPP) for shield tunnelling performance after five rings, which reflects the spatio-temporal characteristics of shield tunnelling with the structure of the Informer model and verifies the effect of the new model on the prediction of performance through experiments.

2. Methodology

2.1. Basic Structure and Principles of Informer

Informer was developed from Transformer, and its topological structure is shown in Figure 1, which consists of three parts: an input layer, an encoding–decoding layer, and an output layer. The input layer receives and preprocesses the original time series data. In the encoding–decoding layer, the encoder extracts long-term dependencies in the sequence through stacked self-attention layers and feedforward neural networks. It uses the ProbSparse self-attention mechanism to reduce computational complexity. The decoder combines the encoder's context information and input to generate predictions for future time steps. It uses a generative decoding strategy to generate multi-step predictions gradually. The output layer converts the output of the decoder into a final prediction, usually including a linear transformation and an inverse data preprocessing step to return to the original scale. This structure allows Informer to process large-scale time series data while remaining efficient and accurate [23].

From the model structure, it can be seen that the ProbSparse self-attention mechanism in the encoder and the generative decoder play an important role in improving the performance of long-range prediction:

1. ProbSparse self-attention is based on self-attention probability distributions with sparse sampling [25,26]. Its distinctive feature is that it selectively computes the attention weights between a subset of key values, rather than computing the attention weights between all key values. In the case of extremely long time series, the conventional full attention mechanism requires the computation of attention weights with a complexity of $O(N^2)$, where N represents the length of the sequence. In contrast, ProbSparse self-attention only requires the calculation of $O(N\log N)$ attention weights. This significantly reduces the computational complexity. The attention mechanism is embedded within the encoder and learns sparse attention matrices to reduce the cost of computations during the inference stage. This mechanism collaborates with other components within the encoder, such as feedforward neural networks and residual connections, to achieve efficient time series prediction.

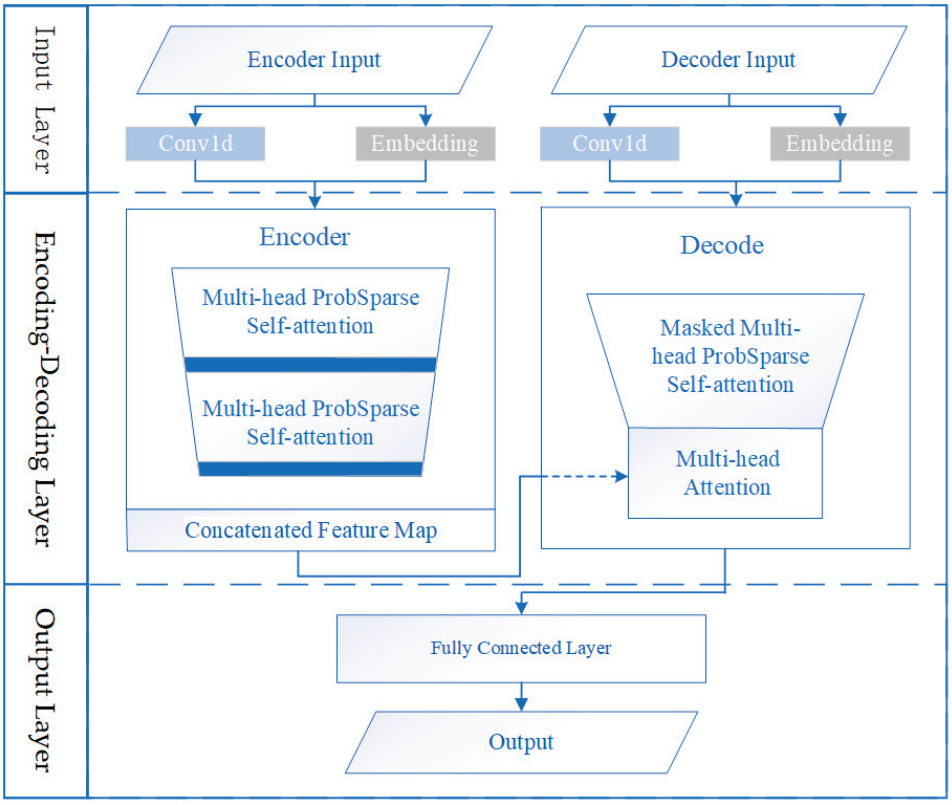

Figure 1. Informer model topology.

2. The generation-based encoder adopts the start token technique [27], which assists the model in accurately identifying the initial position of the predicted sequence and thereby reduces the cumulative error in long-range prediction. In long-range forecasting, the model's prediction of the future is always based on previous results. Suppose there are any errors in the prediction results of each step. In that case, these errors will accumulate with the increase in the prediction sequence length, ultimately leading to the deterioration of the overall prediction quality. Using the start token technique allows the model to reinitialize its position at the onset of each new prediction, thereby mitigating the impact of cumulative errors because the start token gives the model a novel reference point, enabling it to return to the correct starting point when generating each new sequence [28,29].

2.2. LSPP Model Design

2.2.1. Basic Structure

The LSPP model is based on the Informer algorithm, and the model framework is shown in Figure 2, which consists of three modules: data preparation, encoding–decoding, and performance prediction. Firstly, the time series data of shield tunnelling are subjected to preprocessing and feature extraction, and the data are position-encoded and input into the encoder to obtain the time series data features. Then, the decoder outputs the predicted time series feature representation in the form of multidimensional vectors based on the feature representation of the historical sequence given by the encoder and a part of the target sequence. Finally, the prediction module converts the feature vector from the decoder output into the final predicted values of the model.

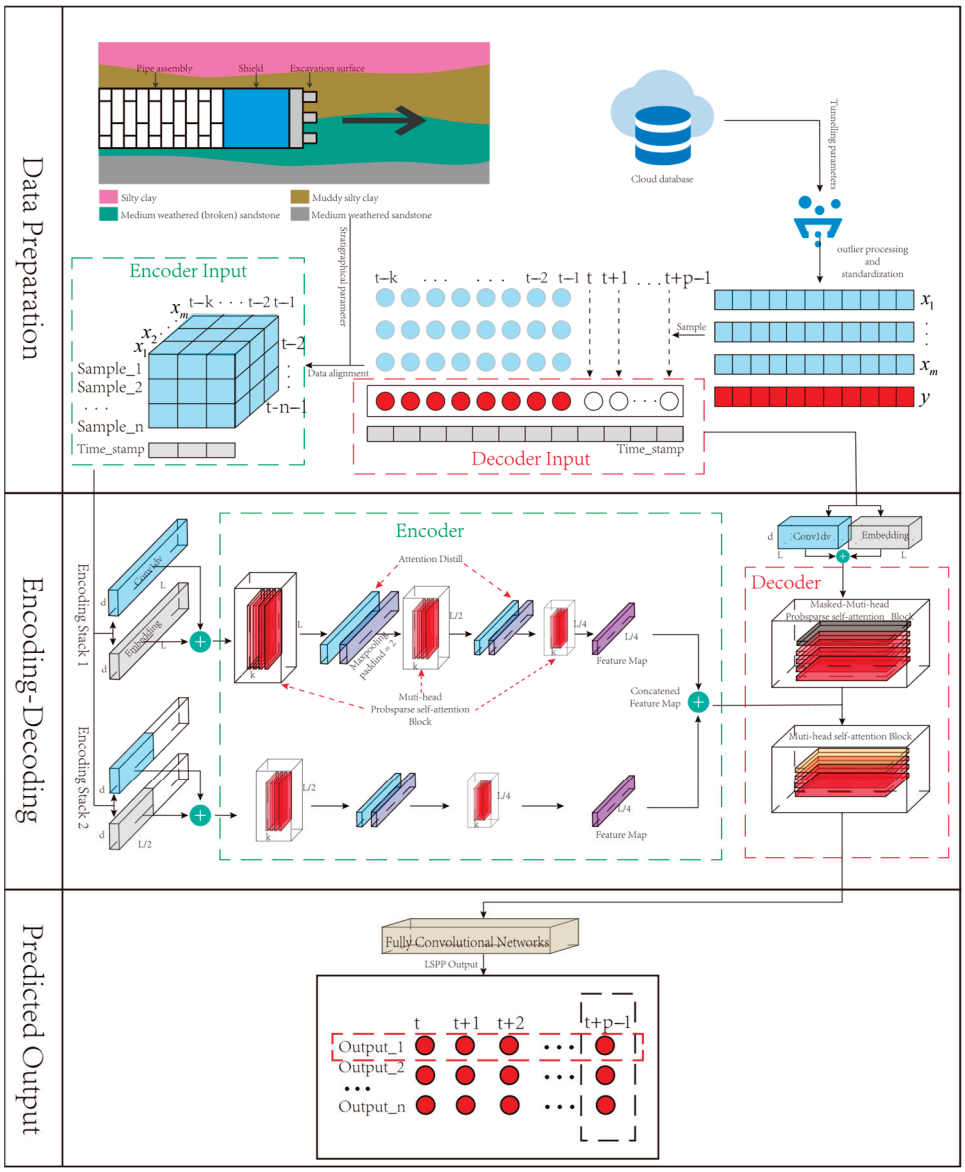

Figure 2. LSPP model framework.

2.2.2. Data Preparation

1. Selection of construction parameters

There are many factors affecting the penetration in shield construction, including geological parameters, mechanical conditions, and tunnelling parameters [30]. Table 1 summarizes the parameters used in some literature on shield tunnelling performance prediction from 2021 to 2024.

As seen from Table 1, many features affect shield tunnelling performance, more than thirty of them, and they are relatively scattered. To elucidate the salient influencing factors while circumventing the intricacies of the model, the present study methodically screens these factors from the perspectives of both theoretical underpinnings and engineering feasibility. *CS*, *CT*, *EP*, *SS*, and *CC* are routine monitoring data during shield construction; *CS* and *CT* directly affect the cutting ability and rock breaking efficiency of the shield machine; and *EP* directly reflects the force of the stratum on the shield machine, which affects the stability of digging and cutting efficiency, especially under complex geological conditions, and plays a significant role. *SS* affects the efficiency of soil discharge, which is closely related to

the stability and efficiency of the shield machine. *CC* is an approximate characterization of *CP*, which reflects the blade loading and cutting difficulty, and is an important index in evaluating the energy consumption and performance of shield tunnelling.

Table 1. Overview of shield performance prediction models.

Literature	Models	Tunnelling Parameters	Geological Conditions	Prediction Target
[3]	LSTM	*CP*, *CT*, *TF*	-	*PR*
[9]	XGBoost	*CS*, *CT*, *TF*	*BTS*, *UCS*	*PR*
[12]	BPNN	*CS*, *CT*, *EP*, *SS*, *TF*	*CD*, *ET*, *K*, *P*, *UCS*	*AS*
[15]	LSTM	*CS*, *CT*, *EP*, *TF*	-	*PR*
[19]	KF-CNN-BiGRU	*AD*, *CT*, *DR*, *EP*, *FR*, *GP*, *PA*, *RA*, *TF*	-	*AS*
[20]	LSTM	*CP*, *CS*, *CT*, *SE*, *TF*, *TAP*	-	*PR*
[21]	Attention-ResNet-LSTM	*CS*, *CT*, *TF*	*BC*, *E*	*AS*
[31]	GRU	*CS*, *EP*, *FV*, *FP*, *GV*, *GP*, *PR*, *TF*	*CD*, *TMR*, *TS*, *TSC*, *TSWR*	*AS*
[32]	ANN	*AD*, *AVE*, *CS*, *CT*, *EP*, *GV*, *GP*, *SS*, *TF*, *JS*	-	*AS*
[33]	KCNN-LSTM	*AS*, *CS*, *CT*, *PR*, *TF*	*CD*, *E*, *W*, φ	*CP*
[34]	GWO-GRNN	*CS*, *CT*, *EP*, *FP*, *GP*, *GV*, *PR*, *TF*	*AVE*, *CD*, φ	*AS* *GS*
[35]	MRFO-AT-TELM	*CS*, *CP*, *EP*, *TAP*	-	*TF*

AD: attitude deviation, *AS*: advancing speed, *AVE*: actual volume excavation, *BC*: bearing capacity, *BTS*: Brazilian tensile strength, *CC*: cutterhead current, *CD*: cover depth, *CP*: cutterhead power, *CS*: cutterhead rotation speed, *CT*: cutterhead torque, *DR*: discharge pipe flow rate, *E*: elasticity modulus, *EP*: earth pressure, *ET*: earth type, *FP*: foam pressure, *FR*: feed pipe flow rate, *FV*: foam volume, *GP*: grouting pressure, *GS*: ground settlement, *GV*: grouting volume, *JS*: Jack Stroke, *K*: upper coefficient of lateral earth pressure, *P*: composite ratio, *PA*: pitching angle, *PR*: penetration rate, *RA*: rolling angle, *SE*: specific energy, *SS*: screw conveyor speed, *TAP*: total absorbed power, *TS*: thickness of slit, *TSC*: thickness of slit clay, *TMR*: thickness of mixed rock, *TSWR*: thickness of weathered rock, *TF*: thrust force, *UCS*: uniaxial compressive strength, *W*: water content, φ: friction angle.

In addition to these direct construction parameters, a number of calculation-based metrics better reflect the performance of shield tunnelling. *PR* and *SE* can reflect the comprehensive performance of the shield, which can be obtained through the calculation of conventional monitoring data. *PR* is calculated as shown in Equation (1), which reflects the penetration ability of the cutter plate of the shield machine to the stratum in the process of digging. *SE* synthesizes the thrust, torque, and radius of the cutter plate and quantifies the energy consumption required to excavate a unit volume of soil in units of "MJ/m^3". Since it is not convenient to count the actual energy consumed and the volume removed by

the shield in actual construction, this paper adopts an approximation of the calculation as shown in Equation (2), where R is the radius of the cutter head (in metres); TF is the total thrust (in KN); and CT and PR can be found in Table 2 [36,37]. CD and ET are important characterizations of the geological conditions. CD affects the load of shield propulsion, while ET directly determines the strength of the soil and the difficulty of cutting, which is usually clearly documented at the stage of construction geological investigation and forms the basic data during construction. Ultimately, the input and output parameters of the model selected in this paper are shown in Table 2.

$$PR = \frac{AS}{CS} \tag{1}$$

$$SE = \frac{TF \cdot PR + 2\pi \cdot CT}{\pi \cdot R^2 \cdot PR} \tag{2}$$

Table 2. Input and output parameters of the LSPP model.

	Type	Full Name	Variable	Unit
Input	Tunnelling parameters	Cutterhead rotation speed	CS	RPM
		Cutterhead torque	CT	KN·m
		Earth pressure	EP	MPa
		Screw conveyor speed	SS	RPM
		Cutterhead current	CC	A
		Specific energy	SE	MJ/m^3
	Geological conditions	Cover depth	CD	m
		Earth type	ET	-
Output	Tunnelling parameters	Penetration rate	PR	mm/rev

2. Data filtering

Due to the complexity of the tunnelling environment, there is often a high level of volatility and noise in the tunnelling data, making it difficult to identify data patterns. The data were therefore grouped and filtered on the basis of the number of advancement rings. Tukey's fences method was used to identify and filter noise data within each ring, preventing the negative impact of data fluctuations on the model's training [38]. This method is used to filter the observation value by setting the upper and lower limits of the data range, as shown in Equations (3)–(6).

$$L_{\text{upper}} = Q3 + 1.5 \times IQR \tag{3}$$

$$L_{\text{lower}} = Q1 - 1.5 \times IQR \tag{4}$$

$$IQR = Q3 - Q1 \tag{5}$$

$$Ds = \begin{cases} \text{outliers} & \left(Ds < L_{\text{lower}} \text{ or } Ds > L_{\text{upper}}\right) \\ \text{non-outliers} & \left(L_{\text{lower}} < Ds < L_{\text{upper}}\right) \end{cases} \tag{6}$$

where $Q1$ is the lower quarter quantile of the data, $Q3$ is the upper quarter quantile, IQR is the interquartile range, L_{upper} is the upper limit of non-outliers, L_{lower} is the lower limit of non-outliers, and Ds is the data point in the selected area.

3. Data standardization

During the model training process, the different dimensions and magnitudes of the input features will affect the training effect [39]. The data are normalized by the Z-score normalization method, as shown in Equation (7), which eliminates the potential bias caused by the dimension difference.

$$Z = \frac{X - \mu}{\sigma} \tag{7}$$

where Z represents the standardized data, X represents the sample value of the excavation feature, μ represents the mean corresponding to the sample feature, and σ represents the standard deviation corresponding to the excavation feature X.

4. Spatial alignment of data

Due to the sparseness of the geologic information of the construction site compared with the tunnel construction data, we calculated the geological data surrounding the borehole using Inverse Distance Weighting (IDW) [40] in conjunction with the geological exploration data to determine the soil information of each segment ring. The determination of the weight of the influence of the sample point on the value to be interpolated is achieved by calculating the Euclidean distance between the sample point and the value to be interpolated. The weights of the sample points are calculated according to Equation (8).

$$w_i = \frac{1}{d_i^2} \tag{8}$$

where w_i represents the weight of the i-th sample point and d_i represents the distance between the sample point and the position to be interpolated. The interpolation position is aligned with the mileage required for calculation, ensuring the correct association between the formation information and the excavation parameters.

2.2.3. Encoder–Decoder

1. Encoder

The tunnelling and geological parameters listed in Table 2 form the input to the encoder. The data are arranged and entered in batches to improve computational performance. When the batch size is n, the time relationship of the sample data in the same batch is shown in Figure 3. The time range of sample 1 is $[t_1, t_k]$, and the time range of sample 2 is $[t_2, t_{k+2}]$; until n samples are obtained, the time range of sample n is $[t_n, t_{k+n}]$. The data flow in the encoder is shown in Figure 4. The input features have 8 dimensions. If the batch size is 32 and the historical sequence length (seq_len) = 96, the initial data shape is $32 \times 96 \times 8$. The data are first mapped to a higher dimension through the embedding layer. After the Encoding Stacking 1 mapping is completed, the shape of the data is $32 \times 96 \times 512$. The length of Encoding Stacking 2 is halved. Then, the data flow into the Muti-head ProbSparse self-attention Block in the encoder to calculate the attention score, extracting the long-range dependency between the data and calculating the output feature map.

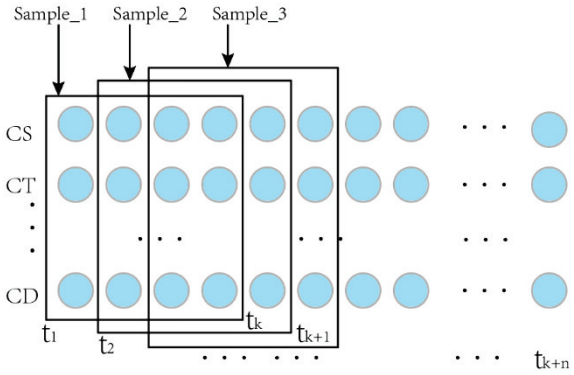

Figure 3. Schematic diagram of the time relationship between samples.

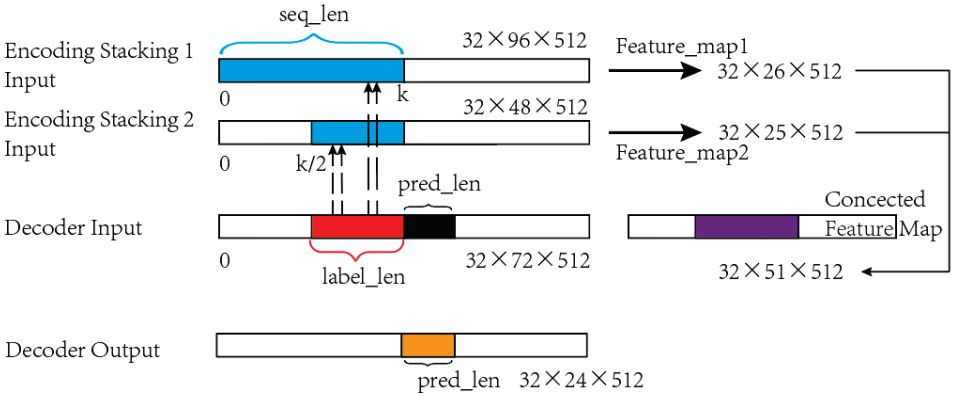

Figure 4. Schematic encoder–decoder data structure.

2. Decoder

The input to the decoder consists of the feature map from the encoder, the history label sequence data of the predicted target, and the mask data, where the mask length is the same as the predicted sequence length of the model. When the label sequence length (label_len) is 48 and the predicted sequence length (pred_len) is 24, this part of the initial input data has the shape of $32 \times (48 + 24) \times 8$, which is mapped to $32 \times 72 \times 512$ after embedding. Prediction results are computed by a fully connected layer in combination with the computational attention mechanism.

2.2.4. Performance Prediction

The prediction results are organized into an $n \times p$ two-dimensional matrix, where n represents the number of predicted samples and each row represents a predicted sequence of length p, which intuitively demonstrates the prediction ability of the model at different time points. By extracting the last column, the prediction results after p moments can be obtained.

2.3. Long Short-Term Memory Networks

Long short-term memory (LSTM) is an RNN model that was proposed by Hochreiter and Schmidhuber in 1997 [41]. It introduces memory cells and gating mechanisms to control the transmission of information, thereby enabling the network to capture long-term dependencies between features. The core structure of LSTM contains three gates: Forget Gate: this decides which information needs to be discarded; Input Gate: this controls how much of the current input information is stored in the cell state; and Output Gate: this determines how the current cell state affects the output of the network. By regulating these

gates, LSTM can efficiently retain information for extended periods and avoid the issue of gradient vanishing that traditional RNNs encounter when dealing with long sequences.

2.4. Gated Recurrent Unit Networks

The gated recurrent unit (GRU) was proposed by Cho et al. in 2014 [42]. It is a relatively simplified variant of LSTM. GRUs reduce the complexity of LSTM while retaining its ability to process long sequences. A distinguishing feature of GRUs is their integration of some of the gates present in LSTM, contributing to a more streamlined structure. The architecture of GRUs comprises two primary gates: Update Gate: this gate determines the extent to which the network retains historical information for the current moment. The Reset Gate governs the discarding of historical information that is not pertinent to the current input. The GRU employs these two gates to adaptively select between save and forget strategies over time steps.

3. Case Study

3.1. Engineering Background

The right-line tunnel between the Wenjing Road Station and Chalukou Station of Nanjing Metro Line 5 is about 1270 m long and buried at a depth of 16.4 to 25.5 m. The geological environment along the line is complex, and it passes through various strata such as silt, clay, rock, and composite strata. The geological profile is shown in Figure 5. During the shield tunnelling process, due to the variability and uncertainty of the strata, it is difficult to formulate a reasonable control strategy if the trend of tunnelling performance changes cannot be understood.

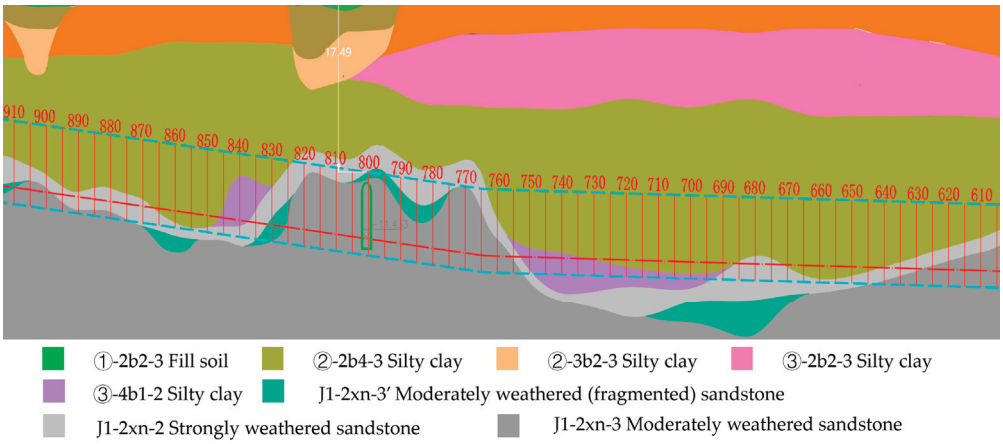

Figure 5. Geological profile of the section between Wenjing Road Station and Chalukou Station.

3.2. Data Processing

The engineering data corresponding to 50–1000 rings of the right line interval from Wenjing Road Station–Chalukou Station were collected for experimental verification. The data were pre-processed according to the steps described in Section 2.2.2. First, the data for the parameters in Table 2 at the time of advancement were extracted from the cloud database. Then, to avoid the influence of the input outliers on the model, the outliers in each ring were identified and removed using Equations (3)–(6), with the original data of 1,846,752 sample points and the remaining 1,779,708 data after processing, with the outliers accounting for 3.7% of the total data. The comparison of penetration before and after processing is shown in Figure 6. It was found that the original penetration data suddenly increased. This may be because the sensor fails to accurately read the excavation speed

or cutter head speed due to the influence of noise, resulting in the above problem. After processing the outliers, the penetration data are within a reasonable range.

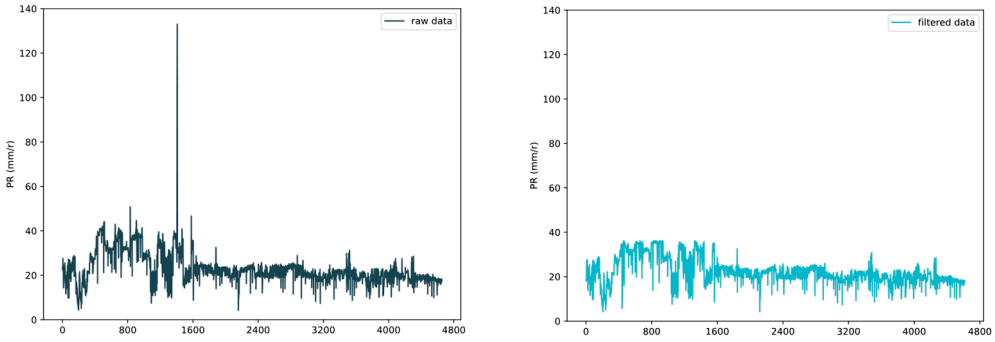

(**a**) (**b**)

Figure 6. Comparison of outliers before and after processing. (**a**) Raw data. (**b**) Filtered data.

After filtering the data, the different types of features were standardized using Equation (7) to eliminate the adverse effects of different magnitudes on the model. Finally, after interpolating the stratigraphic information using Equation (8), the stratigraphic information and construction parameters were spatially aligned to construct the input dataset. The experiments were designed to preserve the original data characteristics and temporal continuity by dividing the dataset into training, validation, and test with a ratio of 7:1:2, in chronological order.

3.3. Data Correlation Analysis

Correlation analysis shows the relationship between different variables, provides a visual understanding of the data, and can be used to assess the correlation between input variables and objectives [43]. The Pearson correlation coefficient (PCC) was used in this study to show the relationship between input variables and *PR* [44]. The correlation between variables is calculated as shown in Equation (9).

$$r = \frac{\sum_{i=1}^{n} (X_i - \overline{X})(Y_i - \overline{Y})}{\sqrt{\sum_{i=1}^{n} (X_i - \overline{X})^2} \sqrt{\sum_{i=1}^{n} (Y_i - \overline{Y})^2}} \tag{9}$$

where r is the Pearson correlation coefficient; X_i, Y_i denote the i-th sample of two different features; $\overline{X}$, $\overline{Y}$ denote the mean of the corresponding feature; and n represents the number of measured data samples.

Figure 7 shows the heatmap of the Pearson correlation coefficient results between *PR* and each feature. It can be seen that *SS* is the most critical feature affecting *PR*, and the Pearson correlation coefficient between *SS* and *PR* is 0.72. In the process of shield advancement, *SS* represents the speed of soil transported by the shield, and in order to maintain the stability of soil pressure inside the shield, *SS* usually needs to be adjusted in conjunction with the advance speed. There is a strong positive correlation between *PR* and *ET*, *CD*, which indicates that when the soil body produces changes, *PR* will appear with corresponding changes and the shield tunnelling performance will be affected. There is a strong negative correlation between *PR*, *CS*, and *SE*, which indicates that when the energy consumed per unit distance is higher, it can reflect that the current tunnelling is difficult.

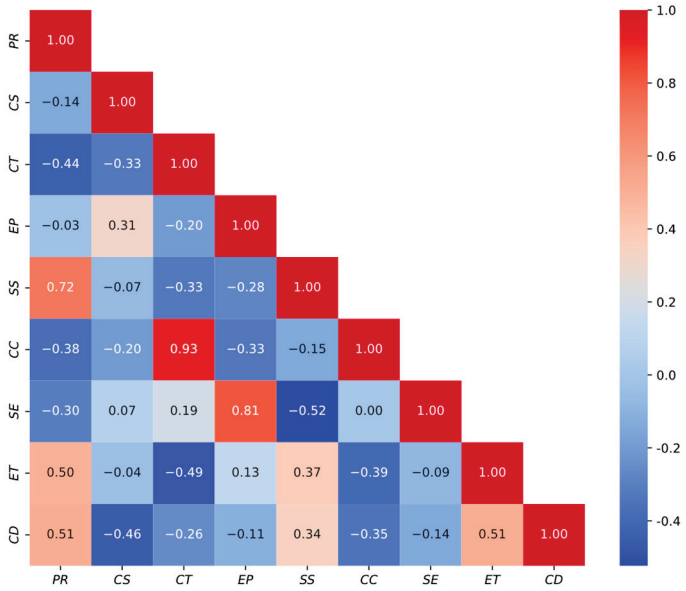

Figure 7. Heatmap of Pearson correlation coefficient.

3.4. Experimental Design

To assess the differences between the LSPP and existing performance prediction methods, as well as to deeply analyze the impact of LSPP parameters on performance prediction, a multi-group experimental design was created.

3.4.1. Effect of Sequence Length

The predicted sequence length was fixed to the 1200 mm ring width. Three groups of nineteen experiments were designed in terms of data interval length (interval_len), historical sequence length, and labelled sequence length, as shown in Table 3.

Table 3. Sequence length parameter setting comparison experiment.

Groups \ Parameters	No	interval_len (mm)	seq_len (mm)	label_len (mm)
A. Data interval length	1	1200	2400	1200
	2	240	2400	1200
	3	120	2400	1200
	4	80	2400	1200
	5	60	2400	1200
	6	48	2400	1200
	7	24	2400	1200
B. History sequence length	1	48	1200	1200
	2	48	2400	1200
	3	48	3600	1200
	4	48	4800	1200
	5	48	6000	1200
	6	48	7200	1200
C. Label sequence length	1	48	7200	1200
	2	48	7200	2400
	3	48	7200	3600
	4	48	7200	4800
	5	48	7200	6000
	6	48	7200	7200

In this experiment, Group A trials fixed the length of the history sequence and the length of the label sequence used in the model and then varied the sampling interval to examine the effect of this parameter on model accuracy. Group B experiments varied the length of the history sequence used in the model and observed a trend in the change in model accuracy. Group C sought to investigate the effect of the length of the label sequence on the model. Initially, the results of Groups A and B were used to determine the appropriate length of the data interval and the length of the history sequence, and then the effect of the choice of label length on model performance was further analyzed.

3.4.2. Model Performance Comparison

Previous studies have shown that the LSTM and GRU models are effective in predicting time series. To evaluate the performance of the LSPP model, we compare it to GRUs and LSTM. To remain unbiased, we performed a grid search to identify the optimal hyperparameters for each model. We designed three different prediction distances, short, medium, and long, as shown in Table 4.

Table 4. Comparative experiment on prediction ability of different models.

Model	Hyperparameter	Value or Space	Predicted Sequence Length (mm)
LSPP	Number of heads Batch size ProbSparse attn factor Learning rate Activation function optimizer	[3, 4, 5, 6, 7, 8, 9] [32, 64, 96, 128] [2, 3, 4, 5, 6, 7, 8, 9, 10, 11] [0.0001, 0.001, 0.01, 0.1] Gelu Adam	[48, 1200, 6000]
LSTM	LSTM units Hidden layer units Learning rate Activation function optimizer	[32, 64, 128] [20, 50, 100] [0.0001, 0.001, 0.01, 0.1] Relu Adam	[48, 1200, 6000]
GRU	GRU units Hidden layer units Learning rate: Activation function optimizer	[32, 64, 128] [20, 50, 100] [0.0001, 0.001, 0.01, 0.1] Relu Adam	[48, 1200, 6000]

3.4.3. Model Performance Evaluation Metrics

After the model training is completed, the data in the test set is predicted and the future results are denormalized. Four performance indicators are employed to evaluate the model performance: mean absolute error (MAE), root mean square error (RMSE), mean absolute percentage error (MAPE), and the determination coefficient (R^2). The formulas are presented in Equations (10)–(13).

$$\mathrm{MAE} = \frac{1}{n}\sum_{i=1}^{n}|(y_i - \hat{y}_i)| \tag{10}$$

$$\mathrm{RMSE} = \sqrt{\frac{1}{n}\sum_{i=1}^{n}(y_i - \hat{y}_i)^2} \tag{11}$$

$$\mathrm{MAPE} = \frac{1}{n} \times \sum_{1}^{n}\left|\frac{y_i - \hat{y}_i}{y_i}\right| \times 100\% \tag{12}$$

$$R^2 = 1 - \frac{\sum_{i=1}^{n} (y_i - \hat{y}_i)^2}{\sum_{i=1}^{n} (y_i - \overline{y})^2} \tag{13}$$

where $\hat{y}_i$ is used to represent the predicted value of the i-th sample point, y_i is the true value of the i-th sample, and $\overline{y}$ is the mean of the true value of the sample.

3.4.4. Significance Test

To further validate the statistical significance of the model parameters, we introduced Student's t-test using the t-statistic and the degrees of freedom (df) to calculate the p-value through the t-distribution, which is used to assess whether there is a significant difference between the predicted value of the model and the true observation. t and df calculations are shown in Equations (14) and (15).

Original hypothesis (H_0): There is no significant difference between the predicted and actual values.

Alternative hypothesis (H_1): There is a significant difference between the predicted and actual values.

$$t = \frac{\overline{x}_1 - \overline{x}_2}{\sqrt{\frac{s_1^2}{n_1} + \frac{s_2^2}{n_2}}} \tag{14}$$

$$df = \frac{\left(\frac{s_1^2}{n_1} + \frac{s_2^2}{n_2}\right)^2}{\frac{\left(\frac{s_1^2}{n_1}\right)^2}{n_1 - 1} + \frac{\left(\frac{s_2^2}{n_2}\right)^2}{n_2 - 1}} \tag{15}$$

where $\overline{x}_1$ is the sample mean of the true value, $\overline{x}_2$ is the sample mean of the predicted value, s_1 is the sample variance of the true value, s_2 is the sample variance of the predicted value, and n_1 equals n_2 to indicate the sample size.

4. Results and Analysis

4.1. Effect of Sequence Length Parameter

Based on the experimental design in Table 3, the impact of different data extraction methods on the performance of the model was explored.

1. The effect of data interval

The prediction results of the LSPP model at different sampling intervals are shown in Figure 8. It can be seen that the performance of the model improves as the sampling interval is reduced. The performance improvement of the model is particularly obvious when the sampling interval is reduced from 1200 mm to 240 mm. When the sampling interval is less than 120 mm, the model performance improves less when the sampling interval is further reduced. The reason for this phenomenon may be that when the sampling interval is too large, some important information may be lost, causing the prediction error of the model to increase.

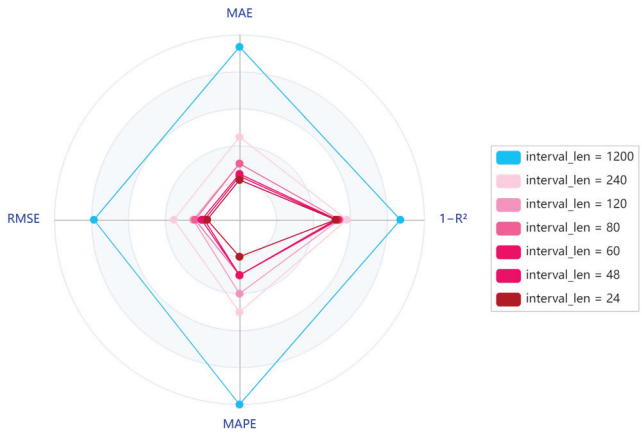

Figure 8. Effects of different data intervals on LSPP prediction.

2. The effect of historical sequence length

The effect of history sequence length on LSPP performance is shown in Figure 9. When the length of the used history sequence increases, it helps to improve the model prediction performance. As the sequence length increases from 1200 mm to 3600 mm, the range covered by each performance indicator shows an obvious contraction trend, but when the sequence length reaches 3600 mm and then continues to increase the history sequence length, the model performance improvement is not obvious. Therefore, appropriately increasing the length of the historical sequence is beneficial to improving the predictive performance of the model.

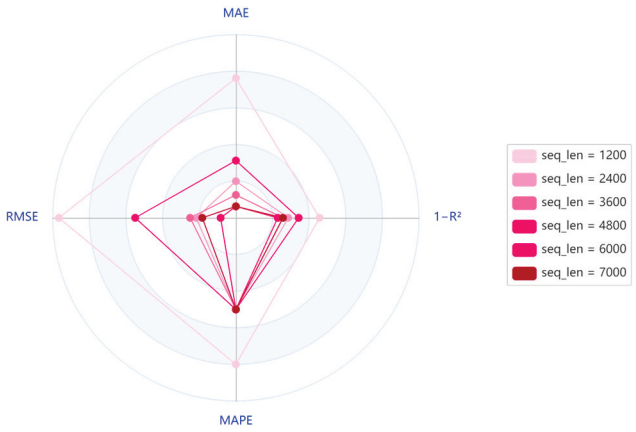

Figure 9. Effect of different history sequence lengths on LSPP prediction.

3. The effect of label sequence length

The prediction performance of the model for different label sequence lengths is shown in Figure 10. As the label sequence length increases, the corresponding four performance indicators of the model gradually increase, indicating that the prediction performance of the model has decreased. The main reason for this phenomenon may be that when the label sequence is too long, the correlation between the information contained in it and the future penetration decreases, causing interference with the prediction of the model, and so the chosen length of the label should not be too long.

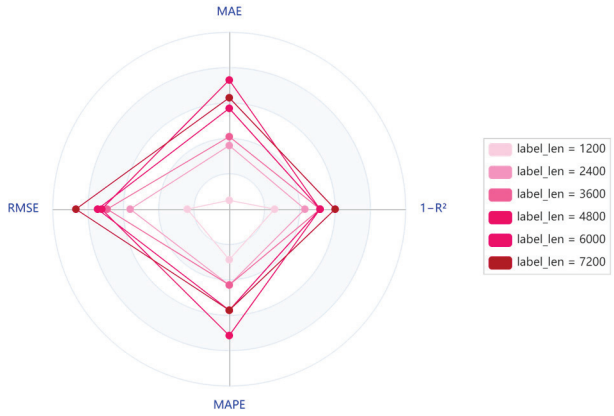

Figure 10. Effect of different label sequence lengths on LSPP prediction.

Through the above experiments, within the data interval length range of 24–1200 mm, reducing the sampled data interval improves model performance. Additionally, when both the history sequence and label sequence lengths are less than 7200 mm, increasing the history sequence length enhances model performance. However, excessively long label sequences degrade model performance.

4.2. LSPP Prediction Performance Analysis

In further exploring the characteristics of the proposed LSPP model, based on the results of the correlation analysis in Section 4.1, the sample data with an interval length of 48 mm (i.e., a unit distance of 48 mm) was selected for this experiment, and different prediction sequence lengths were set to analyze the characteristics of the model as the prediction sequence length increases.

This study optimizes the LSPP model through the grid search method. The historical sequence time length, label sequence length, and prediction performance obtained for different prediction requirements are shown in Table 5. The results show that the overall coefficient of determination (R^2) of the model tends to decrease with the increase in the prediction sequence length. The closer the R^2 is to 1, the more capable the model is of explaining the variability of the data. For example, at a predicted length of 48 mm, the R^2 reaches 0.98, indicating that the model can almost completely explain the observed variability. Meanwhile, a higher R^2 is often accompanied by a lower MAE, RMSE, and MAPE, which reflect a smaller gap between the LSPP predicted and actual observed values. In Table 5, when the predicted length reaches 6000 mm, R^2 = 0.87, which can fit the performance variation in the shield during construction well. In addition, the increase in the length of predicted sequences also leads to a corresponding increase in the length of historical sequences and the length of label sequences required by the model.

Table 5. Performance of LSPP with different prediction sequence lengths.

pred_len (mm)	seq_len (mm)	label_len (mm)	MAE	RMSE	MAPE	R^2
48	1200	192	0.59	0.76	0.03	0.98
1200	1200	192	1.05	1.51	0.05	0.91
2400	2400	240	1.13	1.45	0.05	0.92
3600	2400	240	1.74	2.05	0.08	0.84
4800	3600	240	1.64	1.9	0.08	0.86
6000	3600	576	1.49	1.8	0.07	0.87
7200	4800	1200	1.82	2.13	0.09	0.82

Figure 11 shows the model prediction effect when the length of the predicted sequence is 48 mm, 1200 mm, and 6000 mm, in which, when the length of the predicted sequence is 48 mm, the predicted value of the model keeps the trend of synchronization with the real value, and the RMSE between the predicted value and the real value is only 0.76 mm/rev. With the increase in the length of the predicted sequence, the error tends to be larger, but it is still within the acceptable range, and when the length of the predicted sequence reaches 6000 mm, the model prediction trend still remains the same with the real value. The model performance remains well stabilized in the presence of an increase in the length of the predicted sequence.

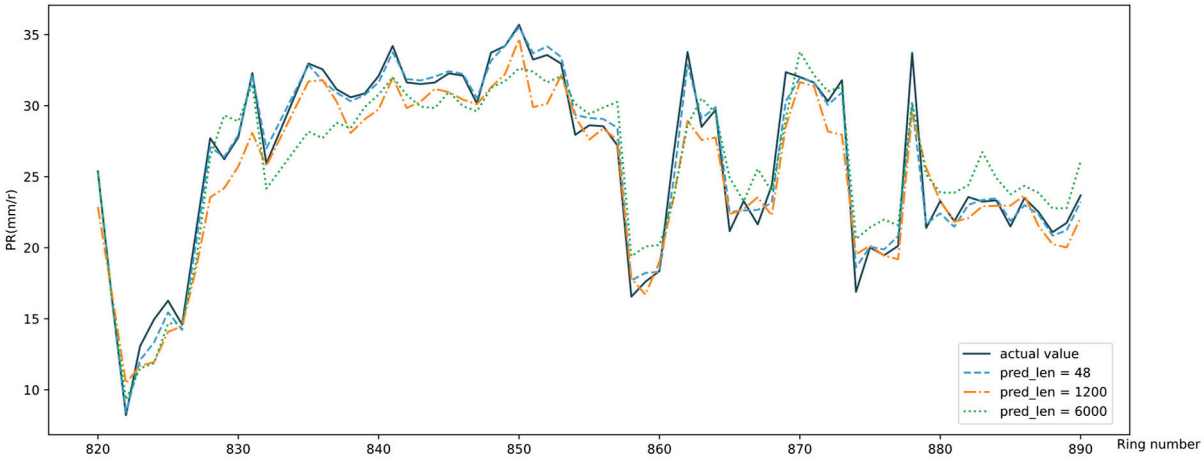

Figure 11. LSPP prediction results of different prediction sequence lengths.

To assess whether there is a significant difference between the predicted and actual values of the shielding performance of LSPP for long distances, the *t*-test was conducted for the predicted and actual values at the predicted length of 6000 mm. The results showed that t = 1.647, while *p*_value = 0.1003, and when the significance level (α) is 0.05, the *p*_value > 0.05, so the original hypothesis is accepted. No significant difference was obtained between the predicted and actual values, verifying the reliability of the model performance.

The prediction results of LSPP for the following six rings are shown in Figure 12. Although the actual value of the penetration has changed abruptly many times and the penetration decreased by 9.9 mm/rev from ring 821 to ring 822, a relatively large change, the model can still predict accurately. The maximum absolute deviation of the model is not more than 5 mm/rev, as seen in the prediction deviation graph of the model, and the relatively large error region is concentrated in the late stage of the advancement. It may be that frequent fluctuations in penetration increase the difficulty of model prediction.

4.3. Comparative Analysis of Model Prediction Performance

4.3.1. Comparison of Different Prediction Sequence Lengths

Table 6 shows the prediction results for the experimental group in Table 4, and we can find that the prediction performance of LSPP is better than that of LSTM and GRUs, which is more obvious in the long-distance prediction experiments. The performance of LSPP degrades more slowly. Comparing LSTM and GRUs, when the prediction sequence length is 48 mm, under this shorter prediction sequence length, the MAE of the LSPP model is only 0.59, the RMSE is 0.76, the MAPE is 0.03, and the R^2 is as high as 0.98, while the LSTM and GRU models do not perform as well as the LSPP in these four metrics, especially in the value of R^2, which is much higher than that of LSTM's 0.85 and GRU's 0.86. This

indicates that the LSPP model is able to capture the trend of the data more accurately in the short-term prediction with higher prediction accuracy.

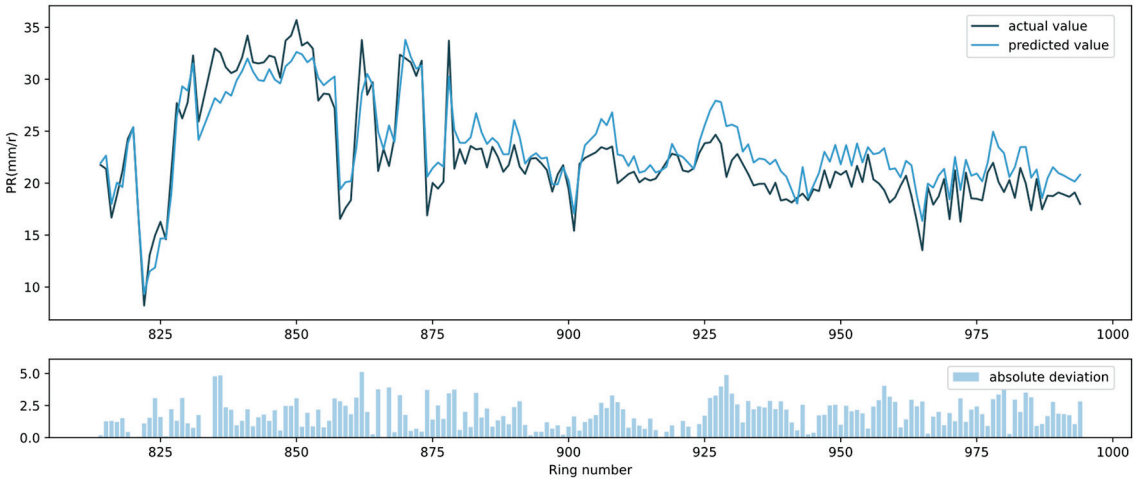

Figure 12. LSPP prediction results for the next 6 rings.

Table 6. Performance comparison of different models.

pred_len (mm)	Model	MAE	RMSE	MAPE	R^2
48	LSPP	0.59	0.76	0.03	0.98
	LSTM	1.48	2.2	0.07	0.85
	GRU	1.86	2.71	0.12	0.86
1200	LSPP	1.05	1.51	0.05	0.91
	LSTM	1.82	2.72	0.09	0.78
	GRU	2.6	3.49	0.17	0.76
6000	LSPP	1.49	1.8	0.07	0.87
	LSTM	2.04	2.98	0.11	0.73
	GRU	2.89	4.09	0.15	0.49

When the prediction sequence length increases to 1200 mm, the LSPP still maintains good prediction performance, its error is still low, and the R^2 remains at a high level (0.91). However, the R^2 of GRUs and LSTM drop significantly to only 0.78 and 0.76. This result shows that as the prediction sequence length increases, LSPP has the advantage of stable performance.

When the prediction sequence length is 6000 mm, although the prediction errors of all models have increased, the MAE, RMSE, and MAPE of LSPP are still lower than those of LSTM and GRUs, and the R^2 value reaches 0.87, which is significantly better than 0.73 for LSTM and 0.49 for GRUs, and the prediction advantage is more significant. This shows that in long-distance prediction, the LSPP model can maintain a relatively low error and show stronger stability.

Observe the performance degradation of the three models from Table 6. It can be found that when the predicted length increases from 1200 mm to 6000 mm, the corresponding R^2 of the GRU model decreases from 0.76 to 0.49, there is a large prediction bias, and the model performance degradation is serious, while at this time, the LSPP only decreases from 0.91 to 0.87 and still has excellent performance. The prediction performance of LSPP for the future 6000 mm even exceeds that of LSTM and GRUs for 1200 mm.

The predicted sequences of the three models for the next 6000 mm are shown separately in Figure 13. Although there is considerable variation in penetration at 899 rings of the

project, the LSPP model predicts closest to the true value and continues to reduce the error after continuous learning. While LSTM and GRUs perform similarly, the overall fluctuation is around the mean without being able to agree with the real value. After 900 rings, the actual penetration is more stable and the prediction results of all three models are close to the real situation. However, in terms of the overall prediction characteristics, LSPP has superior trend catching ability and accuracy, and it can use historical knowledge to infer future trends more effectively. The prediction accuracies of LSTM and GRUs are slightly inferior to LSPP and do not fully reflect the subtle changes in actual penetration.

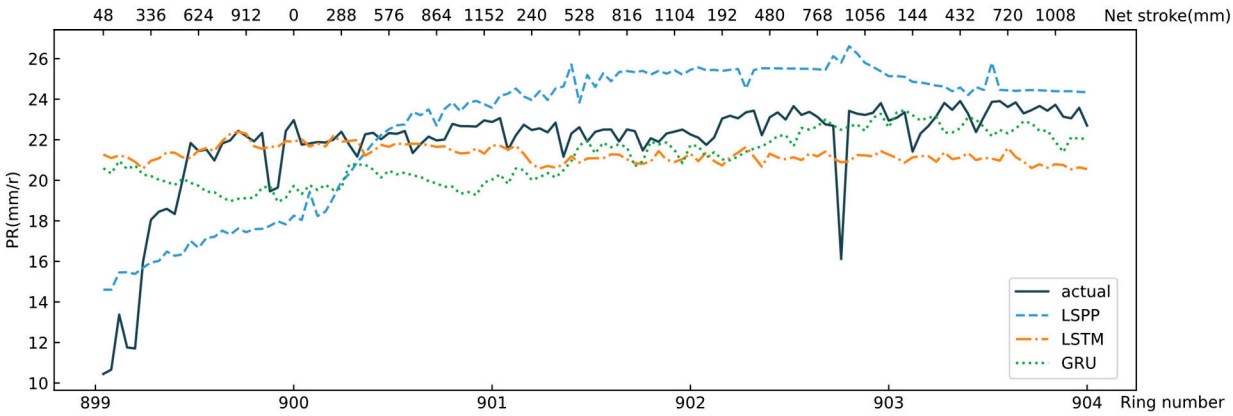

Figure 13. Next 5 rings prediction sequence.

In summary, the LSPP model performs well under different prediction sequence lengths, especially in long-distance prediction with significant advantages. Compared with the traditional LSTM and GRU models, the LSPP can better handle long sequence data and improve prediction accuracy. This advantage stems from LSPP's effective modelling of long-term dependencies and its ability to capture complex patterns.

4.3.2. Analysis of Formation Adaptability of Different Models

For an in-depth analysis of the adaptability of different models in stratigraphy, the prediction results for each of the three soil types, namely medium weathered sandstone, silty clay, and composite strata, are detailed in Figure 14.

When advancing in the medium weathered sandstone, the penetration will have a sudden drop phenomenon, such as in area (a) in Figure 14. According to the absolute deviation results of the model, we find that the deviation of the prediction results of the LSPP in this section is relatively small, especially after the sudden change, the LSPP can track the actual situation in time, and the deviation is only 4 mm/rev, as shown in Figure 15. In the composite strata, due to the constant change in the strata occupation ratio, the change in the shield penetration does not have any obvious pattern, such as in the (b) area in Figure 14, in which the LSTM and the GRU network only fluctuate around a mean value, which cannot effectively predict the future state of the shield structure to provide valuable guidance. Furthermore, the LSPP model can more clearly portray the fluctuation trend, indicating that the shield driver should pay attention to changes in the stratum and alter crucial construction factors, such as advance speed. Under the pulverized clay stratum, such as area (c) in Figure 14, the shield propels smoothly, so even if the LSTM and GRU fluctuate around the mean value, better results can be achieved.

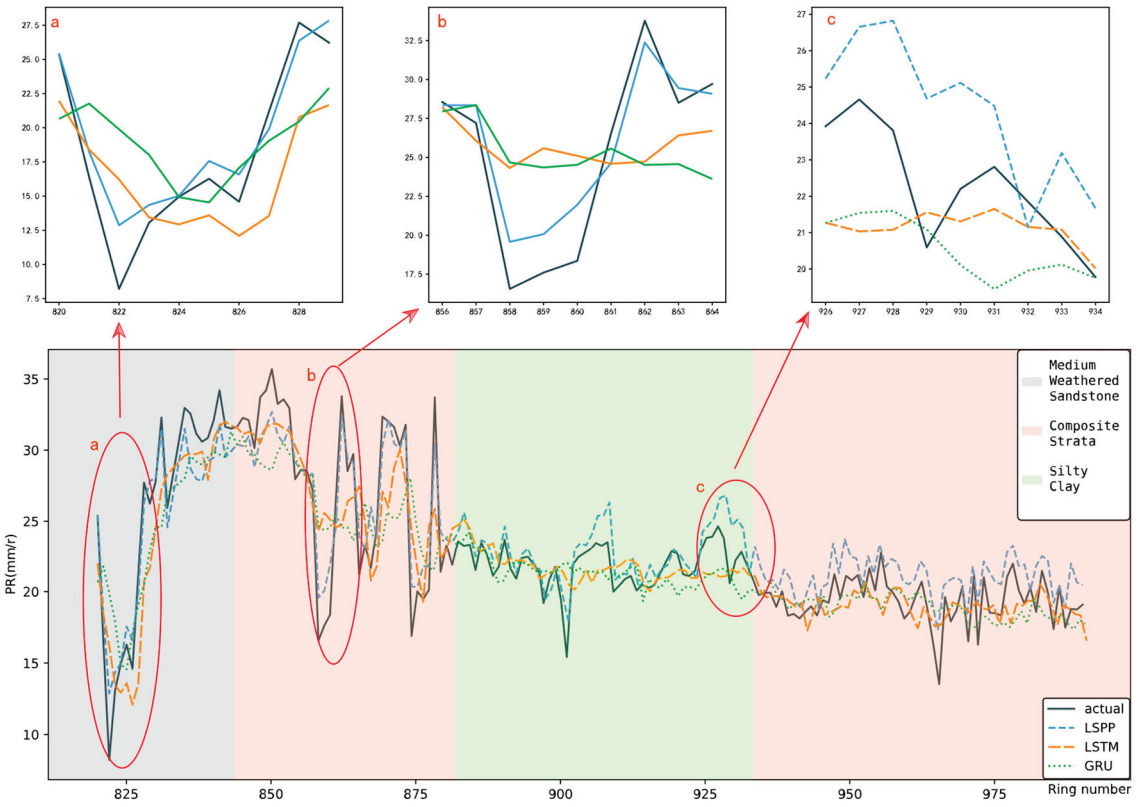

Figure 14. Predicted results of each model at the predicted length of 5 rings. (**a**) Predicted results under medium weathered sandstone. (**b**) Predicted results under composite strata. (**c**) Predicted results under silty clay.

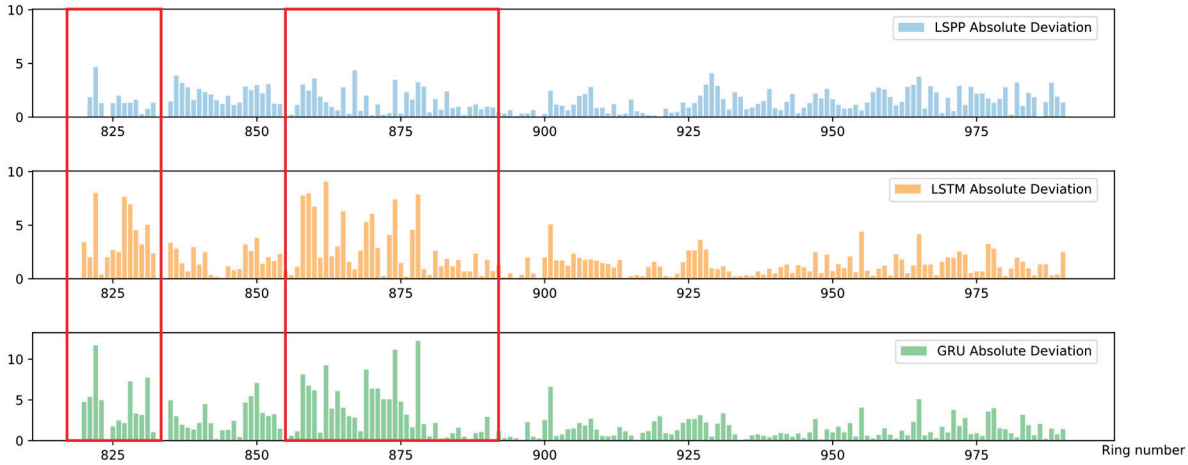

Figure 15. Absolute deviation in predictions of different models.

From the absolute deviation between the predicted and true values of each model, as shown in Figure 15, it can be seen that the overall prediction deviation of the proposed LSPP is small, especially when there is a large change in the shield penetration, the area marked by the red box in the figure, the deviation of the LSTM and the GRU appears to be a significant increase, but the prediction error of the LSPP does not have a significant change. It can be seen that LSPP is also better than LSTM and GRUs in terms of stratigraphic adaptability.

5. Conclusions

The LSPP model proposed in this study is designed to provide an accurate prediction of the performance of the shield tunnelling over long distances. The model draws on the structural advantages of the Informer model in long-range sequence prediction and combines the specific context of engineering practice, which provides sound theoretical support and practical guidance for construction decisions.

With the help of the construction data of the interval of Nanjing Line 5, Wenjing Road Station–Chalukou Station, the performance of the proposed LSPP is compared with that of the LSTM and GRU models for the prediction of the penetration. The conclusions can be summarized as follows: First, LSPP can achieve accurate prediction of shield performance over long distances. The performance indexes are excellent when the length of the prediction sequence reaches six rings, where R^2 reaches 0.82 and the RMSE is only 2.13 mm/rev. Second, compared with the LSTM and GRU models, the proposed LSPP model shows the smallest decrease in performance and the best prediction accuracy with the increase in prediction sequences. Finally, LSPP has better adaptation to different formations in the case selected for this study.

Despite the excellent performance of the LSPP, due to the complexity of the actual construction conditions and the large fluctuation of the real penetration, the model's prediction accuracy still needs to be improved in some extreme cases. In this study, we only focused on a single tunnel project, and the adaptability of LSPP under different geological conditions lacks extensive validation. Future research can improve the applicability and prediction accuracy of the model by increasing the data samples under different tunnels and strata, integrating more construction variables, and describing the actual construction conditions from multiple dimensions, so that it can better meet the needs of actual projects.

Author Contributions: Conceptualization, M.H. and P.C.; Methodology, M.H. and P.C.; Software, P.C.; Validation, M.H.; Formal analysis, M.H. and P.C.; Investigation, M.H. and P.C.; Resources, M.H. and P.C.; Data curation, P.C.; Writing—original draft, P.C.; Writing—review & editing, M.H. and P.C.; Visualization, M.H. and P.C.; Supervision, M.H.; Project administration, M.H.; Funding acquisition, M.H. All authors have read and agreed to the published version of the manuscript.

Funding: This research received no external funding.

Institutional Review Board Statement: Not applicable.

Informed Consent Statement: Not applicable.

Data Availability Statement: The data presented in this study are available on request from the corresponding author. The data in the case study are not publicly available due to the confidentiality requirement of the project.

Conflicts of Interest: The authors declare no conflict of interest.

References

1. Guo, D.; Li, J.; Jiang, S.-H.; Li, X.; Chen, Z. Intelligent Assistant Driving Method for Tunnel Boring Machine Based on Big Data. *Acta Geotech.* **2022**, *17*, 1019–1030. [CrossRef]
2. GUO, W.; LI, N.; WANG, L.; Liu, J. Evaluation Method of EPB Shield Excavation Performance. *J. Tianjin Univ. (Sci. Technol.)* **2012**, *45*, 379–385.
3. Gao, B.; Wang, R.; Lin, C.; Guo, X.; Liu, B.; Zhang, W. TBM Penetration Rate Prediction Based on the Long Short-Term Memory Neural Network. *Undergr. Space* **2021**, *6*, 718–731. [CrossRef]
4. Huang, Y.; Chen, W.; Ding, S.; Liu, X. Explicit prediction analysis of shield tunneling parameters based on feature enhancement. *China Civ. Eng. J.* **2022**, *55*, 49–57. [CrossRef]

5. Jahed Armaghani, D.; Faradonbeh, R.S.; Momeni, E.; Fahimifar, A.; Tahir, M.M. Performance Prediction of Tunnel Boring Machine through Developing a Gene Expression Programming Equation. *Eng. Comput.* **2018**, *34*, 129–141. [CrossRef]
6. Rostami, J. *Development of a Force Estimation Model for Rock Fragmentation with Disc Cutters through Theoretical Modeling and Physical Measurement of Crushed Zone Pressure*; Colorado School of Mines Golden: Golden, CO, USA, 1997; Volume 38.
7. Bruland, A. *Hard Rock Tunnel Boring*; Fakultet for Ingeniørvitenskap og Teknologi: Trondheim, Norway, 2000; pp. 6–31.
8. Zhang, H.; Zhang, K.; Xia, M.; Zhang, Z.; Zhong, G. Shield Tunneling Parameters Control in Medium-Strong Weathered Muddy Siltstone Composite Stratum. *Chin. J. Undergr. Space Eng.* **2022**, *18*, 2016–2026.
9. Wang, Y.; Wang, J.; Wang, R.; Liu, B.; Li, Y. TBM Penetration Rate Prediction Ensemble Model Based on Full-Scale Linear Cutting Test. *Tunn. Undergr. Space Technol.* **2023**, *131*, 104794. [CrossRef]
10. Salimi, A.; Rostami, J.; Moormann, C.; Delisio, A. Application of Non-Linear Regression Analysis and Artificial Intelligence Algorithms for Performance Prediction of Hard Rock TBMs. *Tunn. Undergr. Space Technol.* **2016**, *58*, 236–246. [CrossRef]
11. Benardos, A. Artificial Intelligence in Underground Development: A Study of TBM Performance. In *Underground Spaces: Design, Engineering and Environmental Aspects*; Brebbia, C.A., Kaliampakos, D., Prochazka, P., Eds.; Wit Press: Southampton, UK, 2008; Volume 102, pp. 21–32.
12. Fu, X.; Gong, Q.; Wu, Y.; Zhao, Y.; Li, H. Prediction of EPB Shield Tunneling Advance Rate in Mixed Ground Condition Using Optimized BPNN Model. *Appl. Sci.* **2022**, *12*, 5485. [CrossRef]
13. Zhou, J.; Qiu, Y.; Zhu, S.; Armaghani, D.J.; Khandelwal, M.; Mohamad, E.T. Estimation of the TBM Advance Rate under Hard Rock Conditions Using XGBoost and Bayesian Optimization. *Undergr. Space* **2021**, *6*, 506–515. [CrossRef]
14. Elbaz, K.; Shen, S.-L.; Sun, W.-J.; Yin, Z.-Y.; Zhou, A. Prediction Model of Shield Performance During Tunneling via Incorporating Improved Particle Swarm Optimization Into ANFIS. *IEEE Access* **2020**, *8*, 39659–39671. [CrossRef]
15. Fu, X.; Zhang, L. Spatio-Temporal Feature Fusion for Real-Time Prediction of TBM Operating Parameters: A Deep Learning Approach. *Autom. Constr.* **2021**, *132*, 103937. [CrossRef]
16. Xiao, H.; Chen, Z.; Cao, R.; Cao, Y.; Zhao, L.; Zhao, Y. Prediction of Shield Machine Posture Using the GRU Algorithm with Adaptive Boosting: A Case Study of Chengdu Subway Project. *Transp. Geotech.* **2022**, *37*, 100837. [CrossRef]
17. Xu, C.; Liu, X.; Wang, E.; Wang, S. Prediction of Tunnel Boring Machine Operating Parameters Using Various Machine Learning Algorithms. *Tunn. Undergr. Space Technol.* **2021**, *109*, 103699. [CrossRef]
18. Wang, Q.; Xie, X.; Shahrour, I. Deep Learning Model for Shield Tunneling Advance Rate Prediction in Mixed Ground Condition Considering Past Operations. *IEEE Access* **2020**, *8*, 215310–215326. [CrossRef]
19. Jin, J.; Jin, Q.; Chen, J.; Wang, C.; Li, M.; Yu, L. Prediction of the Tunnelling Advance Speed of a Super-Large-Diameter Shield Machine Based on a KF-CNN-BiGRU Hybrid Neural Network. *Measurement* **2024**, *230*, 114517. [CrossRef]
20. Flor, A.; Sassi, F.; La Morgia, M.; Cernera, F.; Amadini, F.; Mei, A.; Danzi, A. Artificial Intelligence for Tunnel Boring Machine Penetration Rate Prediction. *Tunn. Undergr. Space Technol.* **2023**, *140*, 105249. [CrossRef]
21. Gao, K.; Yu, S.; Xu, W.; Zhang, Z. Novel Prediction Method for Shield Advancing Speed Based on Attention-ResNet-Long Short-Term Memory Hybrid Neural Network. *Tunn. Constr.* **2023**, *43*, 592–601.
22. Shan, F.; He, X.; Jahed Armaghani, D.; Zhang, P.; Sheng, D. Success and Challenges in Predicting TBM Penetration Rate Using Recurrent Neural Networks. *Tunn. Undergr. Space Technol.* **2022**, *130*, 104728. [CrossRef]
23. Zhou, H.; Zhang, S.; Peng, J.; Zhang, S.; Li, J.; Xiong, H.; Zhang, W. Informer: Beyond Efficient Transformer for Long Sequence Time-Series Forecasting. *Proc. AAAI Conf. Artif. Intell.* **2021**, *35*, 11106–11115. [CrossRef]
24. Chen, Z.; Ma, M.; Li, T.; Wang, H.; Li, C. Long Sequence Time-Series Forecasting with Deep Learning: A Survey. *Inf. Fusion* **2023**, *97*, 101819. [CrossRef]
25. Li, S.; Jin, X.; Xuan, Y.; Zhou, X.; Chen, W.; Wang, Y.-X.; Yan, X. Enhancing the Locality and Breaking the Memory Bottleneck of Transformer on Time Series Forecasting. *Adv. Neural Inf. Process. Syst.* **2019**, *32*, 5243–5253.
26. Child, R.; Gray, S.; Radford, A.; Sutskever, I. Generating Long Sequences with Sparse Transformers. *arXiv* **2019**, arXiv:1904.10509.
27. Devlin, J.; Chang, M.-W.; Lee, K.; Toutanova, K. BERT: Pre-Training of Deep Bidirectional Transformers for Language Understanding. *arXiv* **2018**, arXiv:1810.04805.
28. Qin, Y.; Song, D.; Chen, H.; Cheng, W.; Jiang, G.; Cottrell, G. A Dual-Stage Attention-Based Recurrent Neural Network for Time Series Prediction 2017. In Proceedings of the 26th International Joint Conference on Artificial Intelligence (IJCAI'17), Melbourne, Australia, 19–25 August 2017.
29. Liu, Y.; Gong, C.; Yang, L.; Chen, Y. DSTP-RNN: A Dual-Stage Two-Phase Attention-Based Recurrent Neural Network for Long-Term and Multivariate Time Series Prediction. *Expert Syst. Appl.* **2020**, *143*, 113082. [CrossRef]
30. Yan, C.; Wang, H.; Yang, J.; Chen, K.; Zhou, J.; Guo, W. Predicting TBM penetration rate with the coupled model of partial least squares regression and deep neural network. *Rock Soil Mech.* **2021**, *42*, 519–528. [CrossRef]

31. Lin, S.-S.; Shen, S.-L.; Zhang, N.; Zhou, A. Modelling the Performance of EPB Shield Tunnelling Using Machine and Deep Learning Algorithms. *Geosci. Front.* **2021**, *12*, 101177. [CrossRef]
32. Chen, X.; Kang, Q.; Liu, Y. Optimal Control of Operation Parameters During EPB Shield Tunnelling Based on Artificial Neural Network Model. In Proceedings of the 17th East Asian-Pacific Conference on Structural Engineering and Construction, 2022: EASEC-17, Singapore, 27–30 June 2022; Springer: Berlin/Heidelberg, Germany, 2023; pp. 1265–1272.
33. Elbaz, K.; Yan, T.; Zhou, A.; Shen, S.-L. Deep Learning Analysis for Energy Consumption of Shield Tunneling Machine Drive System. *Tunn. Undergr. Space Technol.* **2022**, *123*, 104405. [CrossRef]
34. Liu, W.; Li, A.; Liu, C. Multi-Objective Optimization Control for Tunnel Boring Machine Performance Improvement under Uncertainty. *Autom. Constr.* **2022**, *139*, 104310. [CrossRef]
35. Li, L.; Liu, Z.; Lu, Y.; Wang, F.; Jeon, S. Hard-Rock TBM Thrust Prediction Using an Improved Two-Hidden-Layer Extreme Learning Machine. *IEEE Access* **2022**, *10*, 112695–112712. [CrossRef]
36. Kim, K.-Y.; Jo, S.-A.; Ryu, H.-H.; Cho, G.-C. Prediction of TBM Performance Based on Specific Energy. *Geomech. Eng.* **2020**, *22*, 489–496. [CrossRef]
37. Xue, Y.; Wang, J.; Zhou, M.; Liu, J.; Guo, Y.; Wang, J. Prediction of Optimum TBM Penetration Strategy with Minimum Energy Consumption in Hard Rocks. *Comput. Geotech.* **2022**, *148*, 104844. [CrossRef]
38. Tukey, J.W. *Exploratory Data Analysis*; Addison-Wesley: Reading, MA, USA, 1977.
39. Du, Q.; Zhang, S.; Zhang, C.; Li, X.; Xiao, Y.; Li, X. Prediction Method for Slurry Balance Shield Tunneling Speed Based on Mean Filtering & Denoising and XGBoost Algorithm. *Mod. Tunn. Technol.* **2022**, *59*, 14–23. [CrossRef]
40. Hu, M.; Lu, J.; Zhou, W.; Xu, W.; Wu, Z. A Multistage Model for Rapid Identification of Geological Features in Shield Tunnelling. *Sci. Rep.* **2023**, *13*, 1799. [CrossRef] [PubMed]
41. Hochreiter, S.; Schmidhuber, J. Long Short-Term Memory. *Neural Comput.* **1997**, *9*, 1735–1780. [CrossRef]
42. Cho, K.; van Merriënboer, B.; Gulcehre, C.; Bahdanau, D.; Bougares, F.; Schwenk, H.; Bengio, Y. Learning Phrase Representations Using RNN Encoder–Decoder for Statistical Machine Translation. In Proceedings of the 2014 Conference on Empirical Methods in Natural Language Processing (EMNLP), Doha, Qatar, 25–29 October 2014; Moschitti, A., Pang, B., Daelemans, W., Eds.; Association for Computational Linguistics: Doha, Qatar, 2014; pp. 1724–1734.
43. Yan, T.; Shen, S.-L.; Zhou, A. Identification of Geological Characteristics from Construction Parameters during Shield Tunnelling. *Acta Geotech.* **2023**, *18*, 535–551. [CrossRef]
44. Zhang, P.; Chen, R.-P.; Wu, H.-N. Real-Time Analysis and Regulation of EPB Shield Steering Using Random Forest. *Autom. Constr.* **2019**, *106*, 102860. [CrossRef]

applied sciences

MDPI

Article

The Current Stress State and Seismic Hazard in the Kunlun Pass Region Following the *Ms* 8.1 Earthquake in 2001

Jun Qiu, La Ta *, Jiading Xu, Leilei Li and Lianshan Wang

The First Monitoring and Application Center, China Earthquake Administration, Tianjin 300180, China; zcqiujun@126.com (J.Q.); jdingxu@126.com (J.X.); lileilei91@126.com (L.L.); wls@email.cugb.edu.cn (L.W.)
* Correspondence: tala333@163.com

Abstract: The Kusaihu and Xidatan faults in the western part of the East Kunlun active fault present a miter compound relationship. The Quaternary activity of these two faults is vigorous and closely associated with potent and large earthquakes. The *Ms* 8.1 earthquake occurred on the Kusai Lake fault on 14 November 2001. To understand the current stress state and seismic hazard in the Kunlun pass region following the *Ms* 8.1 Earthquake in 2001, the in situ stress measurement work of four boreholes at two measuring points in this area is conducted through the hydraulic fracturing method, and the in situ stress accumulation level in this area is analyzed using the Coulomb fracture criterion, Byerlee's law, and the fault friction parameter μ_{m}. It is found that the in situ stress accumulation level in the study area is not high, and the possibility of fault slip is low.

Keywords: East Kunlun active fault; in situ stress; stress field; fault slip; seismic hazard

1. Introduction

The occurrence of tectonic earthquakes lies primarily in the movement of geological structures, which gives rise to the contradiction between the in situ stress and the resistance of rock strata [1]. The earthquake is the outcome of this contradiction. After an earthquake, the stress state of the Earth's crust will continue to adjust until a new equilibrium is reached [2]. It has also been verified that the state of in situ stress undergoes substantial changes before and after a major earthquake [3–8]. Hence, it is of paramount significance to study the current tectonic stress field in key tectonic regions.

The East Kunlun fault zone represents a vast left-lateral strike–slip active fault located in the northern region of the Tibetan Plateau. It stretches for approximately 1600 km, spanning from the west of Whaili Lake on the border between Qinghai and Xinjiang to the east of Maqu [3,9–11]. In the western portion of the East Kunlun active fault, the Kusai Lake fault and the Xidatan fault constitute a miter complex [9]. The Quaternary activity of these two faults is intense and is closely correlated with potent and large earthquakes. The research findings suggest that the Kusai Lake fault and the Xidatan fault can rupture independently and simultaneously, resulting in moderate and strong earthquakes. The magnitude 8.1 earthquake occurred on the Kusai Lake fault on 14 November 2001 [12–14]. This indicates that the Kusai Lake fault possesses the activity pattern of large earthquakes of magnitude 8 or above. The displacement of the fault landform of the Xidatan fault also implies that the magnitude of the ancient earthquake is approximately 8, reflecting that these two sections have the capacity for recurrent strong earthquakes. Since approximately 20 ka BP, nearly all the paleoearthquakes of

the Xidatan fault have occurred 70–500 years after the paleoearthquakes of the Kusai Lake fault. After the magnitude 8.1 earthquake in 2001, the Xidatan fault has an elevated risk of strong earthquakes of approximately magnitude 8 within the next 70–100 years and constitutes a potential epicenter area for strong earthquakes in the northern Tibetan Plateau. The history of paleoseismicity in the East Kunlun fault zone holds significant importance for understanding the fracture characteristics and recurrence regularity of strong earthquakes [15]. Liao, C.T. et al. [3] compared and observed the alterations in in situ stress before and after the M8.1 earthquake in the East Kunlun Mountain Pass and discovered that approximately two-thirds of the in situ stress was released after the *Ms* 8.1 earthquake (from May to July 2003). Nevertheless, the piezomagnetic stress relief method was utilized then, and the test depth was relatively shallow. Hence, more and deeper in situ stress data regions are required to study the current stress field characteristics in this area. From the perspective of in situ stress measurement, this paper analyzes the characteristics of in situ stress accumulation and seismic risk in the region, utilizing the stress states of four deep boreholes measured by the author and one borehole measured by previous researchers.

2. The Geological Context

The East Kunlun Mountain active fault system is a significant left-lateral strike–slip active fault system located in the northern region of the Tibetan Plateau. Extending approximately 2000 km from the western shores of Whalei Lake at the Qinghai–Xinjiang border to the eastern part of Maqu, this fault system serves as a crucial boundary between the Hoh Xil active block and the Kunlun active block. Based on its structural characteristics, the East Kunlun Mountain active fault can be subdivided into six distinct seismic fault zones from west to east: the Kusai Lake Fault, the Xidatan Fault, the Arak Lake Fault, the Tuosuo Lake Fault, the Dongqinggou Fault, and the Maqu Fault. Notably, the Kusai Lake Fault and the Xidatan Fault form a miter complex in the western segment of the East Kunlun Mountain active fault (Figure 1). This fault system is also one of the most seismically active regions in the northern Tibetan Plateau, with numerous strong earthquakes recorded over the past century. These include the 8.1 magnitude earthquake that struck the western part of the Kunlun Mountain Pass on 14 November 2001; the 6.8 magnitude earthquake near Tuosuo Lake on 24 March 1971; the 7.0 magnitude earthquake east of Rialake Lake on 19 April 1963; the 7.5 magnitude earthquake in Huashixia on 7 January 1937; and the 7.0 magnitude earthquake east of Rialake Lake on 4 November 1902. Additionally, numerous paleoseismic events have been documented during the Holocene epoch, leaving behind extensive geological evidence such as earthquake ruptures, scarps, uplifts, fault ponds, multi-tiered thrust ridges, and colluvial wedges [9,16–18]. Among these events, the *Ms* 8.1 earthquake that occurred along the Kusai Lake fault on 14 November 2001 represents the largest modern seismic event recorded on the mainland of China following the 8.0-magnitude earthquake in bengcuo, Tibet Autonomous Region in 1951. This earthquake resulted in a surface rupture zone with widths varying from several meters to several hundred meters and extending over a length of 426 km along the southern margin of the Kunlun Mountains. The maximum co-seismic vertical displacement was measured at between 6.4 m and 7.6 m [10].

The left-lateral strike–slip kinematic attributes of the earthquake surface rupture zone imply that the material on the Tibetan Plateau shifts eastward along the East Kunlun fault zone, potentially resulting in the eastward migration of large earthquakes. The Xidatan fault, which is mitered to the Kusai Lake fault, exhibits a high level of activity during the Quaternary period and is closely associated with the occurrence of strong and major

earthquakes, and possesses the propensity to repeat large earthquakes [9]. Since the Xidatan fault is a historical surface rupture type earthquake void region, it is postulated to be a perilous zone for large earthquakes in the future.

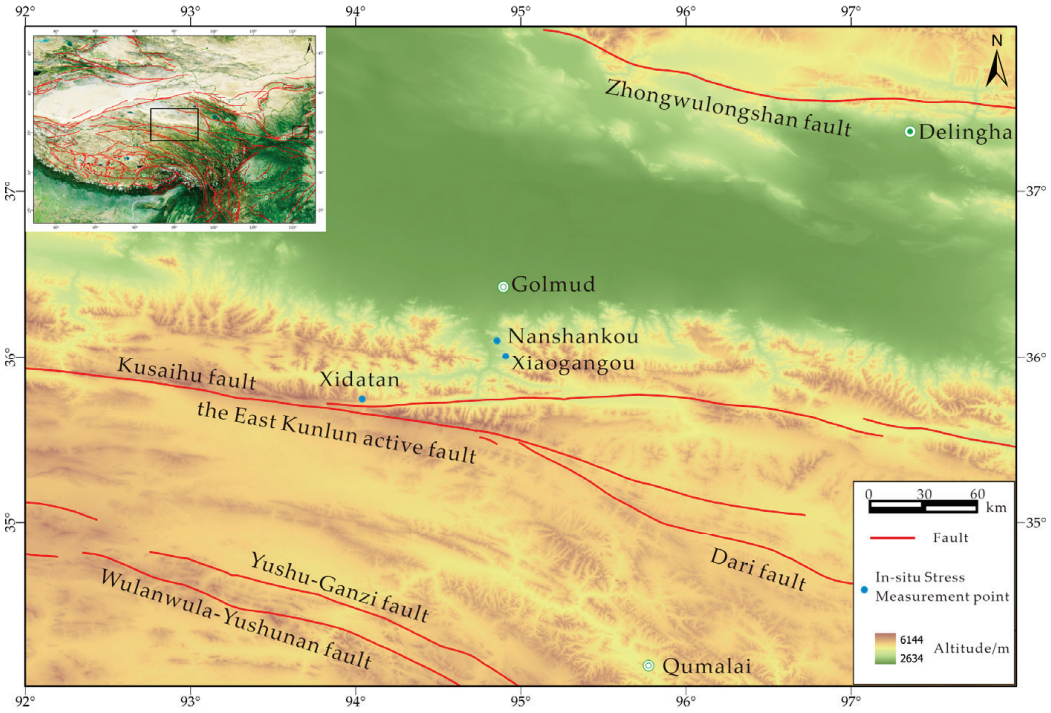

Figure 1. Geological structure map and the location of in situ stress measurement point.

3. Materials and Methods

3.1. The Position of the Measurement Point

There are three in situ stress measurement points in the study area, namely, Nanshankou, Xiaogangou and Xidatan. The measurement point at Nanshankou is situated within the annex of the Nanshankou pumped storage power station, approximately 35 km south of Golmud City. In July and December 2022, hydraulic fracturing in situ stress measurements were conducted at this location, involving one vertical surface borehole and two vertical underground boreholes. The horizontal spacing between these three boreholes is approximately 100 m. Specifically, the first borehole, designated as Surface Borehole No. 1, has a depth of 351.00 m and a water level of 85.50 m. Boreholes No. 2 and No. 3, both located in a tunnel approximately 272 m below ground level, have depths of 180.00 m each. Borehole No. 2 has a water level of 145.30 m, while Borehole No. 3 has a water level of 61.50 m.

The Xiaogangou measurement point is situated approximately 46 km south of Golmud City, adjacent to the Hot Spring pumped storage power station. In August 2024, a hydraulic fracturing in situ stress measurement was conducted at a vertical borehole with a depth of 621.00 m and a water level of 290.00 m.

The measurement point at Xidatan is situated on the granite on the northern side of Jingxiangukou within the Xidatan fault valley. The rock within the borehole is predominantly intact, albeit with some localized fracture zones. In situ stress measurements were performed in a vertical borehole with a depth of 181.83 m and a water level of 14.50 m.

3.2. Overview of the Hydraulic Fracturing Method for In Situ Stress Measurement

All the data employed in this paper are the consequences of in situ stress measurement via the hydraulic fracturing method. The hydraulic fracturing method constitutes one of the two methods recommended by the International Society of Rock Mechanics for in situ stress measurement, and its measurement theory is founded on the plane strain theory of elastic mechanics [19]. This method exhibits the advantages of uncomplicated operation and no necessity of knowing the mechanical parameters of rock, thereby emerging as the most prominent method for deep in situ stress measurement at present. In essence, hydraulic fracturing entails the utilization of a pair of inflatable packers to seal a borehole at a selected measured depth, and subsequently pumping fluid to pressurize the test section (commonly referred to as the fracturing section), fracturing the rock, and collecting pressure curves over time (Figure 2). The instantaneous closing pressure P_s and reopening pressure P_r are acquired by analyzing and computing the curve of pressure variation with time, thereby facilitating the calculation of the minimum and maximum horizontal principal stress during fracturing. Bredehoeft et al. [20] and Haimson [21] put forward the formula for computing horizontal principal stress:

$$\sigma_h = P_s, \tag{1}$$

$$\sigma_H = 3P_s - P_r - P_p, \tag{2}$$

Here, P_s stands for the instantaneous closing pressure, P_r denotes the retention pressure of the fracture surface, P_p pertains to the pore pressure, σ_h represents the minimum horizontal principal stress, σ_H represents the maximum horizontal principal stress, and the direction of σ_h is mutually perpendicular to the direction of σ_H.

The vertical stress, defined as the weight of the overlying strata from the surface to the midpoint of the fracturing section, was calculated using the formula $\sigma_v = \rho gh$, with an average rock density of 26.5 kg/m^3.

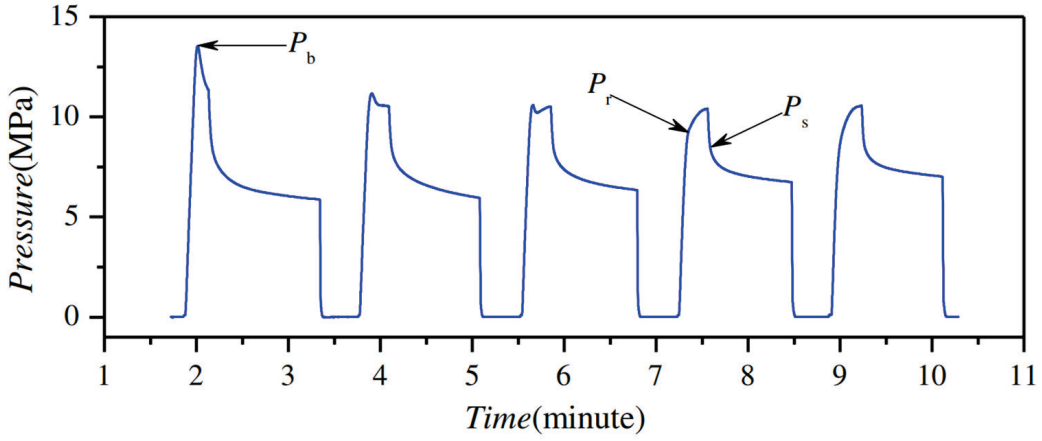

Figure 2. The curves of a typical hydraulic fracturing measurement.

3.3. Overview of Data Analysis Methods

Coulomb's criterion indicates that when the shear stress τ on the fault plane exceeds or is equal to the frictional resistance $\mu\sigma_n$, the fault will slip [20,22–25]. Upon incorporating

the concept of effective stress, the ratio of the maximum to the minimum principal stresses on the fault plane that could lead to sliding becomes a function of the friction coefficient μ.

$$(\sigma_1 - P_0)/(\sigma_3 - P_0) = ((\mu^2 + 1)^{1/2} + \mu)^2, \quad (3)$$

where σ_1 represents the maximum principal stress on the fault surface, σ_3 denotes the minimum principal stress on the fault surface, P_0 indicates pore pressure, and μ is the friction coefficient. Byerlee's law asserts that most rocks exhibit a coefficient of friction ranging from 0.6 to 1.0, which also applies to the shallow crust.

μ_m represents the ratio of the maximum shear stress to the average stress. When accounting for the influence of pore water pressure, the expression for μ_m is as follows:

$$\mu_m = (\sigma_1 - \sigma_3)/(\sigma_1 + \sigma_3 - 2P_0), \quad (4)$$

where σ_1 represents the maximum principal stress, σ_3 denotes the minimum principal stress, and P_0 indicates the pore pressure. In this study, we define σ_1 as σ_H and σ_3 as σ_v when calculating μ_m. The physical interpretation of μ_m is analogous to that of the friction coefficient μ_m, and the relationship between these two parameters is expressed as follows:

$$\mu_m = \mu/(1 + \mu^2)^{1/2}, \quad (5)$$

4. Results and Discussion

4.1. Results of In Situ Stress Measurement

A total of eight hydraulic fracturing in situ stress measurement experiments and two impression experiments were conducted in Borehole No. 1. In Borehole No. 2, seven hydraulic fracturing in situ stress measurement experiments and two impression experiments were performed. Additionally, five hydraulic fracturing in situ stress measurement experiments and two impression experiments were executed in Borehole No. 3. Due to the close proximity of the three test boreholes at Nanshanku, their results were analyzed collectively. The calculations indicate that within the depth range of 34.20 m to 430.90 m, the maximum horizontal principal stress ranges from 2.33 MPa to 16.60 MPa, while the minimum horizontal principal stress varies between 1.86 MPa and 10.79 MPa. The impression results, as illustrated in Table 1, show that the determined directions of the maximum horizontal principal stress are NE42°, NE54°, NE32°, NE21°, NE33°, and NE31°, suggesting that the predominant direction of the maximum horizontal principal stress in the vicinity of the measurement boreholes is the NNE direction.

A total of eight hydraulic fracturing in situ stress measurement experiments and two impression experiments were conducted in the Xiaogangou measurement point. The results indicate that at burial depths ranging from 182.50 m to 595.10 m, the maximum horizontal principal stress varies between 9.37 MPa and 17.20 MPa, while the minimum horizontal principal stress ranges from 4.92 MPa to 10.62 MPa. The impression results, as presented in Table 1, demonstrate that the determined orientations of the maximum horizontal principal stress are NE20° and NE30°. This suggests that the predominant orientation of the maximum horizontal principal stress near the measurement well is directed towards the NNE direction.

In August 2005, Wu et al. [26] conducted seven hydraulic fracturing in situ stress measurement experiments and five impression measurement experiments in the Xidatan borehole. The findings from the borehole suggest that the burial depth varies between 44.00 m and 176.00 m, the maximum horizontal principal stress ranges from 2.32 MPa to 11.07 MPa, while the minimum horizontal principal stress varies between 2.30 MPa and

7.00 MPa. The impression test results are presented in Table 1. The identified orientations of the maximum horizontal principal stress were NE21°, NE29°, NE43°, NE34°, and NE42°, suggesting that the predominant orientation of the maximum horizontal principal stress in the vicinity of the measurement borehole is northeast.

Table 1. Results of hydraulic fracturing stress measurements.

Borehole	No.	Test Interval Burial Depth (m)	Fracturing Parameter (MPa)						Principal Stresses (MPa)			μ_m	Direction of σ_H
			P_H	P_0	P_b	P_r	P_s	T	σ_H	σ_h	σ_v		
Nanshan Pass ZK01	1	34.20	0.34	0.00	8.16	4.57	2.87	3.59	4.04	2.87	0.91	0.63	
	2	36.60	0.37	0.00	5.61	3.24	1.86	2.37	2.33	1.86	0.97	0.41	
	3	61.20	0.61	0.00	5.96	3.31	2.59	2.65	4.46	2.59	1.62	0.47	
	4	110.00	1.10	0.25	10.37	7.21	5.54	3.16	9.17	5.54	2.92	0.54	NE42°
	5	161.80	1.62	0.76	12.84	6.64	6.13	6.20	10.98	6.13	4.29	0.49	
	6	229.30	2.29	1.44	10.78	7.18	4.79	3.60	5.76	4.79	6.08	0.16	
	7	280.60	2.81	1.95	14.60	9.96	7.80	4.64	11.48	7.80	7.44	0.27	NE54°
	8	335.80	3.36	2.50	9.90	7.44	7.31	2.46	11.98	7.31	8.90	0.33	
Nanshan Pass ZK02	1	338.60	0.67	0.00	15.39	9.62	7.08	5.77	11.61	7.08	8.97	0.24	NE35°
	2	380.40	1.08	0.00	14.59	12.26	8.23	2.33	12.44	8.23	10.08	0.20	
	3	401.50	1.3	0.00	13.32	8.86	6.19	4.46	9.70	6.19	10.64	0.26	
	4	405.45	1.33	0.00	13.55	10.26	8.7	3.29	15.85	8.70	10.74	0.29	NE21°
	5	420.05	1.48	0.03	13.34	10.83	7.94	2.51	12.96	7.94	11.13	0.24	
	6	423.10	1.51	0.06	18.88	9.97	7.12	8.91	11.33	7.12	11.21	0.23	
Nanshan Pass ZK03	1	405.20	1.33	0.72	13.7	9.99	7.09	3.71	10.57	7.09	10.74	0.22	NE33°
	2	415.20	1.43	0.82	17.01	14.96	10.79	2.05	16.6	10.79	11.00	0.23	
	3	419.80	1.48	0.86	12.57	9.84	8.54	2.73	14.91	8.54	11.12	0.29	NE31°
	4	423.00	1.51	0.9	12.93	9.09	7.02	3.84	11.08	7.02	11.21	0.25	
	5	430.90	1.59	0.97	12.1	9.53	7.01	2.57	10.52	7.01	11.42	0.27	
	1	182.50	1.83	0.00	12.35	5.39	4.92	6.96	9.37	4.92	4.84	0.32	
	2	212.50	2.13	0.00	11.41	7.20	6.92	4.21	13.57	6.92	5.63	0.41	
	3	316.00	3.16	0.26	7.60	5.60	5.54	2.00	10.75	5.54	8.37	0.33	
	4	403.00	4.03	1.13	10.79	7.55	7.34	3.24	13.34	7.34	10.68	0.33	
	5	541.00	5.41	2.51	15.94	12.09	10.53	3.85	16.99	10.53	14.34	0.29	
	6	544.00	5.44	2.54	13.28	9.46	9.08	3.82	15.25	9.08	14.42	0.32	NE20°
	7	572.10	5.72	2.82	16.38	10.05	9.97	6.33	17.04	9.97	15.16	0.33	NE30°
	8	595.10	5.95	3.05	15.06	11.61	10.62	3.45	17.20	10.62	15.77	0.30	
Xidatan ZK01	1	44.00	0.44	0.03	5.92	4.25	2.20	1.67	2.32	2.20	1.17	0.34	NE21°
	2	64.00	0.64	0.23	7.66	4.03	2.30	3.63	2.64	2.30	1.70	0.24	
	3	84.00	0.84	0.44	8.92	6.40	3.50	2.52	3.66	3.50	2.23	0.29	NE29°
	4	126.00	1.26	0.86	7.40	7.03	5.20	0.37	7.71	5.20	3.34	0.47	
	5	152.00	1.52	1.12	10.29	8.10	5.70	2.19	7.88	5.70	4.03	0.40	NE43°
	6	168.00	1.68	1.27	9.36	8.66	7.00	0.70	11.07	7.00	4.45	0.51	NE34°
	7	176.00	1.76	1.36	8.70	7.40	6.50	1.30	10.74	6.50	4.66	0.48	NE42°

Note: P_b—in situ rock fracture pressure; P_r—fracture surface retention pressure; P_s—instantaneous fracture surface closure pressure; P_H—hydrostatic pressure; P_0—pore pressure; T—rock tensile strength; σ_H—maximum horizontal principal stress; σ_h—minimum horizontal principal stress; σ_v—vertical principal stress, calculated from the burial depth of the overlying rock (bulk density of 26.5 kN/m^3), μ_m—the ratio of the maximum shear stress to the average stress.

4.2. Characteristics and Magnitude of the In Situ Stress

The distance between the five in situ stress measurement boreholes at the three locations ranges from a minimum of 20 km to a maximum of 50 km, all situated north of the East Kunlun Mountain active fault zone. Consequently, a comprehensive analysis is

conducted on the in situ stress data from these five boreholes when assessing the in situ stress state of the region. By examining the degree distribution diagram of in situ stress with depth in this area, it is observed that both maximum and minimum horizontal principal stresses exhibit a linear trend that increases with depth. The strong linear relationship indicates stability in regional stress field characteristics and consistency in distribution patterns. Through linear regression analysis of the collected data, we derive a regression curve representing in situ stress variation with depth. The regression equations obtained here between horizontal stress and depth (m) are essentially the same as the results for mainland China [27], expressed as follows:

$$\sigma_H = 0.0222 \times H + 4.05 \; R^2 = 0.7410, \tag{6}$$

$$\sigma_h = 0.0127 \times H + 2.84 \; R^2 = 0.7836, \tag{7}$$

As illustrated in Figure 3, the state of in situ stress varies with increasing depth. In the interval from the surface to 206.00 m, the in situ stress condition is characterized by $\sigma_H > \sigma_h > \sigma_v$, indicative of a reverse faulting regime. Below a depth of 206 m, however, the in situ stress state transitions to $\sigma_H > \sigma_v > \sigma_h$, which corresponds to a strike–slip faulting regime.

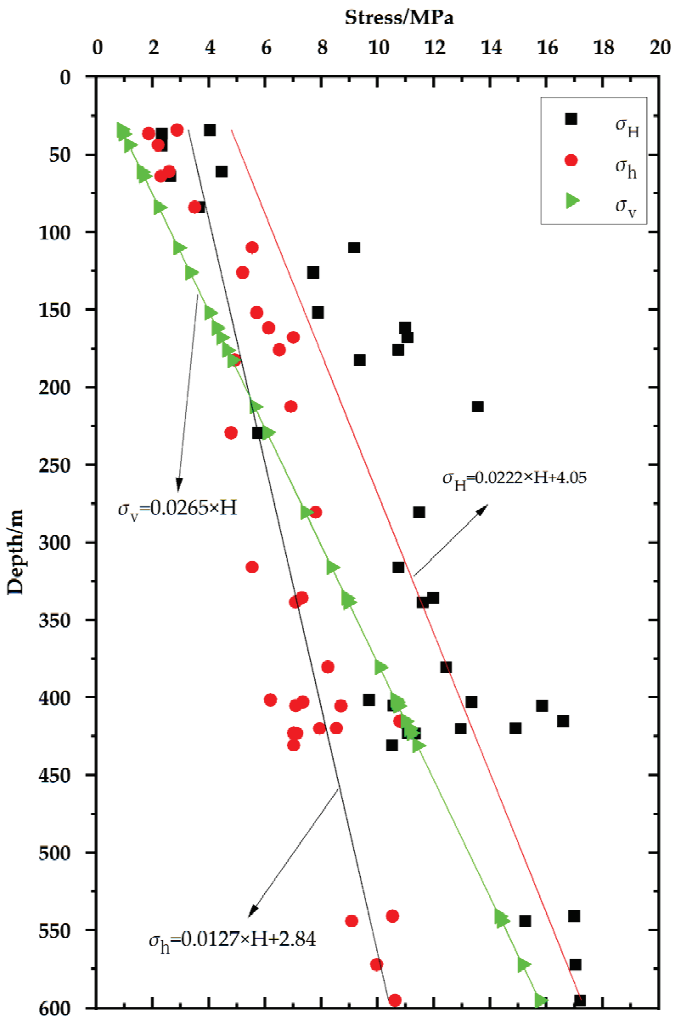

Figure 3. Measured stress value vs. depth at the Kunlun Mountain pass.

4.3. Characteristics of In Situ Stress Direction

The interactions among the Indian Ocean Plate, the Pacific Plate, the Philippine Sea Plate, and the Eurasian Plate, along with the regional blocks within the continental plate, govern the crustal stress field and tectonic movement patterns of the lithosphere in and around the Chinese mainland [28–31]. A key characteristic of the contemporary tectonic stress field of the Tibetan Plateau in China is NNE compression, which aligns with the subduction direction of the adjacent plates, primarily influenced by the subduction and extrusion of the Indian Plate towards Eurasia [32].

Before and after the earthquake, the direction of in situ stress changes, gradually adjusting to align with the pre-earthquake in situ stress orientation. Previous studies indicate that the average direction of maximum principal stress in this region was NE51.5° prior to the earthquake, shifting to 30.5° post event [3,33]. Figure 4 illustrates the directional characteristics of maximum horizontal principal stress in this area, derived from in situ stress tests conducted using hydraulic fracturing methods across five boreholes. The results predominantly fall within the range of NE20°–NE54°, with an average value of NE33°. When compared to earlier research findings, it is evident that the current direction of maximum horizontal principal stress closely resembles that observed after the earthquake. This suggests that while there is ongoing recovery within the current stress field, it has not yet returned to its pre-earthquake levels.

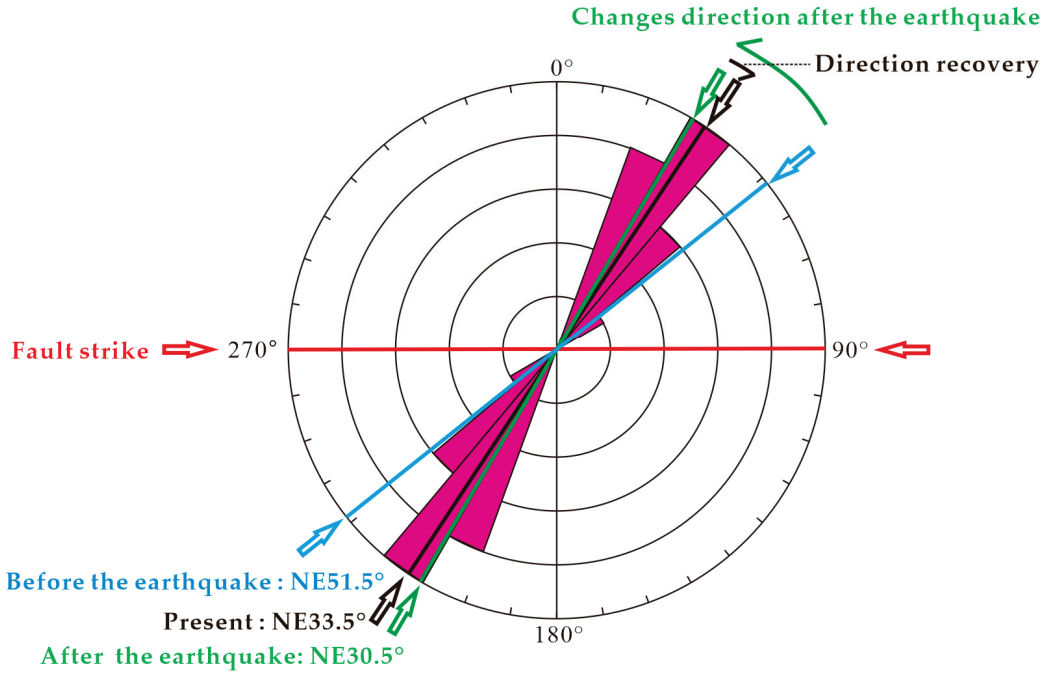

Figure 4. Rose diagram showing the orientations of maximum horizontal principal stress.

4.4. Analysis of In Situ Stress Accumulation Levels and Seismic Risk

Based on actual measurements and linear regression analysis, it has been determined that, in the study area, $\sigma_H > \sigma_h > \sigma_v$ within a depth range from the surface to 206 m corresponds to a reverse fault in situ stress state; conversely, below 206 m, $\sigma_H > \sigma_v > \sigma_h$ characterizes a strike–slip fault in situ stress state. Therefore, Equation (3) is employed in this study to analyze fault stability. For reverse faults, when the ground stress state is at depths greater than 206 m, $\sigma_1 = \sigma_H$ and $\sigma_3 = \sigma_v$; for depths less than 206 m, the ground stress state corresponds to that of a strike–slip fault, with $\sigma_1 = \sigma_H$ and $\sigma_3 = \sigma_h$. The values of σ_3 at various depths were utilized to compute σ_1 at friction coefficients of $\mu = 0.6$

and μ = 1.0. Figure 5 presents the analysis results of the ground stress states in the study area. From Figure 5, it is evident that the maximum horizontal principal stress in several test sections exceeds the lower threshold of the fault slip critical value, whereas the remaining sections remain below this threshold. Therefore, the likelihood of fault slip in this region is minimal. The better linearity and lower μ_m values at the Xidatan may be related to the closer proximity to the fault and more complete stress release after the earthquake.

μ_m represents the ratio of the maximum shear stress to the average stress. As illustrated in Table 1, measurements taken at various points within this region reveal that μ_m ranges from 0.16 to 0.63. With only a few measuring sections exhibiting μ_m values greater than 0.5, most sections show values near 0.3, resulting in an average μ_m value of approximately 0.33. Japanese scholar Tanaka [34] discovered that the parameter μ_m can be utilized to assess the influence of original in situ stress on fault slip. It was observed that μ_m in a given area tends to decrease before and after an earthquake. The value of μ_m represents the level of stress accumulation, which is independent of the direction of stress. A larger μ_m indicates a higher level of stress accumulation, thereby increasing the likelihood of fault slip, and conversely for smaller values. Specifically, when μ_m falls within the range of 0.5–0.7, it suggests that crustal stress is approaching its limit state; a value close to 0.5 signifies high levels of stress accumulation, while values below 0.3 indicate low levels of stress accumulation [33,34]. We believe that the level of stress accumulation in this area is relatively low and consequently suggests a diminished possibility of fault slip.

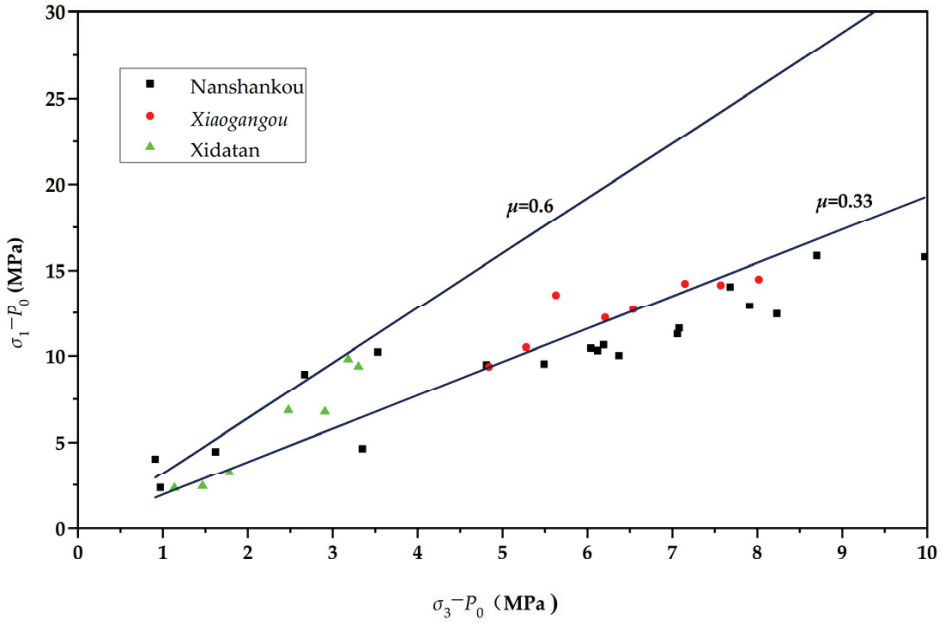

Figure 5. Measured stress value and fault activity analyses at the Kunlun Mountain pass.

5. Conclusions

The in situ stress state of five boreholes near Kunlun Pass was determined using the hydraulic fracturing method for in situ stress measurement. A comprehensive analysis and study were conducted on the level of in situ stress accumulation and seismic hazard in this area. The conclusions are as follows:

1. The minimum and maximum horizontal principal stress measured at the Nanshankou using the hydraulic fracturing method are 1.86–10.79 MPa and 2.33–16.60 MPa, respectively, within a depth range of 34.20 to 430.90 m. In another assessment, the minimum and maximum horizontal principal stress recorded are 4.92–10.62 MPa and

9.37–17.20 MPa, respectively, across a depth range of 182.50 to 595.10 m. Additionally, at the Xidatan test point, the minimum and maximum horizontal principal stresses observed are 2.30–7.00 MPa and 2.32–11.07 MPa, respectively, in a depth range of 44.00 to 176.00 m. The maximum horizontal principal stress and minimum horizontal principal stress observed in the five boreholes exhibit a linear trend of increase with depth, demonstrating a strong linear relationship. In the depth range from the surface to 206 m, the principal stress configuration is characterized by $\sigma_H > \sigma_h > \sigma_v$, indicating a reverse fault in situ stress state. Below 206 m, however, the principal stress arrangement shifts to $\sigma_H > \sigma_v > \sigma_h$, which corresponds to a strike–slip fault in situ stress state;

2. The results of in situ stress measurements indicate that the direction of the maximum principal stress is N20°E–NE54°, with an average orientation of NE33°. This finding aligns with the direction of the regional stress field observed in the area post earthquake, suggesting that the stress field is still undergoing recovery and has not yet returned to pre-earthquake levels. By applying the Coulomb fracture criterion, Byerlee's law, and the fault friction parameter μ_m, it has been determined that the level of ground stress accumulation in the study area is relatively low. Consequently, from an in situ stress perspective, the author posits that there is minimal likelihood of an earthquake occurring in this region.
3. The process of earth stress recovery is the process of earthquake reproduction. In order to understand the relationship between geostress recovery process and earthquake recurrence and the Gusaihu fault and Xidatan fault in the East Kunlun fault zone, it is necessary to strengthen the research of geostress measurement and continuous geostress monitoring in this area.

Author Contributions: Conceptualization, J.Q. and L.T.; methodology, J.X.; formal analysis, L.L.; investigation, L.W.; data curation, L.W.; writing—original draft preparation, J.Q.; writing—review and editing, J.Q.; project administration, L.T.; funding acquisition, J.Q. All authors have read and agreed to the published version of the manuscript.

Funding: This research was funded by the Spark Program of Earthquake Sciences, grant number XH23057YC, and Science and Technology Innovation Director Fund, grant number FMC2024006.

Institutional Review Board Statement: Not applicable.

Informed Consent Statement: Not applicable.

Data Availability Statement: The original contributions presented in this study are included in the article. Further inquiries can be directed to the corresponding author.

Acknowledgments: The authors thank the Institute of Geomechanics, Chinese Academy of Geological Sciences, for assisting with this research.

Conflicts of Interest: The authors declare no conflicts of interest.

References

1. Li, S.G. *The Earthquake*; Geological Publishing House: Beijing, China, 1977.
2. Chen, Q.C.; An, Q.M.; Sun, D.S.; Du, J.J.; Mao, J.Z.; Feng, C.J. Current in-situ stress state of Shanxi Basin and analysis of earthquake risk. *Acta Geol. Sin.* **2010**, *31*, 541–548.
3. Liao, C.T.; Zhang, C.S.; Wu, M.L.; Ma, Y.S.; Ou, M.Y. Stress change near the Kunlun fault before and after the Ms 8.1 Kunlun earthquake. *Geophys. Res. Lett.* **2003**, *30*, 2027. [CrossRef]
4. Wu, M.L.; Zhang, C.Y.; Fan, T.Y. Stress state of the Baoxing segment of the southwestern Longmenshan Fault Zone before and after the Ms 7.0 Lushan earthquake. *J. Asian Earth Sci.* **2016**, *121*, 9–19. [CrossRef]

5. Zhang, C.Y.; Fan, D.J.; Elsworth, D.; He, M.C.; Zhao, X.G.; Zhu, C.; Zhang, Z. Mechanisms of stress- and fluid-pressure-driven fault reactivation in Gonghe granite: Implications for injection-induced earthquakes. *Int. J. Rock Mech. Min. Sci.* **2024**, *174*, 105642. [CrossRef]
6. Qiu, J.; Wu, M.L.; Fan, T.Y.; Zhang, C.Y.; Li, R.; Chen, L.Z. Analysis of in situ stress state in southwestern segment of Longmenshan Fault Zone before and after Lushan earthquake. *Acta Geol. Sin.* **2017**, *91*, 969–978.
7. Qiu, J.; Wu, M.L.; Fan, T.Y.; Zhang, C.Y.; Wang, L.S. Study on the characteristics of in situ stress accumulation and seismic hazard at the junction of Jiangsu and Shandong provinces of the Tanlu fault zone. *Acta Geol. Sin.* **2019**, *93*, 3249–3258.
8. Song, C.; Chen, B. Heterogeneity effect of elastic properties on piezomagnetic fields associated with dislocation source. *Izv. Phys. Solid Earth* **2024**, *60*, 325–332. [CrossRef]
9. Van Der Woerd, J.; Tapponnier, P.; Ryerson, F.J.; Meriaux, A.-S.; Meyer, B.; Gaudemer, Y.; Finkel, R.C.; Caffee, M.W.; Guoguang, Z.; Zhiqin, X. Uniform Postglacial Slip-Rate Along the Central 600 km of the Kunlun Fault (Tibet), from 26A, 10Be, And 14C Dating of Riser Offsets, and Climatic Origin of the Regional Morphology. *Geophys. J. Int.* **2002**, *148*, 356–388. [CrossRef]
10. Chen, J.; Chen, Y.K.; Ding, G.Y.; Tian, Q.J.; Wang, Z.J.; Shan, X.J.; Ren, J.W.; Zhao, R.B.; Wang, Z.C. The surface rupture zone of the 2001 Kunlun M8.1 earthquake. *Quat. Res.* **2003**, *59*, 255–265.
11. Xu, X.W.; Chen, W.B.; Yu, G.H.; Ma, W.T.; Chen, G.H.; Guo, T.C. Characteristic features of the Hoh Sai Hu (Kunlunshan) earthquake (MS8.1), northern Tibetan Plateau, China. *Seismol. Geol.* **2002**, *24*, 1–13.
12. Xu, X.W.; Yu, G.H.; Klinger, Y.; Tapponnier, P.; Van der Woerd, J. Reevaluation of surface rupture parameters and faulting segmentation of the 2001 Kunlunshan earthquake (MW7.8), northern Tibetan Plateau, China. *J. Geophys. Res. Solid Earth* **2006**, *111*, B05316. [CrossRef]
13. Xu, X.W.; Yu, G.H.; Ma, W.T.; Chen, G.H.; Guo, T.C. Rupture behavior and deformation localization of the Kunlunshan earthquake (MW7.8) and their tectonic implications. *Sci. China Earth Sci.* **2008**, *51*, 1361–1374. [CrossRef]
14. Feng, J.Z.; Liao, L.; Li, P.E.; Wu, Q.J. Numerical simulation of spontaneous rupture process of the 2001 MS8.1 west of Kunlun pass earthquake. *Chin. J. Geophys.* **2024**, *67*, 2141–2158.
15. Hu, D.G.; Ye, P.S.; Wu, F.; Zhang, Y.L.; Wu, Z.H.; Liu, Q.S.; Wu, Z.H. Late Quaternary Paleoseismic History on the Xidatan Segment of the East Kunlun Fault Zone in Northern Tibet. *Quat. Sci.* **2008**, *28*, 214–223.
16. Van der Woerd, J.; Ryerson, F.J.; Tapponnier, P.; Gaudemer, Y.; Finkel, R.; Meriaux, A.S.; Caffee, M.W.; Zhao, G.G.; He, Q. Holocene left-slip rate determined by cosmogenic surface dating on the Xidatan segment of the Kunlun Fault (Qinghai, China). *Geology* **1998**, *26*, 695–698. [CrossRef]
17. Van der Woerd, J.; Ryerson, F.J.; Tapponnier, P.; Meriaux, A.S.; Gaudemer, Y.; Meyer, B.; Finkel, R.C.; Caffee, M.W.; Guo, G.Z.; Xu, Z.Q. Uniform slip-rate along the Kunlun Fault: Implications for seismic behaviour and large-scale tectonics. *Geophys. Res. Lett.* **2000**, *27*, 2353–2356. [CrossRef]
18. Wu, Z.H. *Atlas of Active Faults and Geological Hazards Along the Qinghai-Tibet Railway*; Earthquake Press: Beijing, China, 2005.
19. Haimson, B.C.; Cornet, F.H. ISRM Suggested Methods for rock stress estimation—Part 3: Hydraulic fracturing (HF) and/or hydraulic testing of pre-existing fractures (HTPF). *Int. J. Rock Mech. Min. Sci.* **2003**, *40*, 1011–1020. [CrossRef]
20. Bredehoeft, J.D.; Wolff, R.G.; Keys, W.S.; Shuter, E. Hydraulic fracturing to determine the regional in situ stress field, Piceance Basin, Colorado. *Geol. Soc. Am. Bull.* **1976**, *87*, 250–258. [CrossRef]
21. Haimson, B.C. The hydrofracturing stress measuring method and recent field results. *Int. J. Rock Mech. Min. Sci. Geomech. Abstr.* **1978**, *15*, 167–178. [CrossRef]
22. Zoback, M.; Roller, J.; Healy, J. In-situ measurement of the Earth's stress field. *Science* **1978**, *199*, 1232–1237.
23. Zhang, C.Y.; Chen, Q.C.; Qin, X.H.; Hong, B.; Meng, W.; Zhang, Q.F. In-situ stress and fracture characterization of a candidate repository for spent nuclear fuel in Gansu, northwestern China. *Eng. Geol.* **2017**, *231*, 218–229. [CrossRef]
24. Savvides, A.A.; Antoniou, A.A.; Papadopoulos, L.; Monia, A.; Kofina, K. An estimation of clayey-oriented rock mass material properties, sited in Koropi, Athens, Greece, through feed-forward neural networks. *Geotechnics* **2023**, *3*, 975–988. [CrossRef]
25. Liang, G.; Huang, L.; Cao, C. Analysis and prediction of grouting reinforcement performance of broken rock considering joint morphology characteristics. *Mathematics* **2025**, *13*, 264. [CrossRef]
26. Wu, Z.H. *Research on Active Faults and Comprehensive Monitoring of Stress and Strain Along Qinghai-Tibet Railway*; Earthquake Press: Beijing, China, 2009; pp. 188–192.
27. Meng, W.; Chen, Q.C.; Zhao, Z.; Wu, M.L.; Qin, X.H.; Zhang, C.Y. Characteristics and implications of the stress state in the Longmen Shan fault zone, eastern margin of the Tibetan Plateau. *Tectonophysics* **2015**, *656*, 1–19. [CrossRef]
28. Shao, Z.G.; Fu, R.S.; Xue, T.X.; Huang, J.H. Numerical simulation and genetic mechanism of deformation field after Kunlun Ms8.1 earthquake. *Chin. J. Geophys.* **2008**, *51*, 805–816.
29. Li, J.N.; Wei, Y.M.; Chen, Y.; Gao, J.F. Seismic fracture feature extraction from high-resolution optical remote sensing images: A case study of the earthquake in the west Kunlun Mountain Pass. *J. Univ. Chin. Acad. Sci.* **2023**, *40*, 388–396.

30. Feng, Y.S.; Xiong, X.; Shan, B.; Liu, C.L. Coulomb stress loading and seismic activity changes in the surrounding area caused by the 2021 Madol MS7.4 earthquake. *Sci. China Earth Sci.* **2022**, *52*, 1100–1112.
31. Xie, F.R.; Cui, X.F.; Zhao, J.T.; Zhang, H.Y.; Li, H. Regional division of the recent tectonic stress field in China and adjacent areas. *Chin. J. Geophys.* **2004**, *47*, 654–662.
32. Nishiwaki, T.; Lin, A.; Lin, W. Recovery of stress during the interseismic period around the seismogenic fault of the 1995 Mw 6.9 Kobe earthquake, Japan. *Geophys. Res. Lett.* **2018**, *45*, 12814–12820. [CrossRef]
33. Tanaka, Y.; Fujimori, K.; Otsuka, S. In-situ stress measurement and prediction of great earthquake. *Earthq. Res.* **1988**, *50*, 201–208.
34. Wang, C.H.; Song, C.K.; Guo, Q.L.; Zhang, Y.S.; Ding, J.M. Stress build-up in the shallow crust before the Lushan Earthquake based on the in-situ stress measurements. *Chin. J. Geophys.* **2014**, *57*, 102–114.

applied sciences

MDPI

Article

Application of Pipe Slit Anchor Mesh Spraying Supporting Technology Based on Loose Circle Supporting Theory in Makeng Iron Ore Mine

Lixin Zhang, Zehui Deng * and Gang Li

College of Mining, Liaoning Technical University, Fuxin 123000, China; zhanglixin@lntu.edu.cn (L.Z.); ligang@lntu.edu.cn (G.L.)
* Correspondence: dengzehui08@sina.com

Abstract: In order to solve the problems of stress concentration in the roadway peripheral rock and poor support effect in a wide range of high-stress areas under the high-stress environment of MaKeng Iron Mine, this study is based on the theory of loose circle support, combined with the calculation of the anchor suspension theory to determine the reasonable length of pipe slit anchors and other key parameters. Through the two methods of punching and bonding, we examined the destructive effect to determine the thickness of the spray concrete and, finally, put forward the pipe slit anchor mesh spraying support technology program. The numerical model was constructed by using three-dimensional numerical simulation software (FLAC3D 5.0), and the support effect analysis of the support scheme was carried out systematically. The research results show the following: under the high-stress environment dominated by external horizontal tectonic stress, the use of pipe slit anchor net spray support technology can significantly improve the distribution characteristics of the plastic zone, stress field and displacement around the roadway; after the support, the deformation and displacement of the surrounding rock around the empty zone are significantly reduced, effectively preventing the destruction of the surrounding rock under the high-stress environment. The program not only unifies the mine support form and support parameters but also specifies the support construction method and construction quality inspection standard, which provides a scientific technical guarantee for mine shaft support and has an important reference value for the support design and construction of a mine roadway under a similar high-stress environment.

Keywords: roadway support; damage and deformation characteristics; numerical simulation; pipe slit anchor mesh spraying

1. Introduction

In the process of deep mining development, the deformation control of the roadway surrounding rock is a major technical difficulty. Particularly with the increase in mining depth, various obvious large deformation phenomena occur in the roadway peripheral rock under high levels of stress, and the roadway produces serious bottom plate bulging under high levels of stress, which affects the normal use of the roadway. Under high overburden and tectonic stresses, the roadway may collapse or undergo excessive deformation, which not only endangers mining personnel but also reduces the function of the roadway and stops production. Therefore, ensuring the stability of the roadway perimeter rock and

the safety and reliability of the support structure during deep excavation is extremely important for the safe and efficient mining of underground resources [1–8].

Deep mining is in a high-stress state, so the surrounding rock is more likely to reach the limit state, which leads to deformation and damage. In terms of surrounding rock control, scholars have proposed various theories and techniques, ranging from the new Austrian tunneling method [9] to the collapse arch [10,11]. Scholars have proposed the idea of surrounding rock management from the perspective of improving the bearing capacity of surrounding rock and combining it with support. With the development of energy theory [12], the interaction between surrounding rock and support was studied from the perspective of energy regulation. Aydan, Ö et al. [13,14] proposed the joint support theory according to the engineering practice. Kang et al. [15] proposed a resin full-length prestressed anchorage joint support technology. Jia et al. [16] considered that high geostress is an important factor leading to the deformation of deep surrounding rock, analyzed the damage mechanism of soft rock, and proposed a support method applicable to soft rock.

However, most of the existing studies on perimeter rock support are aimed at shallow roads. Influenced by traditional concepts, deep roadway support always adopts the engineering analogy method and empirical method, which leads to the uncertainty of rationality and excessive or insufficient support intensity of the surrounding rock control methods and technical parameters. The disadvantage of the former is that it wastes the support material and increases the support cost, while the latter brings great hidden danger to safety production.

Based on the above, in view of the mining characteristics of the middle zone of Makeng Iron Ore Mine, the distribution law of geostress, the deformation and damage characteristics of the deep roadway, and the peripheral rock support characteristics of the roadway, this study determines the reasonable support process and support design parameters through on-site measurements, theoretical analyses, numerical simulations, and on-site industrial tests and develops the support effect checking inspection standards to meet the specification requirements, so as to form a set of mine-based actual support control methods of the crushed rock body. This study is a reference for the support technology of this kind of broken rock body.

2. Project Overview

Makeng Iron Ore Mine, located 15 km south of Longyan City, Fujian Province, employs a large-diameter deep-hole staged stoping with backfill method. A longitudinal fault runs through the center of the mine, and under the influence of geostress and groundwater, fissures in the surrounding rock transition from a closed to an open state, compromising roadway stability and posing risks to key infrastructure.

The mining of Makeng Iron Mine is carried out by the method of open stope and subsequent filling. The mining activity of the ore body induces the mechanical response mechanism of disturbance and failure in the surrounding rock. With the development of mining, the surrounding rock of the roadway is dynamically driven by the mining stress field (including the initial stress release and secondary stress concentration effect) and presents significant asymmetric deformation characteristics: progressive settlement occurs in the roof, and continuous uplift occurs on the floor. The historical monitoring results show that the deformation of the roof and floor increases nonlinearly with the increase in mining disturbance, and the deformation region shows the expansion behavior of spatio-temporal correlation. The cumulative damage effect of surrounding rock leads to the gradual expansion of the plastic zone, which ultimately poses a direct threat to the stability of the roadway structure and the safety of underground production.

Based on the results of the current stress tests at each section, the component values in the north–south, east–west, vertical and other directions were calculated. The test results of each measuring point are shown in Tables 1 and 2. According to the test results at this time, the maximum principal stress in the mining production area below 90 m and at a level of 18 m reached above 30 MPa, and the horizontal component stress also showed relatively high stress. This indicates that the stress value of the deep part of the ground stress was relatively high. With the expansion of mining, there is a possibility of stress concentration and the emergence of large-scale high-stress areas, which require special attention and high-level concern. The maximum principal stress at the 18 m section measuring point reached 31.33 MPa, with a direction of 224.9° and an inclination angle of 7.0°, which was nearly horizontal. A phenomenon of increased lateral pressure due to the influence of horizontal stress was clearly observed. With the increase in depth, the increase in horizontal stress became more obvious, which is in line with the characteristics of ground stress in a mountainous terrain environment. Figure 1 indicates that as the mining progresses, the stress concentration and the high-stress zones keep expanding. Therefore, active ground pressure management, timely void zone treatment and reinforcement measures need to be adopted to prevent rock failure and ensure the safety of operations. Existing support systems mainly rely on ϕ43 mm hollow grouted rock bolts, supplemented with 100 mm sprayed concrete in weak sections. However, the absence of standardized support selection and evaluation methods results in inconsistent designs and suboptimal performance. Without clear construction quality standards, timely acceptance and assessment of support measures remain challenging, affecting overall site stability.

Table 1. Raw rock stress test results.

Observation Point	Mining Depth (m)	Maximum Principal Stress σ1			Intermediate Principal Stress σ2			Minimum Principal Stress σ3		
		Numerical Value (MPa)	Orientations (°)	Tilt (°)	Numerical Value (MPa)	Orientations (°)	Tilt (°)	Numerical Value (MPa)	Orientations (°)	Tilt (°)
160 m level	510	17.46	211.5	30.8	16.53	−56.8	2.7	13.49	217.7	−59
115 m level	555	24.59	250.4	0.7	20.57	−19.2	18.7	15.27	158.2	71.2
90 m level	580	30.22	229.3	1.2	16.55	−29.2	83.8	14.00	139.1	6.0
18 m level	652	31.33	224.9	7.0	21.86	−41.2	27.8	18.04	121.9	61.1

Table 2. Calculation results of stress components.

Observation Point	Mining Depth (m)	Test Site	Stress Component (MPa)		
			σx	σy	σz
160 m level	510	74# Line Transportation Lane	16.41	16.52	14.54
115 m level	555	74# North Transportation Lane	20.06	20.55	15.82
90 m level	580	74# Line Transportation Lane	23.33	20.91	16.52
18 m level	652	75# Line North Transportation Lane	25.88	26.28	19.08

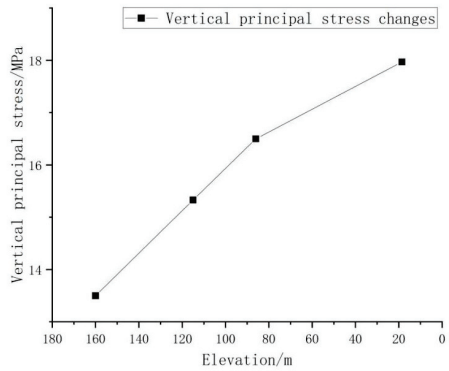

Figure 1. Vertical stress variation from 160 m to −18 m.

To improve safety and efficiency, the mine urgently needs systematic optimization of support technologies, including standardized selection criteria, process controls, and evaluation methods. Establishing a scientific approach to support design based on rock mass conditions will be key to enhancing shaft stability and long-term mining sustainability.

3. Loose Ring Measurement

3.1. Loose Ring Field Test

1. Drilling measurement hole: Drilling with φ90 or higher drilling rig. Each measuring point is drilled according to the designed drilling position, the drilling azimuth is 5–10° down the tying angle, the drilling depth is at least 5 m, and the hole depth is measured with a ruler.
2. Hole cleaning and water filling: Clean the drilling slag in the drilling hole, send the test probe into the bottom of the hole through the extendable tube of the self-made probe, and then send the water filling pipe into the drilling hole to fill the water.
3. Test process: Measure the distance between receivers, input data such as project number, hole depth and distance between receivers into the test equipment. After the hole is filled with water, keep the hole full of water, and then slowly and evenly pull the test line to pull out the probe. As the probe is pulled out, readings are taken every 20 cm until the transducer is completely detached from the borehole, as shown in the top view. With the different position of the drill, that is, the different depth from the two sides of the roadway, the reading on the tester changes due to the different degrees of fragmentation of the rock mass. After the measurement, the computer data analysis system is used to take the best and representative readings as the final analysis data of the measurement results.

The testing process is shown in Figure 2.

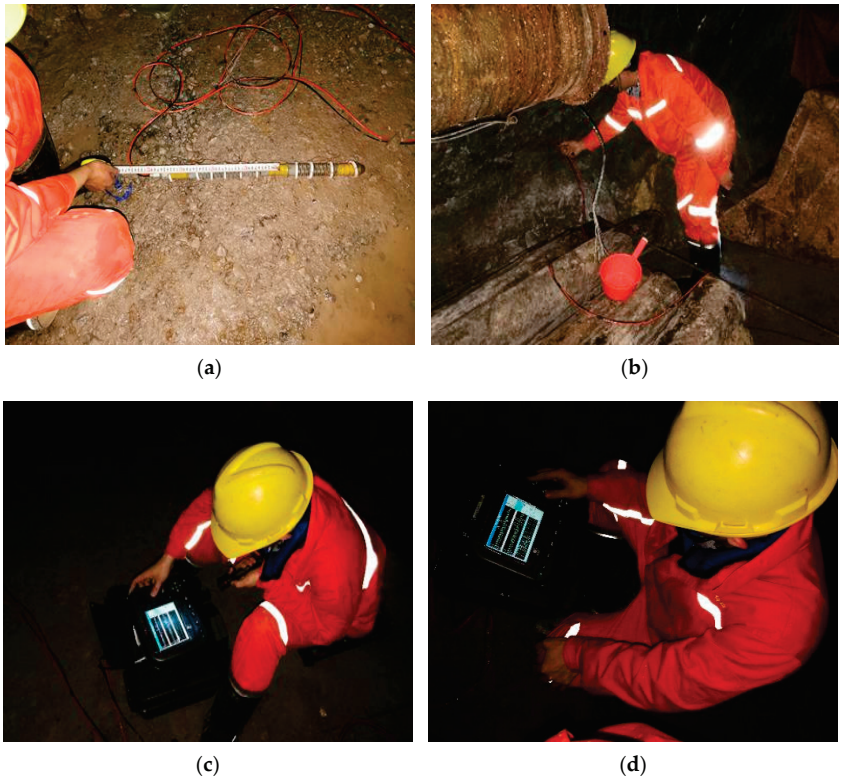

Figure 2. Field work drawing. (**a**) Measure the distance between receiving points, (**b**) pull out 20 cm each time during measurement, (**c**) acquisition head wave, (**d**) data reading and storage.

3.2. Sonic Method for Testing Loose Rings

Due to rock fragmentation within the loosening ring, ultrasound propagates through the fractured rock at a lower velocity compared to intact rock. The extent of the loosening circle can be determined by identifying the inflection point on the velocity curve, where a sudden change in sound speed occurs. By screening, analyzing, and processing the data collected from the measurement points at the Makeng Iron Mine, a depth–sound velocity variation curve for the lithology at each measurement point was obtained, as shown in Table 3 and Figure 3.

Table 3. Locations of test holes and measured sound velocities for each ore body at Makeng Iron Ore Mine.

Hole Number	Position	Rockiness	Depth of Hole (m)	Effective Hole Distance (m)	Average Speed of Sound (m/s)	Rock Average Sound Velocity (m/s)	Note
1	85 level 24# transverse drift	ore body	10	0.8~4	3254	3624	vertical hole
2	115 level 28# transverse drift	ore body	7	0.8~4	3977		\
3	145 level 28# transverse drift	ore body	6	0.8~4	3645		\

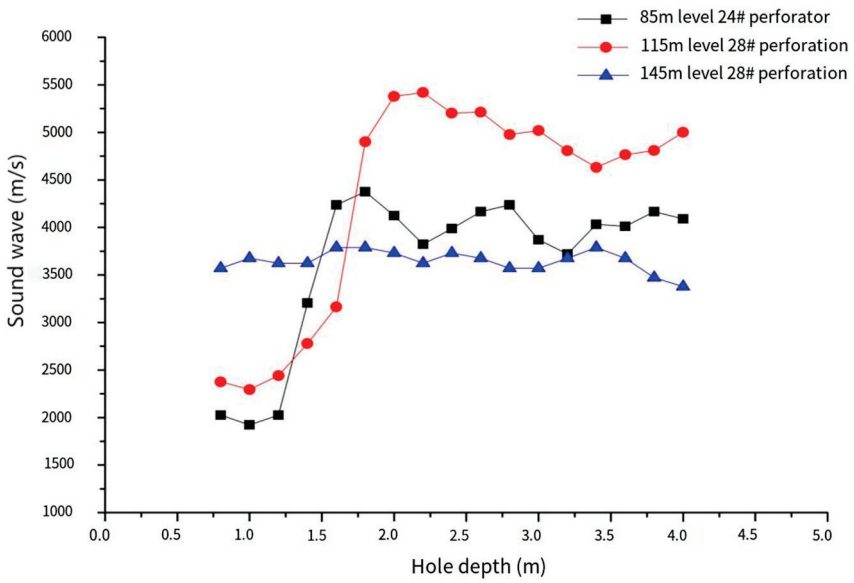

Figure 3. Curve of hole depth versus sound velocity in the ore body.

In the 85 m, 115 m, and 145 m subsections, the relationship between ore body hole depth and acoustic wave velocity was analyzed. As shown in Figure 3, the measurement section at the 85 m level ranges from 0.8 m to 4.0 m. Within the 1.5 m to 4.0 m range, the rock wave velocity remains relatively stable between 3800 m/s and 4300 m/s, indicating that this section of the ore body is relatively intact. It has not been significantly affected by the stress changes induced by roadway excavation.

However, between 1.2 m and 1.8 m, the wave velocity shows a noticeable decline. Specifically, within the 0.8 m to 1.4 m range, the average wave velocity is approximately 2112 m/s, which is significantly lower than the intact rock. This suggests that the rock mass in this section contains more fissures and is more fragmented due to the influence of

roadway excavation. Based on this analysis, the loosening circle radius for the 85 m section is determined to be 1.2 m.

Similarly, in the 115 m subsection, as shown in Figure 3, the acoustic wave test data exhibit the same trend as the 85 m section. Based on these results, the loosening circle radius for the 115 m level is determined to be 1.4 m.

For the 145 m level, the measured wave velocity remains relatively stable within the 0.8 m to 4.0 m range. However, an overall decreasing trend in wave velocity suggests that, while the rock mass in this section remains largely intact, it is still influenced by excavation activities near the roadway. Consequently, the loosening circle radius in this section is relatively small.

The sonic test results across different roadway sections within the ore body rock layers exhibit a consistent distribution pattern, with multiple factors influencing the extent of the rock loosening circle. Based on sonic testing and data analysis, it is concluded that the loosening circle size in the 85 m section is approximately 1.2 m, while in the 115 m section, it is around 1.4 m. In the 145 m section, the ore body exhibits better integrity, with only a small loosening circle present. These findings provide valuable insights into roadway stability and serve as a basis for optimizing support measures.

4. Determination of Parameters for Slit Pipe Anchor Net Spray Support

In the combined support system of anchor, mesh, and sprayed concrete, the addition of a metal mesh enhances the crack resistance of the sprayed concrete layer while improving its overall flexural, tensile, and shear strength. This reinforcement helps to effectively seal the surrounding rock, preventing weathering and protecting anchor rods from water erosion. Additionally, it optimizes the joint support function of the anchor rods and metal mesh, ensuring a more stable roadway structure. The sprayed concrete also acts as an isolating layer, further safeguarding the anchor rods and metal mesh from environmental factors. For economic efficiency, a metal mesh size of 2000 mm $\times$ 1000 mm with a 100 mm $\times$ 100 mm mesh hole is selected.

The drill bit specification used for excavation in the Makeng Iron Mine is φ38 mm, with the actual construction hole diameter ranging between 38 mm and 40 mm. For analysis, the 115 m level, section 28# through the vein, is chosen as the application site. Based on the loosening circle calculation, the loosening circle radius at the 115 m level for section 28# is 1.4 m. The roadway specifications are 3.9 m in width and 3.6 m in height.

According to the suspension theory, after the excavation of the roadway, the original in situ stress in the surrounding rock redistributes, changing from the original three-dimensional stress to two-dimensional corresponding stress and creating a stress concentration area. In this area, the original joints, fissures, bedding, faults, and other discontinuities in the rock mass may further develop. Affected by this development, some rock loosening, sliding and fracture phenomena will occur. Further, new discontinuities may be generated, and caving may occur under the action of self-weight. The suspension function of the anchor bolt is to give sufficient restraint to the subregion at this time and anchor these loose and broken rocks in the hard and stable rock stratum inside the surrounding rock (Figure 4).

Using the anchor suspension theory and inputting these parameters into the calculation formula (Equation (1)), it is determined that the distance should not be less than 1.02 m. Based on the mesh specifications, the distance between anchor rods is set to 1 m $\times$ 1 m.

$$a < \sqrt{\frac{G}{kL_b\gamma}} \quad (1)$$

where: a—anchor bar spacing, row spacing, m;

G is the anchor design anchoring force, taken as 70 KN/root;

k is the safety factor, take 2;

L_b is the thickness of the unstable rock layer to be suspended, determined by the radius of the circle of loose surrounding rock, here taken as 1.4 m;

γ is the bulk weight of the rock, determined by the nature of the surrounding rock, here take 24 KN/m^3.

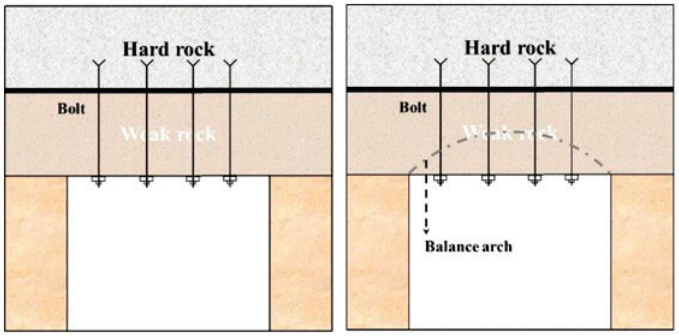

Figure 4. Schematic diagram of suspension theory.

The total length L of the anchor consists of three parts: the anchoring length L_a of the anchor deeper into the more stable rock layer, the thickness L_b of the unstable rock layer to be suspended and the thickness L_c of the upper pallet and anchorage, where the thickness L_c of the upper pallet and anchorage is taken as 0.15 m.

$$L = L_a + L_b + L_c \quad (2)$$

The anchorage length L_a for deeper penetration into the more stable rock layer is determined by Equation (3). The anchorage length is calculated to be 0.45 m, so the total length of the anchor L is 2 m.

$$L_a \geq K\frac{df_s}{4f_c} \quad (3)$$

where: K is a safety factor, generally taken as 2;

d is the diameter of the anchor, 0.02 m;

f_s is the tensile strength of the anchor, taken as 315 MPa;

f_c is the bonding strength of anchor and cement paste, taken as 7 MPa.

Spray layer damage is mainly dominated by cut layer damage and bonding damage. According to the previous report, the weight of the dangerous stone is 12,096 kg, and the length of the dangerous stone periphery is 3519 cm; therefore, substituting the relevant parameters into Equation (4), the thickness of the spray layer under the cut layer damage is not less than 14.32 mm.

$$H_c \geq k_c G/(S\delta) \quad (4)$$

where: H_c—thickness of spray layer, cm;

G—weight of dangerous stones, G = 12,096 kg;

S—dangerous rock perimeter long, S = 3519 cm;

δ—concrete shear strength, generally taken as δ = 6 kg/cm^2;

k_c—safety factor, k = 2.5.

Equation (5) shows that the thickness of the spray layer under the bonding damage should not be less than 34.37 mm.

$$H_b \geq 3.65 \times k_b \left[\frac{G}{S\delta_N}\right]^{\frac{4}{3}} \left[\frac{K}{E}\right]^{\frac{1}{3}} \approx \frac{k_b G}{S\delta_N} \quad (5)$$

where:

δ_N—bond strength of shotcrete, 3 kg/cm^2;

K—rock elasticity tensile coefficient, 1×10^4 kg/cm^2;

E—modulus of elasticity of rocks, E = 415,100 kg/cm^2

k_b—safety factor, k = 3.

The results demonstrate that, based on calculations considering both the punching and cutting destructive effects and the bonding effects, the minimum thickness of the sprayed concrete layer should not be less than 34.37 mm. Furthermore, a protective concrete layer with a thickness of at least 20 mm is required to ensure the integrity of the metal mesh and to provide a smoother roadway surface, thereby promoting a more uniform distribution of stress. To achieve consistency in the design of support parameters, a 100 mm thick concrete layer is adopted. This thickness aligns with the specifications used for plain sprayed concrete support in roadways characterized by more developed joints and fissures, as well as lower stability conditions. This approach ensures both structural reliability and compatibility with existing support practices.

5. Simulation Analysis of Support Effectiveness

5.1. Modelling

To assess the damage status of the roadway and determine an appropriate support scheme for the Makeng Iron Ore Mine, an engineering geological model was developed. This model considers key factors, such as roadway location, surrounding rock lithology, and fault distribution. The model dimensions are 36 m × 30 m × 34 m, comprising 144,600 units and 153,078 nodes. The relevant parameters required for numerical simulation are shown in Tables 4 and 5.

Table 4. Rock mechanical parameter.

Grouping Name	Soil Natural Density (g/cm^{-3})	Elasticity Modulus (GPa)	Poisson's Ratio	Cohesive Force (MPa)	Internal Friction Angle (°)
Marbled limestone	2.69	41.51	0.27	18.28	41.89
mine	3.82	47.70	0.27	27.65	47.88
Quartzized limestone	2.54	36.83	0.28	27.14	41.05

Table 5. Supporting mechanical parameters.

Parameter	Density (g/cm^{-3})	Elasticity Modulus (GPa)	Poisson's Ratio
lining concrete	2.50	28.00	0.27
Anchor bolt	7.80	210.00	0.30

Boundary conditions are defined as follows: the bottom boundary is subject to vertical constraints, the four side boundaries are constrained horizontally, and the upper boundary is a free surface. Stress boundary conditions are applied based on measured in situ stress data. The Mohr–Coulomb model is adopted as the yield criterion. The numerical simulation model is illustrated in Figure 5.

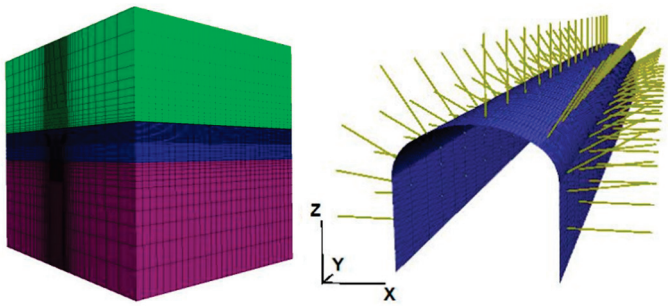

Figure 5. Numerical simulation model.

To ensure that the numerical calculations accurately reflect the actual engineering geological conditions of the Makeng Iron Ore Mine, the following assumptions are made in the modeling process:

1. The ore-bearing rock mass is considered an ideal elastic–plastic material. After reaching the yield point, neither the material strength nor volume changes with plastic flow, and strain hardening or softening effects are not taken into account.
2. Both the ore body and surrounding rock are assumed to be locally homogeneous and isotropic. The plastic flow does not alter the isotropic nature of the materials.
3. All physical parameters involved in the analysis are considered time-independent, reflecting the brittle nature of the rock.
4. Given the limitations of finite difference calculations, tectonic activity is disregarded. The in situ stress field is assumed to be geostatic, rock layers are in full contact with each other, and the interior of each rock layer is treated as a continuous medium. Groundwater effects are also excluded from the model.
5. The calculation considers only the effects of geostress, neglecting the impact of seismic waves, explosive shock waves, and groundwater on the stability of the rock mass.

5.2. Stress Analysis of the Roadway Perimeter Rock

Figure 6 illustrates the distribution characteristics of the maximum principal stress, minimum principal stress, and vertical stress (z-direction) in the surrounding rock under two working conditions: without support and with anchor net shotcrete support.

Under unsupported conditions, stress concentration is primarily observed in the shoulder area of the roadway and at the base of the sidewalls. The maximum principal stress reaches 16.90 MPa, concentrated at the roadway shoulders, indicating that this zone experiences high compressive stress due to excavation-induced disturbance and is, thus, prone to compressive shear failure. The minimum principal stress is concentrated near the floor, exhibiting tensile characteristics, which may lead to tensile failure of the rock mass. The maximum vertical stress is 10.25 MPa, and although its distribution is relatively uniform, localized concentration is still present at the junction between the roof and floor, potentially causing structural stress imbalance.

With the application of the anchor net shotcrete support, the stress distribution within the surrounding rock improves significantly. The maximum principal stress is reduced to 14.23 MPa, reflecting a 15.8% decrease, and the extent of the stress concentration zone is markedly reduced. This indicates that the support system effectively redistributes and alleviates the high compressive stress at the roadway shoulders, thus mitigating the risk of localized failure. Additionally, the range of tensile stress is significantly reduced, with the minimum principal stress increasing, suggesting that the support system suppresses tensile stress development, particularly at the wall bases. The maximum vertical stress decreases to

7.74 MPa, a reduction of approximately 24.5%, and its distribution becomes more uniform, which facilitates the maintenance of overall stress equilibrium in the surrounding rock mass.

From a mechanical perspective, the anchor rods link the shallow fractured rock with the deeper stable strata, thereby enhancing the structural integrity and overall load-bearing capacity of the surrounding rock. Meanwhile, the shotcrete layer and steel mesh rapidly seal surface cracks, restrict deformation and crack propagation, and inhibit the formation of new stress concentration zones. As a result, the stress within the surrounding rock is redistributed more uniformly, and localized high-stress regions are effectively weakened, significantly improving the stability and safety of the roadway.

In summary, the anchor net shotcrete support exhibits a notable capacity to relieve local stress concentrations and optimize the stress distribution in the surrounding rock, providing a critical safeguard for the long-term stable performance of the roadway structure.

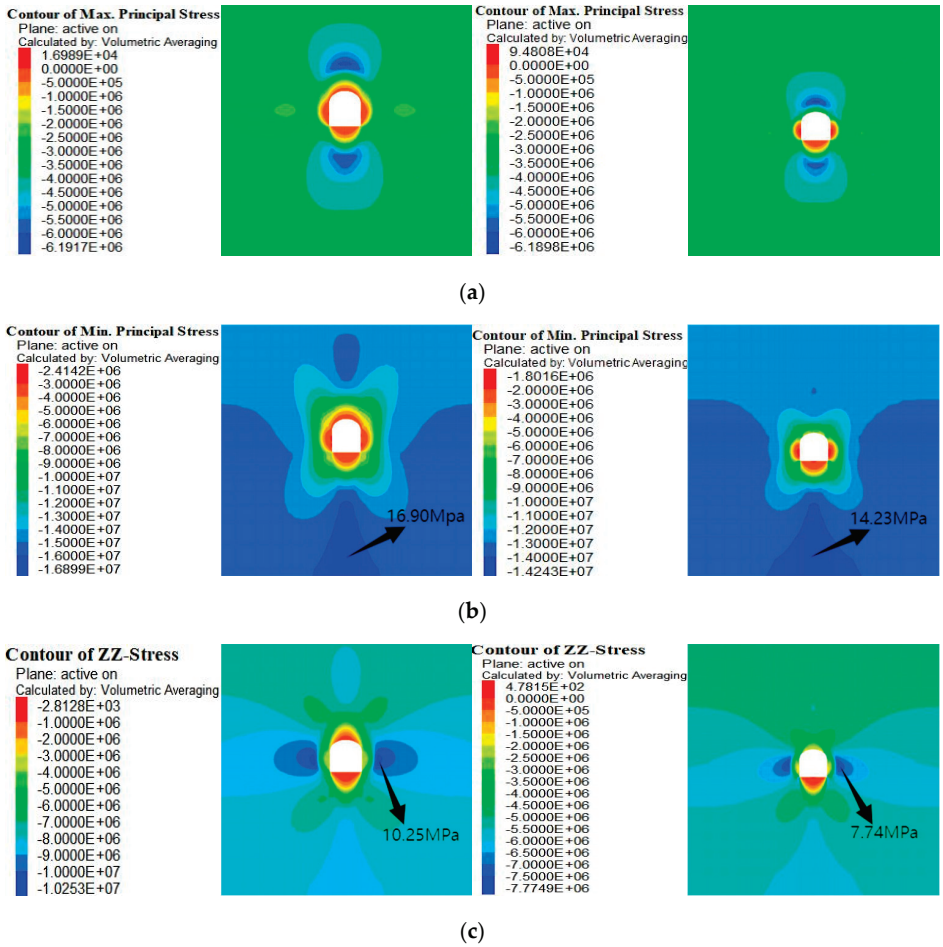

Figure 6. Diagram of stress distribution before and after support. (**a**) Decreasing trend of maximum principal stress before and after support, (**b**) decreasing trend of minimum principal stress before and after support, (**c**) decreasing trend of vertical stress before and after support.

5.3. Analysis of the Deformation of the Roadway Perimeter Rock

The deformation characteristics of surrounding rock are an important index for evaluating the support effect, which directly reflects the stability of the roadway in the excavation and support process. In this study, three monitoring points were selected at the top plate and gang part of the roadway for displacement analysis; the distances of the monitoring

points from the top plate were 0.2 m, 0.6 m and 1.0 m, respectively, and the results are shown in Figures 7 and 8. The position diagram of the measuring point is shown in Figure 9.

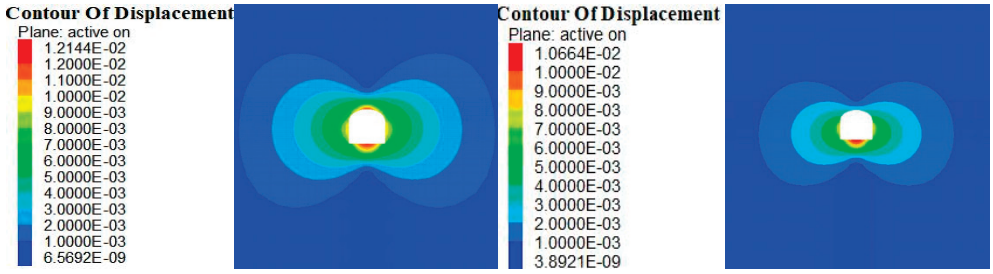

Figure 7. Comparison of deformation of surrounding rock in unsupported condition and spray anchor net support condition.

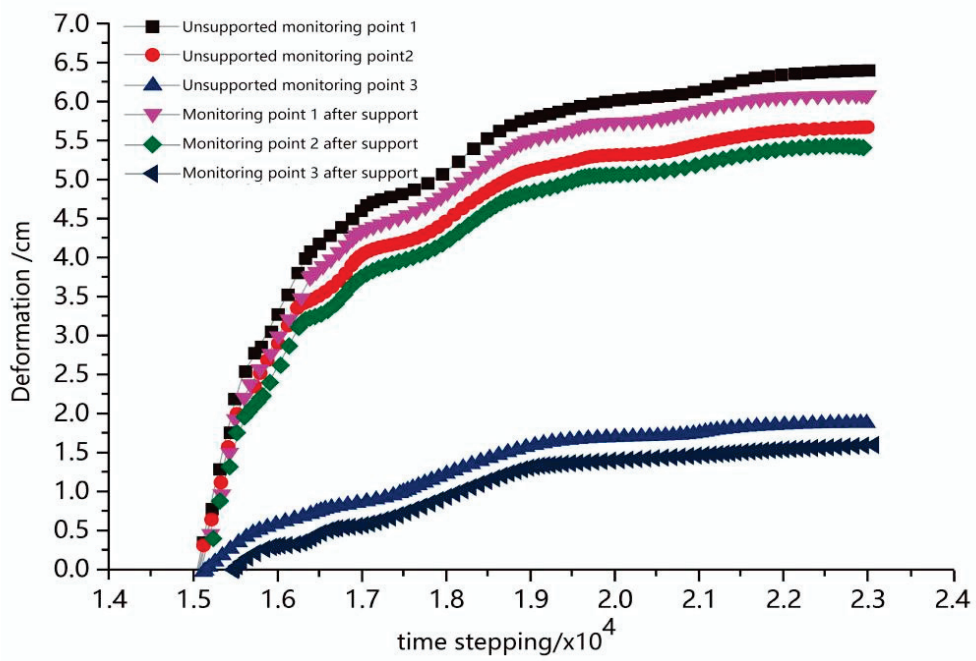

Figure 8. Distribution of monitoring points for tunneling and support of the perimeter rock roadway.

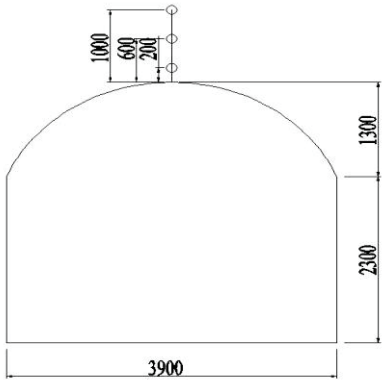

Figure 9. Schematic diagram of measuring point location.

Under the unsupported condition, the deformation of the tunnel perimeter rock is more significant. The maximum displacement of the roof plate reaches 7.0 cm, which is mainly concentrated in the middle part of the roof plate, indicating that the peripheral rock

in this area has insufficient bearing capacity and there is a greater risk of deformation. The maximum displacement of the gang section was 6.2 cm, which was mainly distributed in the middle and upper part of the gang section, indicating that the peripheral rock of the gang section also deformed significantly under the unsupported condition. In addition, the displacement of the top plate at 0.6 m was 6.5 cm, and the displacement of the top plate at 1.0 m was 5.9 cm, which further indicated that the deformation of the top plate gradually decreased from the surface to the depth of the roadway, but the overall deformation was still large.

After adopting anchor net spray support, the deformation of surrounding rock was effectively controlled. The top slab displacement was reduced to 5.8 cm, which was about 17.1% less, indicating that the support system played a significant role in restraining the deformation of the top plate and surrounding rock. Gang displacement decreased to 5.1 cm, a reduction of about 17.7%, indicating that the support measures also have a good effect on the deformation of the surrounding rocks at the gang section. In addition, the displacement at 0.6 m of the roof slab decreased from 6.5 cm to 5.4 cm, a decrease of about 16.9%, and the displacement at 1.0 m of the roof slab decreased from 5.9 cm to 4.9 cm, a decrease of about 16.9%. These data show that the support system can not only effectively control the deformation on the surface of the roadway but also inhibit the displacement of the deep surrounding rock, thus improving the overall stability of the roadway.

By comparing the deformation characteristics under the two conditions, it can be found that the anchor net spraying support significantly reduces the deformation of the surrounding rock and improves the deformation distribution law of the roadway, which provides an important guarantee for the safe use of the roadway.

5.4. Analysis of the Damage to the Roadway Perimeter Rock

The distribution range of the plastic zone directly reflects the damage degree of surrounding rock, which is an important index for evaluating the stability of the roadway. Figure 10 shows the distribution of the plastic zone of the surrounding rock under different support conditions.

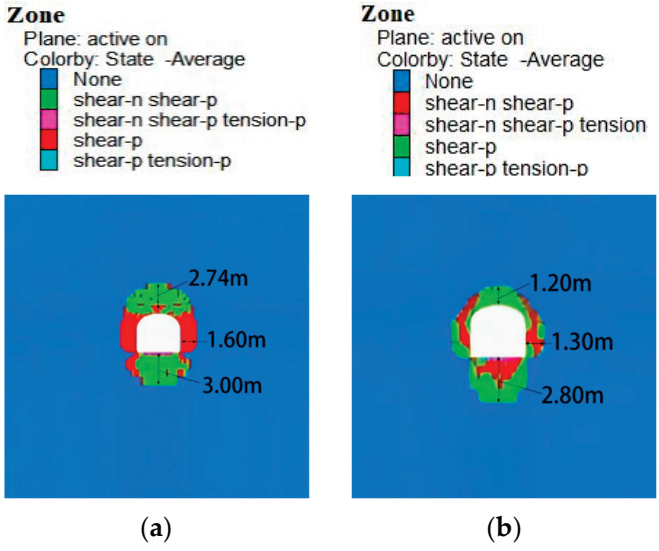

(**a**) (**b**)

Figure 10. Comparison of the plastic zone in the unsupported condition and the spray anchor network supported condition of the enclosing rock. (**a**) Unsupported state of the surrounding rock, (**b**) supporting state of surrounding rock.

In the unsupported condition, the plastic zone of the surrounding rock of the roadway has a large range. The maximum depth of the plastic zone in the top slab is 2.74 m, which is mainly concentrated in the middle of the top slab, indicating that the surrounding rock in this area has undergone significant plastic deformation and there is a high risk of damage. The maximum depth of the plastic zone in the bottom plate is 3.0 m, which is slightly larger than that of the top plate, indicating that the surrounding rock of the bottom plate has undergone a wide range of plastic damage under the condition of no support. The maximum depth of the plastic zone in the gang section is 1.6 m, which is mainly concentrated in the middle and upper part of the gang section, indicating that the surrounding rock in this area has insufficient bearing capacity and is prone to plastic deformation. These data show that the plastic zone of the tunnel peripheral rock in the unsupported condition is large, and there is a high risk of instability.

After adopting the anchor net spraying support, the range of the plastic zone of the roadway surrounding rock was significantly reduced. The depth of the plastic zone of the top slab was reduced from 2.74 m to 1.20 m, which was reduced by about 56.0%, indicating that the support system had significantly suppressed the plastic deformation of the surrounding rock of the top slab. The depth of the plastic zone in the base plate is reduced from 3.00 m to 2.80 m, with a reduction of about 6.7%, indicating that the supporting measures also have a certain effect on the plastic deformation of the base plate surrounding rock. The depth of the plastic zone in the gang section is reduced from 1.60 m to 1.30 m, which is about 19.0%, indicating that the support system can effectively enhance the bearing capacity of the surrounding rock in the gang section and reduce the range of plastic damage.

By comparing the distribution characteristics of the plastic zone under the two conditions, it can be found that the anchor mesh spraying support significantly reduces the range of the plastic zone of the tunnel surrounding rock, especially the plastic zone of the roof plate, which has the largest reduction, indicating that the support measures can effectively enhance the bearing capacity of the surrounding rock and reduce the risk of plastic damage, so as to improve the long-term stability of the tunnel.

6. Engineering Applications

6.1. Rock Support

Based on the above calculations and the geological conditions of the site, the anchor-mesh spray support system is adopted. The pipe slit anchors have a length of 2.0 m and are arranged in a 1.0 × 1.0 m grid pattern. The anchors are spaced 1000 mm apart in each row, with nine anchors per row, and the distance between the anchor and the base plate is 100 mm. Steel mesh is added, with each mesh panel measuring 2000 × 1000 mm, a diameter of 6 mm, and a grid size of 100 × 100 mm. The sprayed concrete has a thickness of 100 mm and a strength rating of C20. This support system enhances roadway stability by effectively controlling deformation and minimizing plastic zone expansion. Figure 11 shows a schematic diagram of the design.

6.2. Monitoring Method of Tunnel Convergence Deformation and Setting of Measuring Point

Roadway surface displacement is the most direct basis for the evaluation of the roadway supporting effect and surrounding rock stability, and its monitoring content includes the displacement of two sides and the displacement of the top and bottom. According to the monitoring results, the improved support effect and deformation rule of surrounding rock can be judged, and the feasibility of support can be verified. The convergence deformation

of surrounding rock on the roadway surface was monitored using the cross-distribution method, as shown in Figure 12.

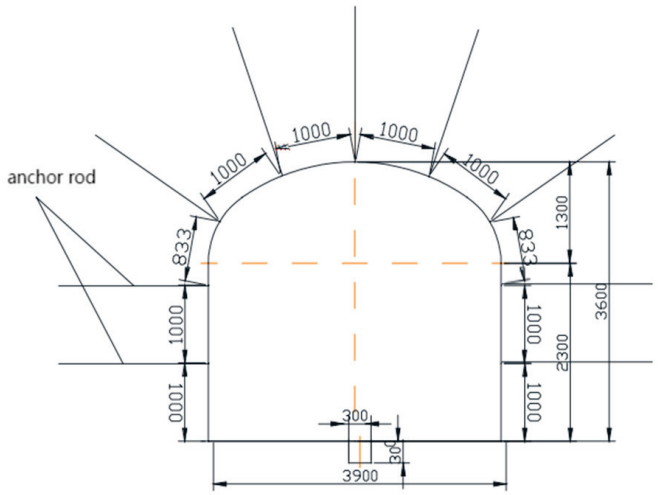

Figure 11. Support program diagram.

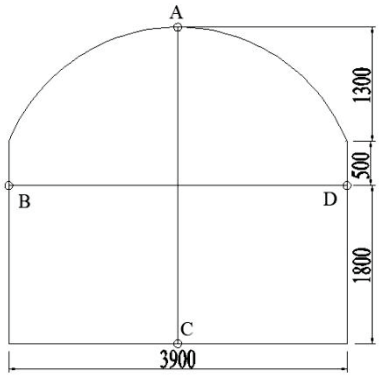

Figure 12. Distribution diagram of key points in roadway section.

Figure 13 shows that in the initial stage of measuring point arrangement, the coupling between the supporting system and surrounding rock is weak, supporting bodies such as the anchor net have not fully played their roles, and the deformation rate of the roadway is fast. With the increase in roadway deformation, the coupling between roadway surrounding rock and the supporting system was greatly enhanced on the 10th to 15th days, and the roadway deformation rate slowed down significantly. After the 15th day, the roadway deformation rate tended to be stable.

Through field monitoring, the displacement value of the surrounding rock of the roadway measuring station can be obtained, and then the stability of the roadway can be evaluated using the convergence rate, as shown in Table 6. Based on the empirical value summarized from long-term engineering practice, when the relative convergence rate of the largest two sides and roof and floor of the roadway does not exceed 2%, the roadway is judged to be in a stable state, indicating that the roadway supporting parameters are feasible.

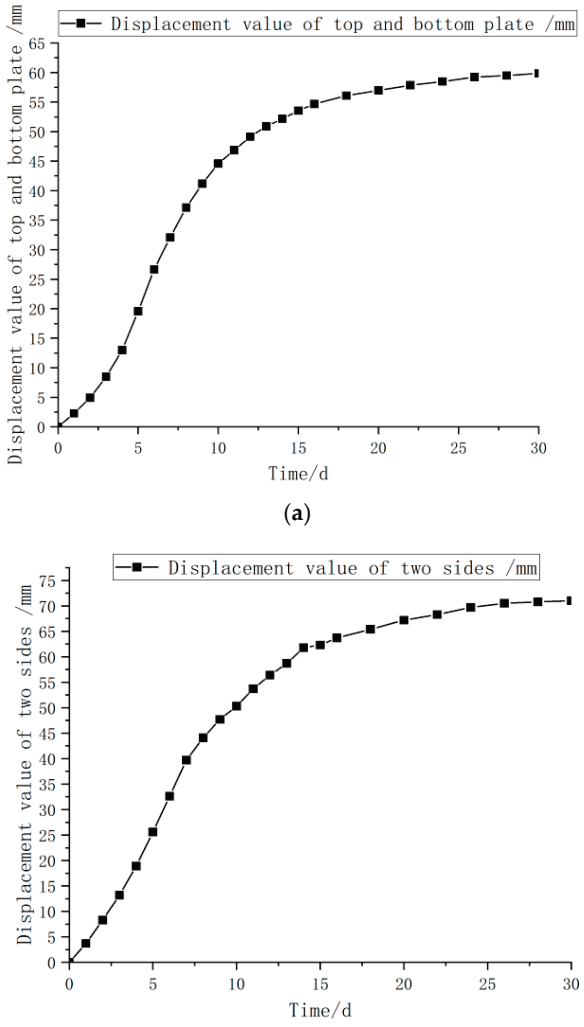

Figure 13. Tunnel convergence deformation monitoring. (**a**) Roof-to-floor convergence, (**b**) two sides move closer.

Table 6. Stability evaluation of mining roadway.

Displacement Value of Top and Bottom Plate (mm)	The Displacement Value of the Two Sides (mm)	Top and Bottom Relative Convergence Rate (%)	Relative Convergence Rate (%)
59.85	71.00	1.66	1.82

As can be seen from Table 6, the relative convergence rates of the top and bottom plates and the two sides of the measuring points are 1.66% and 1.82%, respectively, both of which are less than 2% and within the allowable convergence rate range. Therefore, the roadway is judged to be in a stable state. It shows that the roadway supporting parameters are feasible and can provide reference for similar roadway supporting.

After determining the parameters of anchor net spraying support and implementing the engineering application in Makeng Iron Mine, under the influence of the vibration of deep hole blasting in the quarry, the sprayed concrete layer close to the blasting point will be cracked, but no spalling phenomenon will occur. Due to the blasting disturbance, the service life of the roadway near the blasting point supported by sewing pipe-type anchor

net spraying is relatively short. In order to improve this situation, the mine adopts the method of filling after the stage mining room and follows the principle of "quick mining, quick exit, quick filling" for the management of the quarry. By filling the hollow area in time, it effectively reduces the deformation and displacement of surrounding rocks around the hollow area, inhibits the further expansion of cracks in the shotcrete layer, and, thus, avoids the occurrence of concrete layer spalling. After the filling is completed, only the local cracked area needs to be shotcrete repaired to restore its integrity and ensure the long-term stability of the supporting structure. Practice shows that this method can significantly improve the stability of the roadway surrounding rock, providing a strong guarantee for the safe production of the mine.

6.3. Field Analysis and Follow-Up Measures

After determining the parameters of anchor net spraying support and implementing the engineering application in MaKeng Iron Mine, under the influence of vibration of deep hole blasting in the quarry, the sprayed concrete layer close to the blasting point will be cracked, but no spalling phenomenon occurs. Due to the blasting disturbance, the service life of the roadway near the blasting point supported by sewing pipe type anchor net spraying is relatively short. In order to improve this situation, the mine adopts the method of filling after the stage mining room, and follows the principle of "quick mining, quick exit, quick filling" for the management of the quarry. By filling the hollow area in time, it effectively reduces the deformation and displacement of surrounding rocks around the hollow area, inhibits the further expansion of cracks in the shotcrete layer, and thus avoids the occurrence of concrete layer spalling. After the filling is completed, only the local cracked area needs to be shotcrete repaired to restore its integrity and ensure the long-term stability of the supporting structure. Practice shows that this method can significantly improve the stability of the roadway surrounding rock, providing a strong guarantee for the safe production of the mine.

7. Conclusions

1. Based on the loosening zone theory, the quantitative analysis of the support requirements of the surrounding rock of the roadway was conducted, and an optimized scheme of combined support with grouting, anchor rods and mesh was proposed. Through theoretical calculations, key parameters such as the length of anchor rods (2.5–3.0 m), spacing (0.8 × 0.8 m) and thickness of the sprayed layer (120–150 mm) were determined. A quantitative design system for supporting parameters of high-stress roadways was established.
2. The support system reduces the maximum principal stress to 14.23 MPa, a decrease of 15.8%, and the vertical stress to 7.74 MPa, a decrease of 24.5%, while weakening the stress concentration and promoting uniform distribution. The increase in minimum principal stress and reduction in the tensile zone indicate the effective suppression of tensile stress, particularly at wall bases.
3. After applying the anchor net shotcrete support, roof and gang displacements are reduced by 17.1% and 17.7%, respectively, with consistent 16.9% reductions at 0.6 m and 1.0 m depths. The support system effectively controls both surface and deep deformation, enhancing the overall stability and safety of the roadway.
4. After applying anchor net shotcrete support, the plastic zone was significantly reduced: the roof decreased from 2.74 m to 1.20 m, a reduction of 56%; the base plate from 3.00 m to 2.80 m, a reduction of 6.7%; and the gang section from 1.60 m to 1.30 m, a reduction of 19%. These results indicate that the support system effectively

enhances the bearing capacity and suppresses plastic deformation, particularly in the roof, thereby improving the tunnel's long-term stability.

5. Displacement monitoring shows that support–rock coupling improves significantly after 10–15 days, leading to stabilized deformation. The relative convergence rates of roof–floor and sidewalls are 1.66% and 1.82%, confirming the support effectiveness and roadway stability. In Makeng Mine, local cracking near blasting points was controlled through timely backfilling, which reduced deformation and prevented spalling. This strategy enhances long-term structural stability and ensures safe mining operations.
6. After applying anchor net shotcrete support in Makeng Iron Mine, blasting-induced vibrations caused local cracking of the concrete layer near the blasting point, but no spalling occurred. To address this, the mine adopted a "rapid mining, rapid exit, rapid filling" approach, backfilling hollow areas to reduce surrounding rock deformation, prevent crack propagation, and avoid spalling. Localized shotcrete repairs were applied after filling, restoring structural integrity and ensuring long-term stability. This method significantly improves roadway stability and ensures safe mining operations.

Author Contributions: Validation, L.Z. and G.L.; Formal analysis, Z.D.; Writing—original draft, Z.D.; Visualization, Z.D.; Funding acquisition, G.L. All authors have read and agreed to the published version of the manuscript.

Funding: National Natural Science Foundation of China: 52174077.

Institutional Review Board Statement: Not applicable.

Informed Consent Statement: Not applicable.

Data Availability Statement: The original contributions presented in this study are included in the article. Further inquiries can be directed to the corresponding author(s).

Conflicts of Interest: The authors declare no conflict of interest.

References

1. Hao, Y.; Liu, C.; Wu, Y.; Pu, H.; Chen, Y.; Shen, L.; Li, G. Numerical Modeling on Strain Energy Evolution in Rock System Interaction with Energy-Absorbing Prop and Rock Bolt. *Int. J. Min. Sci. Technol.* **2023**, *33*, 1273–1288. [CrossRef]
2. Jiang, B.; Xin, Z.; Zhang, X.; Deng, Y.; Wang, M.; Li, S.; Ren, W. Mechanical Properties and Influence Mechanism of Confined Concrete Arches in High-Stress Tunnels. *Int. J. Min. Sci. Technol.* **2023**, *33*, 829–841. [CrossRef]
3. Kang, Y.; Geng, Z.; Liu, B.; Chen, J. Study on Gas Extraction Efficiency Using In-Seam Borehole Method Considering Influence of Plastic Zone Induced by Borehole Drilling. *Geomech. Energy Environ.* **2023**, *33*, 100426. [CrossRef]
4. Sharifzadeh, M.; Lou, J.; Crompton, B. Dynamic Performance of Energy-Absorbing Rockbolts Based on Laboratory Test Results. Part I: Evolution, Deformation Mechanisms, Dynamic Performance and Classification. *Tunn. Undergr. Space Technol.* **2020**, *105*, 103510. [CrossRef]
5. Zhang, Z.; Deng, M.; Bai, J.; Yan, S.; Yu, X. Stability Control of Gob-Side Entry Retained under the Gob with Close Distance Coal Seams. *Int. J. Min. Sci. Technol.* **2021**, *31*, 321–332. [CrossRef]
6. Zuo, J.; Wen, J.; Liu, D.; Wu, L.; Sun, Y. Control Theory of Uniform Strength Support in Deep Roadway. *J. Min. Sci. Technol.* **2021**, *6*, 148–159. [CrossRef]
7. Shen, B. Coal mine roadway stability in soft rock: A case study. *Rock Mech. Rock Eng.* **2014**, *47*, 2225–2238. [CrossRef]
8. Li, H.; Lin, B.; Hong, Y.; Gao, Y.; Yang, W.; Liu, T.; Huang, Z. Effects of in-situ stress on the stability of a roadway excavated through a coal seam. *Int. J. Min. Sci. Technol.* **2017**, *27*, 917–927. [CrossRef]
9. Farmer, I.W. Stress Distribution along a Resin Grouted Rock Anchor. *Int. J. Rock Mech. Min. Sci. Geomech. Abstr.* **1975**, *12*, 347–351. [CrossRef]
10. Cai, M.; He, M.; Liu, D. *Rock Mechanics and Engineering*; Science and Technology Press: Beijing, China, 2002.
11. Hoek, E.; Carranza-Torres, C.; Corkum, B. Hoek-Brown Failure Criterion-2002 Edition. *Proc. NARMS-Tac* **2002**, *1*, 267–273.

12. Gao, M.-s.; Zhang, N.; Dou, L.-m.; Wang, K.; Kan, J.-g. Study of Roadway Support Parameters Subjected to Rock Burst Based on Energy Balance Theory. *Zhongguo Kuangye Daxue Xuebao* **2007**, *36*, 426–430.
13. Aydan, Ö. *Rock Mechanics and Rock Engineering: Volume 2: Applications of Rock Mechanics-Rock Engineering*; CRC Press: Boca Raton, FL, USA, 2019.
14. Hashemi, M.; Moghaddas, S.; Ajalloeian, R. Application of Rock Mass Characterization for Determining the Mechanical Properties of Rock Mass: A Comparative Study. *Rock Mech. Rock Eng.* **2010**, *43*, 305–320. [CrossRef]
15. Kang, H.; Wang, J.; Lin, J. Case Studies of Rock Bolting in Coal Mine Roadways. *Yanshilixue Yu Gongcheng Xuebao* **2010**, *29*, 649–664.
16. Jia, H.; Wang, H. Principle and Application of the Double Cacheable and Gradually Deformable Supporting Shells for Soft Rock Tunneling. *Rock Soil Mech.* **2015**, *36*, 1119–1126.

applied sciences

MDPI

Article

Investigation of the Evolution of Anisotropic Full-Field Strain Characteristics of Coal Samples Under Creep Loading Conditions

Xuguang Li [1,2], Yu Wang [3,*], Xuefeng Yi [3] and Xinyu Bai [3]

[1] Shenyang Geological Survey Center, China Geological Survey, Shenyang 110034, China; xuguangli_2008@126.com
[2] Field Scientific Observation and Research Station for Landslide Disaster in Fushun Open Pit Mine, Ministry of Natural Resources, Fushun 113004, China
[3] Department of Mechanical Science and Engineering, School of Resource & Safety Engineering, University of Science & Technology Beijing, Beijing 100083, China; yxfeng_ustb@sina.com (X.Y.); baixy_ustb@126.com (X.B.)
* Correspondence: wyzhou@ustb.edu.cn

Abstract

This work aims to reveal the full-field strain evolution characteristics and failure mechanisms of anisotropic coal samples under creep loading. A series of compression tests combined with digital image correlation (DIC) monitoring were employed to characterize the strain evolution process of coal specimens with bedding angles of 0°, 30°, 60°, and 90°. Testing results show that the peak strength, peak strain, and the creep loading stage of coal are significantly influenced by the bedding angle. The peak strength initially decreases and then increases as the bedding angle increases. In addition, the creep failure of coal manifests as a process of instantaneous deformation, decelerating creep, steady-state creep, accelerating creep, and failure. Under graded creep loading conditions, coal specimens exhibit distinct creep characteristics at high stress levels. Moreover, the bedding angle significantly influences the strain field evolution of the coal samples. Finally, for coal specimens with bedding angles of 0° and 90°, the final macroscopic fracture pattern upon failure is characterized by longitudinal tensile splitting. In contrast, coal samples with bedding angles of 30° and 60° tend to exhibit failure along the bedding interfaces, forming tensile-shear fractures. The results of this study will provide theoretical guidance for the prevention, early warning, and safety management of coal mine disasters.

Keywords: coal sample; anisotropy failure; DIC; creep loading; full-field strain

1. Introduction

Coal, as a naturally discontinuous and heterogeneous geological material, exhibits an inherent anisotropic bedding structure due to prolonged geological sedimentation processes. Influenced by the dip of the coal seam and the surrounding rock stress field, coal is highly susceptible to the formation of random and disordered fractures, which complicate the initiation and propagation of cracks. During the underground mining process, various protective coal pillars are often left in place. However, as mining activities redistribute the stresses around the coal pillars, these pillars are subjected to long-term static loading from the overlying strata, leading to creep instability. Therefore, investigating the anisotropic mechanical behavior of coal rock under the influence of bedding and understanding the failure mechanisms of anisotropic coal rock under creep loading is of significant importance

for the prevention, early warning, and safety management of coal mine disasters, ultimately contributing to ensuring safe coal mine operations.

The influence of anisotropic bedding on the macroscopic mechanical properties of coal rock has been extensively studied in recent years. Research findings indicate that the failure characteristics of coal rock are significantly affected by both anisotropy and loading conditions. Through a series of uniaxial compression [1–3], triaxial compression [4–7], and dynamic impact [6–9] tests, scholars have observed that the bedding angle and peak strength characteristic curves of anisotropic coal rock typically exhibit a "U"-shaped or near "U"-shaped form. Furthermore, it has been noted that the directional distribution of the coal rock's internal microstructure leads to systematic variations in its mechanical properties [10]. Although the static and dynamic instantaneous strength characteristics of anisotropic coal rock have been extensively validated in previous studies, as a typical soft rock, coal exhibits significant time-dependent rheological properties. Under varying stress levels, coal rock demonstrates distinct creep deformation behaviors, prompting the widespread application of multistage creep loading tests to investigate the creep deformation characteristics of coal rock. Poulsen and Adhikary [11] performed numerical studies to reveal the scale effect of coal samples, and the results indicated macro failure in compression initiated by micro tensile fractures coalescing at mid-height and resulting in a wasting observed underground in over-stressed coal pillars. Yang et al. [12] conducted experimental studies on the deformation and acoustic properties of extremely heterogeneous coal under incremental creep stress, noting that long-term coal creep results from multiple structural deformations, including particle dislocation, pore closure, matrix cracking, and clay mineral compaction. These structural changes in coal led to fluctuations in ultrasonic velocity and dynamic modulus. Zhang et al. [13] performed multistage and graded cyclic creep tests on intact coal rock, finding that the Burgers model could effectively predict the transient and secondary creep behaviors of intact coal rock. Huang et al. [14] conducted triaxial multistage creep tests on coal rock with initial damage, and the results indicated that increased initial damage significantly reduced the creep time and long-term strength of the coal samples. While significant progress has been made in studying the creep deformation characteristics of coal rock, current research primarily focuses on exploring and predicting the axial average deformation evolution process of coal samples. There is limited research on the full-field strain evolution and crack propagation characteristics of anisotropic coal rock under creep loading.

Although plenty of studies have been performed to investigate the anistropic creep behaviors of different type of rock samples [15–18], the investigations on the full-field deformation and fracture characterization of coal samples subjected to creep loading historites are not well understood. Therefore, the aim of this study is to investigate the full-field strain characteristics and the fracture evolution of anisotropic coal samples under multiple-level creep loading. Using the RFTS 1000 rock mechanics testing system, graded creep loading tests were performed on anisotropic coal rock specimens with varying bedding orientations. Combined with the DIC testing system, this study quantitatively characterizes the full-field strain evolution and crack propagation behaviors of coal rock under creep loading.

2. Sample Preparation and Experimental Methods

2.1. Principles of Digital Image Correlation (DIC) Technology

Digital image correlation (DIC) technology utilizes the black-and-white speckle pattern sprayed onto the surface of the coal sample or the natural surface texture of the specimen. Based on a grayscale recognition digital matching algorithm, it calculates the displacement

vectors of corresponding pixels across sequential deformation images of the loaded sample. This enables the determination of the full-field displacement and strain information of the coal rock surface [19–23]. The fundamental principles of digital image correlation are illustrated in Figure 1.

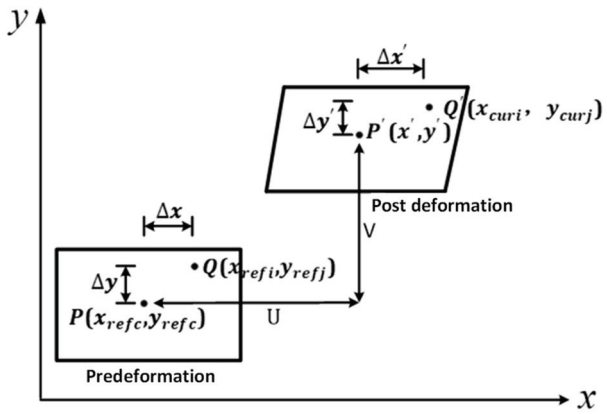

Figure 1. The basic principle of the digital image correlation method.

Figure 1 illustrates the process of displacement of a single subset and its internal coordinate points before and after deformation. Let the center of the subset before deformation be denoted as point P, and its position after deformation shifts to point P′. For any arbitrary coordinate point Q within the subset, its position after deformation moves to point Q′. Since the deformation of the coordinate points within the subset includes translational, shear, and other deformation types, the displacement components along the x and y axes, u and v, are complex functions of x and y. From this, the following relationships can be derived:

$$\begin{cases} x' = x_{refc} + u(x,y) \\ y' = y_{refc} + v(x,y) \end{cases} \tag{1}$$

$$\begin{cases} \Delta x' = \Delta x + \Delta u(x,y) \\ \Delta y' = \Delta y + \Delta v(x,y) \end{cases} \tag{2}$$

$$\begin{cases} \widetilde{x}_{curi} = x' + \Delta x' \\ \widetilde{y}_{curj} = y' + \Delta y' \end{cases} \tag{3}$$

$$\begin{cases} \Delta u(x,y) = \frac{\partial u(x,y)}{\partial x}\Delta x + \frac{\partial u(x,y)}{\partial y}\Delta y \\ \Delta v(x,y) = \frac{\partial v(x,y)}{\partial x}\Delta x + \frac{\partial v(x,y)}{\partial y}\Delta y \end{cases} \tag{4}$$

By simultaneously solving Equations (1)–(4), the coordinates of any point within the subset after deformation can be determined as follows:

$$\begin{cases} \widetilde{x}_{curi} = x_{refc} + u(x,y) + \left[1 + \frac{\partial u(x,y)}{\partial x}\right]\Delta x + \frac{\partial u(x,y)}{\partial y}\Delta y \\ \widetilde{y}_{curj} = y_{refc} + v(x,y) + \frac{\partial v(x,y)}{\partial x}\Delta x + \left[1 + \frac{\partial u(x,y)}{\partial y}\right]\Delta y \end{cases} \tag{5}$$

From Equation (5), it can be seen that once the deformation information of the subset's center point is obtained, the deformation information of any arbitrary point within the subset can be derived accordingly from the deformation of the center point.

2.2. Sample Preparation and Speckle Spraying

In order to investigate the influence of bedding angle on the anisotropic characteristics of coal samples, rectangular specimens with bedding angles of 0°, 30°, 60°, and 90° were first drilled using a core drilling machine, with the drilling angle β controlled, where β is the angle between the drilling direction and the horizontal plane, as shown in Figure 2a. Here, 0° represents horizontal bedding, and 90° represents vertical bedding. The drilled cores were then cut into rectangular samples with dimensions of 60 mm × 30 mm × 120 mm using an automatic cutting machine. Following this, the ends of the coal specimens were ground flat using a double-end grinding machine. During the grinding process, the parallelism error between the two end faces of the specimen was controlled to within 0.005 mm, the flatness error of the top and bottom faces was limited to 0.02 mm, and the diameter error of the specimen's end faces was kept within 0.3 mm. Furthermore, the top and bottom faces were ensured to be perpendicular to the central axis of the specimen, with the maximum angular error not exceeding 0.25°. The prepared samples are shown in Figure 2b.

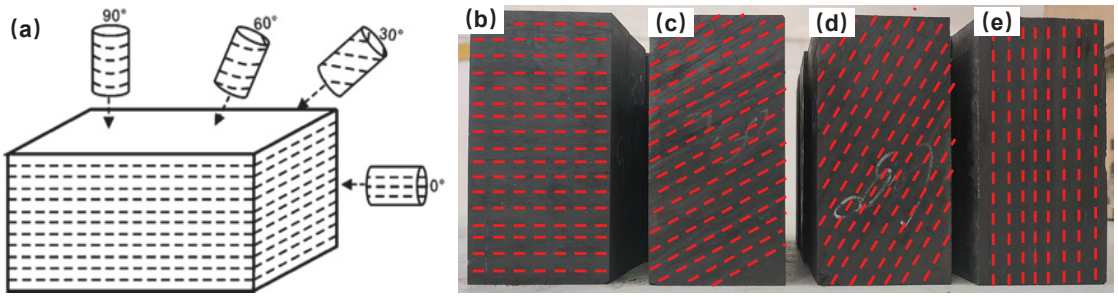

Figure 2. Coal sample preparation of different bedding angles. (**a**) Core sampling of coal with different bedding angles; (**b**–**e**) Square coal samples with different bedding angles.

The spraying of the speckle pattern on the surface of the specimen is crucial for the accuracy of the DIC measurement process. Therefore, prior to the experiment, a spray nozzle was used to apply a speckle pattern to the prepared specimens. Before spraying, it is essential to ensure that the specimen surface is smooth, clean, and flat, so that the speckles can adhere firmly to the surface and the speckle images exhibit good contrast. The spraying procedure involves first applying a matte white base coat to the specimen's surface, followed by the application of black speckle paint to create a high-contrast random pattern. Typically, each speckle should occupy 4 to 6 image pixels. The speckle pattern on the coal rock specimens is shown in Figure 3.

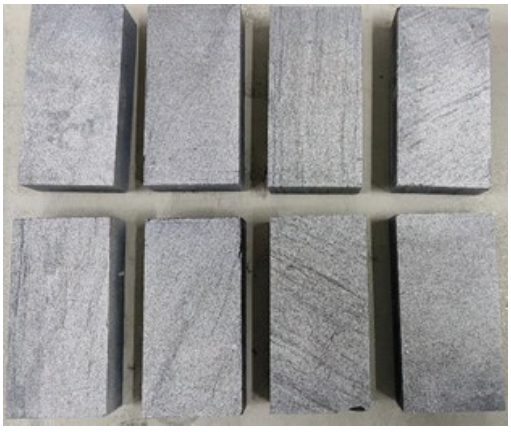

Figure 3. Speckle pattern creation on coal samples with different bedding angles.

2.3. Experimental Equipment and Test Scheme

The coal sample creep tests were conducted using the RTFS 2000 rock mechanics testing system, as shown in Figure 4a, with loading applied, and the DIC digital image correlation testing system, shown in Figure 4b, was used to precisely measure the deformation and displacement of the speckle-marked coal rock specimens in the Figure 3. The digital image correlation system is an optical observation system for full-field, non-contact deformation measurement, primarily consisting of a camera module, LED light source, trigger acquisition unit, and numerical image processing software.

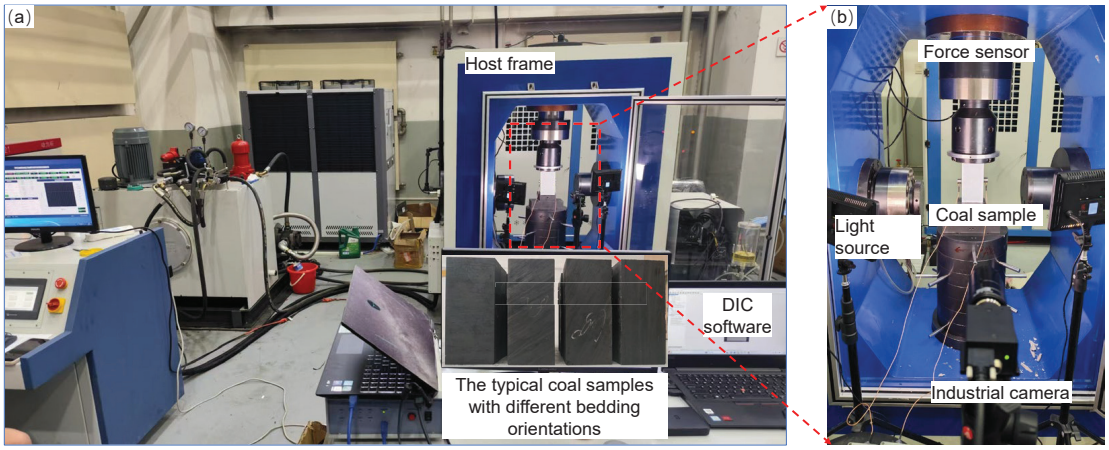

Figure 4. Experimental equipment used for creep digital image correlation testing of coal samples.

The graded creep test loading scheme is depicted in Figure 5. The load was first stabilized at 4 kN with a loading rate of 0.06 mm/min until the first creep stage was reached, followed by a creep loading phase lasting 1 h. Upon completion of the initial creep phase, the loading was continued in increments of 4 kN for each creep stage, until the specimen failed.

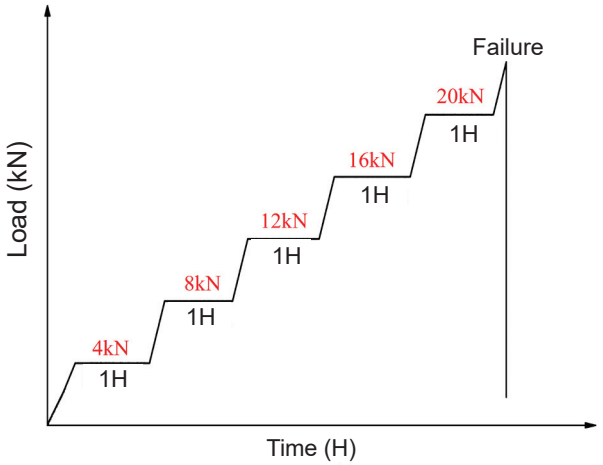

Figure 5. Graded creep loading test scheme.

3. Experimental Results and Analysis

3.1. Stress and Strain Responses

Figure 6a shows the stress–strain curves of coal rock at different bedding angles. The peak strengths of coal rock with bedding angles of 0°, 30°, 60°, and 90° were 30.59 MPa, 19.61 Mpa, 11.69 Mpa, and 28.93 Mpa, respectively. The peak strength of coal rock initially decreases and then increases as the bedding angle increases, indicating that the peak

strength of coal rock under creep loading is significantly influenced by the bedding angle. For coal samples with bedding angles of 0° and 90°, the peak strengths are the highest, and the strength values for these two bedding angles are nearly identical. For coal samples with a bedding angle of 30°, the peak strength is reduced by 35.9% compared to the 0° bedding angle specimens. For samples with a bedding angle of 60°, the weakening of peak strength is even more pronounced, with a 61.8% decrease compared to the 0° bedding angle samples. Therefore, in the process of strip mining in coal mines, attention should be paid to the influence of the bedding angle on the overall strength of coal pillars. It is recommended to retain coal samples with bedding angles close to 0° or 90° for use as supporting pillars.

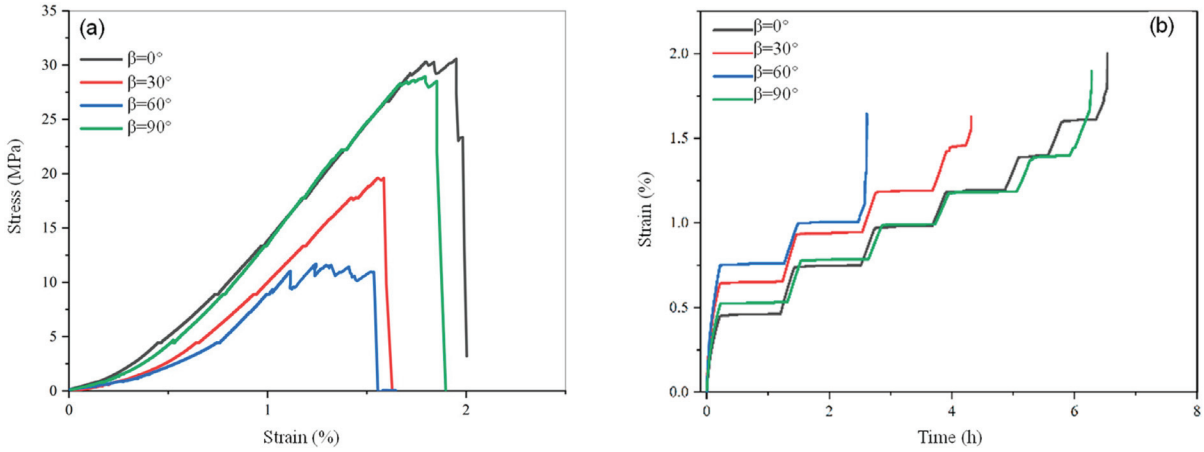

Figure 6. Stress–strain response of coal specimens with different bedding angles. (**a**) Typical stress strain curves; (**b**) The strain–time curves.

The post-peak behavior of the stress=-strain curve of coal samples is closely related to the failure mode of the coal body. Based on the post-peak characteristics of the specimens, the post-peak stage can be divided into two types: (I) linear type and (II) buffering type. The linear type post-peak failure mode is characterized by the specimen's stress rapidly decreasing along a straight line with a certain slope after reaching the peak stress, typically with a steep slope, as seen in coal samples with bedding angles of 0°, 30°, and 90°. This failure mode involves significant damage, with the specimen losing stability rapidly within a short period and no plastic buffering time. In field engineering, this mode is the most destructive, making it difficult to maintain the coal body after the peak stress using engineering techniques. The buffering type post-peak failure mode refers to a stress drop after the peak stress that reaches the residual strength and then maintains this load-carrying capacity for a period of time, as shown in the stress–strain curve of the coal sample with a bedding angle of 60°. In this mode, the coal body does not immediately and completely lose stability, offering the potential for reinforcement and stabilization through engineering measures in the later stages.

The time-strain curves of coal with different bedding angles, as shown in Figure 6b, clearly demonstrate that the peak strain characteristics and creep loading stages of coal rock are also controlled by the bedding angle. For coal rock with bedding angles of 0°, 30°, 60°, and 90°, the peak strains are 1.95%, 1.59%, 1.24%, and 1.79%, respectively, with 7, 5, 3, and 7 creep loading stages applied. Under the same creep stages, the coal samples are subjected to the same stress levels. Coal samples with bedding angles of 0° and 90° exhibit greater resistance to deformation, while the sample with a bedding angle of 60° demonstrates the weakest resistance to deformation, making it more prone to creep slip failure along the bedding planes.

3.2. Graded Creep Deformation Characteristics

Coal rock exhibits different creep deformation characteristics under varying stress levels. Therefore, Figure 7 presents the strain evolution patterns of coal rock at different creep stages. From the figures, it can be observed that the deformation of the coal sample is primarily concentrated during the static loading phase. During the creep stage, the deformation is relatively small and tends to stabilize. However, when the specimen reaches failure, the deformation rapidly increases, and the specimen enters the accelerated deformation phase. Different creep stages correspond to different stress levels, with higher stress levels leading to greater creep deformation. Creep deformation gradually accumulates over time. For each creep stage, the deformation process is divided into two phases: the transition from the accelerated deformation phase to the stabilized deformation phase, and, when the specimen enters the failure stage, it again undergoes accelerated deformation.

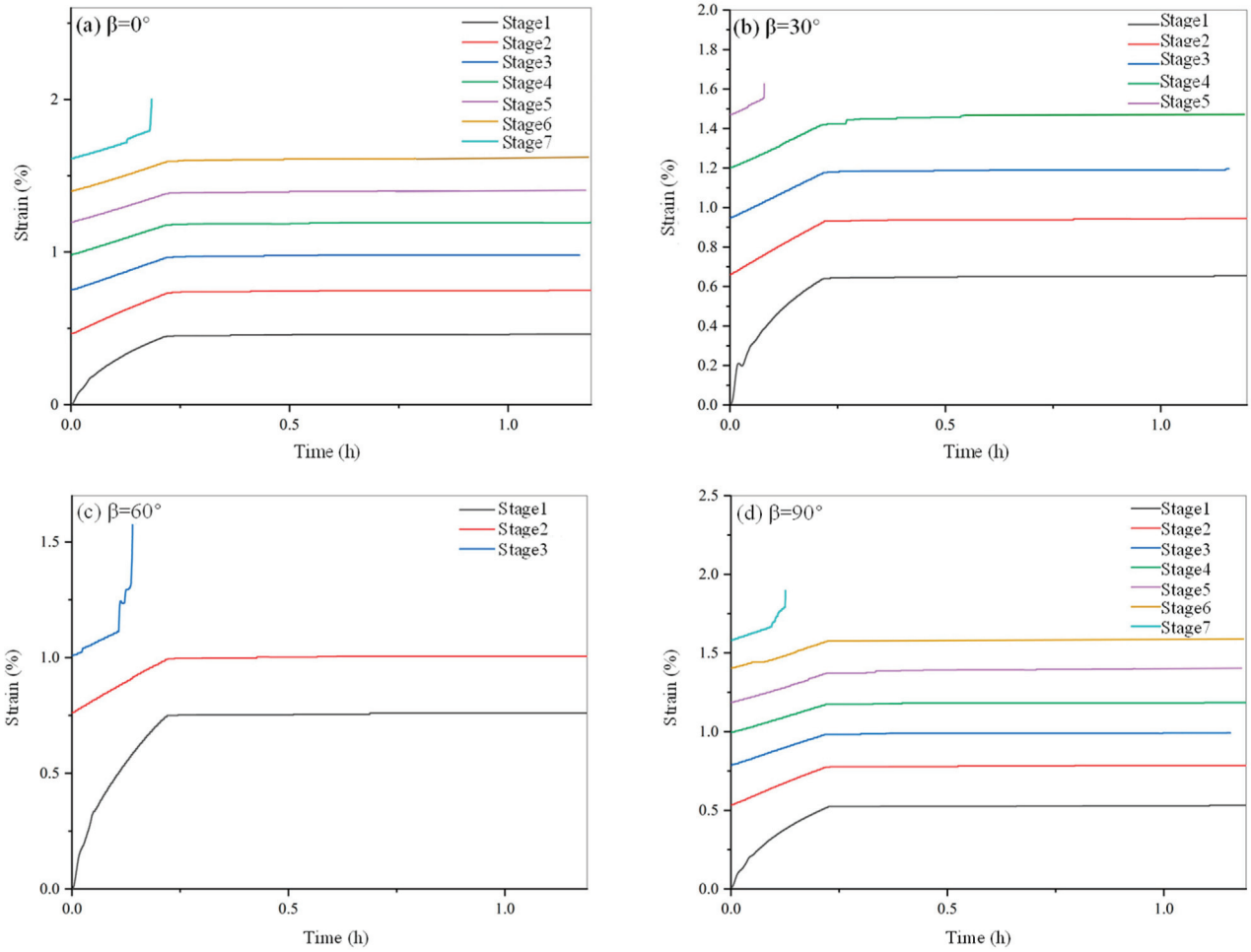

Figure 7. Strain evolution patterns of coal rock at different creep stages: (**a**–**d**) Bedding angles of 0°, 30°, 60°, and 90°, respectively.

3.3. Full-Field Strain Evolution Analysis

The generation, propagation, and stress concentration of microcracks are not easily visible to the naked eye but can be captured by DIC technology. By solving the full-field displacement and strain data obtained from DIC, the Lagrangian full-field strain information, as shown in Figure 8, can be derived. This provides a clear representation of the entire process of crack initiation, propagation, and through-going failure during the creep failure process of anisotropic coal rock. The figure clearly demonstrates the

influence of bedding angle on the strain field evolution of the coal samples. The regions of concentrated displacement changes are typically located at the intersections between bedding planes, where cracks generally initiate and propagate along the bedding interfaces. Throughout the compressive strain process of the coal rock, the specimen remains in a compressed and densified state for a relatively long duration in the early stages. However, in the final few seconds before failure, as the stress approaches the peak value, and the strain exhibits a sharp change, leading to the formation of a crack strain band that eventually results in overall macro-scale failure.

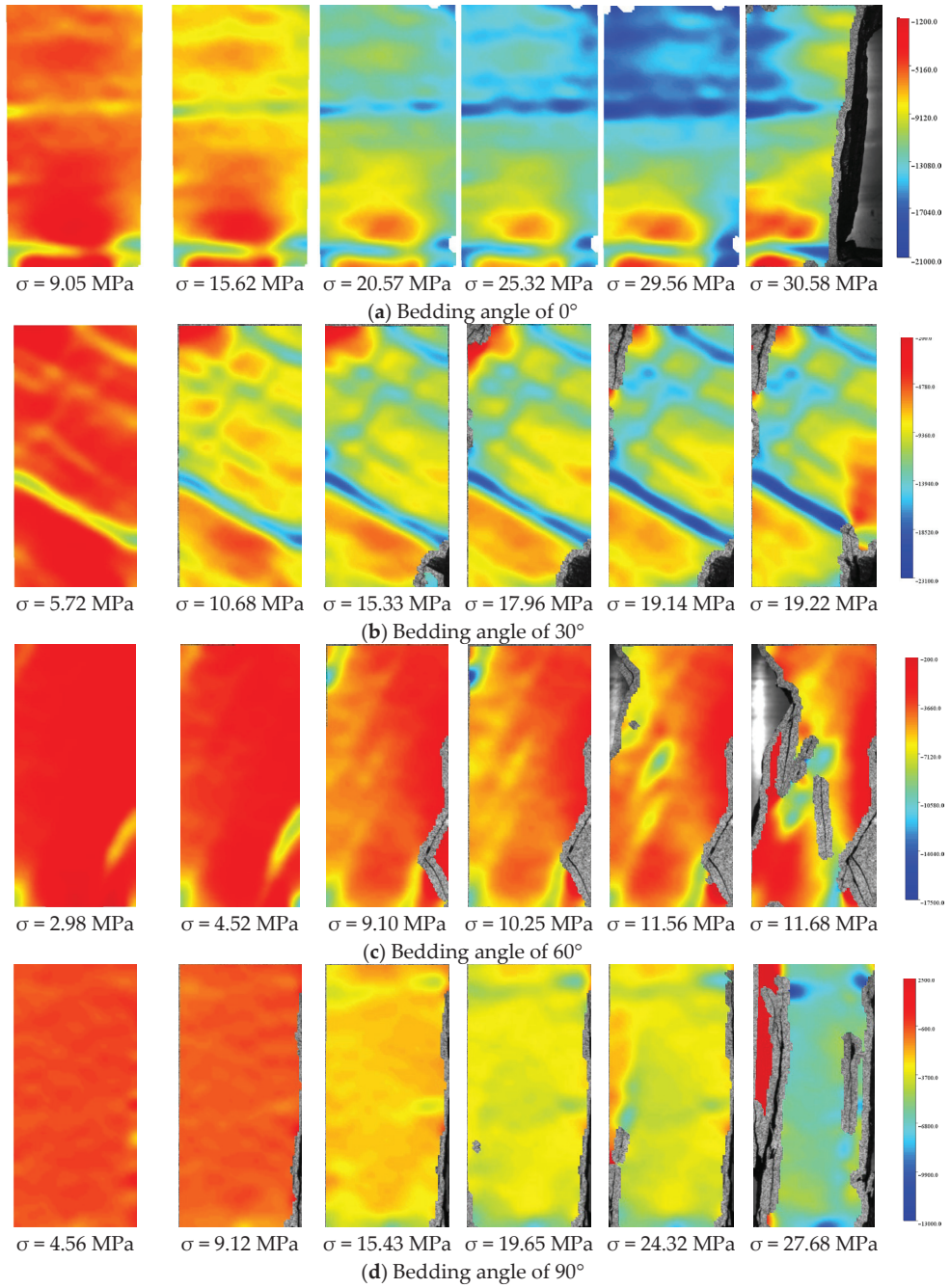

Figure 8. Lagrangian strain field evolution contour maps of coal rock with different bedding angles: (**a**–**d**) Bedding angles of 0°, 30°, 60°, and 90°, respectively.

For the coal sample with a bedding angle of 0°, as shown in Figure 8a, it can be observed that during the loading process, the coal sample remains in a long-term compressed and densified state. Stress concentration exists at the horizontal bedding interface, but no obvious crack initiation or propagation occurs. Just before failure, cracks suddenly initiate and propagate, leading to localized spalling of the coal sample, which results in brittle failure. For the coal sample with a bedding angle of 30°, crack initiation typically concentrates at the junction points of the X-shaped shear strain damage zone. At these junctions, the stress concentration is most pronounced. After reaching the yield limit, local tensile stress is released, causing crack initiation perpendicular to the direction of maximum tensile stress. Often, after cracks initiate, spalling of the material occurs due to the reduced constraint between blocks at the edges of the coal rock sample. The energy release during crack propagation causes the blocks to "bounce" and spall off. The continued propagation of these cracks and their connection with the locally spalled regions contribute significantly to the overall macroscopic failure of the specimen. For the coal sample with a bedding angle of 60°, the strength of the specimen is the lowest, and a shear failure surface, consistent with the bedding angle of 60°, is clearly visible. This indicates that the coal sample with a 60° bedding angle fails along the structural weakness of the interface, where the coal rock is more likely to form tensile or tensile-shear type fractures at the bedding junction, eventually leading to single-shear plane failure or X-shaped conjugate shear failure. For the coal sample with a bedding angle of 90°, the final macroscopic failure mode of the coal sample is longitudinal tensile splitting failure. During loading, longitudinal tensile cracks first initiate at the edges of the specimen and extend inward. After local penetration, the sample experiences localized spalling. As the longitudinal cracks gradually develop, the coal rock sample undergoes overall failure.

3.4. Evolution Characteristics of Spatial Shifting Along Measurement Lines

In order to more clearly depict the displacement and sliding behavior of the bedding planes during the failure process and to reveal the displacement-strain evolution of anisotropic bedding during failure, characteristic monitoring lines were arranged on coal rock samples with different bedding angles, as shown in Figure 9, to record the displacement changes. The monitoring results of the characteristic displacements for coal rock samples with different bedding angles are shown in Figures 10 and 11. These figures present the vertical spatial displacement along Monitoring Line 1 and the horizontal spatial displacement along Monitoring Line 2 for different bedding angles, along with the variations corresponding to different loading stages.

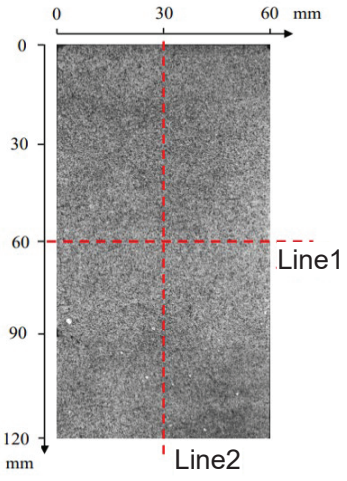

Figure 9. Feature line selection diagram.

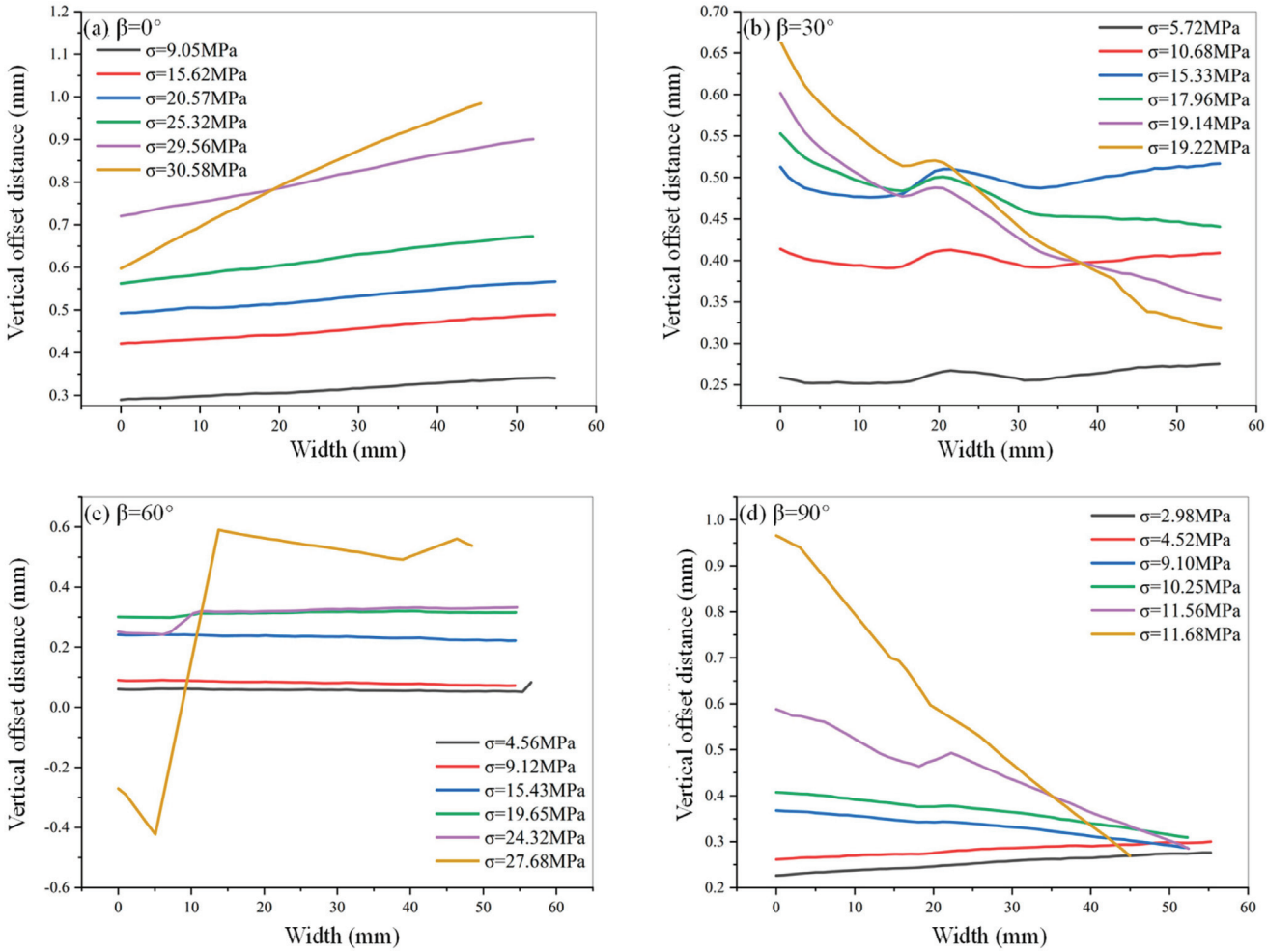

Figure 10. Vertical spatial migration evolution characteristics of Monitoring Line 1: (**a**–**d**) The bedding angles are 0°, 30°, 60° and 90°, respectively.

As shown in Figures 10 and 11,the vertical and horizontal spatial displacement distances for coal samples with different bedding angles are not uniformly distributed along the monitoring lines. The vertical spatial displacement along horizontal Monitoring Line 1 is notably influenced by the bedding angle. For coal samples with bedding angles of 30° and 60°, the vertical displacement shows a characteristic shift along the bedding planes, whereas for coal samples with bedding angles of 0° and 90°, the vertical displacement is parallel to the horizontal Monitoring Line 1. However, for the coal sample with a bedding angle of 90°, significant lateral displacement during failure causes a large variation in the vertical displacement along the horizontal direction.

The distribution of the horizontal spatial displacement along Monitoring Line 2 is significantly influenced by the end effects of the sample during loading. The horizontal displacement at the bottom of the sample is larger, while the top is constrained by the platen, resulting in smaller horizontal displacement at the upper end. As the load increases, both the vertical spatial displacement at the monitoring points along Monitoring Line 1 and the horizontal spatial displacement at the points along Monitoring Line 2 gradually increase. However, for coal samples exhibiting X-shaped conjugate shear failure, there is a sharp reverse increase in the horizontal spatial displacement near failure, just moments before the sample undergoes catastrophic failure.

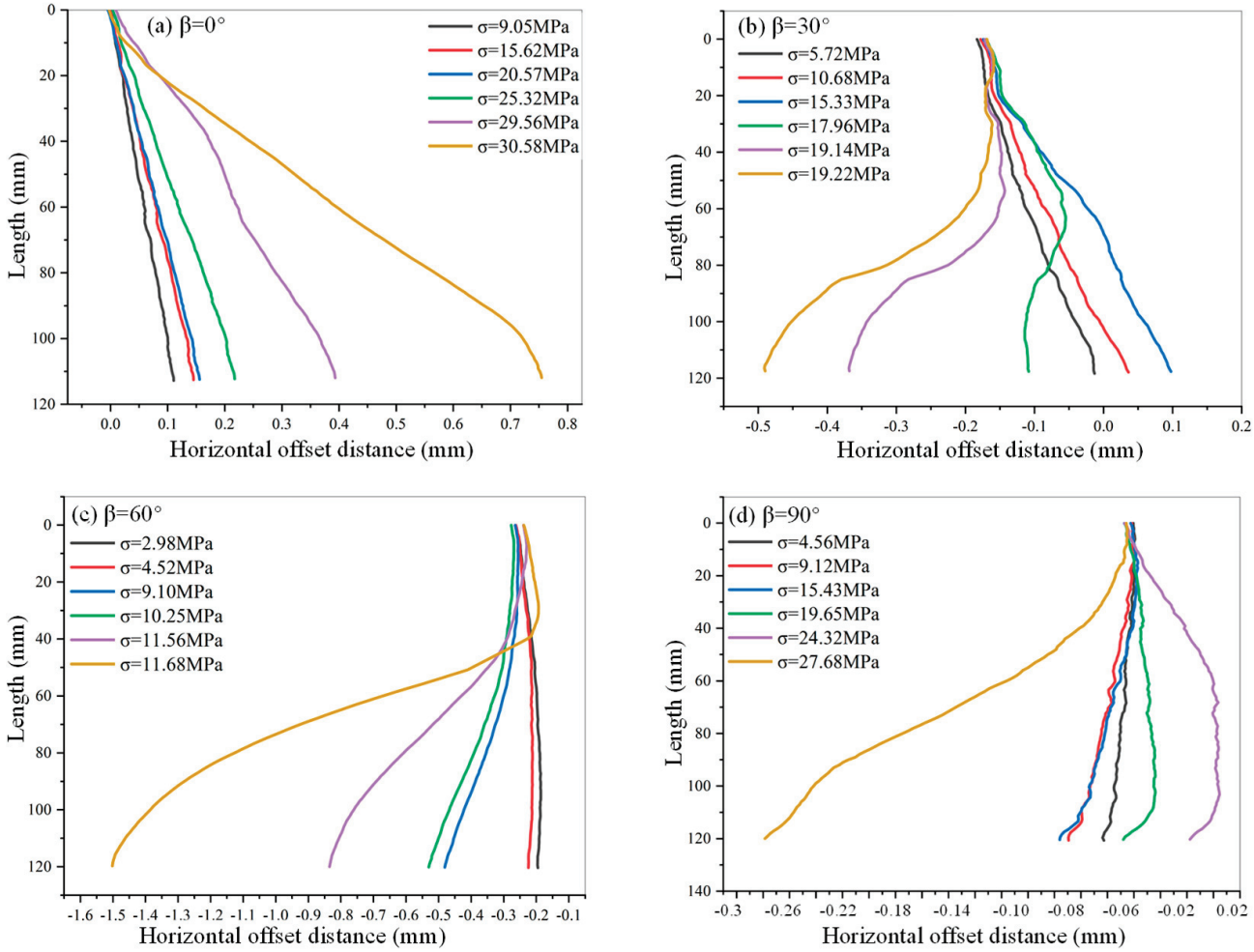

Figure 11. Evolution characteristics of horizontal spatial displacement along characteristic Measurement Line 2: (**a**–**d**) Bedding angles of 0°, 30°, 60°, and 90°, respectively.

4. Discussions

The present study systematically investigates the anisotropic creep behavior and failure mechanisms of coal under sustained loading, employing DIC-based full-field strain monitoring. The results demonstrate that bedding orientation plays a crucial role in governing the mechanical response, creep deformation, and ultimate failure mode of coal specimens. The bedding orientation has obvious influence on the creep properties of coal. The observed non-monotonic variation in peak strength—initially decreasing and then increasing with bedding angle—aligns with previous studies on anisotropic rocks (e.g., shale and layered coal). The minimum strength at intermediate angles (30–60°) suggests that bedding planes act as weak interfaces, facilitating shear slip under load. In contrast, at 0° and 90°, the load is primarily resisted by the intact coal matrix, leading to higher strength. The creep behavior, characterized by distinct stages (instantaneous deformation, decelerating, steady-state, and accelerating creep), is consistent with classic rock creep theory. However, the pronounced creep deformation at high stress levels highlights the time-dependent weakening effect, which is critical for long-term stability assessment in coal mine roadways. The DIC analysis reveals that strain localization evolves differently depending on bedding orientation. For 0° and 90° specimens, strain concentrates along axial planes, culminating in tensile splitting fractures—a typical brittle failure mode under uniaxial compression. In contrast, 30° and 60° specimens exhibit strain accumulation

along bedding planes, leading to combined tensile-shear failure. This transition from matrix-dominated to bedding-controlled failure underscores the importance of structural anisotropy in coal's mechanical behavior. Similar observations have been reported in layered rock mechanics, but the present study provides quantitative strain-field evidence, enhancing understanding of progressive damage evolution.

The findings have direct implications for coal mine disaster prevention. The strong dependence of creep behavior on bedding angle suggests that roadway support strategies should account for local bedding orientation. For instance, in areas with intermediate bedding angles (30–60°), where shear failure dominates, enhanced reinforcement (e.g., bolting and grouting) along weak planes may be necessary. Additionally, the accelerating creep stage prior to failure could serve as a precursor for early warning systems, allowing for timely intervention. While this study provides valuable insights, certain limitations should be addressed in future research. The experiments were conducted under uniaxial conditions, whereas in situ coal is typically under triaxial stress. Future tests should incorporate confining pressure to better simulate underground conditions. A constitutive model incorporating bedding angle effects should be developed to predict coal's time-dependent deformation under various stress paths.

5. Conclusions

This study investigates the full-field strain characteristics of anisotropic coal samples under creep loading using the DIC testing system to investigate the anisotropic deformation characteristics. The full-field strain evolution and crack propagation characteristics under creep loading were obtained, revealing the influence of anisotropic bedding angles on the strength and deformation characteristics of coal samples. The main results are summarized as follows:

(1) The peak strength of coal under creep loading is significantly affected by the bedding angle. As the bedding angle increases, the peak strength first decreases and then increases. Under the same stress level, coal samples with bedding angles of 0° and 90° exhibit stronger resistance to deformation, while coal samples with a bedding angle of 60° show the weakest deformation resistance, making them more prone to creep sliding failure along the bedding planes.

(2) For coal samples with different bedding orientation, creep failure is characterized by a process of instantaneous deformation, decelerating creep, steady-state creep, accelerating creep, and eventual failure. Under multi-stage loading conditions, coal samples show significant creep behavior under higher loading levels in the final stage.

(3) The bedding angle significantly affects the strain field evolution of coal samples. Regions of concentrated displacement changes typically occur at the intersections between bedding planes, and cracks tend to initiate and propagate at bedding interfaces. During the early stages, coal samples remain in a compressed and densified state. Just before failure, within seconds of reaching the peak stress, the strain range shows dramatic changes, followed by the formation of crack bands and overall macro failure.

(4) The post-peak stress–strain curve behavior is closely related to the failure modes of the coal structure. For coal samples with bedding angles of 0° and 90°, the final macroscopic failure mode is characterized by longitudinal tensile splitting failure; for coal samples with bedding angles of 30° and 60°, failure tends to occur along the bedding interfaces, forming tensile or tensile-shear failure, leading to single-shear plane failure or X-shaped conjugate shear failure.

Author Contributions: Experiments and writing, X.L.; funding acquisition, Y.W.; methodology, X.Y.; software, X.B. All authors have read and agreed to the published version of the manuscript.

Funding: This study was supported by the Geological Survey Project of the China Geological Survey (DD20230437).

Institutional Review Board Statement: Not applicable.

Informed Consent Statement: Not applicable.

Data Availability Statement: The original contributions presented in the study are included in the article; further inquiries can be directed to the corresponding author.

Conflicts of Interest: The authors declare no conflicts of interest.

References

1. Mohamed, K.M.; Tulu, I.B.; Klemetti, T. Numerical simulation of deformation and failure process of coal-mass. In Proceedings of the 49th U.S. Rock Mechanics/Geomechanics Symposium, San Francisco, CA, USA, 28 June–1 July 2015.
2. Jenkins, D.R.; Lomas, H.; Mahoney, M. Uniaxial compression of metallurgical coke samples with progressive loading. *Fuel* **2018**, *226*, 163–171. [CrossRef]
3. Li, H.; He, M.; Qiao, Y.; Cheng, T.; Han, Z. Assessing burst proneness and seismogenic process of anisotropic coal via the realistic energy release rate (RERR) index. *Rock Mech. Rock Eng.* **2025**, *58*, 2999–3013. [CrossRef]
4. Ghazvinian, A.; Hadei, M.R.; Madani, B. Behavior of mechanical anisotropic specimens under triaxial testing. In Proceedings of the 42nd U.S. Rock Mechanics Symposium (USRMS), San Francisco, CA, USA, 29 June–2 July 2008.
5. Wang, W.; Zhao, B.; Zhao, Y. Effects of bedding orientation and loading rate on fracture behaviors in coal: Analysis of experiments. *Theor. Appl. Fract. Mech.* **2025**, *139*, 105012. [CrossRef]
6. Shkuratnik, V.L.; Filimonov, Y.L.; Kuchurin, S.V. Regularities of acoustic emission in coal samples under triaxial compression. *J. Min. Sci.* **2005**, *41*, 44–52. [CrossRef]
7. Wang, Y.; Chen, Z.; Xia, Y.; Li, P.; Cai, M. The Effect of Cyclic Disturbed Frequency on Mechanical, Acoustic Emission and Crack Pattern for Rock–Backfill Composites Exposed to Fatigue Loading Condition. *Rock Mech. Rock Eng.* **2025**, *58*, 7041–7066. [CrossRef]
8. Liu, H.; Li, F.; Xu, L. Dynamic response and failure mechanisms of laminated soft coal under impact loads: A comprehensive study. *Soil Dyn. Earthq. Eng.* **2025**, *198*, 109546. [CrossRef]
9. Hu, B.; Wu, Y.; Xie, P.; Wang, H.; Wen, H. A novel DEM for coal–rock dynamic failure based on grain reconstruction and dynamic–static mechanical behaviour calibration. *Powder Technol.* **2025**, *461*, 121101. [CrossRef]
10. Li, J.; Wang, H.C.; Zhang, Q.B. Progressive damage and fracture of biaxially-confined anisotropic coal under repeated impact loads. *Int. J. Rock Mech. Min. Sci.* **2022**, *149*, 104979. [CrossRef]
11. Poulsen, B.A.; Adhikary, D.P. A numerical study of the scale effect in coal strength. *Int. J. Rock Mech. Min. Sci.* **2013**, *63*, 62–71. [CrossRef]
12. Yang, S.; Zhang, N.; Feng, X.; Kan, J. Experimental investigation of the creep behaviour of coal by monitoring changes of acoustic properties. *Appl. Sci.* **2018**, *8*, 633. [CrossRef]
13. Zhang, L.; Li, X.; Ren, T. A theoretical and experimental study of stress–strain, creep and failure mechanisms of intact coal. *Rock Mech. Rock Eng.* **2020**, *53*, 5641–5658. [CrossRef]
14. Huang, P.; Zhang, J.; Spearing, A.S.; Chai, J.; Dong, C. Experimental study of the creep properties of coal considering initial damage. *Int. J. Rock Mech. Min. Sci.* **2021**, *139*, 104629. [CrossRef]
15. Guo, J.; Zong, D.; Ma, L. Creep damage characteristics and constitutive model of pre-damage coal. *Eng. Fail. Anal.* **2024**, *158*, 108002. [CrossRef]
16. Mishra, B.; Verma, P. Uniaxial and triaxial single and multistage creep tests on coal-measure shale rocks. *Int. J. Coal Geol.* **2015**, *137*, 55–65. [CrossRef]
17. Reuter, M.; Krach, M.; Kießling, U.; Veksler, Y. Zonal disintegration of rocks around breakage headings. *J. Min. Sci.* **2015**, *51*, 237–242. [CrossRef]
18. Li, X.; Zhao, E.; Liu, Z.; Liu, Y.; Feng, X.; Gu, Z. Experimental study on multiple propagation characteristics of stress wave and surface displacement behavior in coal based on SHPB and DIC. *Bull. Eng. Geol. Environ.* **2023**, *82*, 246. [CrossRef]
19. Yi, X.; Wang, Y.; Xia, Y.; Li, P.; Cai, M. Macro–Meso Failure Behaviors of Weak Interlayer Contained Hollow Cylindrical Granite Exposed to Alternative Fatigue–Creep–Unloading Conditions. *Fatigue Fract. Eng. Mater. Struct.* **2025**, *48*, 3092–3109. [CrossRef]

20. Wang, G.; Xu, J.; Yuan, Y.; Hu, C.; Mei, Y. Innovative surface scanning and digital image correlation analysis of cracking in compacted loess during drying-wetting cycles. *Bull. Eng. Geol. Environ.* **2025**, *84*, 375. [CrossRef]
21. Chen, J.; Yang, C.; Pan, X.; Chen, Z.; Li, Z.; Du, J. Crack evolution behaviors and AE-DIC characteristics of double fractured sandstone considering the influence of high temperature. *Theor. Appl. Fract. Mech.* **2025**, *139*, 104990. [CrossRef]
22. Zhang, Y.; Sun, B.; Ren, Y. Full-field deformation evolution characteristics of freeze-thawed fault zone rock mass revealed by digital image correlation: A lab-scale investigation. *Front. Mater.* **2025**, *12*, 1615128. [CrossRef]
23. Munoz, H.; Taheri, A.; Chanda, E.K. Pre-peak and post-peak rock strain characteristics during uniaxial compression by 3D digital image correlation. *Rock Mech. Rock Eng.* **2016**, *49*, 2541–2554. [CrossRef]

applied sciences

MDPI

Article

Characteristics of Mining-Induced Stress Rotation Due to Unloading in Deep Roadway Excavation and Surrounding Rock Control Countermeasures

Diyuan Li, Hao Gong, Zhenyu Han *, Wenkai Ru and Pingkuang Luo

School of Resources and Safety Engineering, Central South University, Changsha 410083, China; gonghao13044486112@163.com (H.G.)
* Correspondence: zhenyu.han@csu.edu.cn

Abstract

As metal mines advance into deep mining, the increase in tectonic stress and horizontal stress leads to a higher degree of joint and fissure development in roadway surrounding rocks, along with a significant rise in both the fragmentation degree of the rock mass and the support cost. This paper adopts field monitoring and numerical simulation methods to analyze the characteristics of mining-induced stress rotation after unloading due to deep roadway excavation in the Jinchuan mining area, and proposes corresponding surrounding rock control countermeasures and optimized schemes for the original support. The research results show that after the unloading caused by the excavation of deep roadway surrounding rock, the magnitudes and directions of the maximum, intermediate, and minimum principal stresses all exhibit a trend of slow change, followed by drastic change, and finally gradual stabilization. When the roadway advances to 4 m in front of the monitor section, the adjustment of the magnitude of principal stress of the surrounding rock is the most drastic. Moreover, as the working face moves away from the monitor section, the principal stress gradually stabilizes and becomes lower than the initial stress value. When the roadway advances to 6 m in front of the monitor section, the adjustment of the direction of the principal stress of the surrounding rock is the most drastic. The rotation angle of the maximum principal stress shows a trend of first increasing and then decreasing with the increase in the excavation step, while the rotation angles of the intermediate and minimum principal stresses show a trend of first decreasing and then increasing as the excavation step increases. Based on the spatial distribution characteristics of joints and fissures in the roadway surrounding rock, the sensitive area for the rotation of mining-induced stress direction is defined. By changing the advancing direction of the roadway, the rotation trajectory of the principal stress can be deviated from the sensitive area, thereby improving the self-stabilization ability of the roadway surrounding rock. It is proposed that asymmetric coupling support be adopted to reinforce the positions where the principal stress rotation of the rock mass around the anchorage is severe, which can effectively reduce the range of the plastic zone in the roadway surrounding rock. The research results provide new ideas for the surrounding rock control of deep roadways, as well as a theoretical basis for the design and optimization of roadway support parameters in similar mines.

Keywords: deep mines; principal stress rotation; joints and fissures; surrounding rock stability; asymmetric support

1. Introduction

As metal mines gradually move into deep mining, the increase in tectonic stress and the enhancement of mining disturbance effects have led to a higher degree of development of joints and fissures in the surrounding rock of deep roadways, as well as an aggravation of rock mass fragmentation [1–4]. Affected by mining disturbance effects, engineering disasters such as floor heave in deep roadways [5], large deformation of surrounding rock on both sides [6], roof subsidence [7], and failure of support structures [8] occur frequently, which seriously affect the tunneling efficiency of deep mines and the safe recovery of resources [9,10]. Therefore, existing supports for deep roadways are not enough to control the impact of mining-induced stress rotation on the damage and failure of the surrounding rock, so it is necessary to optimize the support scheme according to the characteristics of mining-induced stress rotation of the surrounding rock [11].

After the excavation and unloading of deep roadways, the initial in situ stress is redistributed, which is mainly manifested in the changes in the magnitude and the rotation of the direction of the principal stress [12]. Kaiser et al. [13,14] hold that the change in the direction of the principal stress in the roadway surrounding rock has a significant impact on the failure mode of the rock mass and the fracture propagation path. Eberhardt et al. [15] argue that during the excavation of underground space engineering, the rotation of principal stresses plays a decisive role in the propagation path of fractures. Therefore, the change in the magnitude of the principal stress controls the depth of the propagation of joints and fissures in rock mass in the vicinity of roadway, while the change in the direction of the principal stress controls the direction and density of such propagation [16,17]. Due to the limitations of indoor test equipment, most studies on the stress paths of deep rock masses are based on tests such as uniaxial compression [18], triaxial compression [19], dynamic loading [20], and combined dynamic–static loading [21], often neglecting the impact of stress rotation paths on roadway surrounding rock [22]. At present, the hollow torsional shear test is one of the methods used to study the influence of principal stress rotation paths on the mechanical properties of roadway surrounding rocks [23], and the rotation angle of principal stress significantly affects the development degree of torsional shear cracks in the rock mass during the failure process [24]. In terms of theoretical analysis, Zuo et al. [25] established a mechanical model of deep roadways under three-dimensional stress conditions and revealed the influences of the two types of stress adjustments on the failure modes of roadways based on the magnitude and rotation law of principal stresses. Xiong et al. [26] established a comprehensive criterion that accounts for the coupling effects of multiple factors, quantifying the influence of the principal stress rotation angle on the stability of support structures. In terms of numerical simulation, Wang et al. [27,28] studied the rotation characteristics of mining-induced stress in deep mines with ultra-long working faces and proposed a method to control deep rock masses by utilizing these rotation characteristics. Lu et al. [29] analyzed the evolution law of the principal stress direction during fault activation using numerical software. In terms of field applications, Oliva et al. [30] hold that the rotation of the stress field reflects the key role played by rift magmatic activities in shaping landforms and plate stress states, as well as volcanic and tectonic processes.

To sum up, the characteristics of principal stress rotation in the surrounding rock of deep roadways have an impact on the mechanical properties, crack propagation paths, and final failure modes of the rock mass. Due to the fact that the law of principal stress rotation induced by roadway excavation in deep hard rock metal mines is still unclear, conventional support methods are difficult to effectively control the large deformation of surrounding rock. Therefore, taking the deep roadways in the Jinchuan mining area as the

engineering background and based on the FLAC^{3D} 6.0 numerical simulation software, this paper studies the evolution laws of the magnitude and direction of the subsequent stress in the surrounding rock after roadway excavation. In response to the characteristics of mining-induced stress rotation in rock mass in the vicinity of a roadway, the concept of a principal stress direction sensitive area is proposed. By altering the trajectory of mining-induced stress rotation, the self-stabilization capacity of the rock mass is enhanced. Additionally, this paper optimizes the original support scheme and puts forward a suggestion: the adoption of asymmetric coupled support can effectively control the deformation degree of roadway surrounding rocks and improve the self-stability of rock mass.

2. Engineering Background and Numerical Simulation

2.1. Engineering Background

As shown in Figure 1, this paper takes the deep roadway in Jinchuan II Mining Area, Jinchang City, Gansu Province, China, as the engineering background. The common cross-sectional form of deep roadways in the Jinchuan mining area is a straight-wall semicircular arch, with a straight-wall height of 2 m, a semicircular arch radius of 2.5 m, an overall roadway height of 4.5 m, and an overall roadway width of 5 m. Most of the roadways adopt combined shotcrete–bolt–mesh support. The roadway is buried at a depth of over 1100 m, with well-developed joints and fissures in the rock mass. Under the compression of high in situ stress, the surrounding rock is severely broken, and the mechanical conditions are complex, leading to poor overall stability of the surrounding rock in the deep roadway.

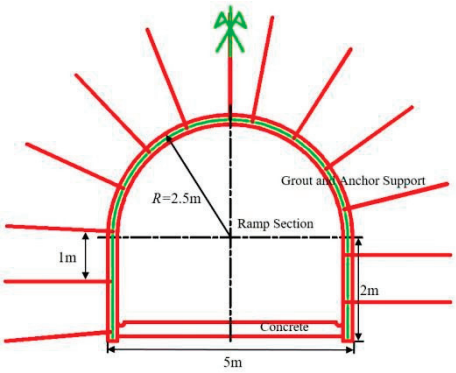

Figure 1. Support parameters of development roadways.

As shown in Figure 2, the development system of Jinchuan II Mining Area adopts a combined development mode of a main ramp and a vertical shaft. In situ stress testing is carried out using the hollow inclusion stress relief method. The in situ stress measurement is conducted in other areas of Jinchuan II Mine. Fitting analysis of the statistical results reveals that the in situ stress is dominated by horizontal stress, with the maximum horizontal in situ stress exceeding 50 MPa and the lateral pressure coefficients being 1.15 and 1.80, respectively. The Rock Quality Designation (RQD) value of the roadway surrounding rock is 29. As shown in Figure 3, Poisson's ratio, elastic modulus, and unconfined compressive strength (UCS) are obtained through uniaxial compression tests; tensile strength is obtained through Brazilian splitting tests; and cohesion and internal friction angle are obtained through variable-angle shear tests. The basic physical and mechanical properties of the rock mass are shown in Table 1. Due to the strong rheological properties of deep rock masses, the surrounding rock of the roadway undergoes various forms of structural damage, mainly including roof crushing failure, shear dislocation of the sidewall surrounding rock, and tensile floor heave failure. The surrounding rock of deep roadways generally exhibits

a full-section convergence and deformation mode, which not only increases the number of roadway repairs but also severely restricts the driving efficiency and raises the roadway repair cost.

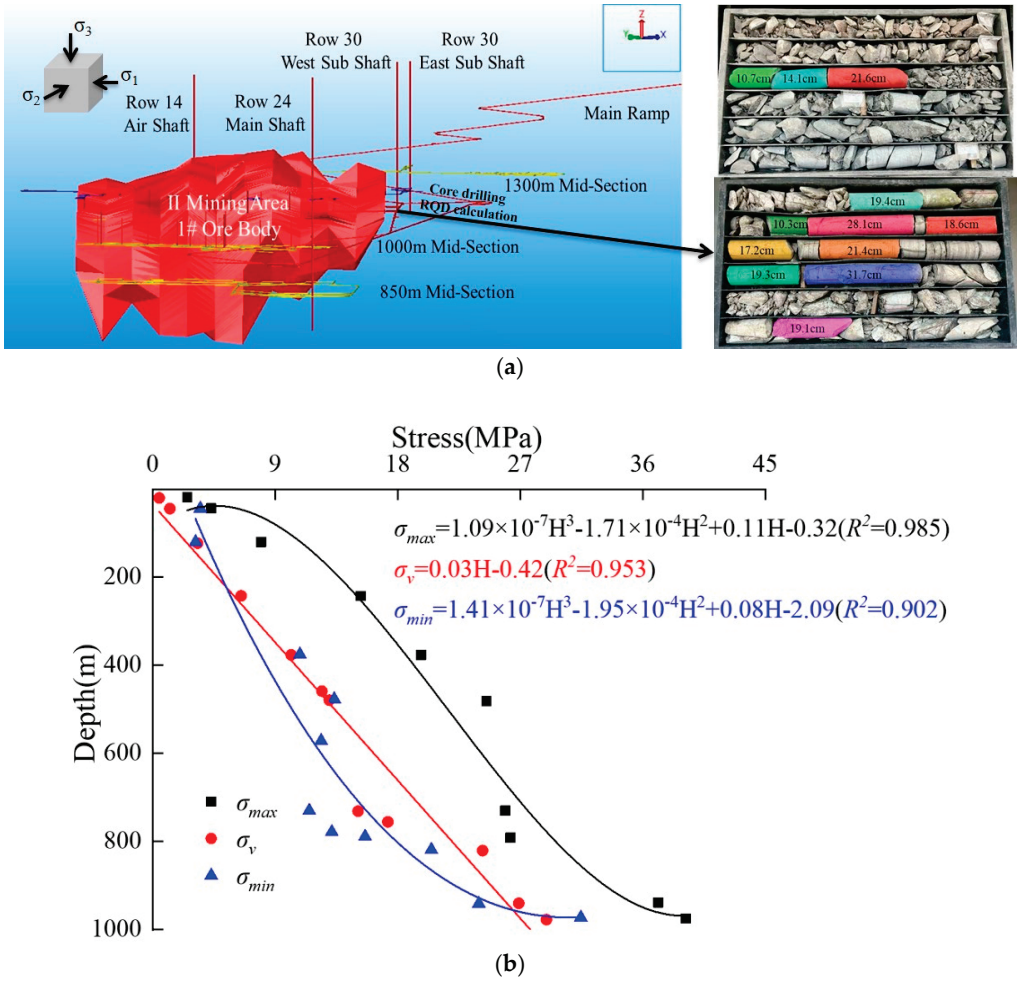

Figure 2. Roadway development engineering and in situ stress distribution in Jinchuan II Mining Area: (**a**) roadway development engineering; (**b**) in situ stress distribution.

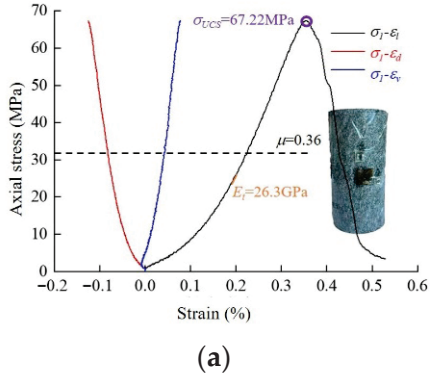

Figure 3. *Cont.*

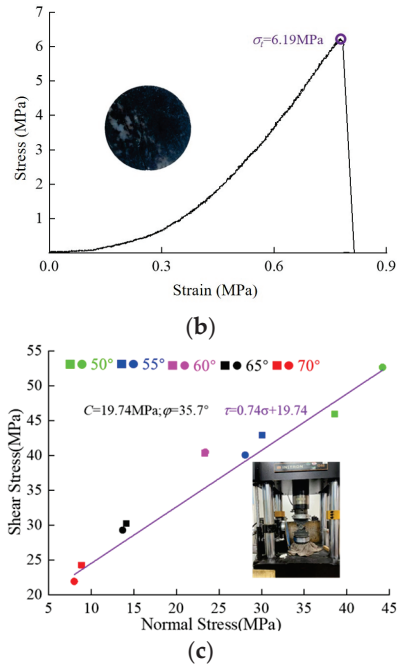

Figure 3. Testing of rocks mechanical parameters: (**a**) uniaxial compression tests; (**b**) Brazilian splitting tests; (**c**) variable-angle shear tests.

Table 1. Basic mechanical parameters of rocks in deep roadways.

Lithology	σ_c (MPa)	σ_t (MPa)	Cohesion (MPa)	Friction Angle (°)	Elastic Modulus (GPa)	Poisson's Ratio	Density (g/cm^3)
Diorite	67.22	6.19	19.74	35.7	26.3	0.36	2.84

2.2. Construction and Reliability Verification of Numerical Model

As shown in Figure 4, in order to study the evolution laws of the magnitude and direction of the maximum, intermediate, and minimum principal stresses during the excavation and unloading process of the surrounding rock in deep roadways, this paper constructs a three-dimensional numerical model based on the FLAC^{3D} numerical simulation software. The numerical model is a cube with a side length of 40 m, and the roadway cross-section is a standard straight-wall semicircular arch commonly used in the Jinchuan mining area. The nodes at the bottom and surrounding sides of the numerical model adopt sliding displacement boundary conditions, where the boundaries are only fixed in displacement in their normal direction, while sliding is allowed in the direction parallel to the normal direction. Stress boundary conditions are applied to the nodes at the top of the numerical model to simulate the self-weight stress of the unmodeled rock strata. The maximum principal stress σ_1 (58.85 MPa) of the initial stress field in the numerical model is set to be perpendicular to the roadway advance direction (along the *X*-axis), the intermediate principal stress σ_2 (37.47 MPa) parallel to the roadway advance direction (along the *Y*-axis), and the minimum principal stress σ_3 (32.58 MPa) distributed along the vertical direction (along the *Z*-axis). As shown in Figure 5, the geological strength index GSI values for deep roadway surrounding rock are firstly determined. Secondly, the grading parameters and strength parameters of the generalized Hoek–Brown strength criterion are calculated. Finally, the Hoek–Brown strength criterion grading parameters and strength parameters of different lithological surrounding rock are imported into RockData 3.0 software to establish the Hoek–Brown strength criterion and Mohr–Coulomb strength relationship. The surrounding rock of the deep roadway is altered diorite. The specific mechanical parameters are shown in

Table 2. The constitutive model assigned to the numerical simulation elements is the ideal elastoplastic model (Mohr–Coulomb constitutive model).

$$\sigma_1 = \sigma_3 + \sigma_{ci}\left(m_b \frac{\sigma_3}{\sigma_{ci}} + s\right)^a \tag{1}$$

$$m_b = m_i \exp\left(\frac{GSI - 100}{28 - 14D}\right) \tag{2}$$

$$s = \exp\left(\frac{GSI - 100}{9 - 3D}\right) \tag{3}$$

$$a = \frac{1}{2} + \frac{\exp(-GSI/15) - \exp(-20/3)}{6} \tag{4}$$

where σ_{ci} is the uniaxial compressive strength of the rock, MPa; m_b, s, a are semi-empirical parameters for rock mass properties; m_i is the rock material constant; and D is the weakening factor of the rock mass disturbed by anthropogenic or natural factors, taking the value of 0.5.

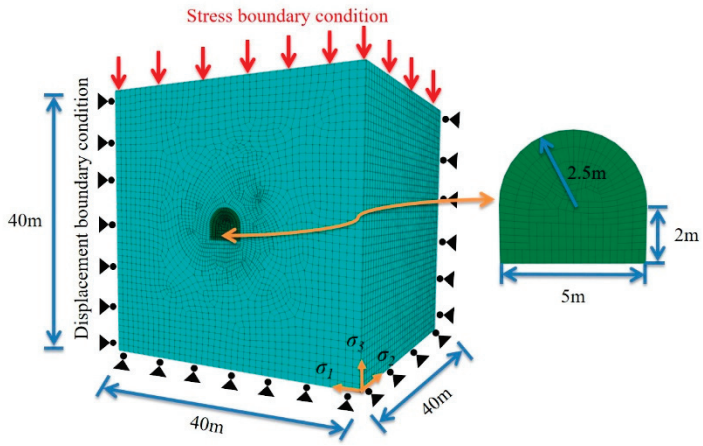

Figure 4. Construction of numerical model.

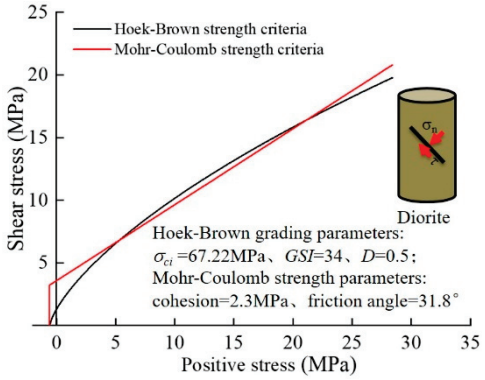

Figure 5. Determination of deep roadway surrounding rock parameters based on RockData 3.0 software.

Table 2. Basic mechanical parameters of surrounding rock in deep roadways.

Lithology	Cohesion (MPa)	Friction Angle (°)	Elastic Modulus (GPa)	Poisson's Ratio	Tension Strength (MPa)
Diorite	2.3	31.8	2.63	0.32	1.17

As shown in Figure 6, due to the fact that the traditional drilling and blasting technology is adopted for roadway excavation in the Jinchuan mining area, with an advance footage of approximately 2 m, the roadway excavation is carried out in a step-by-step manner, with a step distance of 2 m. Stress monitoring points are arranged on the roof, two sidewalls, and floor of the deep roadway, respectively, with 15 monitoring points at each location, and the distance between each monitoring point is 1 m. The mining distance of the deep roadway along the *Y*-axis is 40 m, and the stress monitoring points are arranged at the middle position of the *Y*-axis, with an advancing distance $L = 0$.

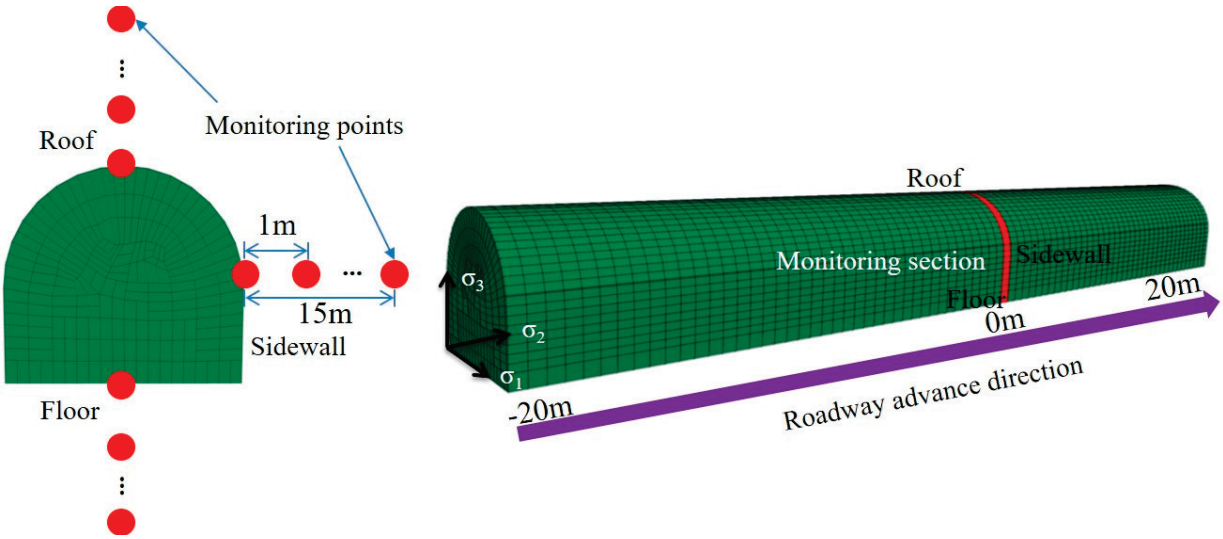

Figure 6. Layout of monitoring points for surrounding rock of deep roadways.

As shown in Figure 7, to verify the reliability of the numerical model, displacement monitoring points are arranged on the roof, floor, and sidewall surrounding rocks of the 1150 m sublevel ramp in Jinchuan II Mining Area. The deformation of the roadway surrounding rocks is monitored in real time by a multi-point displacement meter, with an overall monitoring period of 30 d. Since installing multi-point displacement meter on the roadway floor for displacement monitoring would interfere with vehicle traffic, no on-site monitoring of the floor surrounding rock is conducted. The multi-point displacement meter is 8 m, contains 5 monitoring points, and can cover deformation monitoring in the depth range of 0–6 m. It is mainly arranged on the roof and sidewalls of deep roadways. The displacement vectors of the monitoring points in the surrounding rock of the deep roadway all point to the free surface. The deformation of the floor surrounding rock is the largest, followed by that of the two sidewalls, with the maximum deformation reaching 310 mm. The deformation magnitude of the surrounding rock in the deep roadways of the Jinchuan mining area shows a variation trend of first increasing and then decreasing as the monitoring time increases. Due to the three stages of rapid accumulation, sudden release, and slow adjustment of elastic energy in the surrounding rock after the excavation and unloading of deep roadways, the convergent deformation of the surrounding rock also undergoes three stages: slow initiation, rapid development, and stable growth. Since the deformation of the roadway surrounding rock extracted from the numerical simulation is close to the on-site monitoring results and the variation trends are consistent, the subsequent research on the rotation characteristics of mining-induced stress can be carried out.

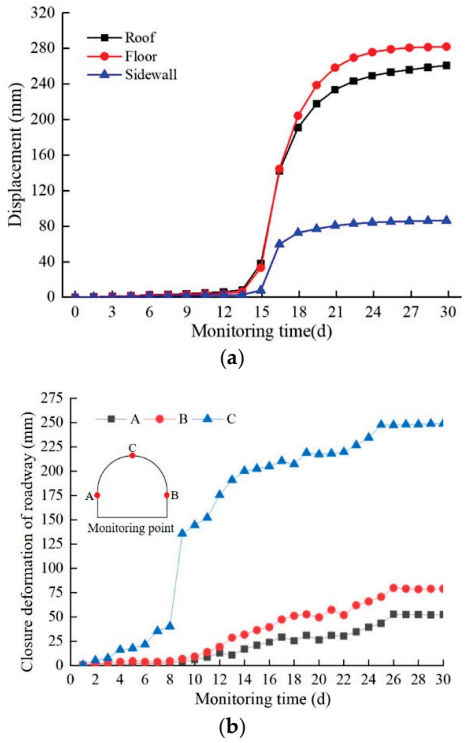

Figure 7. Monitoring of surrounding rock deformation in deep roadways: (**a**) numerical simulation results; (**b**) field monitoring results.

3. Evolution Characteristics of Mining-Induced Stress in Surrounding Rock During Excavation and Unloading of Deep Roadways

3.1. Mechanism of Principal Stress Rotation in Surrounding Rock

As shown in Figure 8, before being disturbed by mining activities, the surrounding rock of the deep roadway is in a state of triaxial stress. When the surrounding rock of the roadway is disturbed by excavation, the initial stress state of the rock mass is broken, and the stress field begins to redistribute, which is mainly manifested in two aspects: the change in the magnitude of the principal stress and the rotation of its direction. Obvious shear dislocation phenomena begin to occur between deep rock layers, and shear stress emerges inside the surrounding rock. The new principal stress plane of the surrounding rock can be determined by the Mohr stress circle, and the angle between the new principal stress plane and the initial principal stress plane is the principal stress rotation angle θ.

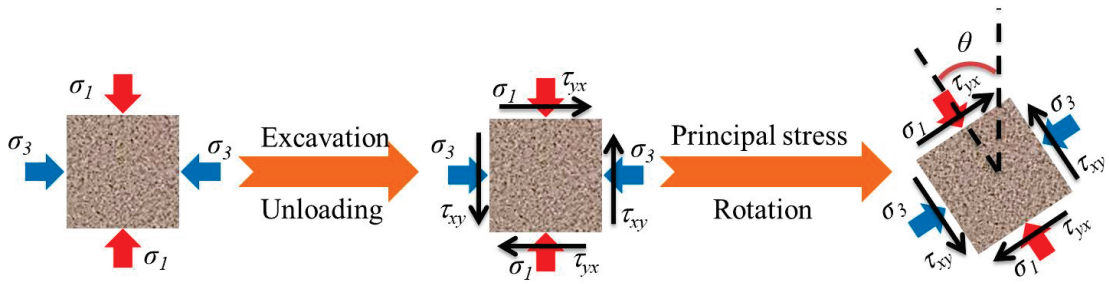

Figure 8. Schematic diagram of principal stress rotation in surrounding rock of deep roadways.

In the FLAC^{3D} numerical simulation software, the six stress components, namely, σ_x, σ_y, σ_z, τ_{xy}, τ_{yz}, and τ_{zx}, of each monitoring point can be extracted through the Zone.stress() function. According to the theory of generalized plastic mechanics [31], the three principal

stress directions acting on a rock mass element are orthogonal to each other. Therefore, the rotation angle θ of the principal stress is calculated by solving the cosine values of the angles between the three principal stress directions and their respective plane axes (X, Y, Z), to describe the variation process of principal stress directions. Reference [12] provides the calculation formulas for the cosine values L_i, M_i, N_i corresponding to the principal stress σ_i (i = 1, 2, 3) and the X, Y, Z axes. The angles α_i, β_i, γ_i between the principal stress σ_i and the X, Y, Z axes can be solved by Equations (5)–(9).

$$L_i = \frac{\sigma_i + \tau_{xy}\tau_{yz} - \sigma_y}{\sqrt{\left[(\sigma_x - \sigma_i)(\sigma_y - \sigma_i) - \tau_{xy}^2\right]^2 + \left[\tau_{xy}\tau_{zx} - (\sigma_x - \sigma_i)\right]^2 + \left[\tau_{xy}\tau_{yz} - (\sigma_y - \sigma_i)\right]^2}} \tag{5}$$

$$M_i = \frac{\sigma_i + \tau_{xy}\tau_{zx} - \sigma_x}{\sqrt{\left[(\sigma_x - \sigma_i)(\sigma_y - \sigma_i) - \tau_{xy}^2\right]^2 + \left[\tau_{xy}\tau_{zx} - (\sigma_x - \sigma_i)\right]^2 + \left[\tau_{xy}\tau_{yz} - (\sigma_y - \sigma_i)\right]^2}} \tag{6}$$

$$N_i = \frac{(\sigma_x - \sigma_i)(\sigma_y - \sigma_i) - \tau_{xy}^2}{\sqrt{\left[(\sigma_x - \sigma_i)(\sigma_y - \sigma_i) - \tau_{xy}^2\right]^2 + \left[\tau_{xy}\tau_{zx} - (\sigma_x - \sigma_i)\right]^2 + \left[\tau_{xy}\tau_{yz} - (\sigma_y - \sigma_i)\right]^2}} \tag{7}$$

$$L_i^2 + M_i^2 + N_i^2 = 1 \tag{8}$$

$$\begin{cases} \alpha_i = \arccos L_i \\ \beta_i = \arccos M_i \\ \gamma_i = \arccos N_i \end{cases} \tag{9}$$

As shown in Figure 9, after the surrounding rock of the deep roadway is disturbed by excavation, the directions of the maximum, intermediate, and minimum principal stresses change, and their variation process can be described by the dip angle and azimuth angle. Define the rotation dip angle θ_i of the initial principal stress and secondary principal stress as the angle between the direction of the principal stress and the XOY plane; define the rotation azimuth angle ψ_i of the principal stress as the angle through which the projection of the principal stress direction onto the XOY plane rotates clockwise to the reference point.

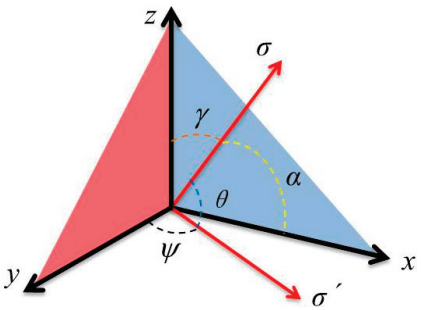

Figure 9. Schematic diagram of rotation dip angle and azimuth angle of principal stress in surrounding rock of deep roadways.

It can be known from Equation (9) that the rotation dip angle θ_i and rotation azimuth angle ψ_i of the principal stress can be calculated through the angles α_i, β_i, γ_i between the principal stress σ_i and the X, Y, Z axes.

$$\theta_i = 90^\circ - \gamma_i \tag{10}$$

$$\psi_i = 180^\circ - \arctan(\frac{L_i}{N_i}) \tag{11}$$

3.2. Variation Process of the Principal Stress Magnitude in the Surrounding Rock

As shown in Figure 10, this is the variation process of the principal stress magnitude at different monitoring points in the surrounding rock of the deep roadway. When the driving face is in front of the monitoring section, with the increase in the roadway advance distance, the maximum, intermediate, and minimum principal stresses of the surrounding rock begin to increase slowly, which is mainly due to the small disturbance of the monitoring section in the early stage of roadway excavation. When the disturbance range of roadway excavation is 4 m away from the monitor section, the stress magnitude of the surrounding rock begins to adjust drastically. At this time, the maximum and intermediate principal stresses of the surrounding rock around the roadway increase rapidly, while the minimum principal stress starts to decrease, indicating that the excavation disturbance has a severe impact on the principal stress magnitude of the monitoring section. When the disturbance from roadway excavation advances to the monitor section, the principal stress of the surrounding rock reaches its peak value. The peak stress of the surrounding rock at the roadway floor is the largest (78.71 MPa) with a stress concentration factor of approximately 1.34; the peak stress of the surrounding rock at the two sides is the smallest (66.15 MPa) with a stress concentration factor of about 1.12, which indicates that the surrounding rock at the roadway floor is failing more severely. During the stage of severe adjustment of the principal stress in the roadway surrounding rock, the magnitude of the maximum principal stress changes most drastically, while the magnitude of the minimum principal stress changes relatively slowly. When the roadway driving face is located behind the monitoring section, the maximum and minimum principal stresses begin to decrease rapidly, and when reaching the position 2 m away from the monitoring section, the principal stresses gradually tend to stabilize. The intermediate principal stress shows a trend of first decreasing and then increasing, and gradually stabilizes at a position 10 m away from the monitoring section. Moreover, after the principal stress of the surrounding rock stabilizes, it is significantly lower than the initial stress value.

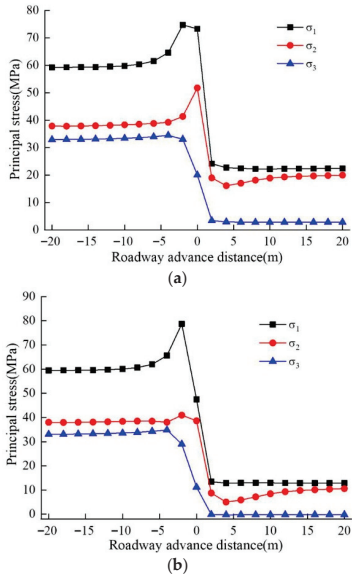

Figure 10. *Cont.*

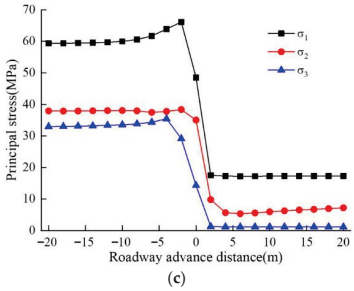

Figure 10. Variation process of principal stress magnitude at different monitoring points in surrounding rock of deep roadways: (**a**) roof surrounding rock; (**b**) floor surrounding rock; (**c**) sidewall surrounding rock.

3.3. Evolution Law of Principal Stress Direction in Surrounding Rock

As shown in Figure 11, this is the process of changes in the principal stress direction of the rock mass at different monitoring points in the deep roadways of the Jinchuan mining area. When the roadway driving face is far from the monitoring section, the degree of change in the principal stress dip angles of the rock mass in the roadway roof, floor, and both sidewalls is relatively slow. The rotation dip angle θ_1 of the maximum principal stress in the surrounding rock of the deep roadway increases slowly from the initial 0°, while the rotation dip angles θ_2 and θ_3 of the intermediate and minimum principal stresses decrease slowly from the initial 90°. When the disturbance range of roadway excavation is 6 m away from the monitor section, the principal stress direction of the surrounding rock begins to adjust drastically. The principal stress direction of the surrounding rock at the sidewalls undergoes the most significant change, while that of the surrounding rock at the floor changes the least. When the disturbance from roadway excavation advances to the monitor section, the rotation of the directions of the maximum and intermediate principal stresses in the surrounding rock reaches their peak values. The rotation dip angles of the maximum principal stress (θ_1) in the surrounding rock of the roof, floor, and sidewalls increase from 0° to their maximum values, which are 40.91°, 33.22°, and 88.94°, respectively; while the rotation dip angles of the intermediate principal stress (θ_2) decrease from 90° to their minimum values, which are 38.74°, 35.39°, and 1.13°, respectively. When the driving face is behind the monitor section, the rotation dip angle of the maximum principal stress in the roadway surrounding rock gradually decreases and tends to stabilize, while the rotation dip angle of the intermediate principal stress shows a trend of first increasing, then decreasing, and finally stabilizing. When the roadway driving face is approximately 2 m away from the monitoring section, the rotation dip angle θ_3 of the minimum principal stress in the rock mass decreases from 90° to its minimum values, which are 32.73°, 38.81°, and 3.05° respectively. As the roadway driving face moves away from the monitoring section, the rotation dip angle θ_3 of the minimum principal stress in the roadway rock mass gradually tends to stabilize.

It can be known from the variation process of the magnitude and direction of the principal stress in the rock mass of the deep roadways in the Jinchuan mining area that the variation trends of the magnitude and direction of the principal stress in the surrounding rock are similar. Given that the drastic changes in the direction of the principal stress in the roadway surrounding rock occur earlier than those in the magnitude of the principal stress, while the stabilization of the principal stress direction lags behind that of the principal stress magnitude, it can be inferred that after the excavation and unloading of the surrounding rock in the deep roadways of the Jinchuan mining area, and before the rock mass reaches the peak stress, the propagation path of the failure fractures in the rock mass undergoes

corresponding adjustments due to the change in the principal stress direction. Hence, the impact of principal stress rotation on the deformation and failure of the surrounding rock should be taken into account.

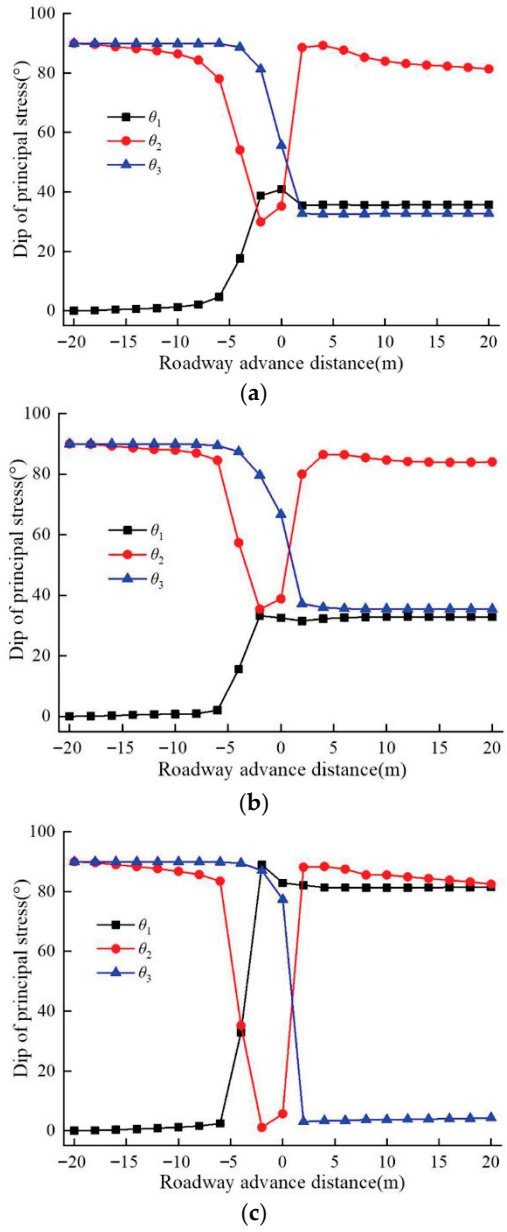

Figure 11. Evolution law of principal stress direction at different monitoring points in the surrounding rock of deep roadways: (**a**) roof surrounding rock; (**b**) floor surrounding rock; (**c**) sidewall surrounding rock.

As shown in Figure 12, these are the mining-induced stress rotation trajectories of the surrounding rock in the roof, floor, and sidewalls of the deep roadway. The mining-induced stress rotation trajectory of the surrounding rock in deep roadways refers to the path that mining-induced stress undergoes from its initial state to the mining-induced state. The stereographic projection enables the effective representation of spatial three-dimensional information on a two-dimensional plane, and the principal stress direction of the rock mass can be described by points in the stereographic projection. In the stereographic projection, the center position indicates that the principal stress direction is horizontal,

while the peripheral positions indicate that the principal stress direction is vertical. The circumferential scale of the stereographic projection represents the azimuth angle ψ_i of the principal stress direction inside the roadway rock mass, and the radial scale represents the dip angle θ_i of the principal stress direction inside the surrounding rock. Therefore, the rotation trajectory of mining-induced stress can be described by the change in the position of the points representing the principal stress in the stereographic projection.

Given that the dip angle range of each principal stress in the rock mass of deep roadways is from 0° to 90° and the azimuth angle ranges from 0° to 360°, under the initial state, the dip angle and azimuth angle of the maximum principal stress are 0° and 90°, respectively; the dip angle and azimuth angle of the intermediate principal stress are 90° and 0°, respectively; and the dip angle and azimuth angle of the minimum principal stress are 90° and 90°, respectively. When the roadway driving face is located 10 m in front of the monitoring section, the direction of the principal stress in the rock mass begins to change significantly; furthermore, as the distance from the roadway contour surface increases, the rotation angles of the maximum, intermediate, and minimum principal stresses all start to decrease. The direction of the maximum principal stress in the rock mass of the roof and two sidewalls of the deep roadway begins to rotate downward, while that in the surrounding rock of the floor begins to deflect upward, indicating that both the dip angle and azimuth angle of the maximum principal stress direction in the roadway surrounding rock are gradually increasing. The dip angle and azimuth angle of the maximum principal stress in the floor surrounding rock exhibit the largest rotation amplitude, with the dip angle ranging from 0° to 4.7° and the azimuth angle ranging from 90° to 180°. Along the survey line, the rotation amplitudes of both the intermediate and minimum principal stresses in the floor surrounding rock remain the largest, followed by those in the roof surrounding rock, with the smallest observed in the sidewall surrounding rock. When the roadway driving face advances to the monitoring section, the variation degree of the maximum, intermediate, and minimum principal stresses in the rock mass becomes more significant. Furthermore, the variation degree of the maximum principal stress in the surrounding rock of the roadway roof and floor increases slowly as the distance from the contour surface increases, while the variation degree of the maximum principal stress in the surrounding rock of the two sidewalls shows a trend of first increasing and then decreasing with the increase in distance from the contour surface.

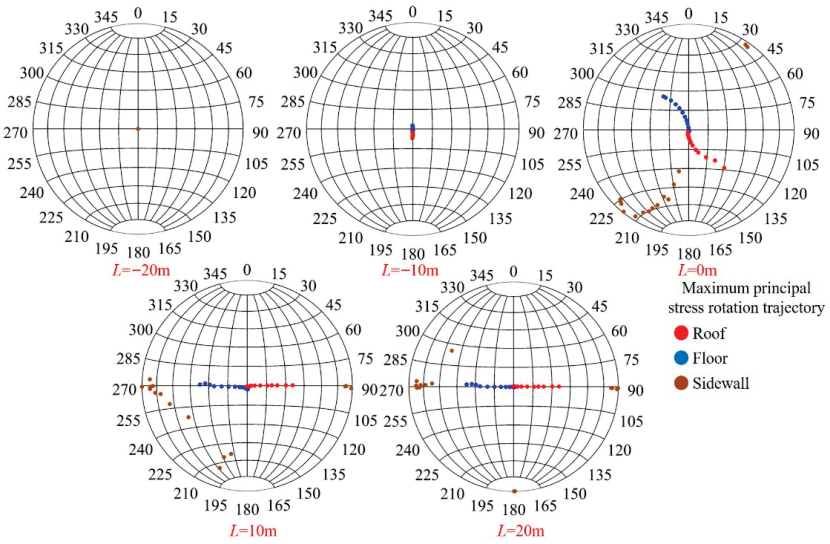

(**a**)

Figure 12. *Cont.*

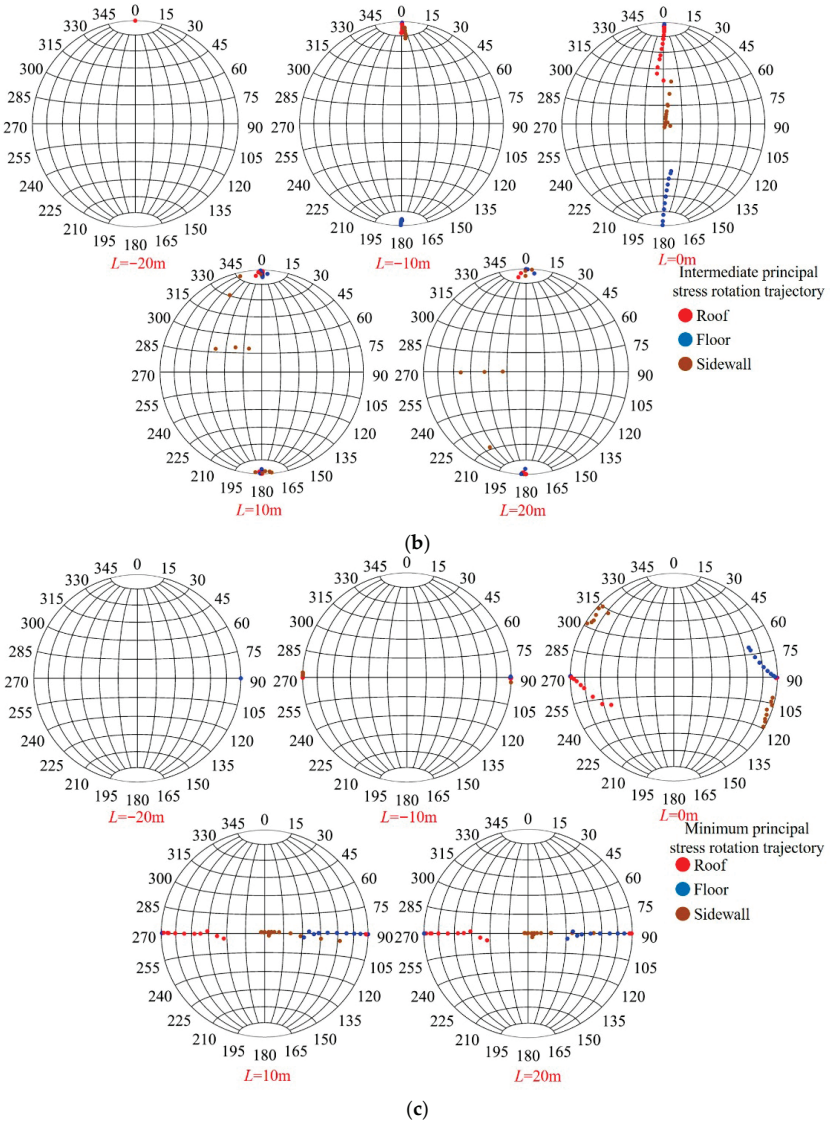

Figure 12. Mining-induced stress rotation trajectories of deep roadway surrounding rock: (**a**) maximum principal stress; (**b**) intermediate principal stress; (**c**) minimum principal stress.

The rotation directions of the maximum principal stress in the surrounding rock of the roadway roof and floor are 32.5°/143° and 40.9°/317°, respectively. The rotation direction of the maximum principal stress in the sidewall surrounding rock reaches a peak at 12 m along the survey line, approximately 82.9°/43.7°. This indicates that the direction of the maximum principal stress in the rock mass of the two sidewalls has rotated from being parallel to the *X*-axis to being perpendicular to the *X*-axis. The angle of the intermediate principal stress direction in the roadway roof surrounding rock shows a trend of first increasing and then decreasing as the distance from the contour surface increases. The angle of the intermediate principal stress direction in the floor surrounding rock exhibits a trend of slowly increasing with the increasing distance from the contour surface, while the intermediate principal stress direction in the sidewall surrounding rock rotates from being parallel to the *Y*-axis to being perpendicular to the *Y*-axis. The minimum principal stress in the roadway roof surrounding rock exhibits the highest rotational sensitivity, followed by that in the floor surrounding rock, with the lowest in the sidewall surrounding rock. When the driving face is 20 m behind the monitor section, the rotation degree of the principal stress in the roadway surrounding rock gradually tends to stabilize compared with the

previous stage. As the distance from the monitoring surface increases, the rotation angle of the maximum principal stress direction in the rock mass of the roof and floor gradually increases, while the angle of the maximum principal stress direction in the rock mass of the two sidewalls gradually decreases. At this time, the intermediate principal stress in the rock mass of the roof and floor of the deep roadway gradually returns to its initial state. Meanwhile, the minimum principal stress in the rock mass of the two sidewalls of the roadway changes from its initial state of being parallel to the *Z*-axis to a state of being perpendicular to the *Z*-axis. The angles of the minimum principal stress direction in the surrounding rock of the roadway roof and floor show an increasing trend as the distance from the contour surface increases.

As shown in Figure 13, by integrating the principal stress rotation characteristics of the three survey lines on the monitor section of deep roadway surrounding rock, the schematic diagram of the principal stress direction rotation in the surrounding rock after excavation disturbance can be drawn. After the excavation and unloading of deep roadways, the secondary stress causes different forms of structural failure to the surrounding rock. The failure range is approximately 4 m near the roof and floor surrounding rock, and about 2 m near the sidewall surrounding rock. The rotation dip angles and azimuth angles of the maximum principal stress in the surrounding rock of the roadway roof and floor show a trend of first increasing and then decreasing as the excavation step increases. As the roadway excavation step increases, the rotation dip angle of the maximum principal stress in the rock mass of the two roadway sidewalls first increases and then decreases, while the variation trend of the rotation azimuth angle of the maximum principal stress is the opposite. Ultimately, the direction of the principal stress in the rock mass located in the original rock stress area gradually returns to its initial state. Therefore, after the excavation and unloading of deep roadway surrounding rock, the rotation of principal stress leads to the generation of a large number of macroscopic fractures inside the rock mass, resulting in the rapid development and expansion of the surrounding rock plastic zone. The key areas for support should focus on the range where the principal stress rotation is intense.

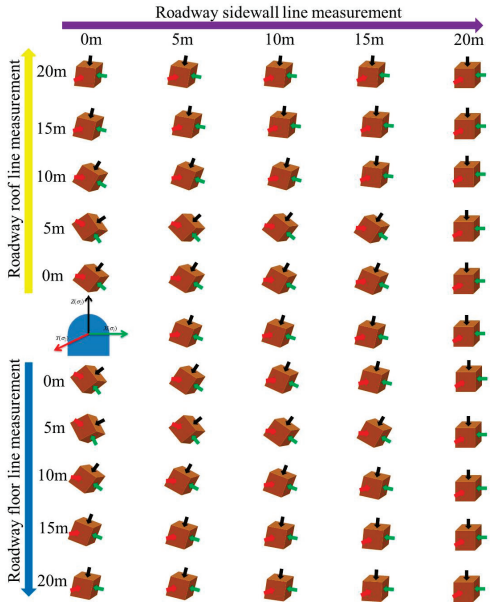

Figure 13. Schematic diagram of principal stress direction rotation in deep roadway surrounding rock.

4. Mining-Induced Stress Rotation Guiding Roadway Surrounding Rock Control

4.1. Determination of Dominant Rotation Trajectory of Mining-Induced Stress

Due to the fact that the development depth of the underground engineering in Jinchuan II Mine Area exceeds 1100 m, the surrounding rock of the deep roadway has undergone long-term geological tectonic movements, resulting in a large number of joints and fissures in the rock mass. Dominant joint and fissure groups in the surrounding rock of deep roadways can be obtained through on-site surveys. According to rock mechanics theory, the bearing capacity of roadway surrounding rock is affected by the spatial positional relationship between the loading direction and the direction of joints and fissures [32]. Therefore, during the development of large main ramps, the mining-induced stress rotation trajectory of the surrounding rock can be controlled by adjusting the roadway advancement direction, the principal stress direction, and the dip angle direction of the dominant joint and fissure groups can satisfy a certain relationship. An advantageous stress rotation trajectory can effectively enhance the self-stabilization capacity of the surrounding rock and reduce the number of roadway repair operations. Reference [33] provides the determination formulas for the uniaxial compressive strength of intact rock and fractured rock masses. When the calculation result of Equation (13) is smaller than that of Equation (12), it indicates that the stability of roadway surrounding rock is severely affected by the direction of joints and fissures, and the rock masses exhibit obvious damage and deterioration. At this time, the angle Φ between the direction of the maximum principal stress and the external normal direction of the joints and fissures surface satisfies Equation (14).

$$R_c = \frac{2C\cos\varphi}{1-\sin\varphi} \tag{12}$$

$$R_{cf} = \frac{2C_f}{\sin 2\phi(1-\cot\phi\tan\varphi_f)} \tag{13}$$

$$f(\phi) = \frac{C_f\cot\varphi_f(1-\sin\varphi)}{2C\cos\varphi} + \cos^2\phi - \cot\varphi_f\sin\phi\cos\phi \le 0 \tag{14}$$

where R_C and R_{CF} are the uniaxial compressive strengths of intact rock and fractured rock masses, in MPa; C, φ and C_f, φ_f are the cohesion and internal friction angles of intact rock and fractured rock masses, respectively, in MPa and °.

As shown in Figure 14, this is the curve shape distribution of the function $f(\Phi)$. When the angle Φ between the direction of the maximum principal stress and the external normal direction of the joints and fissures surface is equal to Φ_1 or Φ_2, the function $f(\Phi)$ is equal to 0 at this point. When the angle Φ is within the interval [Φ_1, Φ_2], the mechanical properties of the deep roadway rock mass are greatly affected by the occurrence of joints and fissures, and the excavation unloading of the surrounding rock reduces its overall stability. Therefore, the interval [Φ_1, Φ_2] can be defined as the sensitive area of the principal stress direction in the roadway surrounding rock. Since the occurrence distribution of joints and fissures in the deep roadway surrounding rock is mainly determined by early geological tectonic movements and is less affected by mining disturbances. The angle Φ between the direction of the maximum principal stress and the external normal direction of the joint and fissure surfaces can be kept away from the principal stress sensitive interval of the surrounding rock by changing the mining-induced stress rotation trajectory, to achieve the goal of improving the self-stabilization capacity of the roadway surrounding rock.

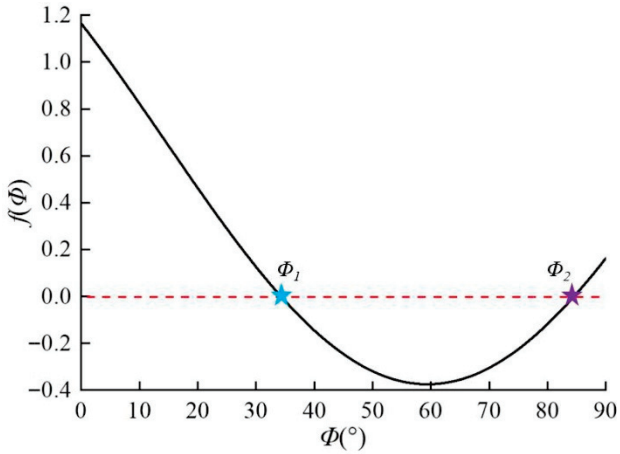

Figure 14. Determination of the sensitive area for principal stress direction in deep roadway surrounding rock.

As shown in Figure 15, the angles Φ_1 and Φ_2 between the direction of the maximum principal stress and the external normal direction of the dominant joint-fissure groups are represented as boundary lines in the stereographic projection diagram. The red area indicates that the overall strength of the deep roadway rock mass is greatly affected by mining-induced stress, and this area is defined as the sensitive area for the rotation direction of the principal stress. The green area indicates that the bearing capacity of the deep roadway surrounding rock is less affected by mining-induced stress, and it is defined as the principal stress direction retardation area. When the occurrence of the dominant joint-fissure groups in the deep roadway surrounding rock is determined, the sensitive area of the principal stress direction partially covers the stereographic projection diagram. To prevent the rock mass from increasing damage and deterioration due to mining-induced stress rotation, the rotation trajectory of the maximum principal stress in the surrounding rock can be made to deviate from the principal stress sensitive area or the range where the rotation trajectory falls into the principal stress sensitive area can be shortened by changing the roadway advancement direction. This turns the rotation trajectory of the principal stress into a dominant rotation trajectory, thereby improving the self-stabilization capacity of the roadway surrounding rock. When the occurrence of joints and fissures in the deep roadway surrounding rock is randomly distributed, the sensitive area of the principal stress direction fully covers the stereographic projection diagram. At this time, the rotation trajectory of mining-induced stress after excavation disturbance in deep roadways will drive the surrounding rock to undergo damage and deterioration, leading to instability of the roadway structure. To reduce the degree of damage and deterioration of deep roadway surrounding rock, the amplitude of the maximum principal stress rotation trajectory can be reduced by changing the roadway advancement direction, thereby shortening the extension length of the rotation trajectory in the stereographic projection diagram.

4.2. Asymmetric Coupling Support Scheme

After the excavation and unloading of deep roadways, the direction and magnitude of the principal stress in the rock mass change significantly, leading to varying degrees of non-uniform structural failure in the surrounding rock. Therefore, based on the influence of mining-induced stress rotation in deep roadways on the failure of the surrounding rock, the conventional support methods in Jinchuan II mining area are optimized, with enhanced support applied to the surrounding rock of the roof and floor where the principal stress rotates violently. The parameters of the anchor structural elements are shown in

Table 3. As shown in Figure 16, the conventional support scheme fails to effectively control the long-term rheological failure of the surrounding rock in the roadway roof, and the surrounding rock in the floor is not effectively supported. Under unsupported conditions, the maximum plastic zone depth of the surrounding rock in deep roadways is approximately 4.16 m. Therefore, for the surrounding rock of the two sides of the deep roadway, the conventional 2.25 m-long mortar bolts are still used for support, while the surrounding rock of the roof and floor is supported by 4.3 m-long anchor cables with a spacing and row spacing of 1 × 1 m. Under the original support conditions, the maximum plastic zone depth of the surrounding rock is approximately 3.94 m. The plastic zones in the floor and roof surrounding rock have not been effectively restrained, and they still belong to risk areas. Under the condition of asymmetric coupling support, the maximum plastic zone depth of the surrounding rock is approximately 2.31 m. The designed anchor length exceeds the plastic zone range of the surrounding rock in the entire cross-section of the roadway, allowing the anchors to fully exert their suspension effect. Compared with the unsupported condition, both the original support and the new support can reduce the plastic zone volume of the roadway surrounding rock by approximately 29.5% and 63.4% respectively, indicating that the asymmetric coupling support can significantly improve the stability of rock masses.

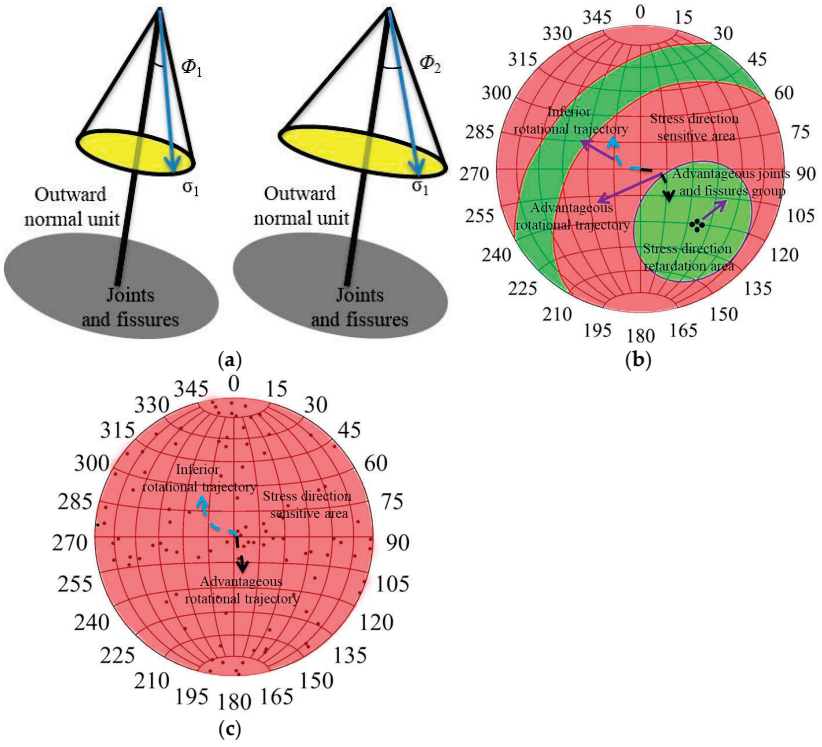

Figure 15. Influence of mining-induced stress rotation trajectory on the stability of deep roadway surrounding rock: (**a**) determination of the angle *Φ*; (**b**) determination of the dominant joints–fissures group; (**c**) random distribution of joints and fissures.

Table 3. The parameters of the anchor structural elements.

Structural Type	Yong Modulus (GPa)	Poisson's Ratio	Cross-Sectional Area (m^2)	Yield Tension (GPa)	Grout Cohesion (GPa)
Anchor	73.9	0.21	6×10^{-3}	5.12	1.75

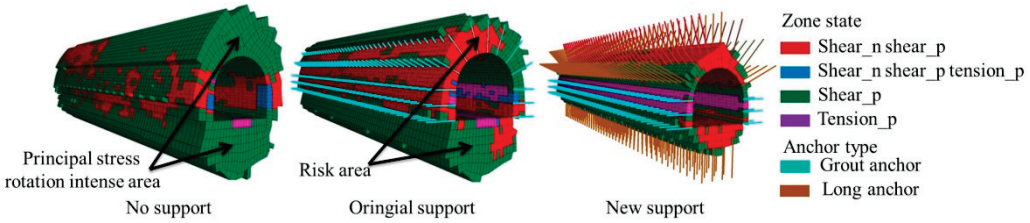

Figure 16. Distribution of plastic zones in deep roadway surrounding rock under different support methods.

5. Conclusions

(1) For the straight-wall semicircular arch-shaped diorite roadway, after the excavation and unloading of the surrounding rock, the variation processes of the magnitude and direction of the maximum, intermediate, and minimum principal stresses in the rock mass are similar, all following a trend of slow change at first, then drastic change, and finally stabilization. When the driving face is 4 m away from the monitor section, the adjustment of the principal stress magnitude in the surrounding rock is the most drastic, and the principal stress decreases rapidly after reaching its peak value. As the roadway driving face moves away from the monitoring section, the variation degree of the rock mass's principal stress magnitude gradually stabilizes and becomes significantly lower than the initial in situ stress value.

(2) For the straight-wall semicircular arch diorite roadway, the maximum principal stress rotation angle of the surrounding rock shows a trend of first increasing and then decreasing with the increase in excavation step distance, while the rotation angles of the intermediate and minimum principal stresses show a trend of first decreasing and then increasing with the increase in excavation step distance. Moreover, both the direction and magnitude of the principal stress in the rock mass located in the original rock stress area gradually return to their initial state.

(3) The characteristics of mining-induced stress rotation affect the bearing capacity and failure mode of the surrounding rock in deep roadways. Based on the spatial distribution characteristics of joints and fissures in the surrounding rock, the mining-induced stress rotation sensitive area can be characterized by stereographic projection diagrams. When the occurrence of joints and fissures is stable, the mining-induced stress rotation sensitive area partially covers the stereographic projection diagram, and the dominant mining-induced stress rotation trajectory should deviate from the sensitive area. When the occurrence of joints and fissures is randomly distributed, the mining-induced stress rotation sensitive area fully covers the stereographic projection diagram, and the dominant mining-induced stress rotation trajectory should reduce the rotation amplitude and shorten the extension length.

(4) Based on the variation process of the magnitude and direction of the principal stress in the surrounding rock of deep roadways, an asymmetric coupling support is proposed to strengthen the positions where the principal stress rotation in the rock mass around the anchorage is intense. The maximum plastic zone depth of the new support is reduced to 2.31 m, and the plastic zone volume is decreased by 63.4%. Asymmetric strong anchoring can control the degree of damage and deterioration of surrounding rock caused by mining-induced stress rotation, and significantly improve the overall stability of rock masses.

Author Contributions: Resources, D.L.; Writing—original draft, H.G.; Writing—review & editing, Z.H., W.R. and P.L.; Funding acquisition, D.L. All authors have read and agreed to the published version of the manuscript.

Funding: The authors are thankful for the financial support from the National Natural Science Foundation of China (Nos. 52374153 and 52504110) and Natural Science Foundation of Changsha of China (kq2502150).

Data Availability Statement: Data will be made available on reasonable request.

Conflicts of Interest: The authors declare that they have no known competing financial interests or personal relationships that could have appeared to influence the work reported in this paper.

References

1. Dai, L.; Feng, D.; Pan, Y.; Wang, A.; Ma, Y.; Xiao, Y.; Zhang, J. Quantitative principles of dynamic interaction between rock support and surrounding rock in rockburst roadways. *Int. J. Min. Sci. Technol.* **2025**, *35*, 41–55. [CrossRef]
2. Zhang, C.; Li, D.; Su, X.; Luo, P.; Ma, J.; Zhu, Q. Fracture behavior of thermally treated granite under compression-shear loading. *Int. J. Rock. Mech. Min. Sci. Géoméch. Abstr.* **2024**, *184*, 105966. [CrossRef]
3. Si, X.; Zhang, Z.; Li, X.; Yi, G.; Luo, Y.; Tan, L.; Han, K. Influences of maximum principal stress direction and cross-section shape on tunnel stability. *J. Rock. Mech. Geotech. Eng.* **2025**, *17*, 2159–2180. [CrossRef]
4. Han, Z.; Li, D.; Li, X. Dynamic mechanical properties and wave propagation of composite rock-mortar specimens based on SHPB tests. *Int. J. Min. Sci. Technol.* **2022**, *32*, 793–806. [CrossRef]
5. Gong, H.; Li, D.; Luo, P.; Ru, W.; Zhang, G.; Liu, Y. Floor heave mechanism and stiff control technology by I-beam for deep mine roadway. *Eng. Fail. Anal.* **2025**, *175*, 109600. [CrossRef]
6. Zhao, C.; Li, Y.; Liu, G.; Meng, X. Mechanism analysis and control technology of surrounding rock failure in deep soft rock roadway. *Eng. Fail. Anal.* **2020**, *115*, 104611. [CrossRef]
7. Yang, Z.; Tao, M.; Ranjith, P. Novel insights into grain size effect of stressed crystalline rock using weakened grain boundary model. *Int. J. Rock. Mech. Min. Sci. Géoméch. Abstr.* **2025**, *189*, 106098. [CrossRef]
8. Li, G.; Ma, F.; Guo, J.; Zhao, H.; Liu, G. Study on deformation failure mechanism and support technology of deep soft rock roadway. *Eng. Geol.* **2020**, *264*, 105262. [CrossRef]
9. Jing, H.; Wu, J.; Yin, Q.; Wang, K. Deformation and failure characteristics of anchorage structure of surrounding rock in deep roadway. *Int. J. Min. Sci. Technol.* **2020**, *30*, 593–604. [CrossRef]
10. Han, Z.; Li, J.; Wang, H.; Zhao, J. Initiation and propagation of a single internal 3D crack in brittle material under dynamic loads. *Eng. Fract. Mech.* **2023**, *285*, 109299. [CrossRef]
11. Wang, Z.; Sun, W.; Shui, Y.; Liu, P. Mining-induced stress rotation trace and its sensitivity to face advance direction in kilometer deep longwall panel with large face length. *J. China Coal Soc.* **2022**, *47*, 634–650.
12. Liu, J.; Zhu, K.; Zuo, J.; Sun, K.; Sheng, Y.; Jia, B. Soft rock deformation and failure modes under principal stress rotation from roadway excavation. *Bull. Eng. Geol. Environ.* **2024**, *83*, 83. [CrossRef]
13. Diederichs, M.; Kaiser, P.; Eberhardt, E. Damage initiation and propagation in hard rock during tunnelling and the influence of near-face stress rotation. *Int. J. Rock. Mech. Min. Sci. Géoméch. Abstr.* **2004**, *41*, 785–812. [CrossRef]
14. Kaiser, P.; Yazici, S.; Maloney, S. Mining-induced stress change and consequences of stress path on excavation stability—A case study. *Int. J. Rock. Mech. Min. Sci. Géoméch. Abstr.* **2001**, *38*, 167–180. [CrossRef]
15. Eberhardt, E. Numerical modelling of three-dimension stress rotation ahead of an advancing tunnel face. *Int. J. Rock. Mech. Min. Sci. Géoméch. Abstr.* **2001**, *38*, 499–518. [CrossRef]
16. Du, S.; Wu, G.; Zhao, Y.; Ma, L. Re-orientation of principal stresses during tunnel excavation: Model development and support strategy. *Alex. Eng. J.* **2024**, *107*, 591–613. [CrossRef]
17. Ma, J.; Li, D.; Du, S.; Han, Z.; Luo, P.; Zhao, J. Comparison of subcritical crack growth and dynamic fracture propagation in rocks under double-torsion tests. *Int. J. Rock. Mech. Min. Sci. Géoméch. Abstr.* **2023**, *56*, 7905–7922. [CrossRef]
18. Colwell, M.; Frith, R. Why uniaxial compressive strength and Young's modulus are commonly poor indicators of roadway roof stability-except in the tailgate. In Proceedings of the International Conference on Ground Control in Mining, Morgantown, WV, USA, 1–3 August 2006.
19. Li, K.-S.; Luan, Y.-Q.; Zhang, J.-P.; Liu, C.-X. Experimental study on mechanical behavior, AE response and energy evolution of fissure-filled sandstone from mine roadway under conventional triaxial compression. *Theor. Appl. Fract. Mech.* **2024**, *130*, 104334. [CrossRef]
20. Kong, P.; Jiang, L.; Jiang, J.; Wu, Y.; Chen, L.; Ning, J. Numerical analysis of roadway rock-burst hazard under superposed dynamic and static loads. *Energies* **2019**, *12*, 3761. [CrossRef]
21. Zhou, X.; Zhang, D.; Nowamooz, H.; Jiang, C.; Ye, C. Investigation on damage and failure mechanisms of roadway surrounding rock triggered by dynamic–static combined loads. *Rock. Mech. Rock. Eng.* **2022**, *55*, 5639–5657. [CrossRef]

22. Han, Z.; Yan, Z.; Li, D.; Wang, H.; Wang, H. Dynamic fracture mechanism from a pre-existing flaw in granite: Insights from grain-based modelling. *Soil. Dyn. Earthq. Eng.* **2024**, *184*, 108810. [CrossRef]
23. Ma, Q.; He, X.; Zhou, Y.-G.; Chen, Y.-M.; Han, Y.-S. An approach to DEM simulation of hollow torsional shear tests for achieving general loading paths. *Comput. Geotech.* **2024**, *172*, 106402. [CrossRef]
24. Zhou, H.; Jiang, Y.; Lu, J.; Gao, Y.; Chen, J. Development of a hollow cylinder torsional apparatus for rock. *Rock. Mech. Rock. Eng.* **2018**, *51*, 3845–3852. [CrossRef]
25. Zuo, J.; Ma, Z.; Xu, C.; Zhan, S.; Liu, H. Mechanism of principal stress rotation and deformation failure behavior induced by excavation in roadways. *J. Rock. Mech. Geotech. Eng.* **2024**, *16*, 4605–4624. [CrossRef]
26. Xiong, X.; Nie, W.; Ouyang, Y.; Dai, J.; Huang, Y. Principal stress rotation effect and multi-factor coupling support optimization in roadways of inclined coal seams. *Sci. Rep.* **2025**, *15*, 25628. [CrossRef]
27. Wang, J.C.; Wang, Z.H.; Yang, S.L. Stress analysis of longwall top-coal caving face adjacent to the gob. *Int. J. Min. Reclam. Environ.* **2020**, *34*, 476–497. [CrossRef]
28. Wang, J.; Wang, Z.; Yang, S. A coupled macro- and meso-mechanical model for heterogeneous coal. *Int. J. Rock. Mech. Min. Sci. Géoméch. Abstr.* **2017**, *94*, 64–81. [CrossRef]
29. Lu, Z.; Ju, W.; Zhao, Y.; Wang, H.; Zheng, J.; Liu, A. Analysis of the mining induced stress rotation influence on fault stability. *Rock Soil Mech.* **2019**, *40*, 4459–4466.
30. Oliva, S.J.; Ebinger, C.J.; Rivalta, E.; Williams, C.A.; Wauthier, C.; Currie, C.A. State of stress and stress rotations: Quantifying the role of surface topography and subsurface density contrasts in magmatic rift zones (Eastern Rift, Africa). *Earth Planet. Sci. Lett.* **2022**, *584*, 117478. [CrossRef]
31. Zheng, Z.; Feng, X.-T.; Zhang, X.; Zhao, J.; Yang, C.-X. Residual strength characteristics of cjpl marble under true triaxial compression. *Rock. Mech. Rock. Eng.* **2019**, *52*, 1247–1256. [CrossRef]
32. Wang, J.; Wang, Z.; Tang, Y.; Sun, W.; Feng, Y. Regional failure mechanism of main roof and zonal method for ground control inkilometer-deep longwall panel with large face length. *J. China Coal Soc.* **2023**, *48*, 3615–3627.
33. Jaeger, J.C. Shear failure of anistropic rocks. *Geol. Mag.* **1960**, *97*, 65–72. [CrossRef]

MDPI AG
Grosspeteranlage 5
4052 Basel
Switzerland
Tel.: +41 61 683 77 34

MDPI Books Editorial Office
E-mail: books@mdpi.com
www.mdpi.com/books

Academic Open
Access Publishing

mdpi.com

ISBN 978-3-7258-6969-5